ABSTRACT

Title of dissertation: MEASUREMENTS AND MODELING OF THE UNSTEADY FLOW AROUND A THIN WING

Field Hogan Manar, Doctor of Philosophy, 2018

Dissertation directed by: Associate Professor Anya R. Jones
Department of Aerospace Engineering

Unsteady separated flows are encountered in many applications (e.g. dynamic stall in helicopters and wind turbines). Recent efforts to better understand the problem of unsteady separated aerodynamics have been prompted by growing interest in creating small-scale flight vehicles, termed micro air vehicles (MAVs). Because of their small size, all MAVs operate at low Reynolds numbers. In that regime, flow separation is a common occurrence either due to Reynolds number effects or aggressive motion. The dominant and most studied feature of these flows is the leading edge vortex (LEV). The LEV receives its circulation from a shear layer emanating from the leading edge of the wing, where the production of circulation occurs. In spite of its importance to the flow and the resulting forces, the production of circulation has received relatively little experimental attention. To fill this gap, water tank experiments on a surging flat plate wing at a high angle of attack have been performed at varying Reynolds number, acceleration, angle of attack, and aspect ratio. These experiments measured time resolved forces, LEV location, LEV circulation, and leading edge circulation production. These data were then used to explore how the LEV

and the circulation production reacts to changes in kinematic parameters. This resulted in the proposal of a new relationship between the wake state and the leading edge circulation production, termed the boundary layer analogy (BLA). Additionally, existing potential flow modeling techniques were implemented and evaluated against the present experimental data. This analysis focused on evaluating the suitability of applying the Kutta condition at the leading edge. The Kutta condition was found to be a valid leading edge condition capable of predicting the LEV circulation seen in experiments. Representing the shed wake with multiple vortices was found to be necessary to capture the dynamics of vortex roll up and shedding. Other models struggle to account for these events, though simpler models may offer a better route to intuitive understanding of the fluid dynamic origin of the forces. The experimental data collected here, coupled with the novel analysis of the modeling techniques in the light of the leading edge circulation measurements, constitutes a significant step forward in the modeling and understanding of unsteady separated flows.

MEASUREMENTS AND MODELING OF THE UNSTEADY FLOW AROUND A THIN WING

by

Field Hogan Manar

Dissertation submitted to the Faculty of the Graduate School of the
University of Maryland, College Park in partial fulfillment
of the requirements for the degree of
Doctor of Philosophy
2018

Advisory Committee:

Professor Anya R. Jones, Chair/Advisor
Professor Kenneth Kiger
Professor Stuart Laurence
Professor Derek Paley
Professor Amir Riaz, Dean's Representative

Dedication

To my intelligent, beautiful, kick-ass wife, Aditi. Thanks for sticking with me.

Acknowledgments

First and foremost, I would like to thank my wife Aditi for putting up with countless hours of boring talk about fluid flows. I couldn't have done it without you, darling. I would also like to thank my advisor Dr. Anya Jones, for all of the support, encouragement, and guidance towards this degree. Similarly, my labmates Peter Mancini, Gino Perotta, and Andrew Lind have been absolutely a blast to spend the last five and half years working with. This thesis represents nearly as much of their work as it does mine. Thanks also to my mom and brother for enduring the long distances and occasional rants about obscure topics. Finally I would like to gratefully acknowledge the Air Force Office of Scientific Research and the National Science Foundation for their financial support. This work was supported under AFOSR grant FA9550-12- 1-0251 and NSF grant CBET 1510962.

Table of Contents

List of Figures

List of Abbreviations

α	The plate angle to the horizontal, the angle of attack
γ	Vortex sheet strength
Γ	Vortex circualtion
Γ_1	A vortex location criterion
ν	Fluid kinematic viscosity
ω	Vorticity
ρ	Fluid density
ζ	Complex coordinate in the mapped cylinder plane
a	Half-chord
A	Wing planform area
$\mathcal{AR}$	Aspect ratio
b	Wing span location or pitch point, depending on context
c	Wing chord
C_D	Coefficient of drag for whole wing
C_d	Sectional coefficient of drag
C_L	Coefficient of lift for whole wing
C_l	Sectional coefficient of lift
C_N	Coefficient of normal force for whole wing
C_n	Sectional coefficient of normal force
C_T	Coefficient of tangential force for whole wing
C_t	Sectional coefficient of tangential force
Re	The chord based Reynolds number
s/c	Wing travel distance, in chords
s_a/c	The acceleration distance, in chords of travel
t	Wall clock time
t^*	Non-dimensional time, $t^* = tU/c$
U	The plate horizontal velocity
U_f	The final wing velocity
V	The plate vertical velocity
$\tilde{V}$	The place normal velocity
W	A complex velocity, $W = u - iv$
x/c	The LEV horizontal displacement from the leading edge
y/c	The LEV vertical displacement from the leading edge
$\tilde{z}$	Complex coordinate in the plate relative frame
z	Complex coordinate in the lab frame
BLA	Boundary layer analogy
FOV	Field of view
LEV	Leading edge vortex
MAV	Micro air vehicle
PIV	Particle image velocimetry
TEV	Trailing edge vortex

Chapter 1: Introduction

Unsteady aerodynamics has been studied since the early days of the aerospace field, spurred largely by the aeroelastic problems encountered in fixed wing flight [4]. As a result, the theories of attached unsteady flow are well developed and understood. The same cannot be said of unsteady flows with leading edge separation, which are still an open research topic.

1.1 Motivation and Approach

The original impetus for this work stemmed from interest in reproducing insect flapping wing flight in small unmanned "micro air vehicles" (MAVs). The realization of this dream has not yet come to pass in a meaningful way, due largely to limited aerodynamic understanding and a lack of applicable models of the unsteady separated flows that such vehicles rely on. Other factors have certainly contributed to the difficulties in creating a flapping wing MAV, such as the mechanical complexity required, battery energy density, and difficulty in formulating control laws; it is important to acknowledge that aerodynamic understanding is not the sole hurdle. However, the focus of the present work is on addressing the aerodynamic issues. Study of flapping wing aerodynamics has revealed that the flows encountered in flapping wing flight share similar aspects to stalled transient flows in general. Thus the lessons learned here are applicable to a broad range of problems and can be applied to insect flight, MAV gust encounters, dynamic stall, and wind turbines. In these problems flow sep-

aration is often taken as a foregone conclusion, either due to Reynolds number effects or aggressive motion, and the goal becomes leveraging this state of affairs instead of fighting it.

The problem at hand then, is to better understand and predict the low Reynolds number, unsteady, separated, transient flows that are endemic to flapping wing MAV flight and common in many other applications. In order to study the phenomena of leading edge separation from a first principles approach, the problem has been systematically reduced. The first reduction is to use a rectangular flat plate wing as a representative geometry. The airfoil used is a thin flat plate with square edges; this is not too far removed from an insect wing and serves as a canonical geometry for experimentation. The second reduction is to distill the flapping wing kinematics from an oscillatory three degree-of-freedom flapping about a shoulder joint to a rectilinear surge at constant angle of attack. These simpler kinematics are closest to the start and mid-stroke portions of the full insect kinematics, but still differ in their disregard of the rotation motion component. Both of these simplifications are common to the field (e.g. [5]). The reward for making these simplifications is in limiting the parameter space and minimizing obfuscating factors at a relatively small cost in lost flow physics. It is these simplifications that also grant the results their broad applicability by focusing on the fundamental fluid processes and underlying sources of the fluid forces. The full wake is considered, but the driving process behind the flow is shown to be the generation of circulation at the leading edge.

The rate at which circulation is produced at the leading edge drives the flow as a whole. The leading edge vortex (LEV) that forms from the shear layer emanating from the leading edge dominates the unsteady force and moment production of the wing [6, 7]. The leading edge circulation production is the underlying process that determines the strength of the LEV, and how that changes in time. The strength of the LEV directly impacts the induced flow over the wing which in turn drives

the LEV's own convection. Thus the circulation production underlies the entire wake structure. From an inviscid modeling perspective, it encapsulates the critical influence of viscosity and is the most important and least understood boundary condition.

In spite of its importance to the overall flow, only a handful of experimental studies attempt to directly measure the circulation production at the leading edge (e.g. Panah *et al.* [2] and Wojcik and Buchholz [8]). Further, none of the studies in the literature are conducted on translating wings starting from rest; the kinematics used employ either rotation or reciprocating plunge. Rotation, which has an attached LEV, obscures the interplay between LEV convection and circulation production. Reciprocating plunge has some LEV convection, but artificially limits LEV growth through the kinematics. Thus there is a distinct need to study the translation start-up from rest case; indeed this has classically been the most fundamental case for unsteady aerodynamic studies as in Wagner's seminal work [9]. More common than circulation production measurements are experiments measuring total LEV circulation. Measuring the circulation as a whole is a step in the right direction, but it masks the dynamics of production. To understand the circulation results, the studies in the literature generally attempt to connect the circulation in the LEV with the kinematics parameters. They are not concerned with the connection between the wake state and the circulation production. This is to the detriment of these studies, as the wake effect on the circulation production ties the whole problem together and is the driving factor in the overall wake behavior.

On the other hand, those who seek to model the flow and predict the forces from first principles tends use only the flow visualization and force measurements from the experimental studies. The force results of a given model are an amalgamation of many parts of the model interacting, and so using them to diagnose the success of a model leads to vague answers at best. This state of affairs has lead to the continued use of the leading edge Kutta condition while simultaneously doubting its validity. Here

again, direct measurements of the circulation production at the leading edge could serve to shed light on the appropriate treatment of the leading edge in the models.

To remedy these gaps in the literature, experiments have been conducted to directly measure the circulation production at the leading edge of a wing starting from rest, and these measurements form the essential content of this thesis. The thesis also evaluates the current low order physically based modeling techniques in the context of these measurements. The goal of the model evaluation is to assess the strengths and weaknesses of the current methods and identify avenues for improvement. Close inspection of the models also aids in understanding how the forces produced relate to the fluid processes.

1.2 Present Work

The present work seeks to improve the state of the art in flapping wing MAV vehicle design and dynamic stall prediction by addressing the need for improved aerodynamics measurements and modeling. The condition at the leading edge is given particular consideration because the leading edge closure term is the critical, and least studied, portion of low order potential models. Canonically, the Kutta condition is applied there, largely due to lack of other options. The caveat is usually then given that Kutta condition is inappropriate for the leading edge.

This thesis combines experimental measurements of force, LEV location and circulation, and most importantly, leading edge circulation production to evaluate the current state-of-the-art low order modeling techniques. The validity of applying the Kutta condition at the leading edge is evaluated against experimental measurement of the circulation production. Further, a new relationship between the flow state and the circulation production is proposed and evaluated across a broad range of kinematics. In the lead-up to this evaluation, significant contributions to the measurement and quantification of flapping wing relevant flow were also made.

The contributions of the present work are:

1. To add to the existing understanding of the forces and wake features on starting wings at high angles of attack. Qualitatively, this entails relating the observed wake features to the generation of circulation at the leading edge. Additionally, novel quantitative measurements of the LEV evolution and leading edge circulation production will be taken. This adds to the existing body of knowledge on transient flows.

2. To evaluate the currently available low order potential flow models in their ability to predict the forces experienced by the wing, and to identify the underlying reasons for their successes and failures. This constitutes a rare evaluation of the models by an experimentalist, rather than the model's creator.

3. To verify or disqualify the use of the Kutta condition as an acceptable model of leading edge separation.

4. To propose a new relationship for the leading edge circulation production built upon the observed characteristics (both qualitative and quantitative) of the wake.

This work not only extends the previous experimental measurements with regards to their scope, but also provides new circulation flux data for transient wing motions. It also serves as one of the first evaluations of potential models against measured wake data. Taken as a whole, the data presented here constitute a significant step forward in documenting, understanding, and predicting the behavior of stalled transient flows. These data are immediately applicable the enhancement of MAV design techniques and dynamic stall modeling.

1.3 Dissertation Outline

The thesis opens with a review of the previous work and an introduction to potential flow models in chapter 2. Chapter 3 describes the experimental methods used in the present work. A detailed look at a single test case is then given in chapter 4 to contextualize the parameter variations of the following chapter. Chapter 5 introduces variation of Reynolds number, acceleration, angle of attack, and aspect ratio used to inform scalings of time and circulation production. Chapter 6 describes the models used in this work. Chapter 7 then evaluates the model predictions on the basis of forces, LEV location and circulation, and leading edge circulation generation against the measured data. Finally, chapter 8 provides a summary of the work, highlights the key contributions, and gives suggestions for future study.

Chapter 2: Background

2.1 Micro Air Vehicles

The MAV concept was birthed by the Defense Advanced Research Projects Agency (DARPA) [10] as part of the global trend towards miniaturization. The goal of the project was to develop small man-portable vehicles that could accomplish reconnaissance and surveillance tasks in a close quarters environment. This mission places lofty requirements on the vehicles [11], which are preferably hover capable, agile, and have high gust tolerance. Meeting those requirements is an ongoing challenge.

There are three main approaches to solving the MAV design problem: fixed wings, rotary wings, and flapping wings. Fixed and rotary wing flight is relatively well understood, as they both rely on steady aerodynamic mechanisms to produce lift [14]. The fixed wing avenue of research has produced viable concepts like the Aerovironment BlackWidow fixed wing MAV [12], shown in figure 2.1a. Fixed wings lack the ability to hover, however, which makes them unsuitable for deployment in tight interior environments and for steady imaging from a fixed point of view. Rotary wing flight allows for hover, and has produced a plethora of quad-rotor (e.g. [15, 16]), and co-axial concepts (e.g. [17, 18]). At small scales, however, rotary wings are not as efficient as either their fixed wing MAV counterparts [19] or their full scale brethren [20]. The latent inefficiencies have, in part, been overcome by more recent work [21], but the problem largely remains. Insect-inspired flapping wing flight presently has only a few extant examples, including the Robotic Hummingbird project

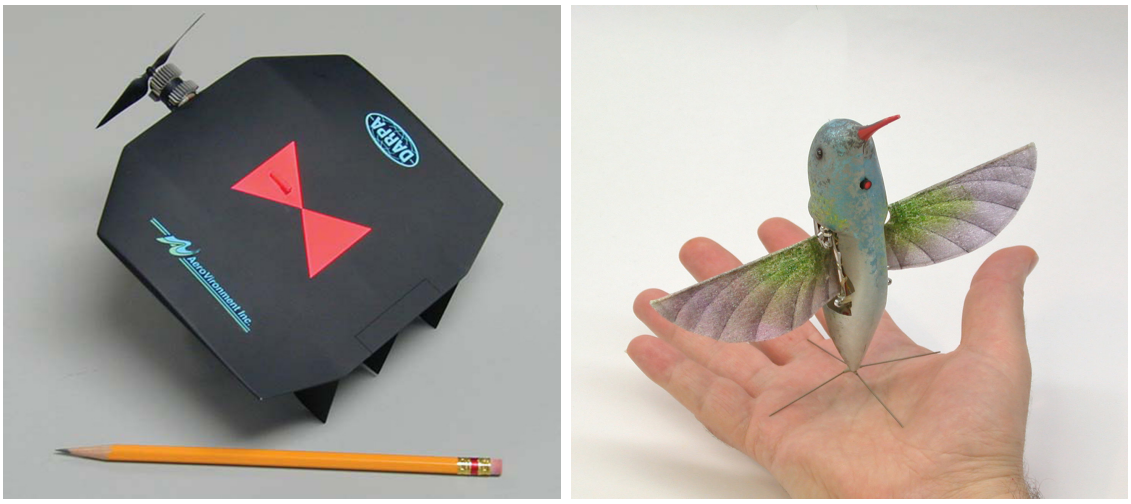

(a) The Black Widow fixed wing MAV [12] (b) The NanoHummingbird flapping wing MAV [13]

Figure 2.1: Examples of MAVs.

[22], Aerovironment's NanoHummingbird [13] shown in figure 2.1b, and the Harvard Robofly project [23]. The relative dearth of flapping wing examples compared with the fixed and rotary wing solutions is due to the unique difficulties in implementing them. The basic premise of using reciprocating wings to supply all the flight forces results in a high degree of mechanical complexity [24, 25]. Similarly, the best methods for control of these vehicles are also still an open research question [26]. Finally, the aerodynamic theories currently available are ill equipped to deal with leading edge flow separation that is crucial to this mode of flight. The observed, often dazzling, maneuverability and efficiency of natural flapping wing fliers (e.g. dragonflies and hummingbirds) makes them a continued target for man made flight in spite of those hurdles. Flapping wing flight promises performance beyond what is possible with more traditional fixed or rotary wing solutions [11, 27].

Small fliers of any type must overcome the difficulties inherent to the low Reynolds number flight regime [28]. MAV applications naturally operate in a Reynolds number range of $Re = \mathcal{O}(10^2 - 10^5)$, much lower than traditional aerospace applications. This change in Reynolds number leads to poor performance of traditional thick

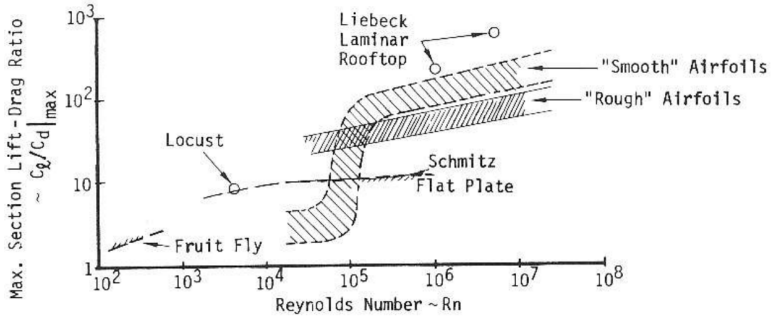

Figure 2.2: Airfoil efficiency trends as a function of Reynolds number, adapted from Mueller [1].

airfoils [29, 30]. The lift to drag performance is summarized in figure 2.2, which shows trends in lift-to-drag ratio, C_l/C_d, as a function of Reynolds number. The lift-to-drag ratio is a good measure of efficiency, as it is the ratio between the useful lift force produced and the drag force. As Reynolds number decreases, the figure shows the clear drop in conventional airfoil performance near $Re = 10^5$. This drop-off as Reynolds number decreases is associated with the onset of stall at lower angles of attack as the boundary layer becomes increasingly laminar and thus more susceptible to separation, resulting in lower values of peak C_l [31, 32]. MAV scale Reynolds numbers are below the drop-off in performance. Additionally, the small size of these vehicles means that they are often subjected to large gusts and rapid maneuvers. The combined effect of low Reynolds numbers and the likelihood of encountering large angles of attack makes separation and dynamic stall nearly a foregone conclusion for MAV flight. Instead of fighting separation, flapping wing flight relies on unsteady separation to produce the lift required [33].

The term "flapping wing flight" also encompasses avian inspired systems. The aerodynamic mechanisms involved in avian flight, while still highly unsteady, are based on attached flow. The presently available theories and tools (e.g. Willis *et al.* [34]) are mature enough to solve the problem of attached flow, even in highly unsteady cases. In contrast, the focus here is on separated flows. Although it is certainly possible for an avian-style flapping wing vehicle to encounter separated

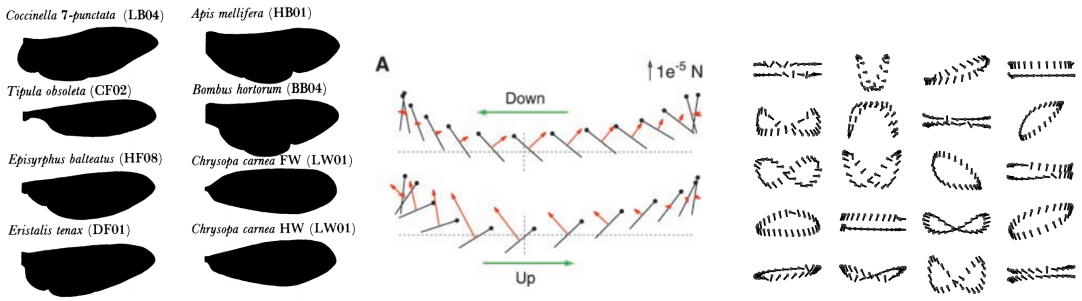

(a) Wing silhouettes from [35]

(b) Measured wing kinematics from [38]

(c) Wing kinematic examples from [43]

Figure 2.3: Examples of insect wing data from the literature.

flow, these systems are not the focus here.

2.2 Insect Flight

Insects have been the subject of much study in the quest to understand their flight ability. Much information has been documented for both their morphology and their kinematics (e.g. [35, 36, 37, 38, 39]). This information serves as a starting point for aerodynamic studies and flapping wing MAV design.

Inspection of insect wings reveals a few basic trends in their shape, structural properties, and kinematics:

- Insect wings are roughly elliptical in nature, as shown in figure 2.3a.
- Broad surveys of insect wings have shown them to have aspect ratios, AR, between 2 and 5 [40].
- Insect wings are quite thin, with a thickness to chord ratio of 3-6% [35, 41].
- Insect wings are flexible, primarily in the chord-wise direction. [37]
- Insects flap their wings in complex figure of eight patterns [42]. Some examples are shown in figure 2.3b and 2.3c.

Using this information about insect wing shapes and kinematics as a guide, experimental studies into the aerodynamic mechanisms sought to determine the aerodynamic mechanisms behind insect flight. Ellington noted early on that insects must be using a novel mechanism of force production [33]. His analysis of the insect kinematics, wing area, and insect weight indicated that the coefficients of lift required to sustain hovering flight were beyond those achievable by conventional airfoils in steady flight. Initial theories for the mechanism behind this extra lift, such as clap-and-fling [44] or wake capture [45], explained some of the extra lift. The primary mechanism for enhanced lift was eventually narrowed to the leading edge vortex (LEV) [46, 47].

As a surrogate for full insect kinematics, many studies have instead used translating wing kinematics to study the problem at hand (e.g. Dickinson and Gotz [5]). This is generally done to produce simpler, easier to understand flows. As such, rectilinear pitching and surging kinematics have been particularly well documented in both experiment [48, 49, 50] and computational studies [51, 52, 53, 54]. Rotating wings, i.e. a wing revolving around an axis, are another common surrogate for full insect kinematics. These maintain the primary stroke plane rotation of insect, but ignore the out of plane motion. They have also received considerable study [55, 56, 57, 58, 59, 60].

2.3 The Leading Edge Vortex

The leading edge vortex (LEV) is a prominent feature in both dynamic stall events [14] and insect flight [46]. The vortex forms when the motion is aggressive enough to cause the flow to separate from the leading edge of the wing and roll up into a vortex above the suction side of the wing, as in the schematic shown in figure 2.4a. This process was initially observed through the use of dye and bubble flow visualization techniques, with some representative results shown in figure 2.4. Insect wings have a thin profile to essentially force this to occur [35, 41].

The wake behind the wing is dominated by a leading edge vortex, which in

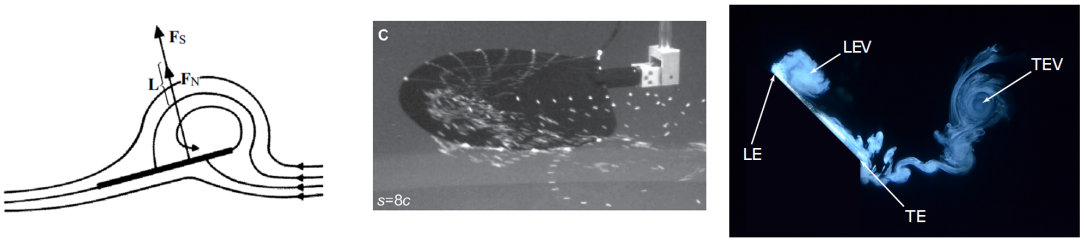

(a) A schematic of the LEV, adapted from [5].

(b) Bubble flow visualization of the LEV on a rotating wing, adapted from [45].

(c) Dye flow visualization of the LEV on a translating wing, adapted from [61].

Figure 2.4: Examples of the LEV from the literature.

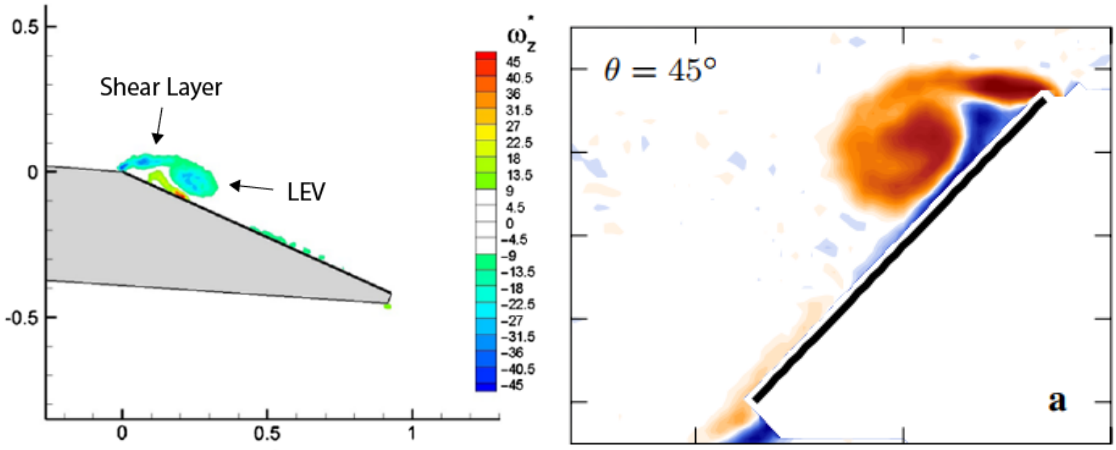

(a) Adapted from [8].

(b) Adapted from [63].

Figure 2.5: Vorticity fields obtained from PIV showing the LEV and feeding shear layer.

turn dominates the force production of the wing [5, 62]. The LEV forms because the sharp leading edge forces the boundary layer to separate there, which then rolls up into a single vortex, as seen in figure 2.5. The circulation in the LEV originates at the leading edge, and is then convected by means of a shear layer extending from the leading edge.

2.3.1 Circulation Production

As previously discussed, numerous PIV studies have confirmed that the primary source of circulation for the LEV is a shear layer emanating from the leading edge

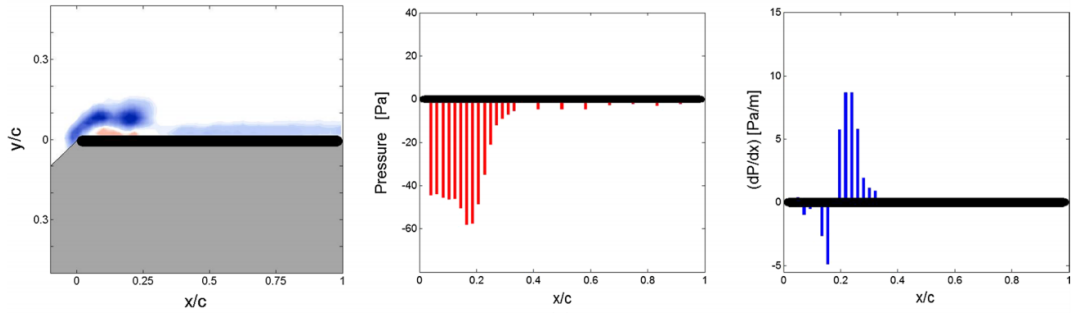

Figure 2.6: PIV, pressure tap, and computed pressure gradient results adapted from Panah *et al.* [2].

of the wing. This has inspired several models of LEV growth based on the leading edge conditions [8, 64, 65, 66, 67, 68]. Most of these studies are concerned with an oscillating wing case (e.g. Buchholz *et al.* [64] and Widmann and Tropea [68]), so the scaling laws they present are largely based on the parameters of the oscillation. This obfuscates the underlying mechanisms for the circulation growth. For example, including the amplitude as a scaling factor, as in Buchholz *et al.* [64], does not make it clear if the vortex is larger because of the increased wing speed or greater distance covered.

Sattari *et al.* [65] proposed using the boundary layer exterior velocity to capture the flux of vorticity in a feeding sheer layer from the trailing edge of a waving plate. Kriegseis *et al.* [66] built on this and used the total flow velocity at the leading edge to successfully collapse the LEV circulations of a plunging wing. In their paper, the total flow velocity is used as a surrogate for the strength of the feeding shear layer, in a very similar fashion to the boundary layer analogy proposed here. Kriegseis *et al.* do not, however, propose a mechanism for determining this velocity outside of direct measurement. Wong *et al.* [67] and Widmann *et al.* [68] use the same philosophy, and do propose a representative velocity. Their goal is an estimate of the size of the LEV, and so they use their representative velocity to estimate the mass flux. However, they still fail to include a wake influence. These pieces of work share a conceptual basis with the present work, but differ in their ultimate form and application.

Vorticity flux measurements similar to those conducted here have been carried out by Panah *et al.* [2] and Wojcik and Buchholz [8]. Sample results from Panah *et al.* [2] have been reproduced in figure 2.6. These studies were primarily concerned with establishing the importance of the secondary vorticity produced in the opposite sign boundary layer below the LEV, seen as the red vorticity in figure 2.6. The analysis of Lighthill [69] indicated that the surface pressure gradient is directly related to the vorticity production at a fluid/solid interface. To measure the secondary vorticity production, Panah *et al.* 's study included surface pressure measurements, as also shown in figure 2.6. This makes for an excellent depiction of the LEV-induced suction. Based on these pressure measurements, both Panah *et al.* [2] and Wojcik and Buchholz [8] concluded that the opposite sign vorticity production on the surface of the plate contributed approximately half the magnitude of circulation as the shear layer from the leading edge to the circulation of the leading edge vortex. Both of these studies, however, focused on kinematics dissimilar to the present surge case: Panah *et al.* [2] used an oscillating plunging wing, and Wojcik and Buchholz [8] used a rotating wing. In both of these cases the LEV is held nearer to the wing than is seen in pure translation, likely resulting a stronger secondary boundary layer below the LEV.

2.4 Rotation

Flapping and rotary wings have a rotational component to the wing's motion. In contrast, fixed wing MAVs operate purely in translation. This has been shown to result in markedly different behavior of the LEV [40]: in the rotation case, the LEV remains attached and persists throughout the motion, while it continually sheds and reforms for translation.

Lentink and Dickinson [40] compared the two types of kinematics in surge and introduced the Rossby number as a measure of the amount of rotation, and hence Coriolis force, present on the wing. They defined the Rossby number as $Ro = R/c$,

where R is the wing tip radius from axis of rotation, and c is the wing chord. By this definition, the Rossby number is nearly equivalent to wing aspect ratio. Studies varying this parameter [59, 70, 71, 72] have reached similar conclusions as those directly comparing translation to rotation [73, 74] . Rotation dominates at low Rossby numbers, resulting in a stable LEV that persists throughout the wing motion [75]. This is in stark contrast to the rectilinear case ($Ro = \infty$), where the LEV sheds from the wing. As the Rossby number increases, a breakdown of the coherent structures occurs and the LEV becomes less well defined [70]. LEV breakdown also occurs across the span of rotating wings, as the local Rossby number increases [72]. This difference in LEV behavior between the rectilinear and rotating (i.e. vortex attachment or shedding) has drawn much attention.

Many studies have attempted to identify the mechanism that enables the stable attachment of the LEV in the rotating case, but the issue has not yet been conclusively settled. It has been suggested that spanwise flow is responsible for enabling long-term leading-edge vortex stability [40, 76], but it has also been shown to be non-essential in vortex attachment [77, 78]. It has further been postulated that it is not the spanwise flow itself, but variations in the radial flow along the span that enables the LEV to remain attachment [79]. Others have attributed LEV attachment to secondary vorticity in the region surrounding the LEV. Wojcik [8, 80] found that the leading edge vortex creates an opposite sign shear layer that annihilates some of the vorticity in the LEV, keeping it from building too much circulation and separating.

A definitive answer for the mechanism of LEV attachment on rotating wings remains elusive. It is likely to be a combination of effects, rather than due to a single source.

2.5 Flexibility

Wing flexibility has been cited as a critical component in the wing strokes of both insects and birds [81, 33, 36]. Adding passive wing flexibility is also attractive as a method of passive flow control and propulsion enhancement [23, 13, 22]. It allows the wing to naturally alleviate abrupt changes in forcing, such as those at either end of a wing stroke [82]. Previous studies in the area have attempted to model the complete physiology of naturally occurring membrane wings such as insect [37, 83, 84] or bat wings, [85, 86, 87] or have studied wings with continuous chordwise flexibility [88, 89, 90, 91, 92]. It has also been argued that a torsional spring at the leading edge is the optimal arrangement of flexibility for efficient force production [90].

The transient force production of rigid wings undergoing insect-like motions has been extensively studied [93, 27, 2], but prior work on wings with discrete compliance (i.e. a rigid wing with hinges) is much more limited. Granlund *et al.* [94] examined the response of a wing free to pivot about the leading edge (but constrained in maximum angle) in an oscillating surge hovering motion. The authors observed that allowing the wing to pivot eliminated any evidence of wake capture, and so a quasi-steady assumption was valid. A similar case was investigated computationally by Wan *et al.* [95] who also varied the location of the hinge along the chord. Wan *et al.* compared their results to a fully driven wing and concluded that adding passive flexibility has no clear effect on the force production, highlighting the need for predictive tools. Beals and Jones [96] and Li *et al.* [97] examined a passively flexible rotating wing hinged at mid-chord with no spring element. Results showed that without a spring, passive flexibility was detrimental to the lift production of the wing, at least in some cases. They observed that the portion of the wing aft of the hinge aligned itself with the flow and provided no aerodynamic benefit. The aforementioned studies did not apply any resistance to wing rotation, but allowed the wing to freely pitch about a hinge.

Adding stiffness to the hinge element has been studied computationally by Eldredge *et al.* [98] and Toomey and Eldredge [99]. Both studies focused on wings hinged at the mid-chord and flapped in a reciprocating pitch and surge motion. Toomey found that the angle of the posterior portion of the wing was largely determined by the pitch kinematics of the wing rather than translation. Eldredge's studies found that a flexible wing made the wing less sensitive to changes in the kinematics, and that the flexibility allowed for better wake capture, in opposition to the results of Granlund [94]. The discrepancy is possibly due to the addition of the spring in Eldredge's configuration. Vanella *et al.* [100] also computationally studied a wing hinged at mid-chord and examined its response to a reciprocating motion of various frequencies. They similarly found that the addition of a hinge aided wake capture.

2.6 Potential Flow Modeling

Interest in flapping wing flight has produced a plethora of approaches to predicting the aerodynamic forces on the wing. The extant models run the gamut from rigorous analytical analysis [9, 101, 102, 103, 90], to modified versions of classical theories [104, 105], to vortex-based computational schemes [106, 3, 107, 108, 109, 110], empirically based models [111, 112, 113], and grid-based CFD methods [114, 115, 116].

One of the principle goals of this thesis is the evaluation and improvement of modeling techniques for the unsteady separated flow around a flat plate. The motivation behind the choice of models is for engineering work, i.e. to capture the maximum amount of flow physics while evaluating the model in the minimum amount of time. Preference is also given to techniques that neatly categorize the various contributors to the force, as this aids in developing intuition.

These requirements strongly point the researcher towards potential flow theory in lieu of solutions to the full Navier-Stokes or Euler equations. Potential flow, in particular complex potential in conjunction with conformal mapping, has long been

the bastion of pen and paper solutions to problems of both steady and unsteady flows. This heritage is due to the simplifications employed, namely inviscid and incompressible flow, which are largely appropriate for the present class of problems. It should be noted that applying these models at the Reynolds numbers considered here ($\mathcal{O}(10^4)$) stretches the limits of the inviscid assumption. Nevertheless, the formation of the LEV from the shear layer presents itself as a convection, rather than diffusion, dominated process.

The basis of potential flow is the incompressible and inviscid Navier-Stokes equation. Making these assumptions simplifies the Navier-Stokes relations to Laplace's equation, whose solutions can be represented by a scalar potential function. Laplace's equation has the great advantage of being linear, and this allows one break the problem down into simpler sub-problems, and then to superimpose known solutions to achieve the full answer. Historically, separating the forces into the contributions from different fluid sources lead to the classification of forces in categories such as added mass and circulatory. Laplace's equation also fits nicely with complex number theory, leading to complex potential and allowing the use of conformal mappings to map from solutions for flow around a cylinder to arbitrary profiles.

Potential flow provides no mechanism with which to generate circulation, and is actually non-unique with regard to total circulation. To fix a solution to the problem, an additional physical consideration must be supplied. This extra, physically based consideration is the crux of this thesis. Historically the Kutta condition is applied at the trailing edge to close the system. For the leading edge, however, it is absolutely not clear a priori that the Kutta condition is valid or useful. A general statement of the Kutta condition is that the flow must leave tangent to the separating edge, but based on flow visualization, the separated shear layer appears to leave in a direction nearer to plate-normal. This difference of direction calls the validity of the Kutta condition into question (further discussion is left for section 2.6.3.1).

The edge condition is only a single part of a potential flow model and all the pieces work together to form the complete solution. In order to properly understand the implications of an edge condition and the context it must implemented in, the rest of the model must also be understood. Any unsteady potential flow model consists of three components: a representation of the body, a representation of the wake, and a method for determining the circulation. These will be discussed in detail in the following sections, followed by outlining the models used in this thesis. For a general introduction to potential flow theory, the reader is referred to any number of fluids texts [117, 118, 119, 120, 121]. The relevant details will be laid down here, and a derivation of the complex potential model is given in appendix A.

2.6.1 Body Representation

The first consideration when modeling an exterior flow problem is how to represent the body in question. The body comes into the overall equations as a no-penetration boundary condition for the fluid at the body surface. Stated simply, it says that the fluid velocity at the surface must match the surface velocity in the their surface normal components. To enforce this, several methods have been developed throughout history: conformal mapping, basis functions for a vortex sheet, and panel methods. Note that this chapter is only concerned with pre-specified kinematics, and not with fluid-structure interaction problems.

2.6.1.1 Conformal Mapping

The oldest method for meeting the no through-flow boundary condition is to use conformal mapping. It is the foundation for the basic unsteady flow solutions that are known throughout the aerospace field such as Wagner's problem of an impulsively started plate [9], or Theodorsen's frequency response [102]. Despite its age, the conformal mapping method still enjoys popularity in recent work on unsteady separated

flows, and is the basis for methods such as Wang and Eldredge [3], Xia and Mohseni [122], Ansari *et al.* [107, 123], and Minotti [124]. Conformal mapping methods imply the use of a complex potential formulation. The method works by stretching space so the (arbitrary) body of interest is transformed into a more manageable configuration, e.g. a cylinder or the upper half plane. Mapping to a cylinder is desirable because the solution to flow around a cylinder is well known and an image system for the wake is easily formulated. A discussion of the details of complex potential flows and conformal mapping is given in appendix A.

Conformal maps have two properties that make them useful in the context of flow problems. First, using an analytic function for the map guarantees that a solution to Laplace's equation in the mapped plane is also a solution in the physical plane. Put another way, after mapping the flow back to the physical plane, the solution is still a valid fluid flow. Second, conformal maps have the property of being angle conserving. The angle between two vectors (e.g. the tangent and normal vectors on the surface of a cylinder) is conserved between the two mapped planes. This means that meeting the no through-flow condition on the cylinder will also meet that boundary condition on the airfoil. Together, these properties are what allow the flow solution around the cylinder to be applicable to an actual airfoil.

A common mapping is the Joukowsky transformation, a basic form of which is given in equation (2.1). This maps a thin flat plate on the real axis, between $z = -a$ and $z = a$, to a cylinder with unit radius centered at the origin of the ζ plane.

$$z = \frac{a}{2}\left(\zeta + \frac{1}{\zeta}\right) \tag{2.1}$$

For steady airfoil flows, the solution is then given by the summation of the free stream, doublet, and bound vortex in the ζ plane. The strength of the bound vortex is selected to satisfy the Kutta condition (discussed in section 2.6.3.1), and the doublet strength

is selected to satisfy no through-flow on the cylinder.

For arbitrary 2D motion rotation must also be taken into account, and this requires the addition of a quadlet singularity, as given by Milne-Thompson [120]. The doublet produces a constant plate-normal velocity across the chord consistent with a translating plate, while the quadlet induces a linearly varying plate-normal velocity consistent with a rotating plate. This separation of solutions to various boundary condition is what allows the complex potential method to break apart the forces into various components. The non-circulatory forces due to translation or rotation can be separated from the circulatory forces from bound or wake vorticity because each has its own singularity to solve for the particular boundary condition. The full derivation of this can be found in appendix A. Separating the forces in this manner makes these methods very strong contenders when it comes to building an intuitive understanding of where the forces come from.

The Joukowsky transform can also be modified to produce thick profiles by shifting the center of the cylinder off of the origin, and finite trailing edge angles can also be had via the Karman-Trefftz transform. Both modifications are discussed in Milne-Thomponson's book [120]. The idea of conformal transformation can be generally extended to accommodate any shape, as well described by Eldredge in his forthcoming book [125]. In fact, the Riemann mapping theorem states that it is always possible to map a given shape onto the unit circle. Conceptually, the two tools available for this are the extension of the Joukowksy mapping into an infinite series in the negative powers of ζ and the Schwartz-Christoffel transformation [120]. While these extensions are not used here, it is good for one to know that they do exist when seeking to jump from thin flat plates to more arbitrary geometry.

The advantage of using the conformal mapping method lies in the compact analytical representation of the body. The boundary conditions are rigorously enforced everywhere, with no approximation. This allows complete inclusion of the infinite

factors (pressure, sheet strength, etc.) that arise at the edges of a flat plate. Having a closed form answer for the enforcement of the boundary condition brings this method the closest to having an analytical solution for the overall unsteady flow. Indeed conformal mapping is the foundation of most of the unsteady solutions available [9, 102, 126, 103]. The analytical flow solutions, however, can not capture the full non-linear (i.e. self-induced) wake motion.

In the negative column for conformal mapping, the level of analyticity can make it cumbersome to work with. A lot of the effort must be done by hand before implementing it in computer code, requiring extensive knowledge of complex mathematics. The spatial dependence of the mapping also makes it difficult to deal with higher order wake representation (e.g. vortex sheets or patches) because linear segments do not remain linear under transformation, and the local circulation per length changes under the transformation. In response, all of the implementations that use conformal mapping to represent the body are forced to also use a point vortex wake. The method also introduces unavoidable singularities at the edges of the plate that make convection of wake particles near those edges close to singular. This can "stiffen" the problem in a computational sense as the vortices near the edge require a smaller time step to accurately resolve their motion in the mapped ζ plane than do vortices further from the plate edges. The method is also limited in that it cannot be extended to three dimensional geometries.

In spite of all these limitations, the conformal mapping body representation is still a reasonable choice for the problem at hand. Its analyticity is particularly powerful when paired with a very simple wake description such as Wang and Eldredge's unsteady strength two vortex wake model [3], which is extremely cheap to evaluate.

2.6.1.2 Basis Functions

The no penetration boundary condition can also be also be fulfilled by solving for the strength of the surface singularities directly. When the body is infinitely thin, a common approach is to represent the body as a sheet of vorticity, and to parameterize the strength of that sheet via a truncated series expansion. To solve no through flow, one must then solve for the coefficients of the series expansion to enforce no through flow at a finite number of collocation points. The two most common basis for the series are a modified Fourier series (usually attributed to Glauert [127]), and a Chebychev series [106]. In either case, the body is represented by a vortex sheet, although it is also possible to use a doublet sheet.

The Glauert approach is documented in many texts [117, 118], and is commonly taught in undergraduate courses as the path to thin airfoil theory. The Glauert approach uses a single term basis for the bound vortex sheet strength, γ:

$$\gamma = 2UA_0\frac{1+\cos(\theta)}{\sin(\theta)} \tag{2.2}$$

In this form, the bound sheet strength is not equipped to deal with any wake vorticity and can only represent plate-normal velocity distributions that are constant across the chord. Thus it must be extended, for example in the manner of Ramesh *et al.* [110], to account for arbitrary velocity distributions:

$$\gamma = 2U\left[A_0\frac{1+\cos(\theta)}{\sin(\theta)} + \sum_{n=1}^{\infty} A_n \sin(n\theta)\right] \tag{2.3}$$

where γ is the bound vortex sheet strength, U is the free stream velocity, and $x = (1/2)(1-\cos(\theta))$. The coefficients, A_0 and A_n, are found from the downwash distribution, $W(\theta)$. Downwash is here defined as the plate-normal velocity induced

by plate motion and wake vorticity.

$$A_0 = -\frac{1}{\pi}\int_0^\pi \frac{W(\theta)}{U}\,\mathrm{d}\theta \tag{2.4a}$$

$$A_n = \frac{2}{\pi}\int_0^\pi \frac{W(\theta)}{U}\cos(n\theta)\,\mathrm{d}\theta \tag{2.4b}$$

The additional $\sin(\theta)$ terms allow the basis function to accommodate arbitrary downwash distributions. This particular approach is still limited, however, by its choice of basis function. It can only represent singular γ distributions at the leading edge, and always enforces the Kutta condition at the trailing edge, $\gamma_{TE} = 0$. This makes it somewhat limited in terms of generality. A more general formulation can be found by using Chebychev functions as a basis instead, as in Jones [106, 128] and Shukla and Eldredge [109]:

$$\gamma = \frac{1}{\sqrt{1-x^2}}\sum_{n=0}^{\infty} B_n T_n(\theta) \tag{2.5}$$

here $T_n(\theta) = \cos(n\theta)$ (the Chebychev functions), allowing for singularities in γ at both ends of the plate.

The strength of these methods lies in their ability to capture either the singularities at the ends of the plate or naturally enforce the Kutta condition, while still maintaining a nice tradeoff between numerical and analytical computation. They also provide a sound analytical basis for the edge suction parameter, which relies on properly capturing the square root singularity in sheet strength at the edge. The main downside of using basis functions is that they do not extend well to arbitrary geometry (e.g. thick airfoil profiles) without explicit modification on the part of the user. It is even less clear how to apply the method for 3D problems.

The original form of these methods was applied only to small angles of attack. The small angle attack assumption was applied to both simplify the downwash expression and to linearize Bernoulli's equation. Keeping the full nonlinear terms in both allows the method to applicable to large angles of attack.

2.6.1.3 Panel Methods

The final way to meet the no through flow boundary condition is to represent the bound vortex sheet with a series of discrete panels, in much the same way as a finite element method works. When compared to the basis function method, using a panel representation trades functional complexity for geometric complexity. Instead of representing the singularity strength with a few complicated functions, it is now represented with many simple functions. Note that bound sheet can be equivalently represented with either doublet panels or vortex panels and the two are equivalent (see Katz and Plotkin [118]). Originally developed for non-lifting flows by Hess and Smith [129, 130], panel codes have developed into a practical and general design tool for both 2D and 3D flows. A good overview of panel methods is given in Katz and Plotkin [118].

In order to enforce the boundary conditions the sheet strength is represented by many panels, each with a low-order polynomial strength distribution, such as constant or linear strength panels. The velocity induced by each panel is computed at all the collocation points and a linear system is formed that can be solved to give the required panel strength such that the induced velocity exactly enforces no through flow at every collocation point. This approach shares many similarities to finite element methods.

Panel methods use simple basis functions combined with discretized geometry to solve the no through-flow problem in a very flexible way that is also quite easy to understand. This has made them the popular choice, particularly for thick airfoil profiles. One has only to look at the widespread use of finite element methods to see the general popularity of this brand of solution. The ideology is also easily extended to three-dimensional problems. This flexibility, however, comes at the cost of poorly representing infinite sheet strengths which has particular ramifications for the edge

suction parameter, discussed later in section 2.6.3.2.

2.6.2 Wake Representation

In addition to computing the effect of the body on the flow, potential models for unsteady flow require the inclusion of vorticity in the fluid. The job of the wake representation is provide a discrete representation of that vorticity to account for its effect on the body and to solve the vorticity evolution equation to propagate the wake forward in time. The vorticity evolution equation arises from taking the curl of the incompressible Navier-Stokes equation. Its full form is:

$$\frac{\mathrm{D}\vec{\omega}}{\mathrm{D}t} = (\vec{\omega} \cdot \nabla)\vec{u} + \nu\nabla^2\vec{\omega} \tag{2.6}$$

where $\mathrm{D}/\mathrm{D}t$ is the material derivative, $\vec{\omega}$ is the vorticity vector, $\vec{u}$ is the velocity vector, and ν is the kinematic viscosity. On the left hand side is the material derivative, while on the right hand side there is the vortex tilting and viscous diffusion terms, respectively. Under the present simplification (i.e. a two-dimensional inviscid incompressible flow) the equation is much simpler:

$$\frac{\mathrm{D}\omega}{\mathrm{D}t} = 0 \tag{2.7}$$

where ω is now a scalar representing the out-of-plane component, as the other two in-plane components are identically zero. This is simply a statement that fluid particles that have vorticity keep that vorticity, and so any vorticity must therefore convect with the fluid. The models considered here all use a Lagrangian representation of the vorticity field. Propagating the wake in time is therefore the problem of convecting the discrete representation with the flow. An Eulerian approach is also possible, but these methods are not as generalizable to low order models, and so not considered here.

The details of vortex convection are considered in section A.5. In the simplest case, it is sufficient to simply solve for the fluid velocity at the vortex location while ignoring the vortex in question. When complex mapping is involved, the Routh correction must also be considered, as discussed in section A.5.2.

The natural way to discretely represent the vorticity field in potential models is to add point vortices that convect with the fluid in accordance with the vorticity form of the Navier-Stokes equation. This leads to the class of methods known as vortex methods, discussed in detail in Cottet and Koumoutsakos [131] and Saffman [132]. The defining feature of these methods is the Lagrangian representation of the vorticity field. There are two prevailing philosophies behind vortex methods. One is to match the full no-slip surface condition, requiring the addition of large numbers of vortices to fully resolve the boundary layer. These methods account for separation by the natural convection of the particles, and also seek to include viscous diffusion. Examples of this class of method can be found in Winckelmans' overview of early work in the field [133], Eldredge's VVPM method [51], the VRM method [134], or Kirchart's recent work [135]. It is not uncommon to see particle counts for these methods in the hundreds of thousands to millions of particles. With such a large particle count comes a commensurate increase in computation time, making them undesirable for the present goal of low cost computations. The second philosophy is to allow for a slip velocity and only add vortices to enforce a surrogate circulation condition, such as the Kutta condition, at a separation point. Note that the separation point must be specified from prior knowledge, or solved for with an additional boundary layer model. Fortuitously, the separation point in the present problem is fixed at the leading and trailing edges. This approach keeps particle counts, and therefore the computational cost, much lower.

As mentioned above, the obvious representation for wake vorticity is the point vortex. However, a problem with point vortices is that their induced velocity tends to

infinity close to their location. This causes problems in numerical simulations, where particles that are too close together can garner unreasonably high velocities and convect themselves out of the simulation domain. The unreasonably high velocities also help propagate instabilities in vortex sheets, causing the interior structure rolled up sheets (as in the LEV) to fall apart and becomes chaotic. To counter this, the vortex is regularized with vortex core model that spreads the vorticity over a finite area rather than a point. The first methods were proposed by Chorin, Krasny, and Bernard to study the problem of vortex sheet roll up [136, 137, 138]. They used a non-physical model of the vortex core that simply added a constant factor to the distance between the vortex and the interrogation point. Other models, such as the more physical Rankine, Burgers, or Lamb-Osseen vortex core can also be used, but are often overlooked because of their computational complexity. An approximation of the Lamb-Osseen vortex core is proposed by Vatistas *et al.* [139], and is used for computations such as Ramesh *et al.* [110]. The concept of a point vortex is applicable in both two and three dimensions. As mentioned previously, the vorticity evolution equation has additional terms in three dimensions however. Some extra work is required to compute vortex stretching and keep the resulting field divergence free. That extra work is made easier when information about the arrangement of the point vortices is kept. This leads to the implementation of higher order discretizations of the vorticity.

In two dimensions, besides point vortices (a zero dimensional representation) it is possible to have vortex lines (a one dimensional represenatation, sometimes referred to as sheets) [106, 109] and patches (a two dimensional representation). Constant strength vortex patch methods are often referred to as a contour dynamics method [140]. In three dimensions, line vortices are by far the most common element, and lead to the vortex lattice or lifting line methods (see, once again, Katz and Plotkin [118]). It is also possible to have sheets (two dimensional) [141, 142], or volumes.

These are attractive, but adding this extra dimensionality also adds more things to keep track of. For the two-dimensional flat plate, the best tradeoff is the use of vortex sheets. This is because the body is itself a vortex sheet, so it is natural that wake should also be. An excellent, if somewhat informal, overview of vortex methods can be found in Stock's overview [143].

In two dimensional models, the strength of the vortices is generally kept constant in order to satisfy the vorticity equation, equation (2.7). Cortelezzi and Leonard [144, 145] relaxed this requirement to form a new low order wake representation. This method was seized upon by Wang and Eldredge [3] for the flat plate problem, and will be discussed in section 6.1. Convecting the changing strength vortices requires an additional consideration to remove the force on the branch cut between the vortex and its shedding edge. This is the Brown-Michael convection scheme, discussed in section A.5.3.

2.6.3 Circulation Conditions

The final piece of the puzzle in creating a potential flow model is to address the creation of circulation. Potential flow provides no method by which circulation could be generated, thus an extra condition must be supplied. This is almost always the Kutta condition, but recently new relations have been developed specifically for the leading edge. The leading edge suction parameter (LESP) is one, and my new boundary layer analogy (BLA) is another.

In a real flow, vorticity is generated at walls via the no-slip condition; and without viscous diffusion it remains trapped there on the fluid/body interface. With diffusion, it forms the boundary layer. A good discussion of how vorticity is generated and spreads can be found in Lighthill's book [69]. Since diffusion is the only mechanism by which vorticity can enter the fluid, the inviscid potential solutions considered here have no hope of capturing that process, and the full viscous solution to

the flow is required to form a complete model. Ideally, a truly physical model would capture the entirety of the boundary layer around the plate by solving the Navier-Stokes equations in the vicinity of the separation point. This would fully capture the dynamics of the separation point and how much circulation leaves in the shear layer. Finding such a solution requires either a numerical or analytical solution method.

Select analytical solutions to the Navier-Stokes equations do exist and have been known for a long time (see, for example, Batchelor's text [121]). Exact solutions only exist for a small subset of cases, and unfortunately that subset does not include the present problem of flow around a sharp corner. The most relevant analytical work is on boundary layer flows using simplifying assumptions to transform the full Navier-Stokes equations into the more tractable boundary layer equations. For a full discussion of boundary layers, the reader is referred to White's `Viscous Flow` text. [31] The boundary layer equations are based on the assumption that gradients normal to the wall are much larger that those tangent to the wall and that the flow is tangential to the wall within the boundary layer. When the flow remains attached as the equations assume, the strength of gradients tangent to the wall is directly related to the wall's radius of curvature, making these equations well suited to situations of negligible to mild curvature. In the present case of leading edge separation on a thin flat plate, however, the wall has extremely high curvature that forces the advent of separation. The boundary layer equations neglect any wall-normal velocity, rendering them incapable of accounting for separation. It would seem this route of separation prediction is closed due to a violation of the assumptions.

Numerical solution methods are unattractive because of their computational cost. Solving the differential equations involves requires either a fine Eulerian mesh or a large number of Lagrangian particles. Either of these methods requires more computational resources than is reasonable when the target use is design or control. At the confluence of the analytical and numerical methods lies viscous-inviscid in-

teraction methods. These methods solve the boundary layer equations in an integral formulation and couple them to an inviscid outer flow solution. This is the method behind the popular XFOIL program. [146] These methods are also discussed in Katz and Plotkin [118]. As discussed above, the boundary layer equations are not especially applicable to the present problem. The overall philosophy of driving a viscous solution with an outer inviscid solution is still viable, and will be revisited for the discussion of the boundary layer analogy (BLA).

2.6.3.1 The Kutta Condition

The de-facto standard for specifying circulation in potential flow models is the Kutta condition. There are many ways to express the condition and a bewildering number of ways to implement those conditions. As Sarpkaya [147] puts it in his vortex method overview: "almost every paper, at least in part, represents a new method." In general, it seems that most methods achieve the same result in practice. The most common condition is enforcing that the flow leave tangent to the shedding edge.

For the steady case, the Kutta condition is commonly implemented by enforcing zero bound vortex sheet strength at the edge:

$$\gamma(\tilde{x} = \tilde{x}_{TE}) = 0 \tag{2.8}$$

where γ is vortex sheet strength in circulation per distance, and $\tilde{x}_{TE}$ is the location of the trailing edge in the plate frame of reference. When conformal mapping is used, the expression of the Kutta condition is to specify that the velocity at the edges in the ζ plane are zero:

$$W(\zeta = \pm 1) = 0 \tag{2.9}$$

This has the effect of canceling the singular factor in the mapping from the ζ to the $\tilde{z}$ plane, resulting in a finite edge velocity and streamlines leaving smoothly from the

edge. For the steady translation case, the only velocity components present are the translation and bound vortex components. This leads to a simple expression for the bound vortex strength,

$$\Gamma = -2\pi a \tilde{V}, \tag{2.10}$$

where Γ is the bound vortex strength, a is the half chord, and $\tilde{V}$ is the plate-normal component of velocity. When substituted back into the expressions for force and moment, the usual results of $C_l = 2\pi \sin(\alpha)$ and zero moment at the quarter chord are obtained. For the unsteady case, the concept of fixing the ζ plane velocity to zero at all times always remains. Unfortunately, this method is always implemented reactively, in the sense that the simulation is updated with new circulation to remove the edge velocity at each time step. Thus it does not lend itself well to a comparison of the circulation rate, $\mathrm{d}\Gamma/\,\mathrm{d}t$, with experimental measurement. As it turns out, a finite plate-tangent velocity at the plate edge maps to an infinite velocity in the circle plane thanks to the singularity in the mapping. This results in a nascent vortex sheet that grows infinitely fast, hence the difficulty in computing the required $\mathrm{d}\Gamma/\,\mathrm{d}t$ to maintain the Kutta condition.

Without resorting to conformal mapping, i.e. when using basis functions or a panel method, the solution, according to the work of Krasny [148, 149] and Jones [106], is to put the ultimate focus on removing any infinite velocities in the flow. This leads to the extremely simple result that:

$$\frac{\mathrm{d}\Gamma}{\mathrm{d}t} = \gamma u \tag{2.11}$$

where $\mathrm{d}\Gamma/\,\mathrm{d}t$ is the rate of circulation being added to the shed vortex sheet, γ is the bound vortex sheet strength at the edge of the plate, and u is the tangent velocity at the plate edge. This, like the conformal mapping method, is difficult to evaluate. The first issue is that γ ties together everything in the flow field, including the motion of the

plate and the location and strength of all wake vorticity. For panel or basis function methods, γ is the solution to a set of equations. Further, the value of γ is generally unbounded at the plate edge unless the Kutta condition is already precisely met. Hence most implementations, as mentioned previously, enforce the Kutta condition reactively by adding circulation to fix the error in edge velocity at each new time step.

Part of the reason for the plethora of methods is that it is not clear from the statement of the Kutta condition alone how exactly to add the new circulation. In a point vortex model, the question becomes where to place the new vortices. A popular answer given by Ansari *et al.* [107] is to place the new vortex one third of the distance from the edge to the most recently shed vortex. For finite angle trailing edges (i.e. on thick airfoil shapes) Xia and Mohseni [150] recently proposed a rigorous momentum analysis theoretically compute the angle and strength of a newly created vortex sheet.

2.6.3.2 The Leading Edge Suction Parameter

The leading edge suction parameter (LESP), as proposed by Ramesh *et al.* [110], is a relaxation of the Kutta condition to allow for the presumed ability of finite thickness profiles to support a suction force at the edges [108]. This idea has been seen elsewhere, as in the philosophy behind the vortex shedding portion of Leishman-Beddoes model [6]. The LESP has the enviable property of reducing to the Kutta condition when the allowable suction is set to zero.

The concept of edge suction came about when early researchers in the field tried to equate the results from integrating pressure on a thin flat plate to the Kutta-Joukowski lift theorem, creating D'Alembert's Paradox. In the paradox, the pressure force, which produces only a plate normal force, contrasts with the Kutta-Joukowski force, which predicts only a force perpendicular to the plate motion. This is remedied by noting the flow velocity is forced to infinity at the leading edge as it turns around

the 180° corner. The infinite velocity likewise creates a pressure on the infinitely small edge is infinitely large, and in a convenient cancellation of infinities ends up producing a finite force: the edge suction. From Garrick [151], the infinite edge velocity has a square root singularity:

$$V_{LE} = \lim_{x \to x_{LE}} \frac{S}{\sqrt{x - x_{LE}}} \tag{2.12}$$

where S is a finite valued parameter that measures the infinite velocity. and can be related to the edge suction force and bound vortex sheet strength. Recalling from section 2.6.1.2 that Ramesh *et al.* [110] uses a basis function based body representation, they were able to relate S to their basis coefficients as $S = \sqrt{c}UA_0$. They thus defined:

$$\text{LESP} = A_0 \tag{2.13}$$

The magnitude of A_0, and therefore the amount of leading edge suction, is monitored during the simulation. If it increases past an empirically defined limit $A_{0,crit}$, shedding is initiated from the edge to maintain $A_0 = A_{0,crit}$. If A_0 begins to fall below $A_{0,crit}$, shedding is ceased. For conformal mapping applications, Eldredge [125] has related this to allowing a finite velocity in the circle plane.

This method has the very attractive property of naturally turning shedding on and off as required. Even at low angles of attack, enforcing the Kutta condition requires shedding from the leading edge, which is problematic numerically. The recently generated vorticity at the leading edge tends to be convected back close to plate surface, and this can lead to numerical instabilities. With the LESP, $A_{0,crit}$ can be set so that low angles of attack correspond to an edge suction smaller than the limiting value, and thus no shedding occurs. It is worth noting that in addition to the switching, the amount of circulation production is also affected by not enforcing the full Kutta condition. Finally, note also that Ramesh's formulation does not implement this condition at the trailing edge, and uses the Kutta condition there.

2.7 Summary

The preceding literature review has examined some prior experimental work on unsteady separated flows as well as the components needed to form a potential model of separated flow. The experimental review highlighted the need for further investigation of the circulation production at the leading edge. The modeling work showed that potential models for separated flows are the sum of several interacting systems. One of those systems accounts for flow separation at the edges of the plate; this is canonically the Kutta condition. The Kutta condition is historically chosen for the lack of other options, and this prompts the need to evaluate its use at the leading edge.

Chapter 3: Experimental Methods

This chapter gives a description of the experimental methods and subsequent data analysis used to produce the results in this thesis. In some cases, it also seeks enlighten the reader on the other possible avenues of analysis that could have been taken and to explain why the present method was chosen.

As this thesis includes results from several experimental campaigns, it is cumbersome to list the details of each experiment. Readers are referred to my previous work [57, 152, 153] for an exact history of the procedures and analysis used in each case. This chapter will cover the general philosophy behind each of the analyses, while also documenting the procedure of my most recent experiments. These experiments were aimed at measuring the circulation flux from the leading edge and constitute the bulk of what is covered in the thesis. Results from outside this most recent campaign will be noted when they are discussed, with references to the particular paper that details their methodology.

3.1 The Test Articles and Facility

The wings used for these experiments where flat aluminum plates. They had a chord, c, of 76.2 mm (3 in) and thickness, t, of 3.175 mm (1/8 in) for a thickness-to-chord ratio of $t/c = 0.42$. Three different aspect ratios were used: $\mathcal{AR} = 4, 6, 8$, though the results will primarily focus on the $\mathcal{AR} = 8$ case. The wings are shown in figure 3.1.

The primary experimental facility used was the 7m $\times$ 1.5m $\times$ 1m towing tank

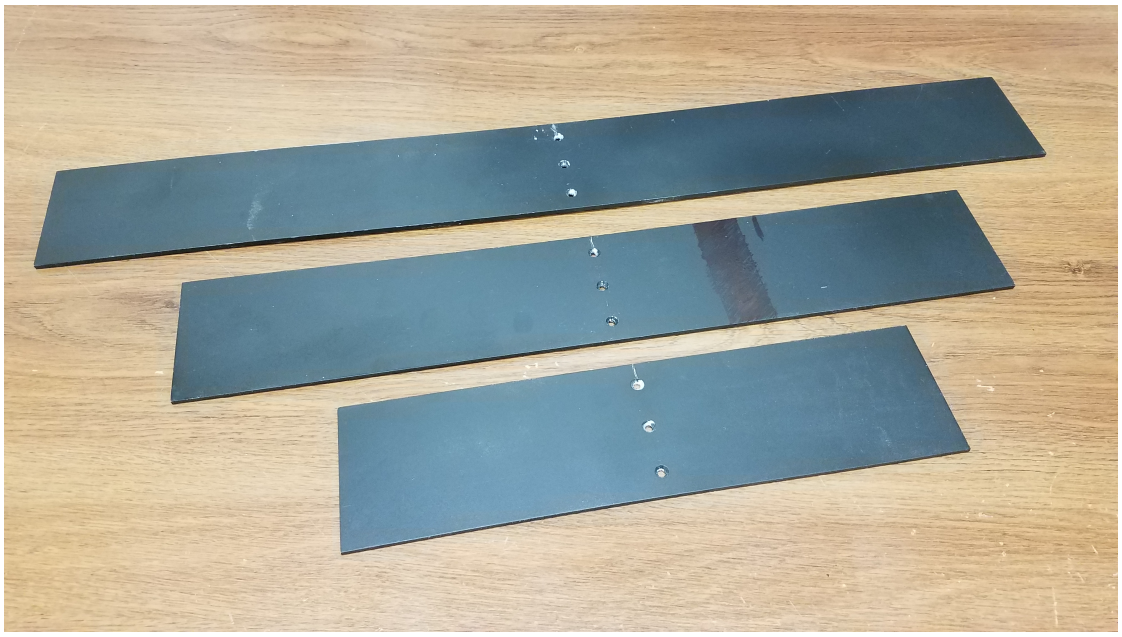

Figure 3.1: The wings used in the experiments. From top to bottom: $\mathcal{AR} = 8$, $\mathcal{AR} = 6$, and $\mathcal{AR} = 4$.

at the University of Maryland. The towing tank is equipped with a 4-axis motion control system for computer-controlled model motion. The motor assembly, shown in figure 3.2a, is mounted on the towing carriage and contains two brushless linear motors, a direct-drive brushless rotary stage, model supports, and a slip ring to transfer power and other signals to/from the equipment on the rotary stage.

Vertical plunge (max displacement $\pm 49\,\mathrm{cm}$) is driven by two independent H2W BLDC-04 brushless linear motors. Continuous rotation can be provided by a H2W TMS7C rotary stage but was not required for the tests conducted here. Carriage translation (max displacement $7\,\mathrm{m}$) is directly driven by a pair of H2W BLDC-08 brushless linear motors. All of the stages are equipped with magnetic encoders which, for the translation stages, report motor positions to within $0.001\,\mathrm{mm}$. The entire traverse system is controlled using a multi-axis Galil DMC 4153 motion controller. A test of the motors showed that the commanded motion profile was reproduced to within 0.250 mm for the tow axis and 0.010 mm for each of the pitch rods.

The wing connects to the vertical plunge rods via pitch linkage shown in fig-

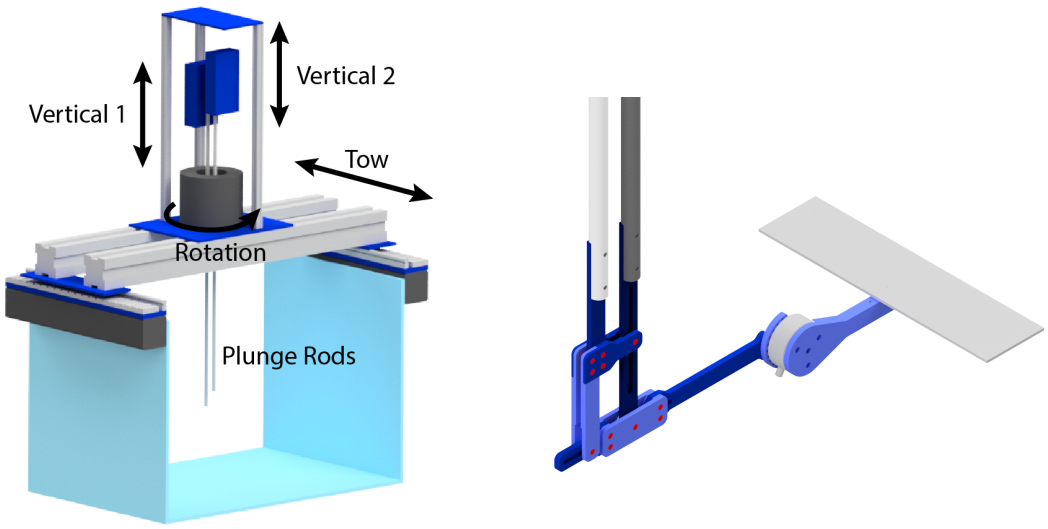

(a) Tank cross section with labeled motors. (b) Tank cross section with labeled motors.

ure 3.2b. The force balance and subsequent wing mount were located on the end of a horizontal sting to ensure good separation of the wing the plunge rods. The connection between the force balance and the pitch linkage allowed the wing to be set at an angle of attack between $\pm 60°$ in $5°$ increments.

3.2 Kinematics

The experiments discussed here make extensive use of piecewise linear trapezoids with smoothed corners like those shown in figure 3.3 for determination of position and velocity as a function of time. Adding smoothing minimizes unnecessary vibrations in the model from rapid changes in the driving force applied. Since the trapezoid shape is used for both position and velocity values, the equations are presented as generic functions $f(t)$. The shape of the trapezoid is defined by its height, f_0, and the times of the segment breaks, t_1, t_2, t_3, and t_4.

For example, if this is a velocity profile such that $U = f(t)$ and $f_0 = U_f$, then the profile corresponds to a constant acceleration phase between t_1 and t_2, followed by a constant velocity phase between t_2 and t_3. The final deceleration occurs between

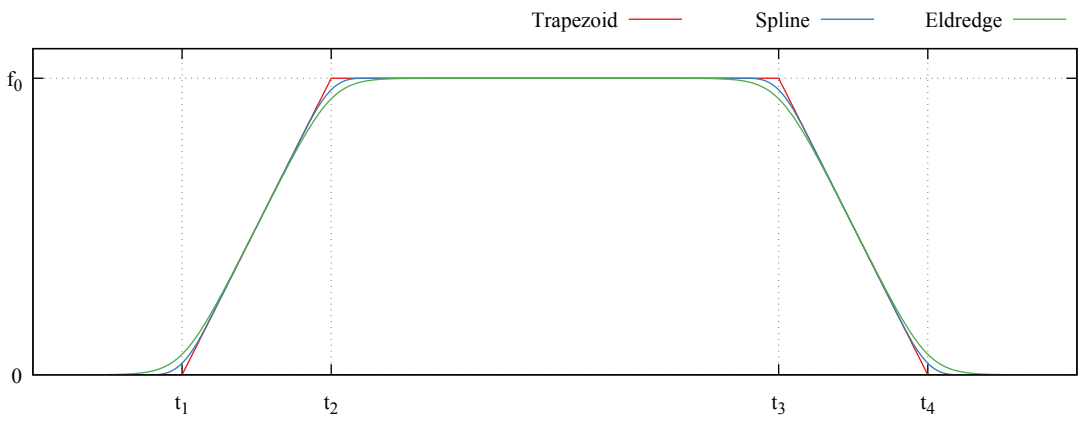

Figure 3.3: Three different trapezoidal profiles.

t_3 and t_4. The force and flow field measurements are not of concern during the final stretch between t_3 and t_4, but that portion of the profile is included for completeness. Figure 3.3 shows the three different methods at arriving the trapezoidal profile.

3.2.1 Linear Trapezoid

Such a piecewise linear function looks like this:

$$f(t) = \begin{cases} 0, & t \leq t_1 \\ f_0 \left(\frac{t - t_1}{t_2 - t_1} \right), & t_1 < t \leq t_2 \\ f_0, & t_2 < t \leq t_3 \\ f_0 \left(\frac{t_4 - t}{t_4 - t_3} \right), & t_3 < t \leq t_4 \\ 0, & t > t_4 \end{cases} \tag{3.1}$$

Using this profile directly results in a motion that has very abrupt changes at t_1 and t_2. These are undesirable as they cause unnecessary vibration in the experimental setup. To rectify this, the corners are smoothed out. There are two different formulations used for the smoothed trapezoids: the Eldredge function and the hermite spline. Both are described below, and the end result can be made very similar. An effort was made in figure 3.3 to differentiate the two methods by intentionally

choosing values of smoothing that set the two methods apart. The version used for each particular experiment will be clearly stated in its description.

3.2.2 The Eldredge Function

The kinematics specified by the so-called "Eldredge" function, given in [154] and shown in figure 3.3, utilize the natural logarithm and hyperbolic cosine functions to create an infinitely differentiable curve that is close to a trapezoid. The exact form is given in equation (3.2):

$$f(t) = \begin{cases} \frac{f_0}{2a(t_2-t_1)} \log\left(\frac{\cosh a(t-t_1)}{\cosh a(t-t_2)}\right) + \frac{f_0}{2}, & 0 \leq t \leq \frac{(t_2+t_3)}{2} \\ \frac{-f_0}{2a(t_4-t_3)} \log\left(\frac{\cosh a(t-t_3)}{\cosh a(t-t_4)}\right) + \frac{f_0}{2}, & \frac{(t_2+t_3)}{2} \leq t \end{cases} \tag{3.2}$$

The parameter a in equation (3.2) controls the amount of smoothing at the corners of the trapezoid. This function was adopted as the standard kinematic for the AVT-202 [93] task group. As such it enjoyed widespread use inside of that group, which the author took part in and was heavily influenced by.

The form of the equation has some flaws, however. The smoothing parameter, a, is non-intuitive to use, and the amount of smoothing necessary is a function of the other parameters (f_0, t_1, etc.). In addition, the function does not ever come to a final value, and only approaches it asymptotically. This is a particular issue when trying to determine the exact time at which the wing begins to move. To counteract this, I proposed to use instead a spline function for smoothing, detailed next.

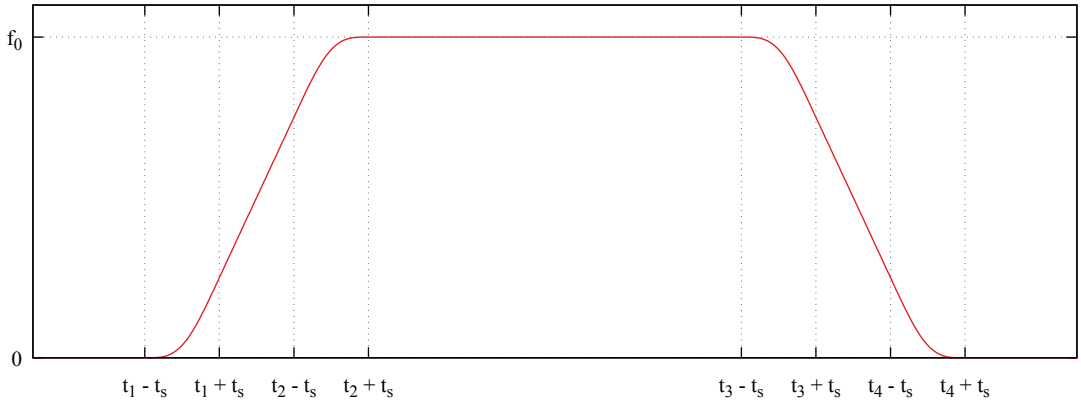

Figure 3.4: The segments of the hermite spline corner profile.

3.2.3 Hermite Spline

The kinematics specified by the Hermite Spline function consist of linear segments joined with 7th order polynomials at the corners. The form is given in equation (3.3):

$$f(t) = \begin{cases} 0, & t \leq t_1 - t_s \\ \sum_{i=0}^{7} C_{1,i} t^i, & t_1 - t_s < t \leq t_1 + t_s \\ f_0 \left(\frac{t - t_1}{t_2 - t_1} \right), & t_1 + t_s < t \leq t_2 - t_s \\ \sum_{i=0}^{7} C_{2,i} t^i, & t_2 - t_s < t \leq t_2 + t_s \\ f_0, & t_2 + t_s < t \leq t_3 - t_s \\ \sum_{i=0}^{7} C_{3,i} t^i, & t_3 - t_s < t \leq t_3 + t_s \\ f_0 \left(\frac{t_4 - t}{t_4 - t_3} \right), & t_3 + t_s < t \leq t_4 - t_s \\ \sum_{i=0}^{7} C_{4,i} t^i, & t_4 - t_s < t \leq t_4 + t_s \\ 0, & t > t_4 + t_s \end{cases} \tag{3.3}$$

Smoothing is determined by the parameter t_s which controls the time interval over which the polynomial applies. These intervals are shown in figure 3.4. The constants defining each corner, $C_{j,i}$, are determined such that the value and first three derivatives of the polynomial are consistent with the linear segments at both ends of the smoothing segment. This results in the following coefficients for the corner j, where

$f_- = f(t_j - t_s)$ and $f_+ = f(t_j + t_s)$:

$$\begin{aligned}
C_{j,0} &= f_- \\
C_{j,1} &= f'_- \\
C_{j,2} &= 0 \\
C_{j,3} &= 0 \\
C_{j,4} &= \tfrac{-5}{(2t_s)^4}\left[7(f_- - f_+) + 2t_2(4f'_- + 3f'_+)\right] \\
C_{j,5} &= \tfrac{3}{(2t_s)^5}\left[28(f_- - f_+) + 2t_2(15f'_- + 13f'_+)\right] \\
C_{j,6} &= \tfrac{-2}{(2t_s)^6}\left[35(f_- - f_+) + 2t_2(18f'_- + 17f'_+)\right] \\
C_{j,7} &= \tfrac{-10}{(2t_s)^7}\left[2(f_- - f_+) + 2t_2(f'_- + f'_+)\right]
\end{aligned} \tag{3.4}$$

This order of polynomial was selected because the UMD tow tank motor system uses cubic hermite splines in position, resulting in segments of constant $f''(t)$ (acceleration) for position profiles. Further ensuring that $f'''(t)$ matches across the segment breaks leads to a function that is easily representable in the motor software and still maintains smooth transitions in acceleration.

3.2.4 Scaling Time

The time axis in our tests will be scaled to help compare the results across different tests. One common way to do this is to use convective time, defined here as:

$$t^* = \frac{U_f t}{c} \tag{3.5}$$

Where U_f is the final constant velocity of the wing, t is the dimensional time, and c is the wing chord. This parameter is natural to use for situations in which the free stream does not vary in time (e.g. most wing tunnel tests). In those cases, it scales time by the time it takes a fluid particle to convect from the leading to the trailing edge in the far field.

A common alternative choice of abscissa is the distance traveled normalized by chord, s/c. This appears in many unsteady studies because it is the independent variable in the Wagner function. The results of Wagner's model for impulsive changes in wing motion [9, 126] predict that the unsteady circulatory forces develop as function only of s/c, independent of wing velocity. Wagner's problem is not necessarily applicable in the present case of high angle of attack and leading edge separation, but similar development of the wake with distance traveled is still a good guiding principal. For the present work, however, t^* is favored instead because s/c obscures the results at early times. This is because the wing starts at rest, and thus a large change in acceleration occurs over a small distance. Using t^* avoids this as time always progresses linearly.

3.2.5 Specifying A Profile

A trapezoidal velocity profile has two degrees of freedom that need to be specified to uniquely define it: the steady state velocity and the acceleration. Taking the parameters from the functions just discussed, this means that $f(t)$ corresponds to the translation velocity of the wing, $U(t)$, and the task at hand is to specify f_0, t_1, t_2, t_3, and t_4. f_0 is defined by the final velocity, U_f, and the interval $t_2 - t_1$ defines the level of acceleration, labeled as the acceleration time t_a. The motion is set to start at $t_1 = 0$ for convenience. t_3 and t_4 are not pertinent to studying the startup of the wing, and so are set to bring the wing smoothly to rest.

The final velocity of the wing is specified using the chord based Reynolds number:

$$Re = U_f c/\nu \tag{3.6}$$

Where U_f is the final wing velocity, c is the wing chord, and ν is the kinematic viscosity of the fluid (water in this case). Non-dimensionalizing tow velocity as Reynolds

number, a ratio of inertial to viscous forces, subtly implies that the dominant effect of changing velocity is to change where the boundary layer transitions to turbulence.[1] This approach works well in the traditional context of attached flows, where boundary layer health directly affects the overall force production of the wing and plays a large role in separation. In the present case of a flat plate at relevant Reynolds numbers ($Re \geq 50$) boundary layer separation is guaranteed at the leading edge, and "Reynolds number effects" in a traditional sense do not occur. Yet we cling to Reynolds number for lack of other more meaningful non-dimensionalizations for velocity. Changing velocity still has an impact on the flow, but not one that is well described by Reynolds number. Looking to Wagner [9, 126], we see that Reynolds number does not ever enter the problem (this is an inviscid solution, hence $Re = \infty$). Instead, U_f determines the amount of bound circulation and the rate at which the wing progresses through the transient. Hence, one expects the results to scale with U_f in both magnitude and timescale. While this can be expressed as a function of Re, it is somewhat misleading to do so. At any rate, the cases are still labeled with Re here in order to conform with tradition. Note that for all cases here, ν and c are constant, so $U_f \propto Re$.

The level of acceleration is specified as the distance traveled during t_a, notated with s_a and usually scaled by the chord to make in dimensionless. This can be related back to the profile parameters with:

$$s_a = \frac{U_f}{2} t_a \tag{3.7}$$

Where t_a is the acceleration interval, $t_2 - t_1$. Applying the definition of $t^* = U_f t/c$

[1] A strange quirk of the aerospace field: aerodynamic forces are usually scaled with dynamic pressure, ρU_f^2, another function of velocity. One would then expect that the coefficient of force (e.g. C_l) is not a function of velocity. This scaling ignores, however, how the force changes with Reynolds number, because it is difficult to capture in a simple coefficient. The upshot is that C_l becomes an empirical function of Re, and results in the somewhat non-nonsensical situation where the coefficient of force is simultaneously independent of and dependent on velocity! This is not to say that non-dimensionalization is not an extremely useful tool. Instead, the author wishes to highlight that there are often complexities in the flow that cannot be captured with simple scalings.

gives the result that $t_a^* = 2s_a/c$. The dimensional acceleration can be found with:

$$\frac{\mathrm{d}U}{\mathrm{d}t} = \frac{U_f^2}{2s_a} = \frac{\nu^2}{2c^3}\frac{Re^2}{s_a/c} \tag{3.8}$$

Where $\mathrm{d}U/\mathrm{d}t$ is the dimensional acceleration, U_f is the final tow velocity, and s_a is the dimensional acceleration distance.

3.3 Force Measurement

The load cell used to acquire force measurements was a submergible ATI Mini40 6-axis force/torque transducer with a 16-bit A/D converter. The sampling rate was 1000 Hz. Each case was run 5 times, starting from different locations in the tank to the reduce the effects of any irregularities in the tracks. The results were ensemble-averaged after smoothing the acquired force signal. The wing was fixed to the force balance with a short sting as depicted in figure 3.2b. Thus the force collected data in a wing-fixed reference frame. To isolate only the fluid loads, the contributions from gravity and buoyancy were removed from the measured force. The average force during the two seconds before the wing motion was taken as the net gravity and buoyancy force, and subtracted from the measurement. Inertial loads were measured in air and were found to be negligible for all of the wing kinematics tested. The measured forces were normalized according to:

$$C_F = \frac{2F}{\rho U_f^2 A} \tag{3.9}$$

where F is the force to be normalized, ρ is the fluid density, U_f is the steady-state wing velocity, and A is the wing area.

The force signals acquired were smoothed in time with Matlab's `smooth` function with the `lowess` option set to attenuate the effects of electrical noise and rig vibration. The smoothing width was set to 0.5 chords of travel at the final wing speed, which corresponds to 0.25 seconds in wall clock time. The `lowess` option implements a

weighted Savitzky-Golay filter, which creates a least squares quadratic fit over the smoothing window and evaluates the resulting quadratic polynomial at the point in question. This method does a good job of rejecting noise without introducing a phase shift, and accurately captures the magnitude of peaks in the signal.

3.4 Flowfield Measurement

In order to make quantitative statements about the evolution of the wake behind the wing, particle image velocimetry (PIV) was used extensively to measure the time-resolved velocities of the flow. The primary focus of these investigations was the leading edge vortex (LEV) that forms, as it will be shown in chapter 4 to be the dominant flow feature. Using PIV to record actual velocities reveals significantly more information than simply employing flow visualization techniques. Flow visualization is an excellent tool for gaining an intuition of the how the flow develops, but it is an inherently qualitative technique. Quantification of the LEV helps to distinguish between cases that have visually similar LEV development but produce radically different forces on the wing. The PIV flow fields will be analyzed in order to track three LEV-related quantities: the vortex location, the vortex circulation, and the circulation production at the leading edge of the wing.

The planar PIV tests were performed in water using a double-pulsed Nd:YLF laser (Litron LDY304, 30 mJ/pulse, 10 kHz max), with the laser sheet oriented in the chordwise direction. Soda-lime glass spheres with an average diameter of 34 μm were used as the tracer particles. Images were acquired using a Phantom v641 camera (4 MP CMOS sensor, up to 3.2 kHz at max resolution) placed orthogonal to the laser sheet and tank wall. After a sliding background subtraction (to increase the signal-to-noise ratio), correlation was performed in DaVis v8.1 using multi-pass interrogation with 50% overlap. A median filter was then applied on 3×3 regions, replacing vectors whose peak ratio (the ratio of the highest correlation peak to the

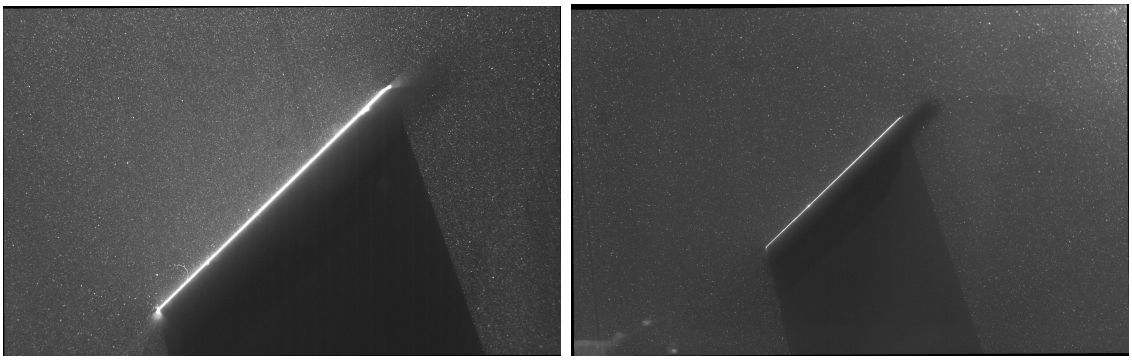

(a) Tight FOV (b) Wide FOV

Figure 3.5: Camera images for the two different fields of view.

second-highest correlation peak) was less than 2 with an interpolated velocity vector.

To asses whether the PIV recordings had sufficient spatial resolution to measure the vorticity flux across the relatively small shear layer, measurements with two different fields of view (FOV) where taken of the same case. A "tight" field of view was used, with sample frame in figure 3.5a, and a "wide" field of view, shown in figure 3.5b. The tight field of view was processed with a 24 pixel window and 50% overlap, resulting in a vector spacing of 0.84% of chord. The wide field of view was processed with a 32 pixel window and 50% overlap, resulting in a vector spacing of 1.90% chord. Thus the tight field of view has about half the vector spacing as the wide field of view (the chord is 76.2 mm for both cases).

The measurements were taken at chord-wise planes spaced one chord length apart, as shown in figure 3.6. The plane at $b/c = 0$ corresponds to the mid-span of the wing. Unfortunately, images could not be captured there because the optics would have impinged on the support structure. The wing shown in figure 3.6 is an $\mathcal{AR} = 8$ wing; for small $\mathcal{AR}$, the outboard planes are neglected.

3.4.1 Vortex Identification and Tracking

Some readers may find it surprising, but the identification and tracking of a vortex is actually an open research question. In a large part the question remains unsettled

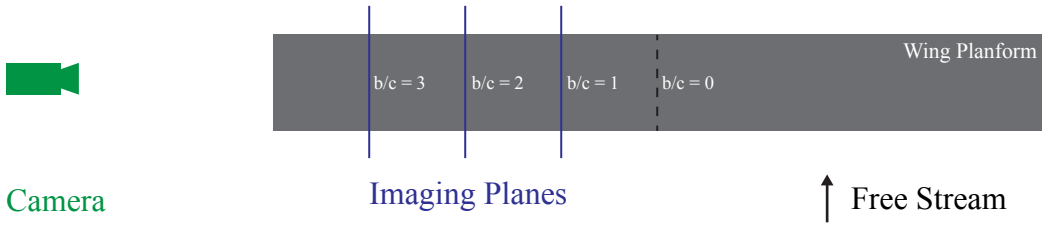

Figure 3.6: Top-down schematic of the camera and imaging plane locations.

because of the lack of a rigorous definition for a vortex. Notionally, a vortex is a mass of fluid rotating together, and it is fairly easy for humans to identify. A useful definition in a computer setting is more difficult. A first thought might be that any mass of vorticity constitutes a vortex, but that also includes shear and boundary layers, which do not pass the intuitive rotation test. The definition can be extended so that a vortex is identified by a maximum in the vorticity field co-located with a minimum in the pressure field. This better matches intuition, but our present measurement technique (PIV) does not give us any information about the pressure field.

To remedy this, a plethora of vortex identification criteria have been proposed. They split into two general camps: local and nonlocal criteria. Local criteria make use of the velocity gradient matrix decompositions and their eigenvalues to classify the flow around a point. Examples include Δ [155], Q [156], λ_2 [157], λ_{ci} [158], λ_r/λ_{ci} [159], and the triple decomposition method [160]. Good overviews of the methods can be found in Chakraborty *et al.* [159] and Kolar *et al.* [160]. These methods are attractive from an analytical standpoint, but suffer from limitations in the context of PIV surveys. First, they rely heavily on the gradient of the velocity field. Taking a derivative of measured data always increases the noise inherent in the measurement, and it can be very hard to produce results smooth enough for these methods to work as intended. This is less of an issue when the problem in question is cyclic and phase averaging over a large number of trials ($N > 50$) is an option. The cases

of interest here are, however, not cyclic and collecting large numbers of samples is simply not feasible. Another drawback is that we are presently dealing with only a two dimensional slice of a fully three dimensional flow, and even then we only have access to two out of three velocity components. Many of these criteria were developed for CFD studies, where the velocity is naturally much smoother and all three components and the full gradient matrix are readily available. This loss of information hinders the local methods.

The other camp consists of non-local methods that use information from the flow around the point rather than just its local gradient. Non-local methods inherently include some smoothing of the data, making them much more suitable for use with PIV data. Most of these methods track Lagrangian points convected with the measured flowfield. Examples can be found in Cucitore *et al.* [161] and the extensive literature put forth by Dr. Green's group on the LCS method [162, 163, 164, 165]. These methods require the convection of particles, and thus end up being more computationally expensive than the Γ_1 criteria. In the author's opinion, they also produce a lot extraneous peaks that make it difficult to identify the vortex without user input. Thus a non-local, non-Lagrangian method is sought.

The leading contender, and indeed the only method of its type the author is aware of, is the Γ_1 and Γ_2 criteria from Graftieaux *et al.* [166]. The Γ_1 function, given in equation (3.10), characterizes the extent to which fluid motion is circular around a point.

$$\Gamma_1(P) = \frac{1}{S}\int_S \sin(\theta)\mathrm{d}S \tag{3.10}$$

Here, S is the area of integration, and θ is the angle between the point P and the velocity vector at $\mathrm{d}S$. The value of the integrand at each point in a vector field is the sine of the angle between the relative location vector and the velocity. A sine (and thus Γ_1) value of 1 everywhere near P indicates the velocity is purely circular in direction and the flow is highly rotational about the point of interest. Computing the

Γ_1 values for the entire velocity field produces a scalar field with values ranging from -1 to +1, where the sign indicates the direction of rotation. In practice, a threshold is applied so that only areas of strong circular flow are identified; here the Γ_1 field was thresholded at $|\Gamma_1| \geq 0.6$. To further improve robustness, the centroid of the first such region leaving the leading of the wing and satisfying this threshold was computed and this point was taken as the location of the LEV. Using the centroid allows for sub-grid scale location of the vortex.

The Γ_1 vortex identification method was chosen because it incorporates elements of spacial averaging that attenuate measurement noise. The thresholded Γ_1 function tends to produce smooth contiguous regions in the flow field, easing the vortex identification process. This is in opposition to velocity gradient methods which tend to amplify measurement noise. The Γ_1 function, however, has a free parameter— the area over which it is computed. For simplicity, this area was defined as a circle of a user-specified radius. The choice of radius does affect the values of the Γ_1 function, but the centroids of the high-level contours are relatively insensitive to the choice of radius.

Another method of determining a vortex location, agnostic to any notion of what constitutes a vortex, is to use the centroid of the vorticity field. This method produces an unambiguous location given a PIV frame, and for isolated vortices matches well with the location returned from other tracking methods. The centroid is computed with the following formula:

$$(x, y)_c = \frac{\int_A (x\omega, y\omega)\, \mathrm{d}A}{\int_A \omega\, \mathrm{d}A} \tag{3.11}$$

Where $(x, y)_c$ is the centroid location, ω is the vorticity, and the bottom of the fraction is simply the total circulation. In order to differentiate the LEV and TEV the vorticity field was split into positive and negative regions along the same lines as

the circulation measurement, discussed in detail in the next section.

3.4.2 Vortex Strength Measurement

A vortex is more than just its location; at the very least a measure of strength is also desired. Ideally, the vortex description would also include some information about its size as well. The classical measurement of vortex strength is its circulation, i.e the sum of the vorticity contained in the vortex. There are two main avenues in the literature for computing circulation from a given flowfield that includes a vortex.

The first is to use a correlation method based on an analytical description of the vortex tangential velocity profile. Some popular models include the Lamb-Oseen [167, 121] model and the Rankine model [168]. These models are designed to represent free vortices floating about in isolation (e.g. wingtip vortices far downstream) that have a radially symmetric velocity profile. They can be used to get information about the vortex circulation and core radius by correlating the model velocity profile with that observed in experiment, and generally perform well given a clean isolated vortex. In the present work however, the vortices in question are close to the wing, and as a result have a deformed shape and feature a feeding shear layer. This makes it difficult to follow the correlation procedure.

The second avenue for computing circulation derives directly from the definition of circulation, i.e. directly computing the area sum of vorticity or the line integral around an area encompassing the vortex:

$$\Gamma = \int_A \omega \, \mathrm{d}A \tag{3.12}$$

Given a velocity field, the question then becomes how to define the area of integration. The simplest approach is to specify a box above the wing, or use the PIV frame as a whole. A slightly more advanced method is to use a level set of one of the vortex

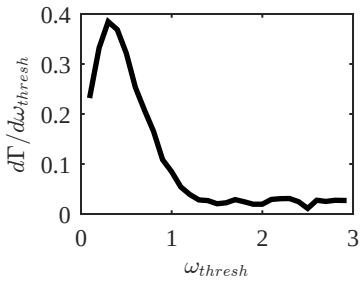

Figure 3.7: Vortex circulation sensitivity to vorticity threshold.

identification criteria discussed in the previous section. Using a contour was found to produce noisy circulation measurements due to the shifting of the contour from frame to frame. Either way, the proximity of the vortex to the boundary layer and shear layer make it difficulty to rigorously specify which areas are in the vortex. As one solution, the distinction is simply ignored, and here circulation is computed as the area integral over the entire PIV frame.

In order to still maintain a distinction between the LEV and TEV, the vorticity was split into positive and negative regions and integrated separately. This required the use of a threshold to remove the background noise. To ensure that a proper threshold was used, a sensitivity study was conducted, with representative results shown in figure 3.7. This study showed that if a large enough threshold was used, the measured quantities were nearly independent of the threshold value, i.e. the rate of change of the vortex quantities with changing threshold level was small. A threshold value of normalized vorticity $\omega_{thresh} = \omega c/U_f = 2.5$ was selected as a conservative result from the sensitivity study, and is 5 standard deviations above the background noise level for all cases.

This method of measuring circulation makes no attempt to distinguish vorticity that is in the vortex versus what is in the shear or boundary layer. The boundary layer is reactive to the flow around it, so it will reflect the changes in plate kinematics and LEV strength, obfuscating the value that would arise from just the vorticity outside the boundary layer. A correction for this has been proposed using a potential

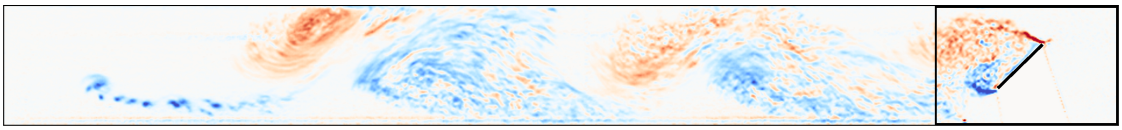

Figure 3.8: The results of applying the frozen wake hypothesis. The extent of the actual PIV frame is shown to the right of the vertical black line.

flow model to capture the circulation in the boundary by computing the vortex sheet on the surface [169, 170]. This method is recent, and unfortunately was not proposed until too late for inclusion in this thesis. Future researchers are highly encouraged to explore this avenue.

3.4.3 Frozen Wake Approximation

One of the limitations of the present PIV setup is that the camera moves with the wing, and thus the wake is continually convected out of the frame. This means that the measurements of circulation and vorticity centroid will inherently not include the entire wake. To alleviate this, the vorticity leaving the frame is assumed to be frozen in place, forming a first order approximation to the wake as a whole. The results of this can be seen in figure 3.8. It allows for a reasonable estimate of the total circulation and centroid of vorticity throughout the entire test run in spite of the wake leaving the frame. Figure 3.8 also shows the alternating LEV and TEV shedding that occurs. The approximation is implemented by adding a small strip of vorticity at the exit of the PIV frame onto a stationary background grid, which maintains a running average of the contributions from all frames.

Obviously, making this approximation has its drawbacks. The vorticity in the wake that would normally convect does not, leading to erroneous locations of the shed vortices. Any vorticity that leaves through the top and bottom of the frame is neglected. Further, vortices that leave the frame slowly become stretched in the fixed-wake representation. Despite the disadvantages, making the fixed-wake approximation is a vast improvement over simply neglecting the wake that has left the

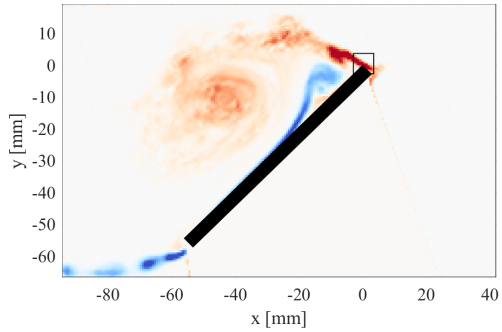

Figure 3.9: The location of flux measurement marked by the black box around the leading edge.

frame.

3.4.4 Circulation Production Measurement

The production of circulation at the leading edge was measured via the flux of vorticity out of a control volume around the leading edge of the wing. The extent of the control volume is depicted in figure 3.9, and measures 8% of chord on a side centered at the upper corner of the leading edge. Along the edge of the box, the vorticity flux was computed with the standard integral:

$$\frac{\mathrm{d}\Gamma}{\mathrm{d}t} = \int_s \omega \vec{u} \cdot \hat{n} \, \mathrm{d}s \tag{3.13}$$

Where $\mathrm{d}\Gamma/\mathrm{d}t$ is the vorticity flux (but expressed as the rate of circulation), ω is the vorticity, $\vec{u} \cdot \hat{n}$ is the velocity component normal to the boundary, s. The vorticity is computed with a three point central differencing scheme in each direction. The integral is discretized with the PIV vector spacing and computed numerically with the trapezoid rule. This method measures the circulation flux slightly behind the leading edge. Doing so was a conscious choice to avoid using vectors that whose correlations might be contaminated with stationary wall pixels.

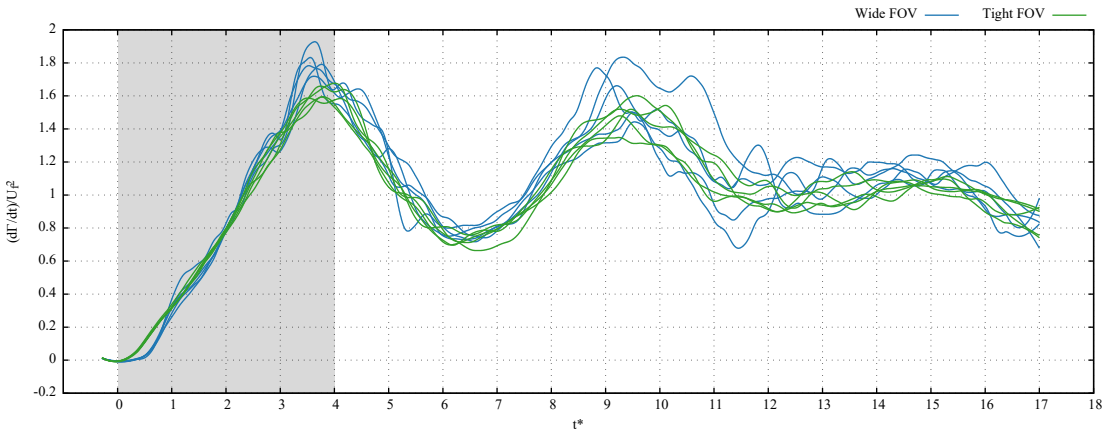

Figure 3.10: Flux measurements for the two different fields of view. Note that each field of view is represented by five independent trials.

The impact of the two difference fields of view, discussed in section 3.4, on the flux measurement is shown in figure 3.10. The impact of halving the resolution is primarily to add noise to the measurements with the wide field of view. The wide field of view also has a slight delay in the start of the measurement compared to the tight field of view. The was due to the measurement plane being displaced slightly further behind the leading edge in the wide field of view to ensure that is captured the whole shear layer. The wide field of view also reports a slightly higher initial peak in the flux measurement. Overall, the two methods report the same trends and magnitude of circulation production. The factor of two difference in their resolution verifies that the shear layer is sufficiently resolved to capture the true value of circulation production.

3.5 Summary

This chapter has documented the experimental procedures used to gather and analyze the data in this thesis. The experiments center around towing a wing through the water tank at the University of Maryland. As the wing was moved through the tank, time resolved forces and flowfield measurements were taken. The flow field

was interrogated with planar PIV, and post processed to measure the LEV location, circulation, and the circulation production at the leading edge.

Chapter 4: Baseline Case

This chapter presents detailed results for a single test case of an aspect ratio eight flat plate in rectilinear translation with a constant angle of attack of 45°. The plate begins motion with a constant acceleration, and then transitions to a constant final velocity. This case has been selected based on personal experience to be representative of the common features in wing start up transients. By studying this case in depth, the reader will be familiarized with the general picture of the flow so that the variations discussed in later chapters will be put in context.

4.1 Kinematics

In keeping with the general premise of simplification, the wing kinematics, shown in figure 4.1, for this case are rather rudimentary. For a detailed discussion of the kinematics the reader is referred back to chapter 3. The abscissa of figure 4.1, and most subsequent plots, uses a non-dimensional time, $t^* = tU_f/c$, where U_f is the final tow velocity, t is wall clock time since the motion start, and c is the wing chord, detailed in section 3.2.4. The kinematics begin with the wing at rest in a quiescent fluid, followed by a constant acceleration to a final constant velocity. For the case shown here, the final velocity, U_f, corresponds to a Reynolds number, $Re = U_f c/\nu$, of 12500. The transition from rest to the final velocity is accomplished with a constant acceleration phase defined by the number of chords traveled during acceleration, s_a/c. In the present case this is two chords of travel, which corresponds to an acceleration

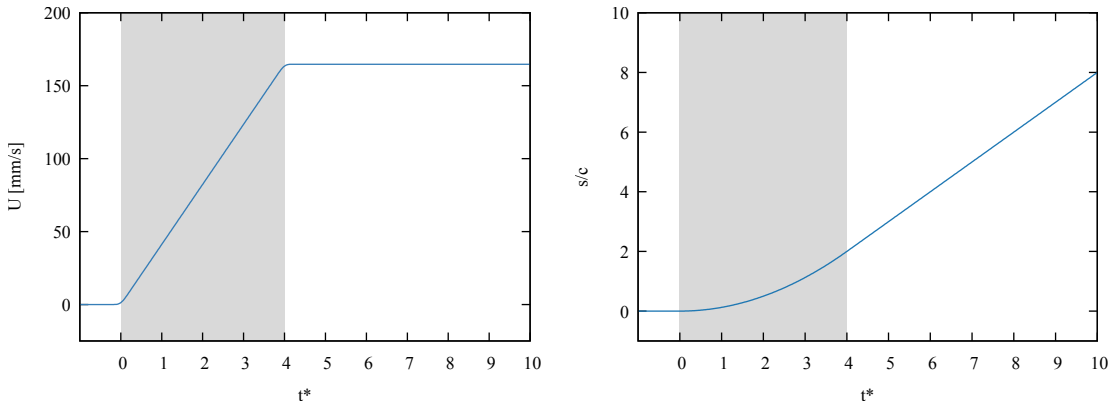

(a) velocity vs. time (b) distance vs. time

Figure 4.1: The speed and distance profiles of the baseline kinematics. The shaded region indicates acceleration phase.

time of $t_a^* = 4$. A detailed discussion of these parameters as the definition of a velocity profile is given in section 3.2.5. Angle of attack is held fixed at $\alpha = 45°$.

4.2 Flow Visualization

Following in the footsteps of many a proud fluids researcher [171], the best diagnostic is often to simply look at the flow. A series of streamline images for the baseline case of a surging wing are presented in figure 4.2. These are line integral convolution (LIC) images [172, 173] of the flow, which is essentially a fancy way of displaying streamlines. The images are created by blurring an image of random noise along streamlines. This gives a visually pleasing picture of the flow with higher streamline density than plotting the actual streamlines.

An easy relation to everyday life is to note that the flow generated by a starting flat plate is not altogether different than that created by an oar when paddling a canoe or by a spoon moved across a cup of coffee. The duration of the unsteady motions considered here are also of the same number of chords traveled as in those cases as well (on the order of 4 or 5 chords of travel) The main difference is that we are concerned here with flows that are asymmetrical, e.g. not at 90° angle of attack,

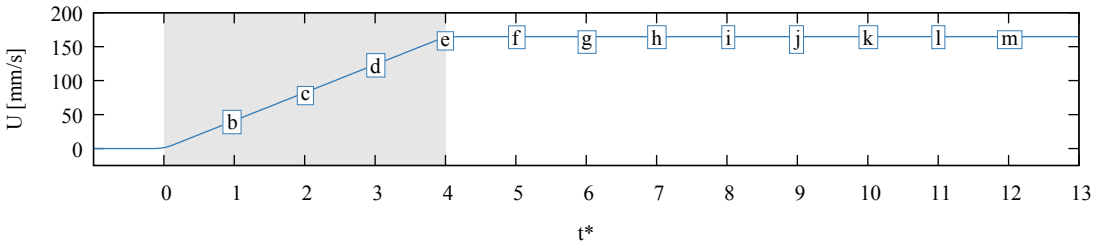

(a) Velocity profile with timing of images.

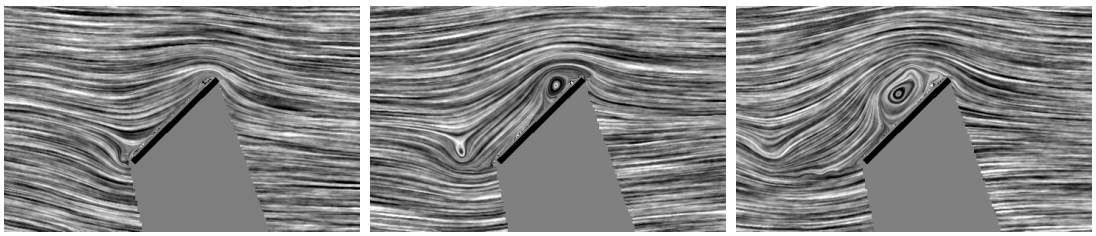

(b) $t^* = 1$, $s/c = 0.13$ (c) $t^* = 2$, $s/c = 0.50$ (d) $t^* = 3$, $s/c = 1.13$

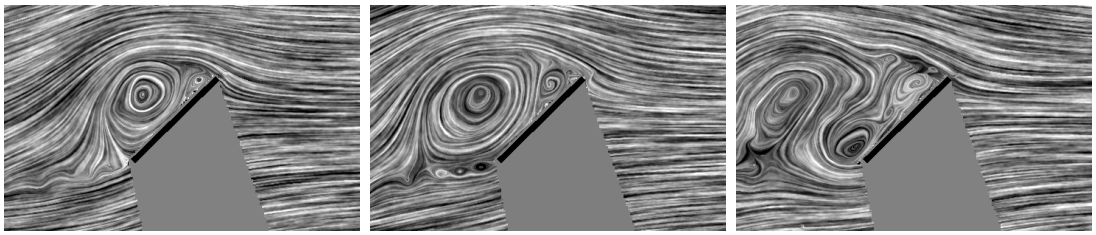

(e) $t^* = 4$, $s/c = 2.00$ (f) $t^* = 5$, $s/c = 3.00$ (g) $t^* = 6$, $s/c = 4.00$

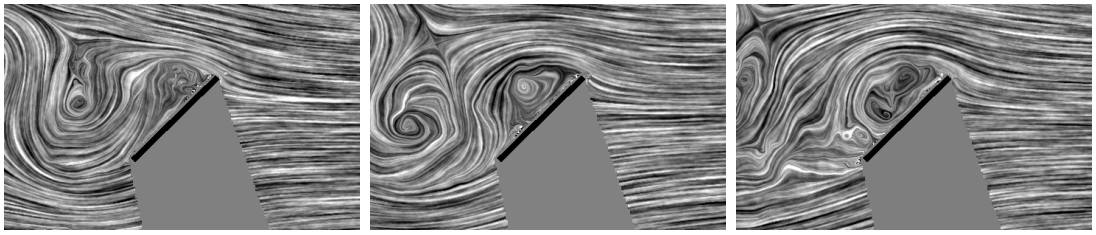

(h) $t^* = 7$, $s/c = 5.00$ (i) $t^* = 8$, $s/c = 6.00$ (j) $t^* = 9$, $s/c = 7.00$

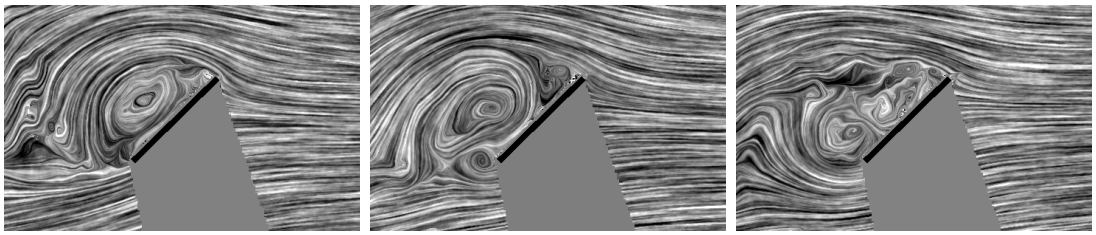

(k) $t^* = 10$, $s/c = 8.00$ (l) $t^* = 11$, $s/c = 9.00$ (m) $t^* = 12$, $s/c = 9.00$

Figure 4.2: Steamline images showing the flow evolution. Flow is from right to left.

and we are highly concerned with predicting the force required to create the motion.

The images in figure 4.2 show flow fields at various stages of development on the $\mathcal{AR} = 8$ wing at a slice one chord from mid span (alternatively, three chords from the wing tip). At $t^* = 1$, the wing has just begun motion ($s/c = 0.13$) and the flow still resembles attached flow with no circulation around the plate. This situation cannot remain, and the boundary layers quickly separate from the edges, as seen at $t^* = 2$. The nascent leading edge vortex, or LEV, is clearly visible at the leading edge. Behind the wing, a shear layer is visible as a kink in the streamlines. As the wing continues to move, the LEV grows considerably until its diameter is roughly the same as the wing chord, near $t^* = 4$ or $t^* = 5$. The LEV then sheds, allowing a trailing edge vortex, TEV, to roll up on top of the wing at $t^* = 6$, followed by a second LEV from $t^* = 7$ through $t^* = 10$, and another TEV at $t^* = 11$ and 12. It is not shown in this figure, but the creation of identifiable structures eventually breaks down. The flow does not end up with a Karman vortex street, most likely because of the 3D effects that play a large role at this aspect ratio ($\mathcal{AR} = 8$).

The corresponding vorticity fields, found via PIV measurements, are shown in figure 4.3. Using vorticity as a flow visualization tool highlights the locations of shear and rotation in the flow, e.g. the boundary layers, shear layers, and vortices. As can be seen in the first picture, the vorticity in the flow is initially confined to boundary layers very close to the wing surface. At the edges of the plate, the LEV and TEV have already begun to concentrate. As time progresses ($t^* = 2, 3, 4, 5$), flow leaves smoothly from the trailing edge of the wing, forming a starting vortex there. Initially, the boundary layer at the leading edge is forced back onto the wing, but it quickly rolls up into an LEV (see $t^* = 2, 3$). As the wing motion progresses, the LEV moves slightly off of the wing surface but remains in the vicinity. While the LEV is near the wing, it continuously gathers circulation fed to it by a shear layer emanating from the leading edge.

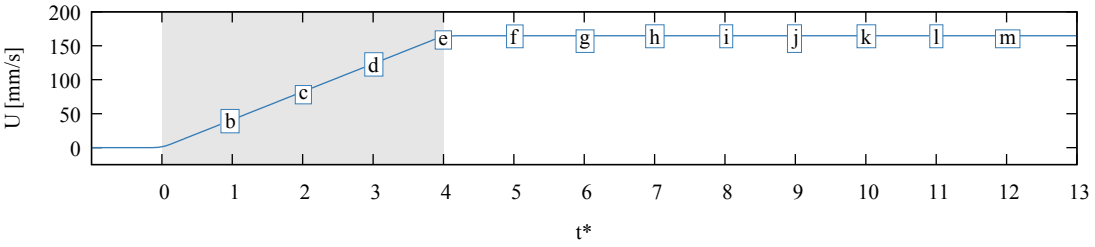

(a) Velocity profile with timing of images.

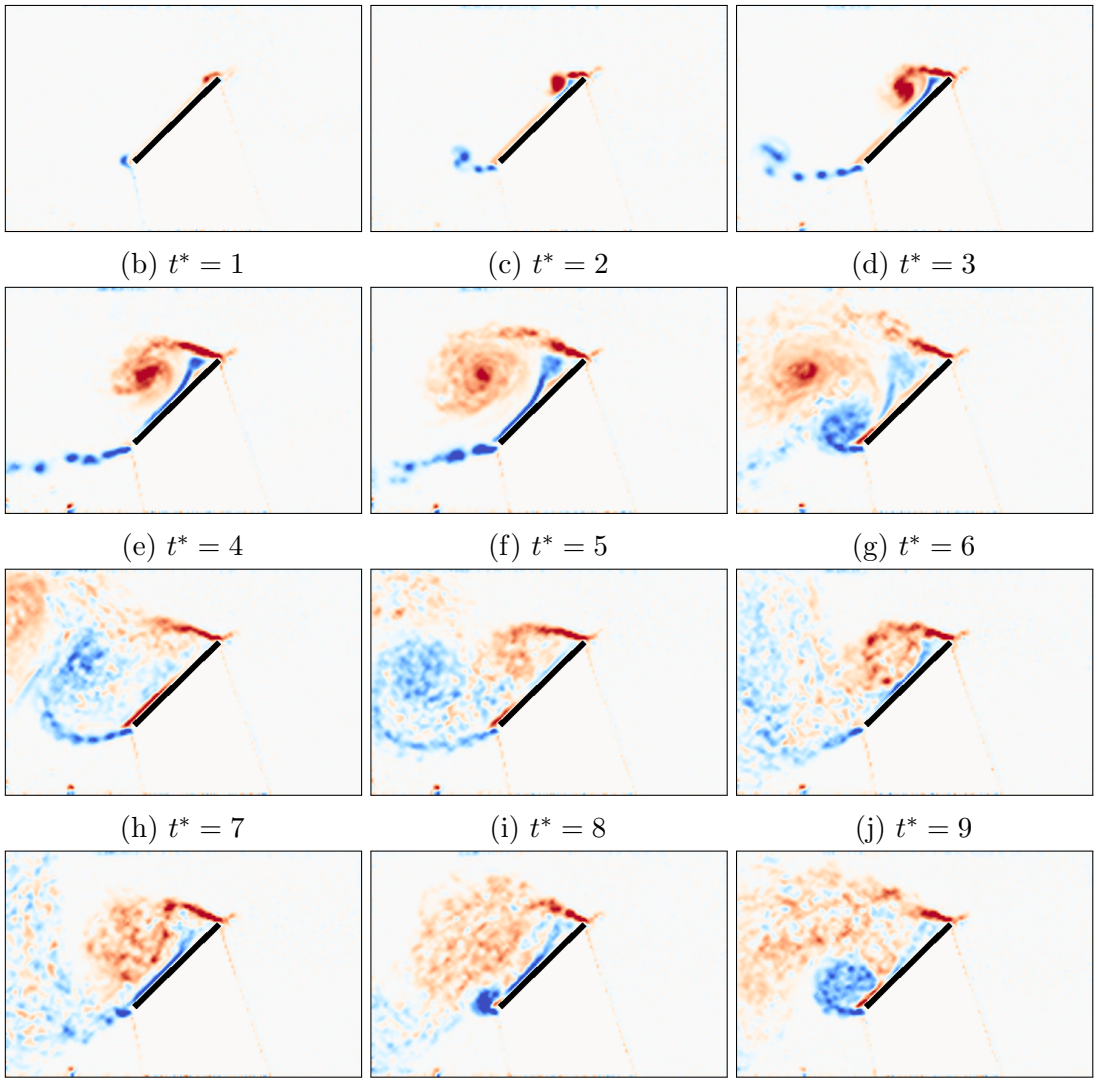

(b) $t^* = 1$ (c) $t^* = 2$ (d) $t^* = 3$

(e) $t^* = 4$ (f) $t^* = 5$ (g) $t^* = 6$

(h) $t^* = 7$ (i) $t^* = 8$ (j) $t^* = 9$

(k) $t^* = 10$ (l) $t^* = 11$ (m) $t^* = 12$

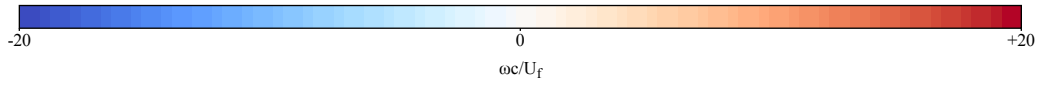

Figure 4.3: Phase averaged vorticity fields. Flow is from right to left. Red is counterclockwise rotation, blue is clockwise.

Eventually, the LEV grows to a size where it can no longer be sheltered from the free stream behind the wing, and it begins to convect away ($t^* = 5, 6$). This is when even the two-dimensional picture starts to get complicated. A new TEV rolls up behind the wing at $t^* = 6$ and shortly thereafter another LEV forms as well ($t^* = 8, 9, 10$), followed by yet another TEV as $t^* = 12$. Under the right conditions (two dimensional, and Reynolds number dependent), this alternating shedding process continues and the wake becomes a Karman vortex street. The long term shedding process is highly dependent on the aspect ratio of the wing, which will be discussed in the aspect ratio comparison section, section 5.4. Indeed, the details of vortex formation after the initial LEV depend on almost every aspect of the flow and are extremely difficult to predict. Looking outside of translational kinematics, rotation about a central axis can even produce a stable LEV [40]. In the present case, the wing is translating and has a finite aspect ratio ($\mathcal{AR} = 8$) and moderately high Reynolds number, so the flow devolves into a chaotic separated wake at longer times ($t^* > 30$) [117].

The two-dimensional chord-wise slice obtained from PIV measurements is our primary method of flow observation, but the full three-dimensional finite wing flow must be kept in mind. The tip vortices must play a role in the overall flow evolution, as mentioned previously as an aspect ratio effect. Spanwise flow is another factor, particularly in the rotating case, that can be easily hidden in a two dimensional analysis. Both of these can produce profound effects on the vortex evolution, but are not captured in the measurement which only records the in plane velocity components. To illustrate this, figure 4.4 shows the flow development at three different spanwise locations with vorticity images. The locations are parameterized by distance from the centerline of wing, b, normalized with the chord. The wing is an aspect ratio eight wing, so $b/c = 4$ is the wing tip. Center span, $b/c = 0$, could not be imaged because of physical limitations of the setup.

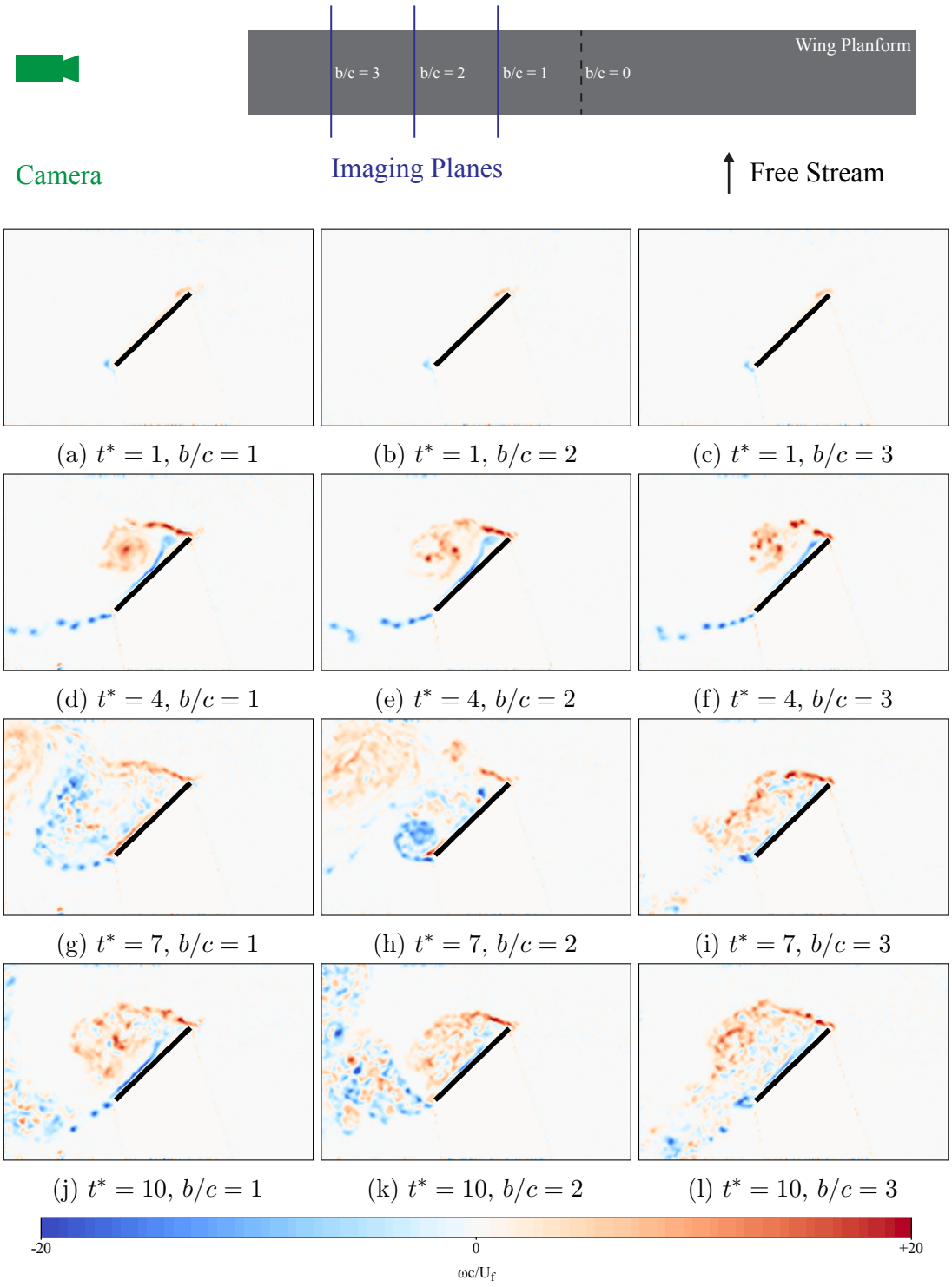

Figure 4.4: Vorticity fields at different convective time, t^*, in each row and different spanwise locations, b/c, in each column. Flow is from right to left. Red is counter-clockwise rotation, blue is clockwise.

Early in the test, at $t^* = 1$ and 4, the flow is very similar across the wing. As time progresses, however, the differences become apparent in the development of the trailing edge vortex (see $t^* = 7$). These differences continue to be exaggerated, resulting in markedly different wakes at $t^* = 10$. These images lead to two results. First, the flow development at early times is largely 2D. This gives one hope that a purely 2D model might work for at least the beginning of the motion, even if becomes less accurate at later times. Secondly, the progression seen here is consistent with the development of a tip vortex. At the beginning of the motion, the tip vortex takes time to grow, just as the LEV does. When it does begin to form and have an effect, that effect is stronger towards the wing tip [66].

The general picture, seen both through the LIC and vorticity, is an initially quiescent flow that is disturbed by the wing motion. The wing has sharp edges that cause the flow to separate, creating a shear layer that rolls up into an LEV that becomes the dominant flow feature for early times. Because the LEV remains close to the wing during its formation, it is expected to have a large effect on the force and moment that the plate experiences; this will be borne out in the force data discussed in the next section, section 4.3. The effect on the forces occurs even though the LEV is not fully attached, and eventually sheds. For this reason, its state and dynamics are of principal focus for both measurements and modeling.

4.3 Forces

It is intuitive that large changes in flow structure will correspond to an equally dynamic force history. The forces measured on the wing are shown in figure 4.5 as a function of $t^* = tU_f/c$. The figure shows four different curves including the lift, C_L, and drag, C_D, in the lab frame. The force coefficients in the wing-relative frame, the wing-normal, C_N, and the wing-tangential, C_T, coefficients are also shown. The force

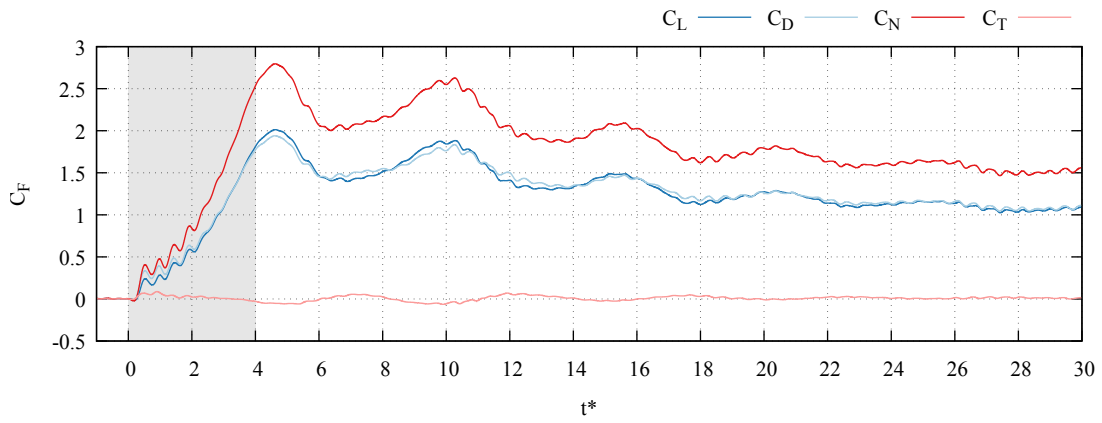

Figure 4.5: The forces on an $\mathcal{AR} = 8$ wing undergoing surge at $\alpha = 45°$. The shaded area corresponds to the acceleration portion of the velocity profile.

coefficients are normalized in the standard way for finite wing coefficients:

$$C_F = \frac{F}{\frac{1}{2}\rho U_f^2 c^2 \mathcal{AR}} \tag{4.1}$$

The data has been smoothed with a quadratic Savitsky-Golay filter (Matlab's `smooth()` function with option `loess`) and a smoothing width of $t^* = 0.868$. Using this method captures the peaks in the data well while rejecting background noise. Some mechanical vibrations are still visible in the data, especially immediately after motion start. These are related to the fundamental frequency of the support rods, and unfortunately occur at too low of a frequency to be filtered out without also attenuating the fluid forces.

Clearly, the lift and drag forces are essentially identical. This is a coincidence due to the choice of angle of attack, $\alpha = 45°$. A more universal observation for flat plates is that the majority of the force is concentrated in the wing-normal component, while the tangential component is essentially zero. Because of this, only the normal force will be shown for future comparisons between cases, since this time history when combined with the angle of attack provides an essentially complete description of the forces on the plate.

The lack of wing-tangential force is a byproduct of the flow separation. Recall from chapter 7 that the Kutta condition can also be expressed as requiring zero suction at the edge of the plate. The plate-tangential component is exactly the force associated with edge suction (neglecting viscous drag). The Kutta condition is presumed to hold at the trailing edge, so the lack of tangential force strongly points to the enforcement of the Kutta condition at the leading edge.

Focusing more on the shape of the curves, there are several distinct features. The forces start at zero in the quiescent flow, and motion begins at $t^* = 0$. At this time there is a nearly instantaneous rise in the force as the wing begins accelerating. This is followed by continued rise to a distinct peak that slightly lags the end of the acceleration. Following that, the forces slowly decay to steady state. The decay is punctuated by several peaks. Based on the flow visualization of figures 4.2 and 4.3, these peaks correspond to the formation and shedding of LEVs above the wing. This is evident from the images at $t^* = 5$ and $t^* = 10$, which show large LEVs and correspond to the peaks in forcing. The cyclic shedding process, shown through $t^* = 12$ in the figures 4.2 and 4.3, gradually wears down, and the forces have nearly finished settling to a steady value by the time the run reaches $t^* = 30$.

4.4 Vortex Tracking

Measuring the wake quantitatively reveals further information about how the flow develops. The measurements shown here will all be derived from PIV of the LEV, as it is the dominant flow feature early in the kinematics. The methods employed here are discussed in detail in section 3.4, but a brief review is in order here. Quantification of the LEV helps to distinguish between cases that produce different forces on the wing, but have visually similar LEV development. The simplest description of a single vortex is that of a point vortex, defined by a location and a circulation. Point vortices do not, however, exist in the real world, and so several vortex core models have been

proposed that describe a more realistic distribution of vorticity and the consequential radial velocity profiles. Some popular models include the Lamb-Oseen [167, 121] model and the Rankine model [168]. These models are designed to represent free vortices floating about in isolation (e.g. wingtip vortices far downstream) that have a radially symmetric velocity profile. They can be used to get information about the vortex circulation and core radius by correlating the model profile with that observed in experiment, and generally perform well in that context. In the present context however, the vortices in question are close to the wing, and as a result have a deformed shape and feature a feeding shear layer. This makes it difficult to follow the correlation procedure used with free vortices. Due to this difficulty, the present work relies on a point vortex description that simply uses location and circulation to characterize the LEV.

Even with a pared down vortex description, quantifying the vortex center and circulation is a challenge, once again due to the proximity of the LEV to the wing. Two methods presented themselves as the most viable in the present context: a maximum of Graftieaux *et al.* 's [166] Γ_1 criteria and the centroid of vorticity. Both are robust methods that are capable of dealing with the noise inherent in PIV measurement. The Γ_1 criteria is a better indication of the notional vortex center as it finds locations of maximum coherent rotation. The centroid of vorticity includes the shear and boundary layers, and so is a first order indicator of the aggregate effect of the whole wake. This approximation works best when the induced velocity is measured far from the centroid, although close to the vortex (e.g. within a chord length) the higher order effects can be dominant and the approximation breaks down.[1] The centroid method has the advantage of being fast and simple to compute. There is some ambiguity in the result from taking the sum of only one sign of vorticity, which causes the background noise to accumulate rather than cancel. To combat this, some

[1]Keeping the higher order terms is one of the fundamental ideas behind the Fast Multipole Method. [174, 175]

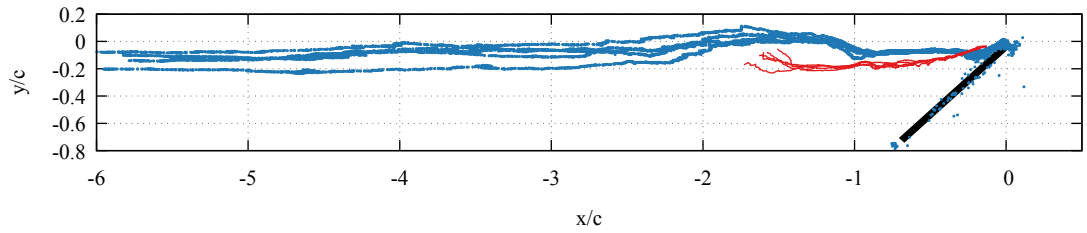

(a) The location history of the vortex in the wing frame.

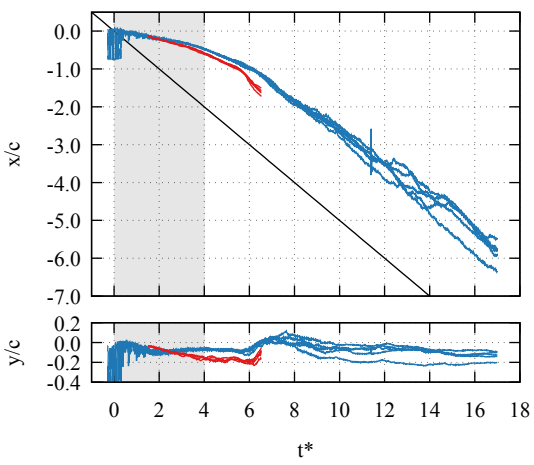

(b) The location of the vortex in time.

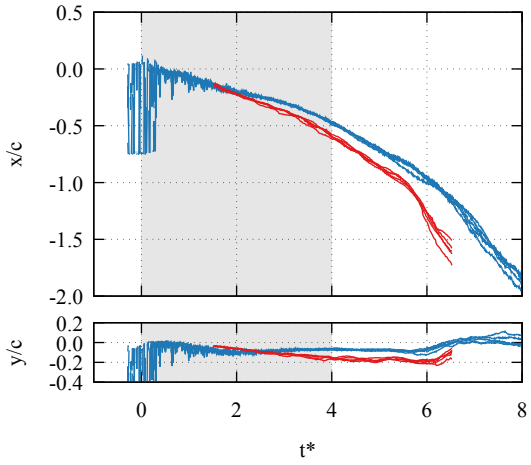

(c) The initial vortex convection.

vorticity centroid Γ_1 method

Figure 4.6: Vortex location measurements on a surging wing. Data from five independent trials is overlaid for both methods.

method of thresholding must be applied. This level of threshold is largely arbitrary, but has been chosen to minimally impact the circulation and location measurements, as discussed in section 3.4.2.

The tracks of the vortex center are shown in figure 4.6. These figures contain the tracks from both the vorticity centroid and Γ_1 criteria. Note that the Γ_1 data is restricted to the duration of time that the first LEV is in the imaging frame. The vorticity centroid method has been extended to account for vorticity leaving the frame with a frozen wake hypothesis, discussed in detail in section 3.4.3. In plots figures 4.6b and 4.6c, the darker lines are the x location and the lighter lines are the y location. The axes are the image axes (i.e. lab x and y) normalized by the wing chord, and both are relative to the leading edge. The centroid method has some noise at the

beginning of the run when the LEV has not yet gathered enough strength to achieve a good signal to noise ratio above the background noise. During this time the Γ_1 method is also unable to detect an LEV. Figure 4.6b also includes a line showing the vortex location as if it had convected downstream at half the free-stream velocity. This is the expected value from a vorticity centroid if the circulation is produced at a constant rate throughout the test and convected back from the wing at the free stream velocity.

Looking at the vortex convection in the wing frame, figure 4.6a, one sees the path of the vortex as it leaves the wing, as well as the discrepancy between the centroid and Γ_1 methods of vortex identification. Note that this figure does not indicate rate of convection, only location. Both methods indicate the LEV leaving the suction surface from approximately a tenth of a chord behind the leading edge. The centroid measurement convects nearly straight aft, while the Γ_1 convects slightly downwards. The centroid measurement also displays a distinct hump between $x/c = -2$ and $x/c = -1$. Figures 4.6b and 4.6c both indicate that an $x/c = -1$ corresponds to $t^* = 6$. Referring back to figure 4.3, the hump in centroid measurement occurs at the same time that the TEV forms and pushes the initial LEV off the wing. It is interesting that this hump is not reflected in the Γ_1 measurement, indicating that the center rotation of the vortex is less affected by TEV formation than the overall vorticity field and leading edge shear layer.

Figure 4.6c examines the initial convection of the LEV. It shows the same data as figure 4.6b, but over a short timespan so that differences in the data are magnified. The path of the LEV does not appear to be linear, but has a distinct curve indicative of the LEV convection velocity increasing in time. The increase in convection picks up considerably at $t^* = 6$, which, as discussed previously, corresponds to the formation of the TEV and the shedding of the first LEV. Figure 4.6b shows that at long times the centroid convects at close to half the free stream without any obvious oscillations. This

leads to the hypothesis that the circulation production reaches a relatively constant value, resulting in a roughly constant vorticity wake. This hypothesis will be tested in the subsequent review of the circulation flux measurements.

The y location is a bit more subtle in its development, staying near to zero and only falling slightly. As a first order approximation one can say that $y = 0$, especially up to $t^* = 6$. Higher order trends are difficult to generalize.

The first takeaway from the vortex tracking is that the vortex is neither "attached" to the wing nor is it swept away the at free stream velocity. From a modeling perspective, this means that the motion of the vortex cannot be accounted for with a simple assumption of fixed location either in the wing or lab reference frame, but requires knowledge of the vortex convection speed. As a solution, an empirical rate of x motion can be used, or the flow itself must by computed (e.g. with a potential flow model).

The second takeaway is that the exact trend in vortex location is difficult to determine from measurement. This stems from the aforementioned difficulty in defining a vortex, especially the present context of a growing vortex near a wing. It is not clear a priori which tracking method produces the "correct" vortex location. The first LEV can be tracked with reasonable success, but subsequent vortices are difficult to assess because of the turbulent nature of the flow (recall the flow images in section 4.2). The methods do agree well with themselves, up to $t^* = 6$.

The vortex location data shown here will serve as one of the methods for evaluating models of unsteady flow. Vortex location and convection is a primary factor in determining the resulting force on the wing, and thus a quantification of model success in this regard helps point out the reasons for success and failure in predicting the forces. The other primary vortex factor is the strength of the vortex, which will be discussed next.

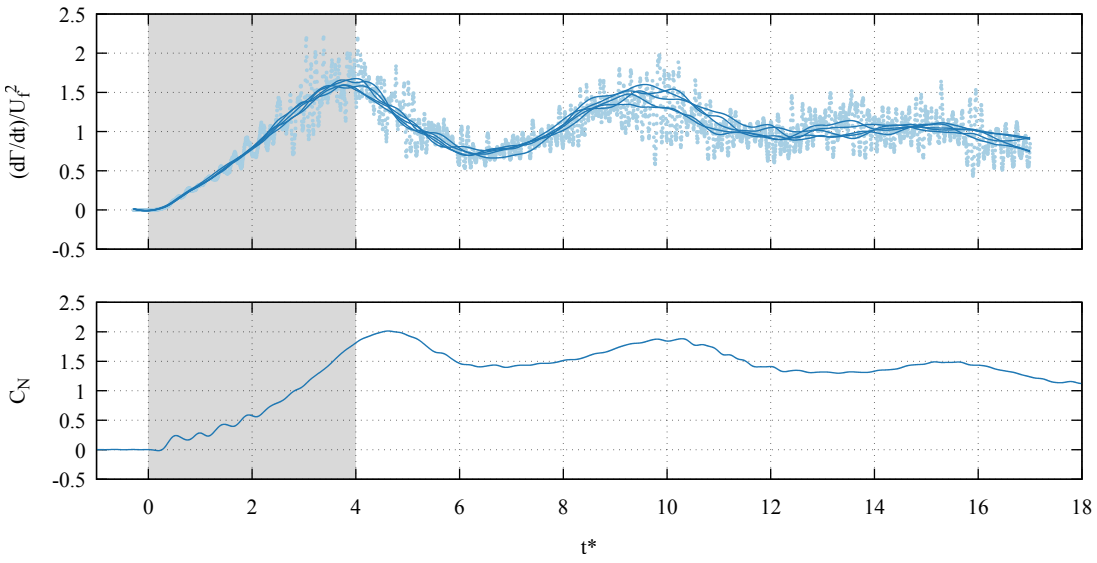

Figure 4.7: The top plot shows circulation production from the leading edge. Raw measurements from a single trial are represented by dots, and the filtered values from five separate trials represented with lines. The bottom plot shows the measured normal force on the same x axis for comparison.

4.5 Vortex Circulation

Because it directly feeds into the time history of vortex strength, the amount of circulation produced at the edge of the plate is one of the most critical components in determining the overall success of a flow simulation . The circulation flux measured for the baseline case is shown in figure 4.7. The circulation flux relates directly to the rate of change of the total circulation in the flow field. The flux from the leading edge is always positive, thus the circulation monotonically increases. The overall shape of the curve offers some interesting insights into what is required for modeling the flux, as well as the development of the flow field.

The first comment to make on the top plot of figure 4.7 is that it contains two sets of data. The points represent the raw flux measurement from a single run, and the lines depict the data from multiple repeated trials after filtering. The raw data shows large oscillations around the filtered history. These oscillations stem from the concentration of the vorticity into clumps near the leading edge before shedding to

join the main bulk of the LEV. This is easy to see in a video of the vorticity field, but difficult to depict in still frames. The filtered version of the data gives a clearer picture of the behavior of the vorticity flux, and so will be used in the ensuing discussion. Note also that there is a delay after $t^* = 0$ before the measurements record a flux of circulation. This is related to the short, but measurable, delay before the LEV forms and convects away from the leading edge. For example, see figure 4.3 at $t^* = 1$. The LEV is still very small, and it is clear that before this, at say $t^* = 0.5$, the LEV could barely be said to exist.

The circulation flux increases nearly linearly from $t^* = 0.5$ as the wing accelerates, reaching a peak near $t^* = 3.5$. The peak occurs before the end of acceleration, in contrast to measurement of the forces, which showed a peak after the end of acceleration. After this point, the wing moves at a constant velocity and the kinematics are fixed. The circulation flux, however, falls off and continues to change, passing through more peaks and valleys as it approaches a steady state. These maxima and minima correspond with the LEV formation and shedding process seen in the flow visualization. See figure 4.3 at $t^* = 4$ for the first peak, $t^* = 6$ for the subsequent minimum, and $t^* = 9, 10$ for the second peak. Note that the circulation production settles to a nearly constant value.

Comparing the flux data to the force data in the bottom plot, it is interesting to note that the timing of the peaks is different. The initial peak in vorticity production occurs at $t^* = 3.5$, while the forces do not peak until $t^* = 4.5$. The second vorticity production peak also leads the second force peak. This leads to the conclusion that the relationship between the LEV and the force on the wing is different than the LEV's relationship to circulation production. The circulation produced at the leading edge takes some time to amass and convect to where it can have a peak force production. The circulation production is also related to the location and strength of the LEV as they determine the strength of the LEV-induced velocity at the leading edge. Thus,

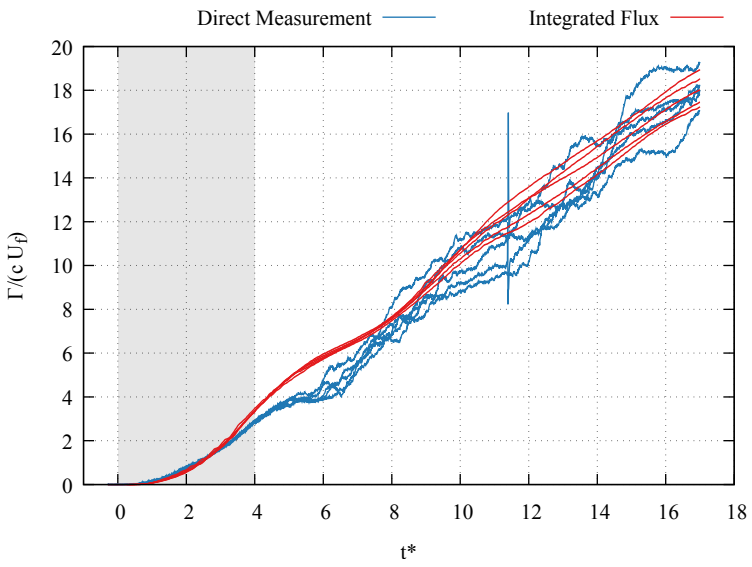

Figure 4.8: The positive circulation nominally in the LEV for 5 independent measurements.

it is easy to conclude that rate of circulation production at the leading edge depends on both the plate kinematics and the wake state. Both of these factors contribute to the flow field experienced by the leading edge, which in turn determines the rate of circulation flux into the wake.

The amount of total positive circulation measured in the flow field, i.e. that nominally in the LEV, is shown in figure 4.8 as a function of time, t^*. The figure shows both the directly measured circulation from each PIV frame and the time integration of the leading edge circulation production. Circulation increases monotonically with time as one would expect based on the overall picture of the flow in section 4.2 and the always positive flux measurements. The vorticity generated at the leading edge becomes a shear layer that feeds into the LEV, continuously increasing its strength. This curve is quite close to linear overall, although the early time has a more curved shape. This curve at the beginning is a direct consequence of the linear increase in circulation flux seen in figure 4.7. When that linear function is integrated in time, a quadratic curve results. The integrated production matches well with the total circulation, except for the period between $t^* = 3$ and 8. This is in opposition

to the results reported by Panah *et al.* [2]. Their study found that the leading edge produce twice as much circulation as was measured directly. The difference was accounted for via their measurements of the secondary vorticity produced under the LEV, which annihilated half of the leading edge production. The discrepancy between their study and the present work likely lies in their use of reciprocating plunge kinematics, although the underlying reasons are not entirely clear. This annihilation effect could also be the reason for the difference between measured and time integrate circulations in the present study between $t^* = 3$ and 8, as this corresponds to a period of very strong secondary vorticity (observe the negative vorticity boundary layer at these times in figure 4.3).

4.6 Summary

This chapter has closely examined the flowfield evolution and force production on a surging wing. The LEV was then quantified in both strength and location to ground its development with numerical data. These data showed that the none of the quantities involved are simple functions. In particular, the analysis of the vorticity flux illuminated its role in tying the entire system together as a whole. The amount of circulation production clearly depends on both the plate kinematics and the state of LEV. The strength of the LEV, in turn, is an integration in time of the circulation production. Further, its location is consequence of how the leading edge shear layer rolls up and the subsequent convection of the vortex as a whole. Thus the separated flow in question is a highly coupled system, and how any one part reacts will be reflected in the other quantities as well. Understanding that coupling and how the system is driven by leading edge shedding is critical in understanding the force results.

Chapter 5: Surge Parameter Variations

The baseline case results were presented in chapter 4 to imbue the reader with knowledge of the prevailing characteristics of the flow. In order to understand the driving factors behind those characteristics, this chapter presents results from systematically varying kinematic parameters. By varying the kinematics, the correct scaling of the results, in particular the circulation production at the leading edge, will be highlighted. The lessons learned seeking the scaling that collapses the circulation across the kinematics will guide efforts to construct a model. The scalings point out the relationship of the circulation to the kinematic parameters.

The chapter details results from variations encompassing simple changes to the surge case presented in chapter 4. These variations are to the final speed, acceleration magnitude, and angle of attack of the wing. A discussion of 3D effects and variations in aspect ratio will also be presented.

5.1 Reynolds Number

Reynolds number variations are achieved via a change in the final wing velocity. The three Reynolds numbers chosen here are $Re = 5,000$, $Re = 12,500$, and $Re = 20,000$, represented by the three velocity profiles shown in figure 5.1. These cases all use the same $\mathcal{AR} = 8$ flat plate wing. Note that the $Re = 12,500$ case is the same as the baseline case discussed in chapter 4, and that the angle of attack is still held constant at 45° for all cases. The acceleration distance is also held fixed at $s_a/c = 2$. Varying

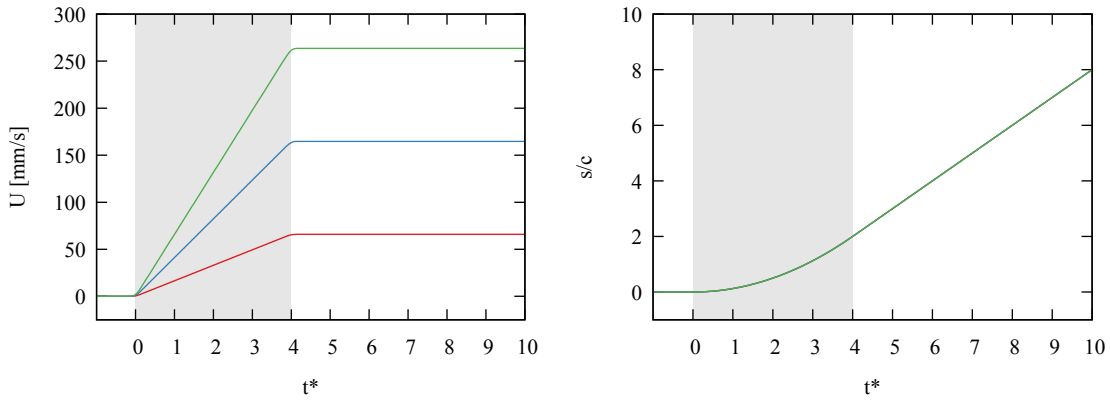

(a) velocity vs. time

(b) distance vs. time

Figure 5.1: The speed and distance profiles for the three different Reynolds numbers. Note that the plot on the right contains all three lines, but they are on top of one another.

final velocity while keeping the acceleration distance fixed has caused the cases to exhibit different dimensional accelerations (the three different slopes in figure 5.1a). On the other hand, prescribing the kinematics in this way means that altering the final velocity has no impact on the variation of distance traveled, s/c, with t^*, as seen in the overlap of the three cases in figure 5.1b. The dimensional acceleration changes with the square of the final velocity according to the equation (3.8). For the range of Reynolds numbers considered here, the force coefficients of wings using similar kinematics have been shown to be minimally dependent on Reynolds number [105, 176]. The focus in the current section is on the flow field measurements, which do vary with velocity.

A general comparison of the wake and overall vortex formation and shedding is shown in figure 5.2 for the three Reynolds numbers tested. These images show the results of making the frozen wake hypothesis discussed in section 3.4.3. The wakes are all shown at $t^* = 17.0$, corresponding to $s/c = 15$. The intensity of the dimensional vorticity varies between the three cases but this has been accounted for by normalizing the vorticity fields with $\omega c/U_f$. Under this normalization, both the arrangement of vorticity (i.e. the wake development) and strength are strikingly similar across the

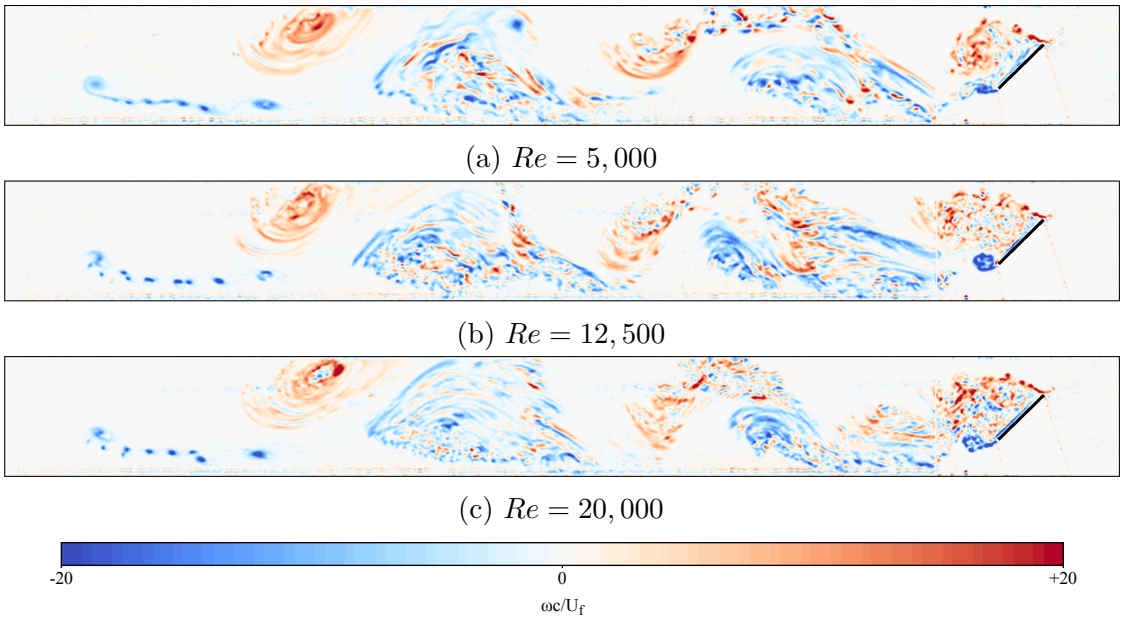

(a) $Re = 5,000$

(b) $Re = 12,500$

(c) $Re = 20,000$

Figure 5.2: Wake comparison at $t^* = 17.0$

three Reynolds numbers. Given the differences in velocity profile just discussed, it was not clear that this would be the case *a priori*.

The similarity in wake configuration is borne out in the vortex tracking measurements, shown in figure 5.3b. As the tracking data show, the location of the centroid of vorticity moves in virtually the same way for the three cases up to $t^* = 6$. Recall from the baseline case results of figure 4.6, which show five separate trials, that the location is highly repeatable during that time period, and so the confidence interval is quite tight here. After $t^* = 6$ the measurements at different Reynolds numbers begin to diverge, but so do the baseline case results. This is just the natural variability in the flow development and not a Reynolds number effect.

The circulation measurements in figure 5.3c tell a similar story of equivalent wake development. Note that the circulation values have been scaled with U_f, just as the vorticity fields. This accounts for the difference in the strength of vorticity seen in figure 5.2, and leads to the overlap in measurement seen up to $t^* = 5$.

The circulation production at the three different Reynolds numbers is compared

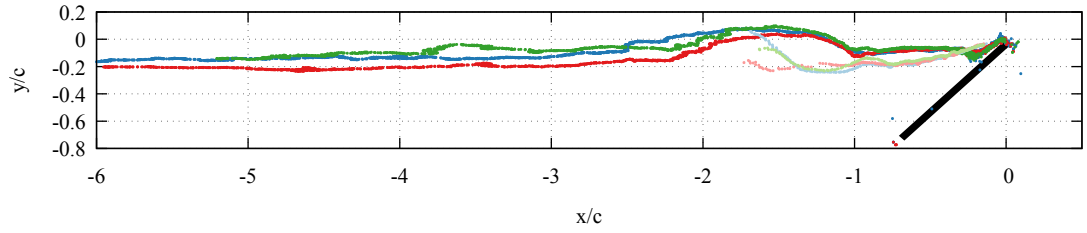

(a) Wing frame vortex locations.

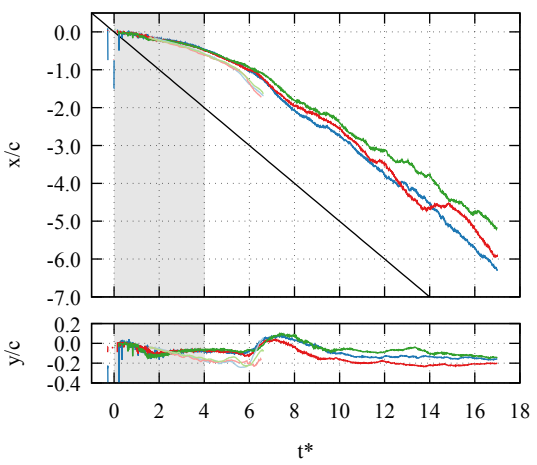

(b) The vortex centroid.

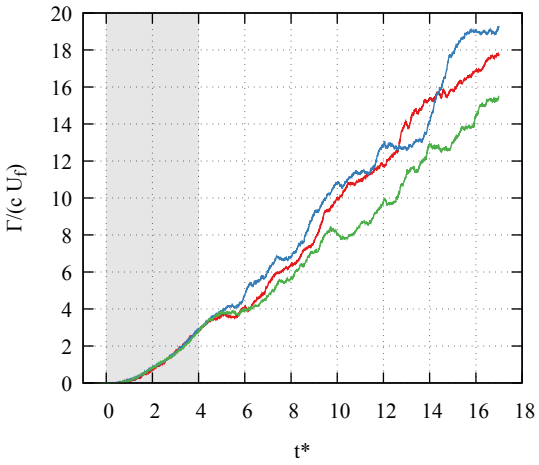

(c) The circulation.

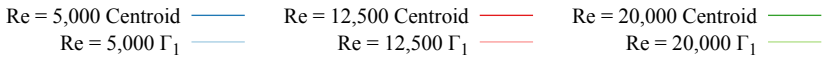

Figure 5.3: The flow field measurement results from three cases with varying Reynolds number. Figure 5.3b contains an extra black line corresponding with half the free stream velocity.

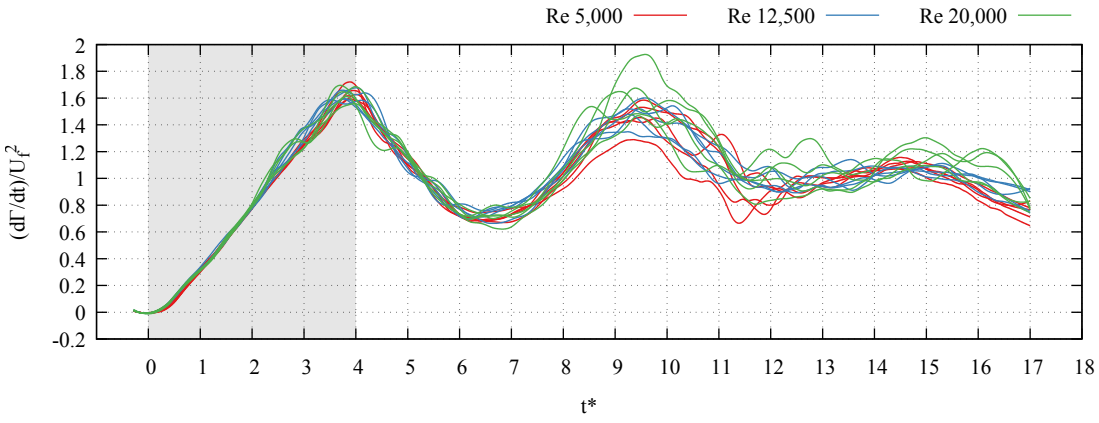

Figure 5.4: The circulation flux at three different Reynolds numbers (i.e. final translation velocity).

in figure 5.4. Recall that this data is all collected with a measurement plane one chord from the wing centerline with the method discussed in section 3.4.4. Each Reynolds number is represented by five different trials on the graph. The agreement of the LEV data seen in the location and circulation data measured is again repeated here. The flux is a local measurement, so no special extrapolation, such as the frozen wake hypothesis, is required to take the measurement over the entire course of the test run. The agreement between the three cases continues across the entire run, neglecting an increase in variability as the test continues.

The alignment of the results in time is evidence in favor of the use of either t^* or s/c as a relevant timescale. Clearly, if dimensional time, t, was used the results would not overlap as they do with t^*, as the scaling factor for t^* includes U_f.

The scaling of the magnitude of the results is also successful. Starting with the vortex location results, figure 5.3b, the x and y locations have been scaled by c. This is a straightforward choice, as it is the only relevant length scale in the problem. The scaling for circulation, Γ, and the circulation flux, $\mathrm{d}\Gamma/\,\mathrm{d}t$, have been chosen based on dimensional analysis, and use the final velocity, U_f. Whatever effect the difference in dimensional acceleration has appears to have been captured in choosing the scaling with U_f. This makes sense in the context of equation (3.8), as the acceleration varies directly with U_f.

Based solely on this Reynolds number study, it appears that the results scale with U_f in both time and magnitude. Further, when this scaling is applied, all of the data presents strong evidence of similar, if not identical, wake development between the three cases. Next, the acceleration distance will be varied while keeping constant final velocity to see how that affects the results.

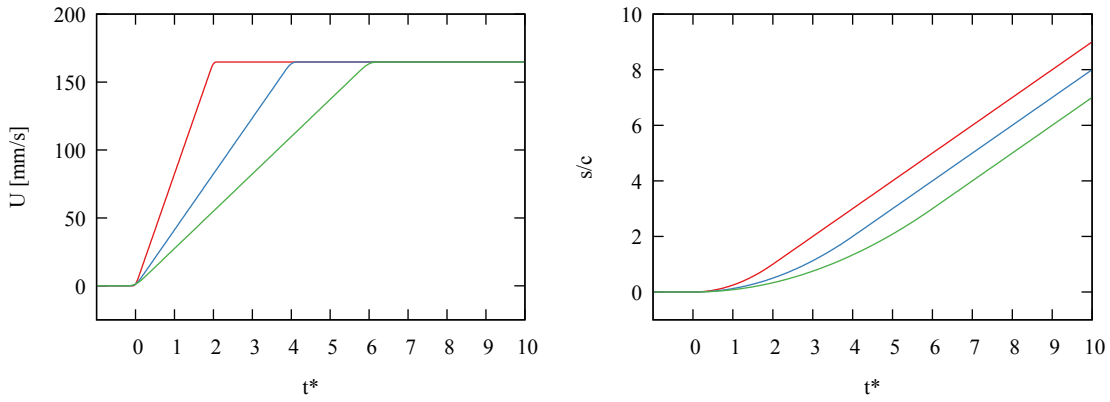

(a) velocity vs. time

(b) distance vs. time

Figure 5.5: The speed and distance profiles for the three different acceleration distances.

5.2 Acceleration Distance

This section discusses the results of varying the distance over which the wing accelerated, and therefore directly varying the level of dimensional acceleration without changing the final velocity. As before with the results at different Reynolds numbers, the same $\mathcal{AR} = 8$ flat plate wing at $\alpha = 45°$ is used and the PIV results are still taken at the chordwise plane located one chord from center span. As stated in equation (3.8), the dimensional acceleration is related to both the final velocity, U_f, and the distance of acceleration, s_a:

$$\frac{\mathrm{d}U}{\mathrm{d}t} = \frac{U_f^2}{2s_a} = \frac{\nu^2}{2c^3}\frac{Re^2}{s_a/c}$$

The three cases here have acceleration distances of $s_a/c = 1, 2$, and 3. This corresponds to $t_a^* = 2, 4$, and 6. Note that the constant acceleration profile means that $t_a^* = 2s_a/c$. These choices result in the kinematic profiles of figure 5.5. A difference between the profiles here and those of section 5.1 is that s/c no longer matches with t^* in the same way for the three cases; this allows for a comparison of t^* and s/c as time scales.

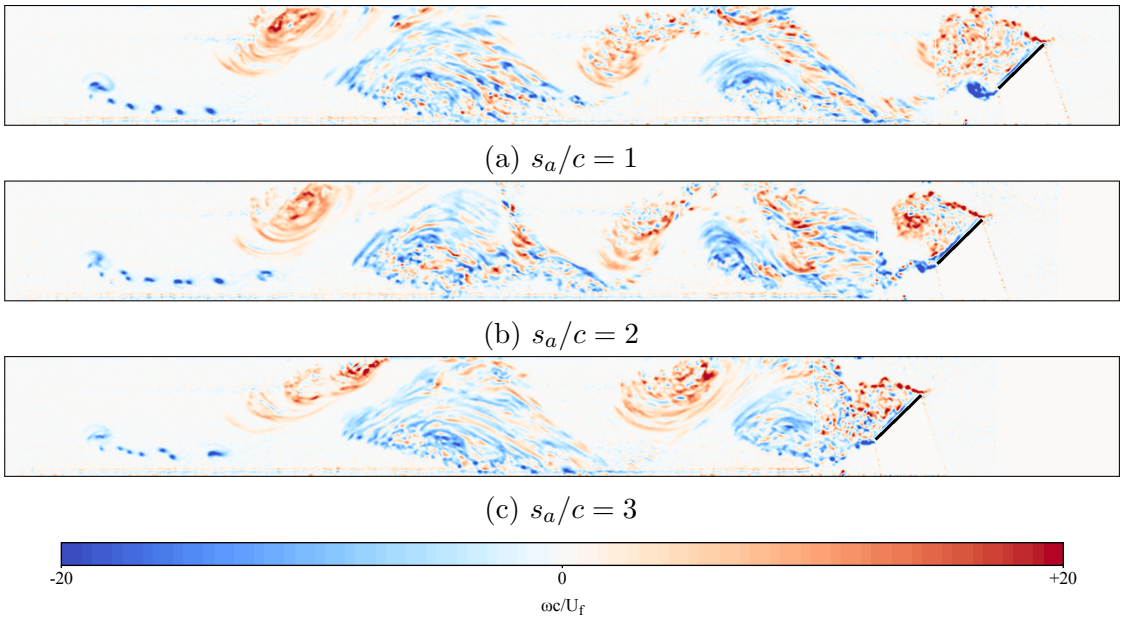

Figure 5.6: Wake comparison at $t^* = 16$.

The frozen wake vorticity fields for the three different acceleration cases at $t^* = 16$ are shown in figure 5.6. Note that for a fixed value of t^* the wake shows different stages of development and the wing has traveled different distances. The wake that has formed does appear similar across the three cases, however. This prompts the use of s/c instead of t^* as the more appropriate time scale for different accelerations.

Figure 5.7 shows the flowfields at the same s/c. By definition, this ensures that the wing is at the same location in each image. In addition, this appears to have generated the same amount of wake development in the three cases. The pattern of vortex shedding is similar, although there are small differences closer to the wing in the shape of the most recently shed TEV.

To quantify how well using s/c aligns the results, the vortex tracks and total circulation measurements are shown versus s/c in figure 5.8. Figure 5.8a shows the tracks in the wing frame of reference. While there are differences, it is hard to attribute them to the change in acceleration given the variability of the baseline

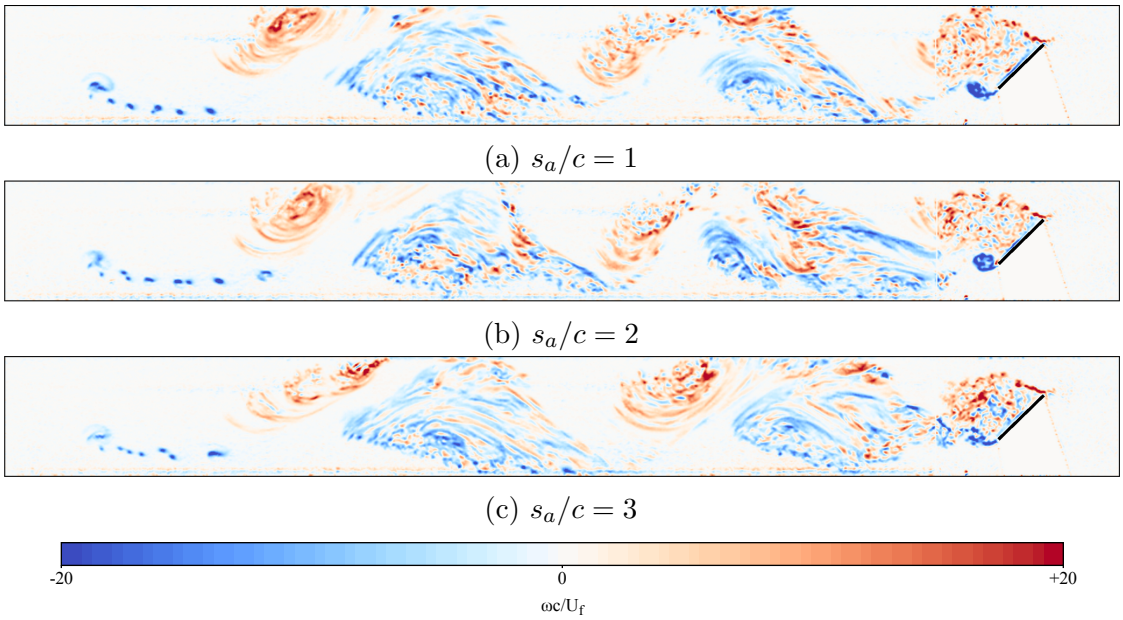

(a) $s_a/c = 1$

(b) $s_a/c = 2$

(c) $s_a/c = 3$

Figure 5.7: Wake comparison at $s/c = 15$.

case shown in figure 4.6. The time histories of x/c and y/c shown in figure 5.8b convey the rate of convection, and they show a definitely diverging trend in x/c centroid measurement. The centroid moves away from the wing faster for the fastest acceleration, and convects slowest for the slowest acceleration. The total circulation also shows a clear trend with acceleration distance. The amount of circulation during the acceleration portion (s/c between 0 and 3) correlates with the magnitude of acceleration.

Figure 5.9 shows the measured vorticity flux with three different normalization schemes. Each case is represented by five trials to give an impression of the repeatability of the measurement. Note that the same set of measurements are displayed in each plot, and only the normalizing factors have changed. The curves in figure 5.9a shows the results normalized in exactly the same fashion as the baseline and Reynolds number cases: $\mathrm{d}\Gamma/\,\mathrm{d}t$ is normalized with U_f and t^* is used for the time axis. This plot makes clear two trends noted in the previous data. The first is the correlation of circulation production to acceleration magnitude noted in the circulation measure-

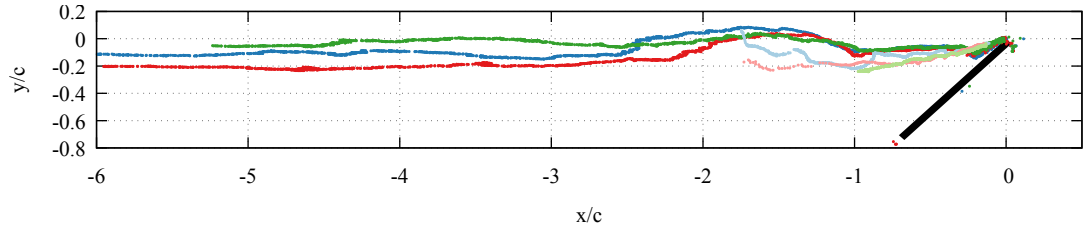

(a) Wing frame vortex locations.

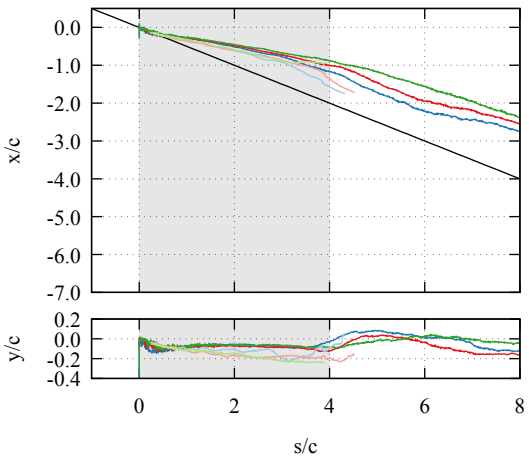

(b) The vortex centroid.

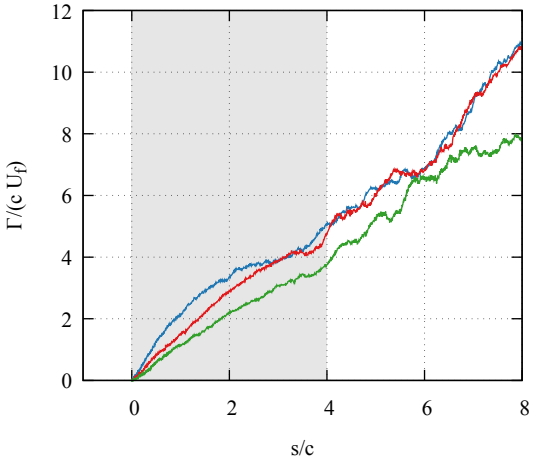

(c) The circulation.

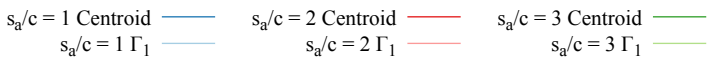

Figure 5.8: The flow field measurement results from three cases with varying acceleration.

ment of figure 5.8c. The second is the timing of the circulation production. The peak circulation production always corresponds with the end of acceleration, but the overall shape of the histories are shifted so that the maxima and minima don't align. This is as expected from the velocity profiles in figure 5.5 and the wake images in figures 5.6.

Displaying the wake at the same value of s/c in figure 5.7 gave good alignment of the wake features. Applying this timescale to the circulation production produces figure 5.9b. This plot shows the reason for avoiding the s/c timescale up to this point. The data at very early times ($t^* < 1$) is compressed into a vertical line, hiding variations in this portion of the test. On the plus side, using s/c has made serious progress in aligning the trends. It shifts the location of the local minima at $s/c = 4.5$ and maxima at $s/c = 7.5$ to correspond across the three cases. The magnitude of the production terms still differ during the acceleration period, but the development of the flow after the acceleration portion now follows (almost) a single trend. The overlap isn't quite perfect, similar to the divergence of the centroid location in figure 5.8b. The overlap does imply that if the acceleration distance could be decreased to 0 (an impulsive start) a single trend could be found that might constitute an indicial response. This quite remarkable, given that while the wings all have the same final velocity and angle of attack, the LEV is not the same across the three cases. One would expect this to have a more pronounced effect on the circulation production given the similarity of the recorded locations.

It is also possible to normalize the flux with acceleration instead of just final velocity, and the results can be seen in figure 5.9c. In order to make the units work, the normalizing factor is $c(\,\mathrm{d}U/\,\mathrm{d}t)$, which becomes $U_f^2/(2s_a/c)$ after some manipulation of equation (3.8). Using both s/c and the normalization with acceleration has caused the magnitude during the acceleration portion to match quite well across the three cases, but has separated the cases in magnitude after the end of acceleration.

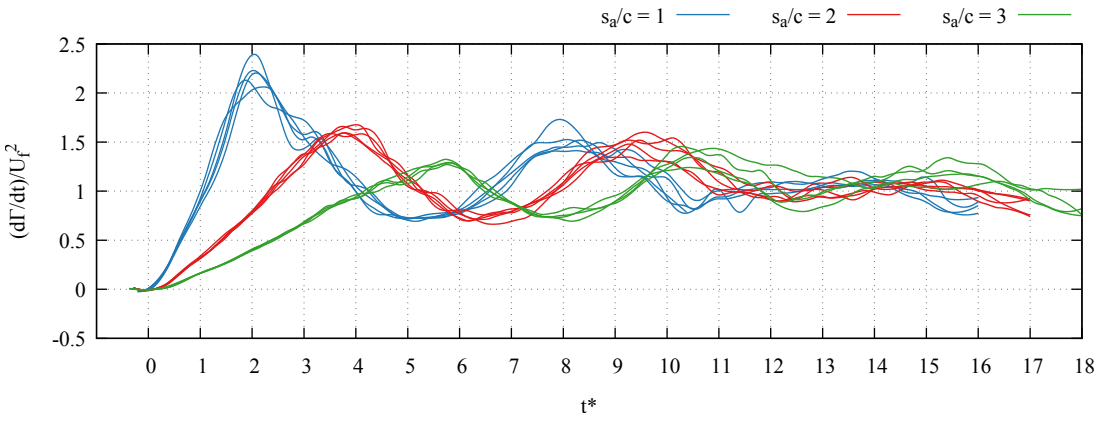

(a) Normalizing as before with $(\mathrm{d}\Gamma/\mathrm{d}t)/U_f^2$ and t^*.

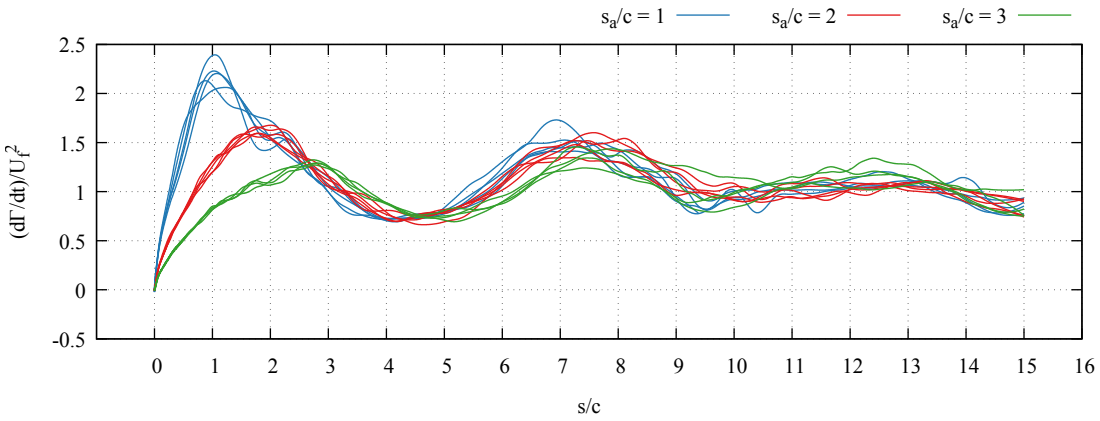

(b) The same results as above, now plotted with s/c instead of t^*.

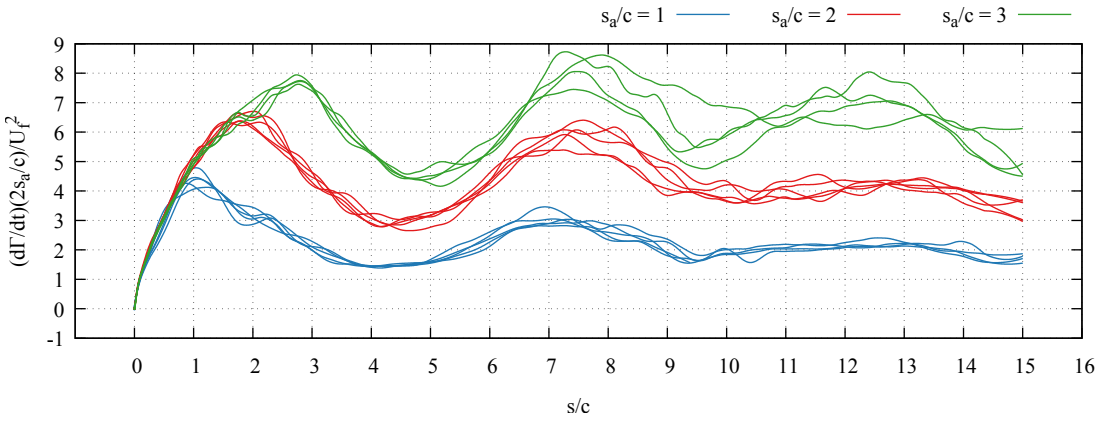

(c) Normalized by dimensional acceleration, $U_f^2/(2s_a/c)$, instead of U_f.

Figure 5.9: Comparing different normalizations for both time and circulation magnitude on the same data.

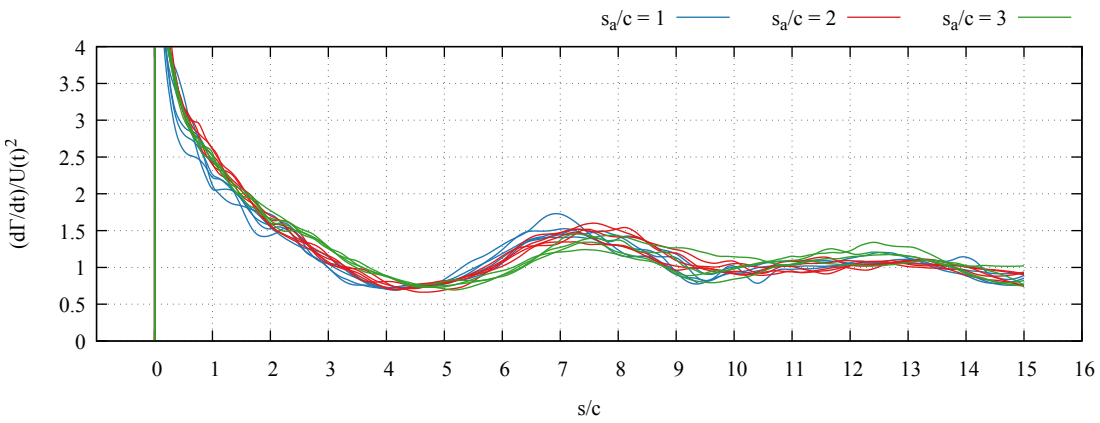

Figure 5.10: Circulation production normalized by the instantaneous velocity.

This appears to stand in contrast with the results from varying the Reynolds number, figure 5.4, which all collapsed when scaled by final velocity squared, U_f^2. The collapse there occurred in spite of a hidden variation in dimensional acceleration between the cases. For those cases, the change in dimensional acceleration was unintentionally captured because the dimensional acceleration scaled, as above, with $U_f^2/(2s_a/c)$, and s_a/c remained constant.

Returning to the cases with varying s_a/c, figures 5.9b and 5.9c imply that different kinematic parameters collapse the circulation production during different portions of the velocity profile. The solution proposed in my previous work [152] was to use the instantaneous velocity. Doing so results in figure 5.10, which is the final variation on the theme of normalizations the reader will be subjected to. Here, the normalized value trends towards infinity at the beginning of the run as a consequence of the normalizing factor (i.e. the velocity) approaching zero. The normalization manages to collapse the values across the entire run. For further confirmation, the scaling has been applied to the Reynolds number variation in figure 5.11. This produces a similar level of collapse as the acceleration study.

The collapse of the circulation production for different velocities profiles when normalized by the instantaneous velocity strongly points towards using the $U(t)^2$ as a

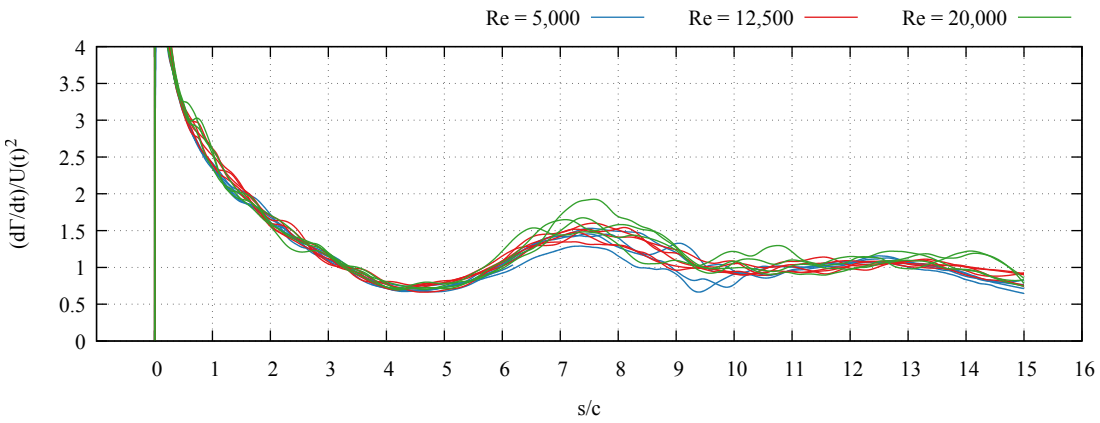

Figure 5.11: Circulation production normalized by the instantaneous velocity.

basis for relating plate kinematics to circulation production. It was fortunate that the wake development in these cases (the variations of Re and s_a/c) was similar enough that they produced the same pattern of vortex shedding. The other factor necessary for prediction of the circulation production is to diagnose how it responds to different types of wake development. This will be the subject of the next two variations, which deal with changing the angle of attack and the aspect ratio.

5.3 Angle of Attack

This section deals with variations in the angle of attack, while keeping the same $\mathcal{AR} = 8$ wing and using the same $Re = 12,500$ and $s_a/c = 2$ kinematics as the baseline case discussed in chapter 4.

Figure 5.12 shows the frozen wake vorticity fields. These are markedly different between the three angles of attack, and here the differences are in the distribution of the wake vorticity instead of just the timing. It is therefore unlikely that a shift in the timing of the run (like the shift from t^* to s/c in section 5.2) will serve to align the circulation production. The $\alpha = 60°$ case in particular deviates from the vortex shedding process see in the previous data. Towards the end of the run, the wake no longer shows distinct vortices, but instead resembles an unorganized stalled flow.

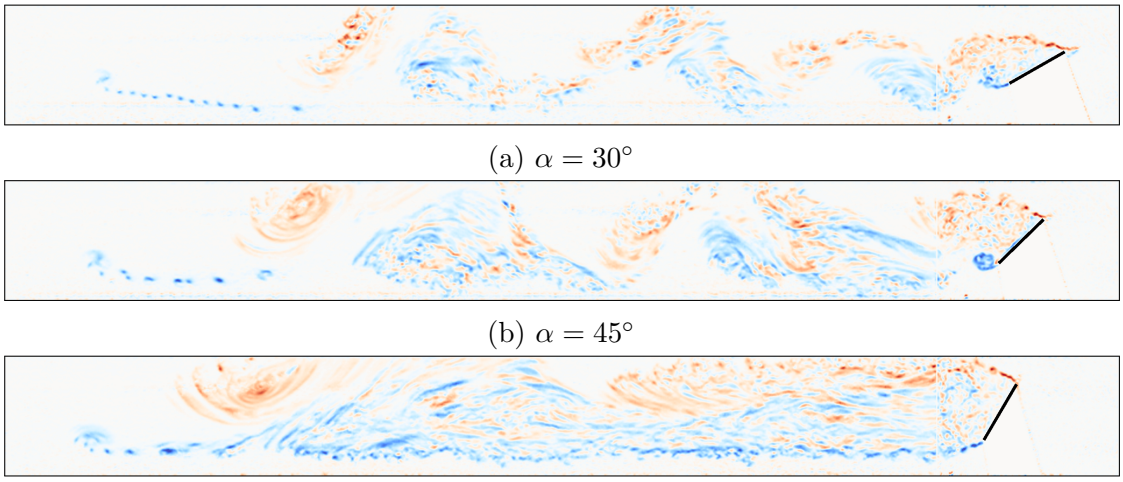

(a) $\alpha = 30°$

(b) $\alpha = 45°$

(c) $\alpha = 60°$

Figure 5.12: Wake comparison.

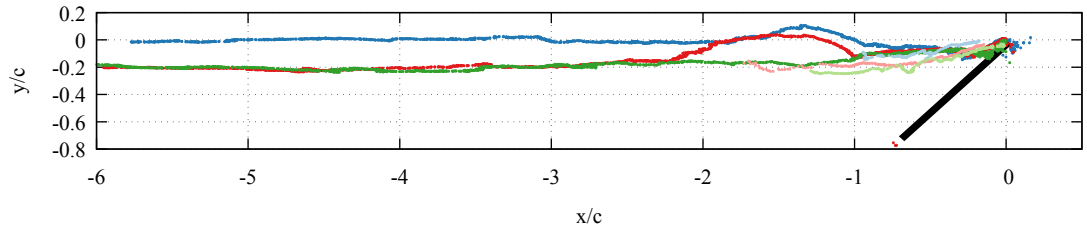

(a) Wing frame vortex locations.

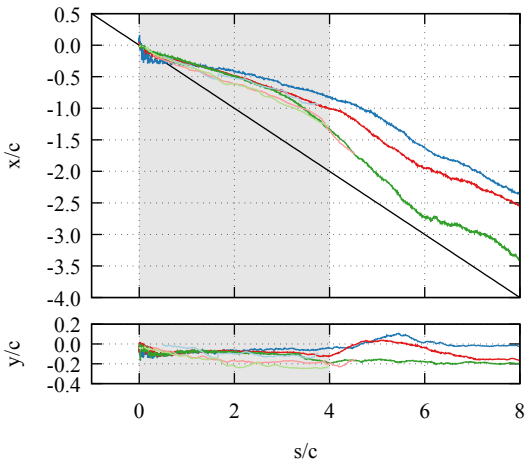

(b) The vortex centroid.

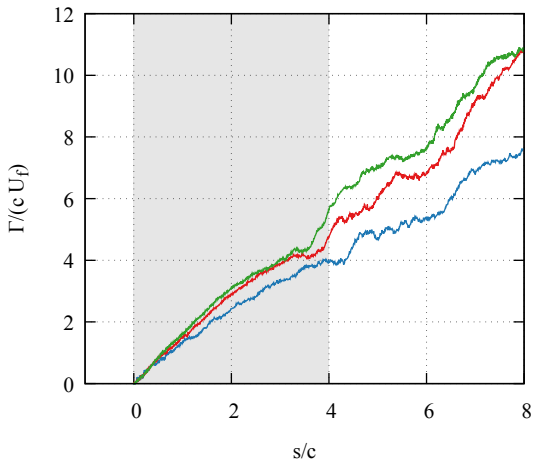

(c) The circulation.

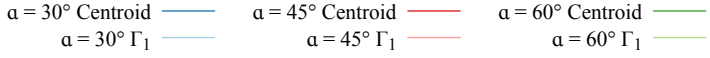

Figure 5.13: The flow field measurement results from three cases with varying angles of attack. Note that in figure 5.13a, the wing is incorrectly represented for the $\alpha = 30°$ and $\alpha = 60°$ cases.

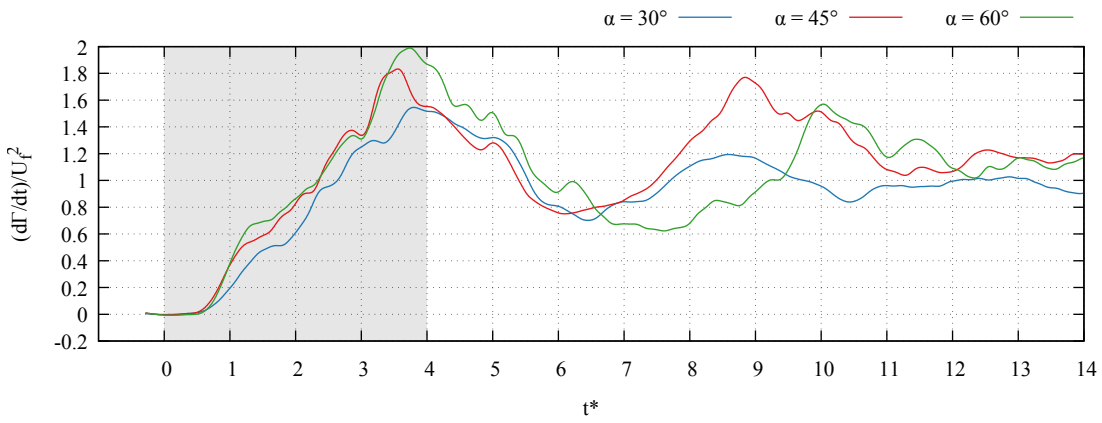

Figure 5.14: The circulation flux at three different angles of attack.

These changes in the wake structure are reflected in a low order sense in the LEV measurements shown in figure 5.13. It is difficult to make conclusive statements about the wing frame vortex locations in figure 5.13a. The x/c location data in figure 5.13b shows slower convection at lower angles of attack (i.e. as α decreases x/c gets closer to zero). The $\alpha = 60°$ case is prominently lacks the characteristic hump in y/c at $t^* = 5$ that is present for the other angles of attack. The total circulation measurements in figure 5.13c display increasing circulation with angle of attack, but the trend is not very strong.

The circulation flux measurements, figure 5.14, show surprisingly little change between the the three angles of attack; certainly not enough to conclusively differentiate them. These flux measurements used the "wide" field of view (discussed in section 3.4 due to difficulties in fitting the wing in frame for the "tight" field of view. The circulation measurements back up the flux measurements by showing the $\alpha = 30°$ case to have the least total circulation, followed by the $\alpha = 45°$ case, and the $\alpha = 60°$ case with only slightly more. The tacit hypothesis was that the circulation production would scale in magnitude with the wing-normal velocity component, $U \sin(\alpha)$, but this does not appear to be the case, as the magnitude of the initial peak at $t^* = 4$ is already within experimental error (see the variation in magnitude between

the "wide" cases in figure 3.10).

Further, past the first vortex shedding the circulation production progresses differently between the three angles of attack. The baseline, $\alpha = 45°$, case has a strong second peak at $t^* = 9$. The $\alpha = 30$ has a second peak at roughly the same time, but with much lower magnitude, and the $\alpha = 60°$ case has a delayed second peak. These changes come as a result of the different wake development noted previously.

In an earlier work, Manar *et al.* [152] proposed that one could alter the timescale to $\sigma(t)$, defined thusly:

$$\sigma(t) = \int_0^t U(\tau) \sin(\alpha(\tau)) \, \mathrm{d}\tau \tag{5.1}$$

This produced a nice collapse of the pitching wing data in that paper. Application to the present set of data is shown in figure 5.15. The circulation production results in the present work are already reasonably aligned using t^*, so shifting them by $\sin(\alpha)$ only served to spread them. The success in the previous work must be related to the use of pitching kinematics in lieu of the fixed angle of attack cases here. How a scaling could work for pitching but not a fixed angle of attack is not clear. Instead, the application of σ serves as an example of the dangers of using distance along the x-axis. Doing so has caused the results of $\sigma/c < 0.5$ to appear to match, but this is merely an artifact of the timescale.

Likely due to the difference in wake structures, a collapse of the results across the different angles of attack could not be achieved with the kinematic parameters. This shows the limits of disregarding the wake development in seeking to predict the circulation production.

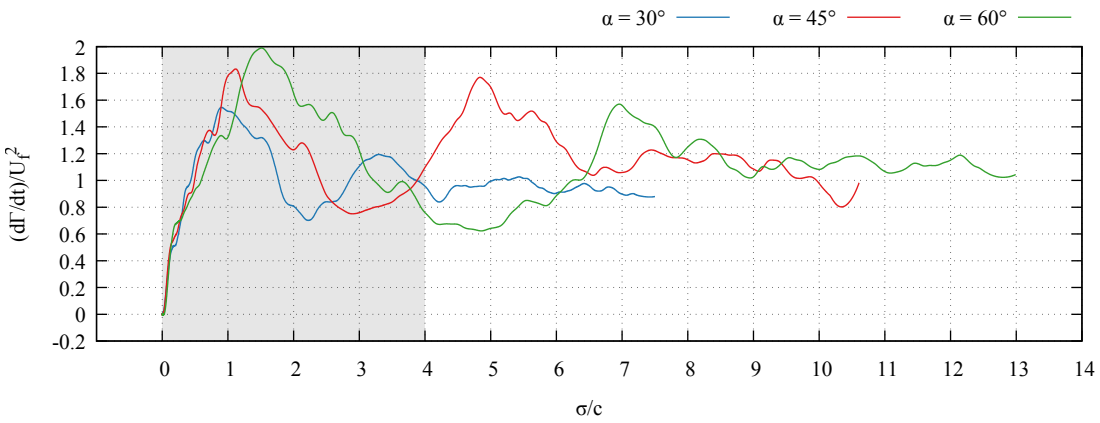

Figure 5.15: The circulation flux at three different angles of attack, plotted with σ/c .

5.4 Aspect Ratio

The tests presented in this thesis have all been conducted with a finite aspect ratio wing, though extensive use of two-dimensional PIV can make this easy to forget. The full flows are three-dimensional, and the differences across the span of the span were considered for the baseline case in the discussion of figure 4.4. The results showed that the flow at early times was close to two-dimensional across the span, though at later times the tip vortex had a marked impact on the LEV shedding process. Altering the aspect ratio simultaneously alters the relative impact of the tip vortex on the total flow. Thus one expects to see differences in LEV formation and shedding on the $\mathcal{AR} = 4, 6$, and 8 cases examined in this section.

The frozen wake vorticity fields for the three different aspect ratios are shown in figure 5.16. These show the wake history one chord from center span. This amounts to different distances from the imaging plane to the tip of the wing: 1 chord for the $\mathcal{AR} = 4$ case, 2 chords for the $\mathcal{AR} = 6$ case, and 3 chords for the $\mathcal{AR} = 8$ case. Unfortunately the $\mathcal{AR} = 4$ data for late in the run was corrupted and is no longer available. The available data shows significant breakdown of the wake vortex structure however. The $\mathcal{AR} = 6$ and $\mathcal{AR} = 8$ wakes are similar. This leads to the conclusion

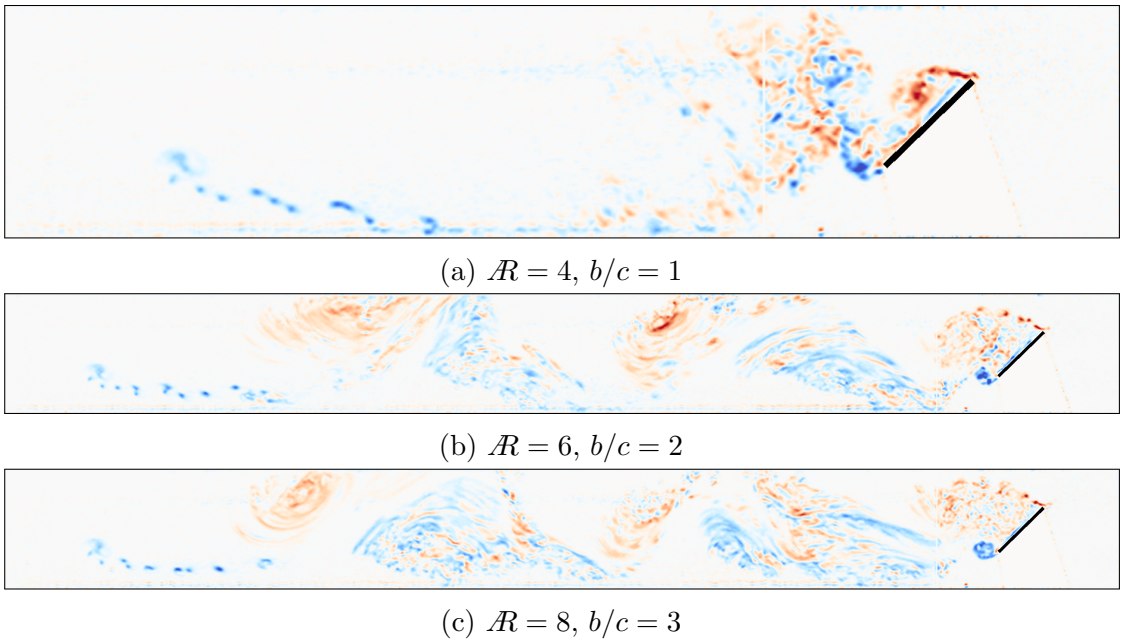

(a) $\mathcal{AR} = 4$, $b/c = 1$

(b) $\mathcal{AR} = 6$, $b/c = 2$

(c) $\mathcal{AR} = 8$, $b/c = 3$

Figure 5.16: Wake comparison one chord from the centerline.

that the distance from the wing tip is the critical factor in determining the wake structure; the tip effects confined to an aspect ratio independent region near the tip. Thus longer wings (i.e. higher aspect ratio) should behave closer to their two dimensional counterparts as tip effects have a smaller relative impact. This is well know in the area of steady aerodynamics [117]. Perhaps the more relevant question here is how close to two dimensional the flow, at any aspect ratio, is near the beginning of the run.

The force results support the hypothesis that aspect ratio has minimal impact at early times. Results for a translating wing at $\alpha = 45°$ are shown in figure 5.17. The figure shows only the normal force coefficient to reduce clutter in the plot. The kinematics here are the same as the baseline case with $Re = 20,000$, $s_a/c = 2$, and $\alpha = 45°$.

The first observation is that the curves are nearly identical during the acceleration, $t^* = 0$ to $t^* = 4$. At the end of the acceleration, the $\mathcal{AR} = 4$ case has a slightly lower peak force than the other two wings. The vortex shedding process and decay

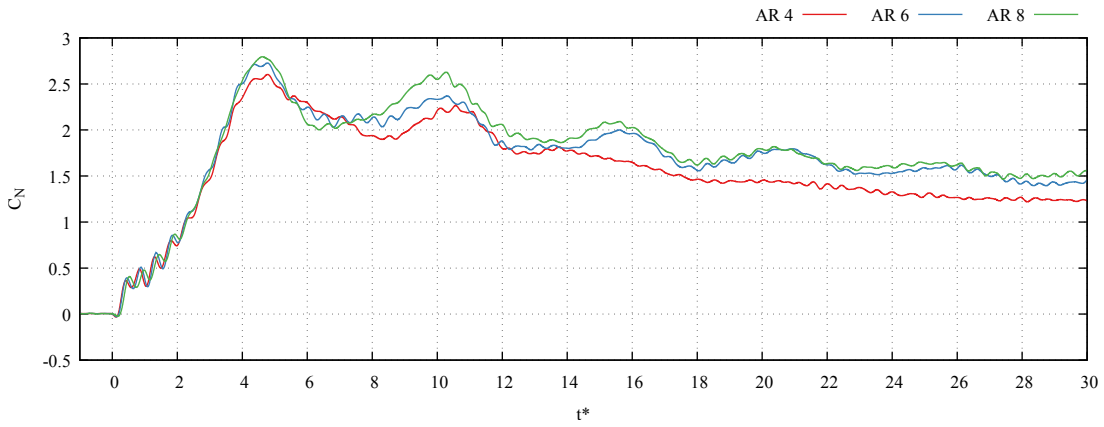

Figure 5.17: The normal force coefficient on wings of $\mathcal{AR} = 4$, $\mathcal{AR} = 6$, and $\mathcal{AR} = 8$.

to steady state after the end of the acceleration is clearly affected by the aspect ratio. The aspect ratio 4 case shows only a single secondary peak in forcing, implying that only one secondary LEV forms after the primary LEV sheds. The $\mathcal{AR} = 6$ and $\mathcal{AR} = 8$ cases show other peaks (for a total of five LEV formations) before settling down to steady state. The implication for two dimensionality is that aspect ratio's largest effect is on the later ($t^* > 12$) vortex formation and shedding process.

The vorticity flux measurements are shown in figure 5.18, and the circulation measurements are shown in figure 5.19c. As in the force results, the $\mathcal{AR} = 4$ case is clearly the most affected. The circulation production for the $\mathcal{AR} = 6$ and the $\mathcal{AR} = 8$ cases are similar, with the $\mathcal{AR} = 8$ case producing slightly more circulation, resulting in a higher total circulation, as seen in figure 5.19c. The difference in flux is slight though, and certainly inside the error bars of measurement. The $\mathcal{AR} = 6$ and $\mathcal{AR} = 8$ cases both have peaks in circulation production (at $t^* = 3.5$ and $t^* = 9$) that precede peaks in forces (at $t^* = 4.3$ and $t^* = 10$). The $\mathcal{AR} = 4$ case stands in contrast to these cases with a single peak in circulation production at $t^* = 5.2$. This is not corroborated in the circulation measurement, which shows similar values throughout the test for all aspect ratios. On the face of it, this would mean that the extra circulation produced is leaving the slice of the flowfield. A simple explanation would be that spanwise flow

induced by the tip vortex. The location of the vortex for the $\mathcal{AR} = 4$ case is also markedly different.

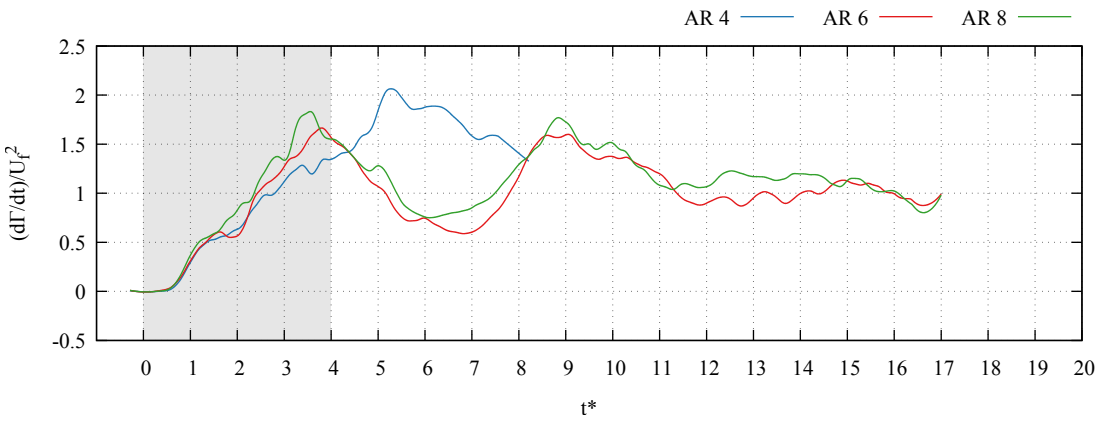

Figure 5.18: The circulation flux on three aspect ratios. The flux was measured at a plane one chord from the centerline for all cases.

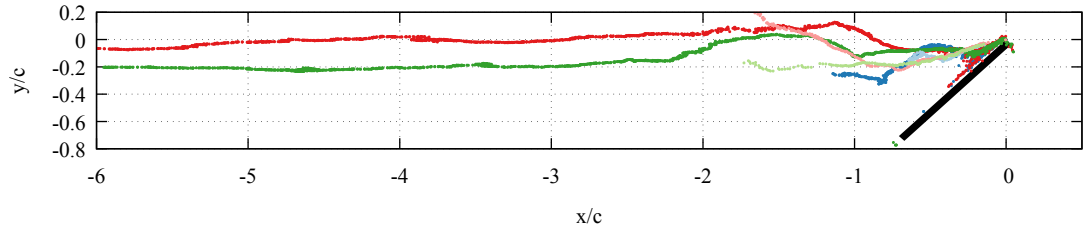

(a) Wing frame vortex locations.

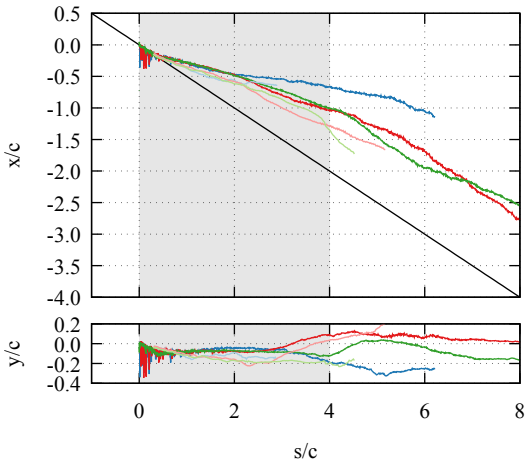

(b) The vortex centroid.

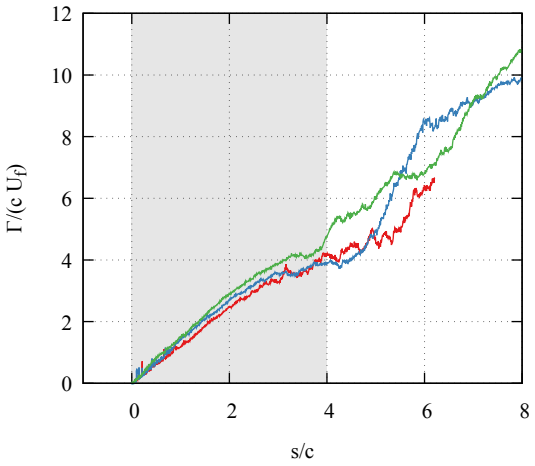

(c) The circulation.

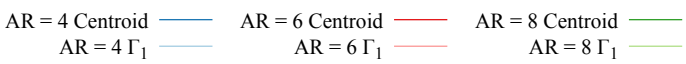

Figure 5.19: The flow field measurement results from three cases with varying aspect ratios.

5.5 Summary

Starting with the variations in Reynolds number, the results showed that circulation production could successfully collapse with a normalization based on the final wing velocity. This was possible thanks to the wake developing and shedding in exactly the same way for each test. Varying the acceleration on its own increases the complexity of the problem. It was shown that the wake development occurred in the same way when the results were plotted versus s/c, similar to the results of Wagner [9]. The magnitude of the circulation production (and thus the circulation) was shown to collapse when scaled with the instantaneous wing velocity. Together, these suggest that the portion of circulation production due to wing motion should be a function of $U(t)^2$, which is a promising result for modeling.

The variations in angle of attack were not so kind in permitting a collapse of the results. These variations produced changes in wake development that kinematic parameters could not account for. This points to the need for a comprehensive wake model that allows for the self convection of the vorticity that sheds from the wing.

Comparing the results at different aspect ratios led primarily to the conclusion that the results at early times are close to two-dimensional. This means that a two-dimensional model is likely to be able to make accurate predictions for at least the first 4 chords of travel, although three-dimensional effects become increasingly relevant as the wing travels further.

The result of the parameter variations in this chapter indicate that searching for a kinematics based scaling parameter will not be a sufficiently general prediction tool. While it may be possible to collapse the results for some kinematic variations, other basic changes to the kinematics (e.g. angle of attack) are likely to break the normalization. The self convection of the wake means that, unlike the Wagner case where convection is neglected, there is no "universal" circulation growth curve that

can be applied, even for this simplified representation of the problem.

Chapter 6: Modeling Methods

This chapter serves to document the exact methods used for the modeling work presented in this thesis, in a similar fashion as the experimental methods are documented in chapter 3. In addition, this chapter details the reasoning and formulation of the boundary layer analogy used to relate the leading edge circulation production to the wake measurements.

6.1 Complete Models

All of these pieces come together to form a complete working model of fluid flow and the forces acting on wing profile. Though they may slightly differ in their particulars, what truly identifies them is the level of fidelity with which they represent the wake.

6.1.1 Quasi-Steady Model

The simplest possible model of the flow is to assume that it is attached, and that the airfoil is undergoing steady translation at an angle of attack. In this model the start of the motion has occurred long ago, and the starting vortex is considered irrelevant except for its image. The image vortex now represents the bound vorticity. The only components in this model then are the plate translation and a bound vortex, and a full derivation of both can be found in appendix A. The bound vortex strength is determined so as to satisfy the Kutta condition at the trailing edge, giving $\Gamma = -2\pi a\tilde{V}$, where $\tilde{V}$ is the plate normal component of plate velocity (not the free stream).

The force on the plate is easily recovered from expressions in equation (A.44) and equation (A.48). Equation (A.44) gives the non-circulatory force and moment on the plate due to translation, and equation (A.48) gives the force and moment due to a bound vortex. The quasi-steady approach neglects the wake entirely, though unsteady motion can still be included. The bound circulation at each moment in time is selected to enforce the Kutta condition at the trailing edge (though which edge is selected as the trailing can change depending on the direction of the motion). The circulation that would be shed into the wake to balance changes in the bound circulation, as required by Kelvin's theorem, are ignored. The force and moment are then given by equation (A.44) and equation (A.47). The $\dot{\Gamma}$ terms are neglected by the quasi-steady assumption, and V set to 0. This results in:

$$\vec{F} \cdot \hat{\imath} = -D = \pi a^2 \rho \dot{U} \sin^2(\alpha) \tag{6.1a}$$

$$\vec{F} \cdot \hat{\jmath} = L = 2\pi\rho a U^2 \sin(\alpha) + \frac{1}{2}\pi a^2 \rho \sin(2\alpha)\dot{U} \tag{6.1b}$$

$$\vec{M}^b \cdot \hat{k} = -\frac{1}{2}\pi\rho a^2 U^2 (2b-1)\sin(2\alpha) \tag{6.1c}$$

where $\vec{F}\cdot\hat{\imath}$ is the force in the x direction of the fixed frame, equal to the negative of the drag force. $\vec{F}\cdot\hat{\jmath}$ is the force in the y direction, equal to the lift force, L. The pitch point is usually specified at the quarter chord, $b = 1/2$, because this causes the moments from the translation and bound vortex to cancel. Applying the same normalization by dynamic pressure, $q = 1/2\rho U_f^2 c$ (note that $c = 2a$), as the experimental data and

substituting $b = 1/2$ results in:

$$C_l = 2\pi \sin(\alpha)\frac{U^2}{U_f^2} + \pi a \sin(\alpha)\cos(\alpha)\frac{\dot{U}}{U_f^2} \tag{6.2a}$$

$$C_d = \pi a \sin^2(\alpha)\frac{\dot{U}}{U_f^2} \tag{6.2b}$$

$$C_{m,c/4} = 0 \tag{6.2c}$$

where the difference between the final velocity, U_f, and current velocity, U has been kept. The lift, C_l, equation has two components, the first is the circulatory contribution from the bound vortex, and the second is the non-circulatory contribution. The drag, C_d, equation only has a non-circulatory component, and predicts zero drag in the steady state. The moment about the quarter chord, $C_{m,c/4}$, is also predicted to be zero. These are the classic results of thin-airfoil theory [117], slightly adapted to account for large angles, the change in wing velocity, and the non-circulatory force.

For attached flow that has only mildly unsteady motions (or the rare unsteady motion with constant bound vortex strength) this turns out to give a good answer. The results of applying the quasi-steady attached flow model to present experimental study are given in section 7.1. That section will also explore the impact of replacing these theory estimates with measured values of C_l and C_d to improve the steady state predictions.

6.1.2 Fixed Wake Model

For flows with greater unsteadiness, the change in bound circulation needs to be balanced by circulation shed from the plate edges in continuous sheets. To still allow for a pen and paper solution, only attached flow is considered and leads naturally to the small angle assumption and only the trailing edge sheet being needed. The

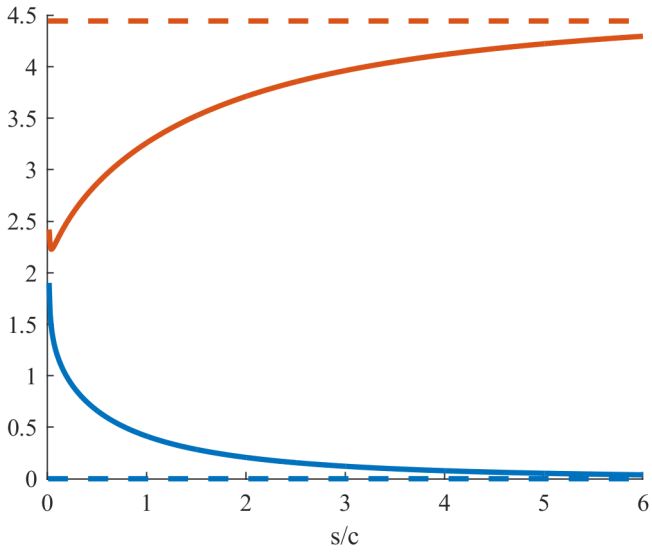

Figure 6.1: The force on an impulsively started translating wing via numerical implementation of Wagner's model.

second assumption is that the wake sheet does not convect (in the fixed frame) but is simply left behind by the wing. Using this approach produces the commonly seen lift deficiency functions that delay the action of circulatory forces, e.g. Wagner's model [9, 126].

To illustrate this, example results are shown in figure 6.1. This displays numerical results from impulsively translating a wing of chord $c = 1$ with $U = 1$ and $\alpha = 5°$. The non-circulatory forces happen only in the first instant and show up as a brief spike, after which the circulatory force gradually builds. The lift force ($L = F_y$) shows the characteristic start from half its steady state value, followed by a slow asymptotic approach to the steady value. The steady values are taken directly from the equations (6.1) in the previous section. The numerical model also includes a transient drag force ($D = -F_x$) that quickly approaches zero, although this is neglected in the analytical solutions due to their small angle assumption. The fixed trailing edge wake is the core principal behind the models of Wagner [9] and Theodorsen [102] which cover impulsive and oscillatory motions, respectively. Several authors have since extended on the basic principle such as Greenberg's oscillating free

stream [177], Leishman's compressibility effects [178], VonKarman and Sears impulse derivation [126], Kussner's sharp edged gust response [179], and Sears' oscillating gust [180]. These approaches have been experimentally validated (e.g. [181]) for attached flows and enjoy widespread use.

The problem with this approach in the present context is that it does not explain the lift increment (as opposed to a deficiency) that is seen in the experimental results when a leading edge vortex is present. Attempts to include the shear layer at the leading edge in have proven un-fruitful.

The fixed wake approach can be extended to include a wake from the leading edge that does not convect, just as the trailing edge wake in the above models. This ends up being a poor representation of how the wake leaves the edges, especially since it is attempting to model flows at large angles of attack. In the real flow, the convection of the wake results in a roll up of the shear layer into a leading edge vortex, and that is not captured. This failure of wake representation in turn affects the strengths of the wake and results in incorrect force prediction. A numerical implementation of this gave results that did not reproduce the purely plate-normal force results in the experiment. Instead, extending the fixed wake model to the leading edge predicted, for a plate at $\alpha = 45°$, a large drag and nearly non-existent lift force.

In the steady state, a fully separated flow can be modeled with free streamline theory (e.g. Roshko [182]). The theory can be used to define the wake geometry at large angle of attack in a more realistic manner than the fixed wake hypothesis. This approach assumes a constant pressure region behind the plate and solves the wake geometry via a conformal mapping. The wake pressure is a free empirically tuned wake parameter, placing that model somewhat outside the bound of a predictive model. In addition, PIV is ill suited for pressure measurements, so this method will not be considered further.

Because of the deficiencies in including the leading edge wake shedding in these

models, only the trailing edge shedding versions will be compared to the experimental results. A comparison of Wagner's model against the baseline case is given in section 7.2.

6.1.3 Short Time Similarity Solutions

An analytical solution to the problem of a vortex sheet shedding from a sharp edge can be obtainedc via a similarity solution to the governing system of equations. However, in order to obtain the solution the answer is represented as an infinite series and then truncated to only include the leading term, limiting the applicability of the results to short times. This is the idea behind the work of Pullin [183] and Cortelezzi and Leonard [144]. Pullin and Wang's paper [103] applies the results in the most applicable fashion for the present circumstance as it models the forces on a finite plate instead of vortex shedding from a single edge. The results of that paper are listed here, and compared to the measured data in section 7.3.

To make an analytical solution tractable, these models assume a velocity profile with a simple polynomial dependence on time:

$$U = Bt^m \tag{6.3}$$

where B is a scaling factor, and m determines if the profile is of constant speed, constant acceleration, etc. For comparison to the present work, a constant acceleration profile of $m = 1$ was used. The value of B was set to correspond with experimental velocity profiles, resulting in $B = 0.25$.

The equations for force given in Pullin and Wang [103] break down into two components: a non-circulatory and a circulatory component. The notation from the paper has been altered to fit the notation used here. The non-circulatory component

is purely plate-normal, and is given as:

$$N = \rho c^2 \sin(\alpha) \frac{\pi}{4} \frac{\mathrm{d}U}{\mathrm{d}t} \tag{6.4}$$

where N is the plate-normal force, and all other quantities have the same meanings as before. This matches the non-circulatory force used in other models and derived in appendix A. It has the same added mass factor, $(\pi/4)\rho c^2$, multiplied by the plate-normal acceleration, $\mathrm{d}U/\,\mathrm{d}t \sin(\alpha)$. The circulatory component is more complicated. Using the simplified velocity profile, the evolution of the shed vortex sheet can be represented by an infinite series similarity solution based on Kaden's spiral. The leading term of the series is then solved for to give the physical shape of the rolled up vortex sheet. In the course of the derivation, it is also argued that the effects of the plate-tangent velocity component only enter the problem at a higher order and are thus ignored. The resulting equation for the circulatory force is given as:

$$N = \frac{2}{3}(5m+2) K \rho c^{1/2} J_0 a^{5/3} t^{\frac{5(1+m)}{3}-2} \Re\left\{\omega_0^{1/2}\right\} \tag{6.5a}$$

$$a = c^{1/2} B \sin(\alpha) \tag{6.5b}$$

$$K = \left[\frac{3}{4(1+m)}\right]^{2/3} \tag{6.5c}$$

where N is once again the normal force, and a and K are convenient scaling factors (not the half chord as used elsewhere in this thesis). The values of ω_0 and J_0 represent the similarity solution shape and circulation, respectively, of the rolled up vortex sheet. They are non-analytical functions of m. Their values are $\omega_0 = -0.17 + 0.33i$ and $J_0 = 2.185$. These are taken, as in Pullin and Wang [103], from the numerical solution in Pullin's previous work [183]. The solution also gives a circulation for the

LEV, which to leading order is:

$$\Gamma = \frac{\delta^2(t)}{K^{3/2}t} J_0 \tag{6.6a}$$

$$\delta(t) = K a^{2/3} t^{2(1+m)/3} \tag{6.6b}$$

where δ is another intermediate scaling factor. The rate of circulation production is the time derivative of the expression for Γ.

These equations present a solution of the problem that satisfies only the leading term in an infinite series, and are thus inherently limited to short times. In addition, several assumptions were used in their derivation that keep them from being generally applicable. In particular, making the solution analytically tractable required the authors to ignore the effect of the LEV on the TEV and vice versa. The results of these simplifications are examined in section 7.3. While the similarity solution based model's stand-alone uses may be limited, they are quite useful in their capacity as a method for kick-starting more general numerical methods [3, 106].

6.1.4 Multi-Vortex Model

In the real flow, vorticity in the wake is not fixed in space, but rather convects with the local fluid velocity as mentioned in the discussion of wake representations in section 2.6.2. To solve this problem, Lagrangian methods were selected as the primary tool. Allowing the wake to convect leads to the roll-up of the shear layers at the leading and trailing edges to form the leading and trailing edge vortices. This natural inclusion of the wake evolution has made them a popular choice, and many examples exist in the literature, such as Katz and Plotkin's book [118], Katz's thick airfoil method [108], Xia and Mohseni's conformal mapping method [122], Ansari *et al.* 's strip theory approach to full 3D [107, 123], and Hammer *et al.* 's work [184], to name but a few.

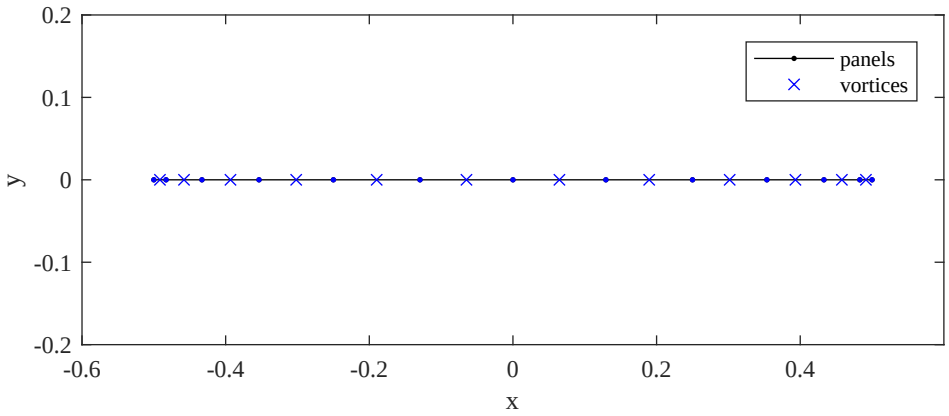

Figure 6.2: A representative panel method mesh with $N = 12$. The actual computations used $N = 64$.

The method implemented for the present thesis is most similar to the one outlined in Katz and Plotkin [118], in that the wing is represented with point vortices. The wing is represented with a total of $N = 64$ panels, with cosine spacing across the chord. The wing mesh is depicted in figure 6.2. Each panel contains a point vortex at the panel center, and collocation points are at the panel edges. This places collocation points exactly at the plate edges. The addition of two new vortices each time step models the shedding of circulation. For the first time step, these vortices were placed a distance of 2% of the chord away from the shedding edge. The exact location of the initially shed vortex was found to have little impact on the results. In subsequent time steps, new vortices were placed at a third of the distance from the shedding edge to the previously shed vortex, as per the method in Ansari *et al.* [107]. The time step size was selected to be $t^* = 0.015$ as in Xia in Mohseni [122].

The net result at each time step is $N + 2$ vortices to solve for no through flow at $N + 1$ collocation points. The system is closed by specifying zero total circulation. This method enforces the Kutta condition by meeting the plate tangent shedding velocity at the edges. This is accomplished implicitly via the placement of collocation points exactly at the plate edges. Vortex locations were evolved in time with an explicit Euler scheme. A vortex core model was not used so that an off-the-shelf

fast multipole solver, FMMLIB2D [185], could be used. Forces were computed with the impulse method of Wu [186], just as in the force derivations in appendix A. However, instead of using the final forms of the force equations in the appendix, section A.7, the impulse integrals were replaced with summations over all vortices, and the time derivative taken numerically with a first order backwards difference. As a final consideration, the model used a linear trapezoid velocity profile rather than one of the smoothed versions discussed in section 3.2.

The downside of using a panel method for the body representation is that it becomes difficult to conceptually separate the force into the intuitive circulatory and non-circulatory components. This could be remedied by instead representing the plate via conformal mapping as in Xia and Mohseni [122], though the point vortex panel method was selected in this case for its extreme ease in calculating the forces via the vortex impulse. The results of applying this model are discussed in section 7.4.

6.1.5 Two Vortex Model

To combat the growth in computational cost and bridge the gap between numerical and analytical models, Wang and Eldredge [3] extended the work of Cortelezzi and Leonard [144] on point vortices with unsteady strengths. Here, the wake is represented by a very small number of point vortices (one for each shedding edge) whose strength changes in time to maintain the Kutta condition. This leads to a very low cost method, but unfortunately does not do particularly well when it comes to predicting the forces, which are generally off by a factor of two or more.

Part of the reason for this failure is premise of the model itself. By enforcing the Kutta condition with a vortex that is increasingly farther away from the plate, the vortex strength must increase unrealistically fast compared to enforcing the same condition with a new shed vortex that is always in close proximity to its shedding edge. Another failure of this model is its inability to model the dynamics of the shear

layer itself. This means that the natural roll up of the sheet into new vortices is not captured, and hence this model is unable not predict the vortex shedding process that leads to, say, a Karman vortex street. Finally, the problem of low angles of attack is present in this model as well. When the leading edge vortex is created at too small of an angle, the numerical simulation tends to become unstable.

In spite of this, the model shows great promise for relatively short times when the flow is dominated by the initially shed LEV and TEV. For the flapping wing application, this may be all that is required before the wing reverses course. The extremely low computational cost also makes it an attractive option. The results of applying the model as presented in the Wang and Eldredge paper [3] are presented in section 7.5.

6.2 Boundary Layer Analogy

I propose an approach separate from the Kutta condition, based on an analogy to a separating boundary layer. The term "analogy" is used to distinguish it from a rigorous analysis. The overarching philosophy is to use potential flow to come up with a representative velocity field near the leading edge, guided by observation of the scalings of a comprehensive set of experimental measurements. The use of a representative velocity is also seen in the work of Kriegseis *et al.* [66], although they took their velocity directly from measurement rather than constructing a relation for prediction. The representative velocity is then related to the circulation production with an integral over the boundary layer. Based on experience, the circulation flux is presumed to be driven by the outer flow velocity normal to the wing chord [68]. Without any wing-normal velocity, a thin flat plate has no effect on the flow. In addition, models of edge separation such as Cortelezzi [145] or Pullin [183] rely on the presence of a free stream velocity with a plate-normal component. Thus the wing-normal component is the component of velocity that notionally drives the shear and

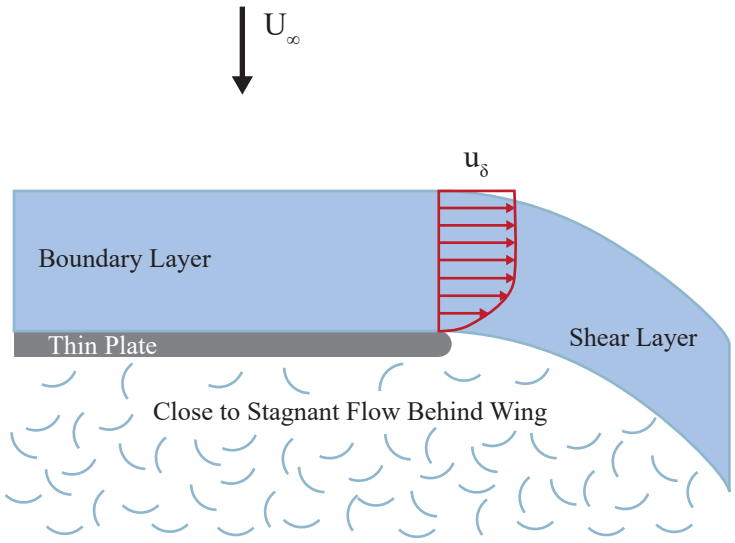

Figure 6.3: A sketch of the boundary layer separating near an edge of the plate.

separation process.

In order to connect a prediction of velocity outside the boundary layer to a vorticity flux, an integral for the vorticity flux through a vertical slice of the boundary layer is formed, as depicted in figure 6.3. This slice is presumed to be located just before the point of separation, therefore any vorticity flux at the slice will subsequently separate and become a shear layer. The integral has the form:

$$\frac{\mathrm{d}\Gamma}{\mathrm{d}t} = \int_0^{\delta} \frac{\mathrm{d}u}{\mathrm{d}y} u \,\mathrm{d}y = \frac{u_\delta^2}{2} \tag{6.7}$$

where the left hand side, $\mathrm{d}\Gamma/\,\mathrm{d}t$ is the rate of circulation passing through a slice of the boundary layer, δ is the height of the boundary layer, and u_δ is the velocity "outside" the boundary layer. The integrand is the vorticity, $\mathrm{d}u/\,\mathrm{d}y$, multiplied by the velocity normal to the integration path, u, to form the flux. This is the same method used in Widmann and Tropea [68].

Note that the vorticity ignores the other two-dimensional component, $\mathrm{d}v/\,\mathrm{d}x$. This omission is arguably valid if one presumes that the flow separates nearly tangential to the plate, as depicted in figure 6.3. This would be the case if the Kutta

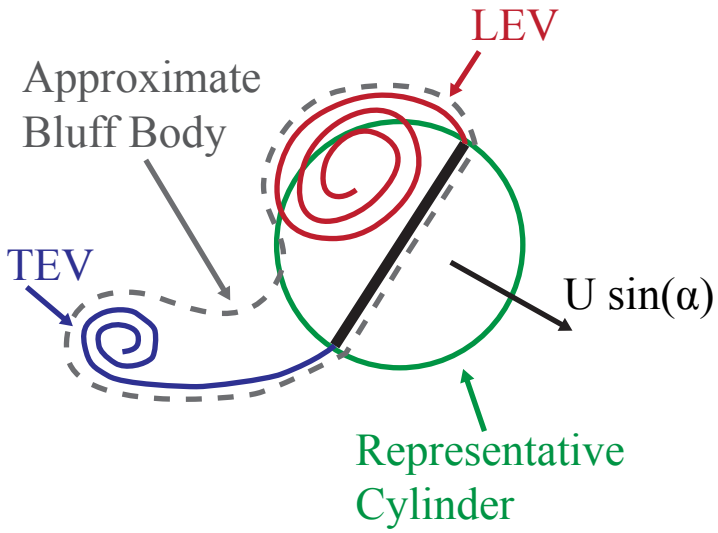

Figure 6.4: A sketch the cylinder representation for the bluff body created by the wing/wake system.

condition were enforced [106, 150]. Even if the Kutta condition is not perfectly met, the momentum of the flow near the plate must be in the plate-tangent direction, limiting the flow curvature at the location of the profile, which is still over the plate. Even if the flow has high curvature in the shear layer just off the plate surface, the vorticity flux is fully captured by the boundary layer profile.

Equation (6.7) corresponds with the results of the Reynolds number and acceleration study of chapter 5, which strongly suggested that the circulation flux was related to the square of the instantaneous velocity. The question then becomes how to determine an appropriate u_δ based on the plate kinematics and wake state.

As far as the plate kinematics, there is already a potential flow solution for flow around a thin flat plate. However, it predicts infinite velocity at the edges of the plate, and thus cannot be directly applied. In reality, there are obviously no infinite velocities thanks to the effects of viscosity and separation. Further, flow does not remain attached around the edge in reality, but separates resulting in a negligible curvature of the streamline at the corner, similar to the sketch in figure 6.3. Since the vortex sheets are streamlines, one can view the separated shear layer as an extension of

the wing, as in the sketch in figure 6.4. A similar view is take in the model of Wong *et al.* [67], who include the LEV as a semi-circular extension of the wing. Taking this view, one can imagine the wing-wake system as a bluff body of some depth, rather than an infinitely thin wing. Pressing the analogy further, one could take the extremely simplified view that our bluff body is not so different from a cylinder, particularly for the leading edge separation. For lack of a more obvious choice, the maximum slip velocity of twice the free stream is taken. This is a reasonable guess, as that velocity occurs at the top and bottom of the cylinder, where the separation nominally occurs on the plate. In addition, the sin() function changes little in the vicinity of its maximum, so using that value is somewhat robust to minor changes in "separation" point.

As a final consideration, the cylinder is presumed to move only with the plate-normal velocity. This hearkens back to the earlier intuition that only the plate-normal component is of importance. It is assumed that the plate-normal velocity determines the strength of the shear layers at the plate edges just as it determines the total bound circulation in the attached flow case. Accounting for the wing/wake system with a cylinder is largely predicated on the plate normal velocity component being dominant. At low angles of attack, this will not be the case, and the cylinder representation is likely to break down.

Using the assumptions of the above discussion results in an expression for the component of u_δ due to the body:

$$u_{\delta,b} = 2U\sin(\alpha) \tag{6.8}$$

where the additional subscript $_b$ denotes that this the body contribution.

The second contribution to u_δ comes from the velocity induced by the wake. Once again, the logic relies heavily on experimental observation and intuition rather

than a rigorous analysis of the problem. To compute the induced velocity from the PIV data, one could imagine that each data point represents a small point vortex, and then sum their contribution, in much the same manner as Graham *et al.* [169]. To make the analysis easier, and to take advantage of the analysis already available, the wake will instead be represented in a simplified fashion with two point vortices. While this might not be a truly accurate representation and in fact neglects the shear layers, it allows for a more general discussion of how the LEV and TEV as a whole affect the shedding process. It also allows the method to be directly applicable in low order models such as Wang and Eldredge [3] or Stevens *et al.* [176].

The velocity induced by the two representative point vortices is tallied at the leading edge, and the normal component is taken. This neglects the response of the plate to the vortices, e.g. the image system in a conformal mapping scheme. It was found that using the images causes the presence of the LEV to reduce the amount of circulation production rather than increase it, as was observed in the measurement.

6.3 Summary

This chapter has laid out the inner workings of several potential flow models and outlined the choices involved when formulating one for the present problem of unsteady separated flow. A detailed, math-driven, derivation of the complex potential model based on conformal mapping can be found in appendix A. This chapter also sought to provide a broad overview of the resources available for Lagrangian vorticity methods in general.

The models to be used in the thesis are given enumerated in sections 6.1.1-6.1.5. They are the quasi-steady model, the Wagner fixed wake model, the similarity solution model, the muli-vortex model, and the two vortex model. The results of applying these models with comparison to the experimental data are given in chapter 7.

Chapter 7: Modeling the Baseline Case

This chapter examines the success of various models from the literature at predicting the forces experienced by the wing in the baseline case ($\mathcal{AR} = 8$, $Re = 12,500$, $s_a/c = 2$, $\alpha = 45°$). Crucially, the model predictions of the LEV parameters, e.g. the circulation and circulation production, are compared to their experimentally measured counterparts. This method of model evaluation is, to the best of the author's knowledge, the first of its kind. In the past, model success has been judged via a qualitative image of the wake vorticity and with a comparison of the force production. These are two global flow measurements and tend to hide the root causes of any problems that may exist.

Comparing the circulation flux in particular is a good method for focusing the evaluation only on the critical leading edge condition, usually implemented as the Kutta condition. While it is not possible to completely separate the leading edge condition from the rest of the flow because of the highly coupled nature of the flow, comparing circulation production is as close as one can come to decoupling the system. This allows for an evaluation of the Kutta condition as a leading edge condition. In addition to the models from the literature, the boundary layer analogy model proposed by the author is considered as a new method for predicting the circulation production at the leading edge.

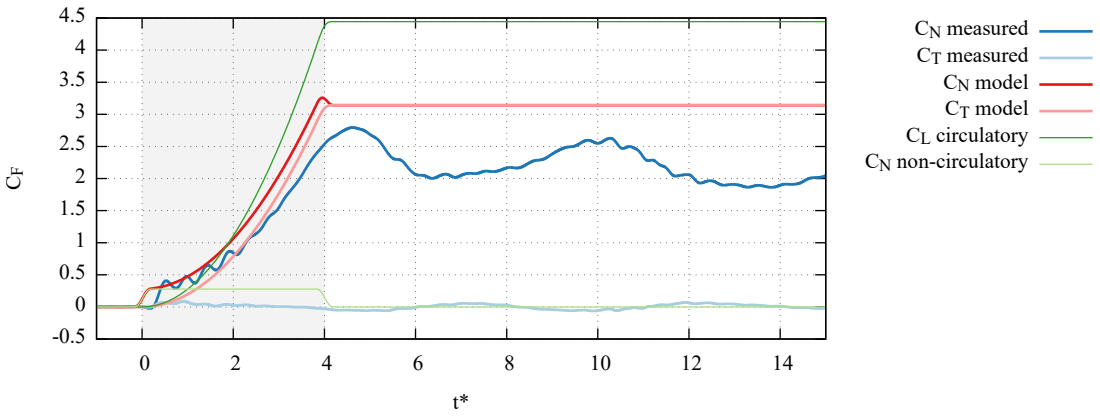

Figure 7.1: The quasi-steady thin airfoil theory model force prediction compared to experimental data.

7.1 Quasi Steady

Coming from traditional aerodynamics of wings, the first approach to predicting forces on an airfoil is often to take the quasi-steady approach, described in detail in section 6.1.1 and derived completely in appendix A. In this approach the force on a wing in translation consists of two components: a circulatory force related to the velocity of the wing, and a non-circulatory force related to the acceleration of the wing (sometimes called the "added mass" force). These two forces can easily be computed for the tow profile considered here, and compared to the dynamic measured forces. In a quasi-steady model, the force components can only depend on the instantaneous wing kinematics (i.e. wing location, angle, and their time derivatives). This makes a quasi-steady model extremely cheap to evaluate, but, as will be shown, it can miss many of the necessary physics.

Figure 7.1 shows the comparison of the measured plate normal, C_N measured, and plate tangential, C_T measured, force coefficients to the predictions of the model, C_N model and C_T model. It also shows the two components of the model in their relevant reference frame: the circulatory lift is shown with "C_L circulatory" line, and the plate normal added mass with the "C_N non-circulatory" line.

The circulatory force, shown as the "C_L circulatory" line is computed from attached flow theory, which enforces the Kutta condition at the trailing edge with the amount of bound circulation on the wing. Note that no consideration is given to the leading edge. This leads to the classic prediction of $C_l = 2\pi \sin\alpha$ and $C_d = 0$, which has been shown to compare favorably with experimental measurement on thick airfoil profiles (see Abbott and Von Doenhoff [187]), at least until stall. This calculation is predicated on the flow staying attached; when the flow stalls the lift force is significantly less and the drag force is significantly more that this prediction. This is clearly the case in these experiments, where the overall normal force is over-predicted, particularly in steady state. In addition, using normal force hides the complete lack of a drag prediction, which fortuitously cancels the over-prediction in lift to bring the normal force closer to experiment. Particularly during the early part of the run ($t^* = 0$ to around 2), the combination of over- and under-prediction gives a result that is surprisingly close to the measured normal force, but not the tangential force.

The non-circulatory force, shown as the "C_N non-circulatory" line is, in fact, quite hard to isolate in experiment. Potential theory predicts a force per unit depth of $F = 0.25\pi c^2 \dot{U} \sin\alpha$ in the plate-normal direction. This is a two-dimensional calculation and hence misses any end effects, but simply multiplying by the span of the wing turns out to be essentially exact for the aspect ratios considered here. [188] The non-circulatory force has a characteristic top-hat shape that corresponds exactly with the acceleration profile, and does a good job of matching the magnitude of the initial jump in forces, if not the exact timing. Perhaps more puzzling is the lack of distinct drop in the measured forces when the wing stops accelerating, at $t^* = 4$.

Comparison of this model with the measured LEV data cannot be done in a direct fashion since it does not include a wake of any sort. A general comparison can be made between the bound circulation of the attached flow model and the strength of

the LEV. This may not be all that far fetched, as it has been argued by Pitt Force and Babinsky [62] that the high angle of attack flat plate case contains very little bound circulation, and thus any circulation that would have been bound is present in the flow as an LEV. The results of this comparison are shown in figure 7.2. Figure 7.2a compares the amount of bound circulation predicted by the attached flow assumption to the measured circulation in the LEV. Figure 7.2b compares the time rate of change of the bound circulation to the measured circulation production at the leading edge. In these figures one sees the underpinnings of the circulatory force prediction, and the reasons for its failings. Up to $t^* = 1$ the circulation matches reasonably well, but the model grows much faster than the measured LEV circulation through $t^* = 4$, and quickly outstrips the actual circulation in the real separated case. The amount of model circulation becomes constant at the same time the wing stops acceleration and reaches its final velocity at $t^* = 4$.

Further, the lack of a wake causes the model to miss the continual production of circulation that occurs throughout the test. Figure 7.2b shows how the model stops "producing" any circulation after $t^* = 4$, resulting in the fixed value of total circulation after $t^* = 4$. This fixed value causes the initial over-prediction of circulation to eventually become an under-prediction as the real flow continues to product circulation at the leading edge. This is indicative of a primary difference between attached and stalled flows. Stalled flows require the continued production of circulation to feed the shear layers at the edges of the plate even in the steady case. Attached steady flow reaches steady state with a certain amount of bound circulation, and thereafter does not produce circulation.

Adding empiricism can mildly improve the force prediction, and this approach is widely adopted in the flapping wing controls community [111, 112, 43]. This approach works best for the rotating wing case because the force rapidly settles to steady state, as seen in Manar *et al.* [152]. It also works well when quasi-steady assumption is valid

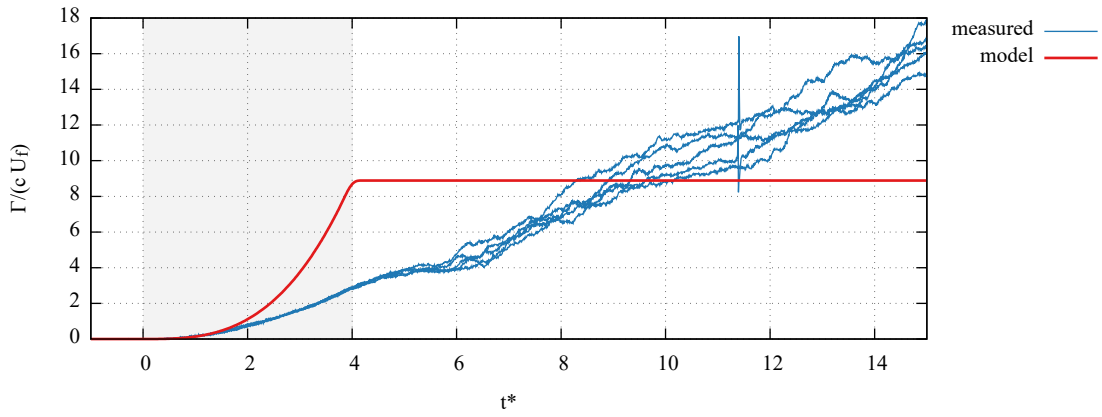

(a) Total Circulation

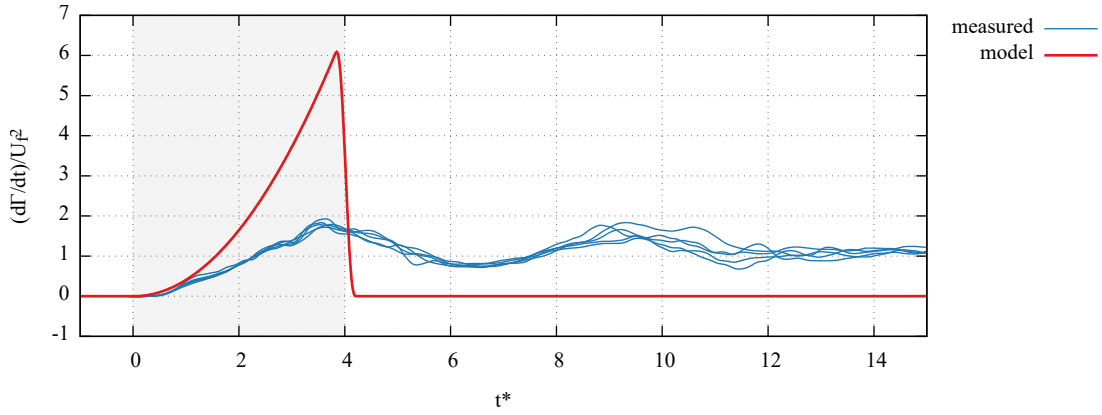

(b) Circulation Production

Figure 7.2: A comparison of the circulation predicted by pure thin airfoil theory and the measured values. Note that technically the measured data is that of the LEV in the wake, while the model curves show bound circulation.

and the results are thus closely related to the steady state. Adding a bit of empirical foreknowledge into the quasi-steady model can be done by simply using a lookup table for C_l and C_d based on the steady state, time averaged, coefficients. Since our test case is fully 3D, values of C_L and C_D (the finite wing form of coefficients) from experiment have been used, and thus finite wing effects are empirically accounted for, resulting in the time history shown in figure 7.3. The steady state values for the coefficients are taken from figure 4.5 at $t^* = 30$. The dependence on dynamic pressure gives the transient a quadratic shape (it is proportional to U^2), followed by a fixed value when the wing remains at its final tow velocity. Note that the C_D line has been

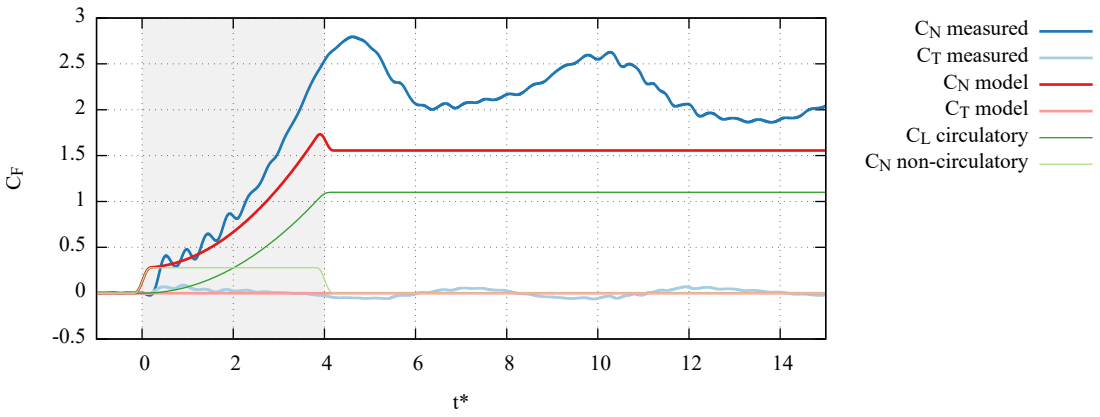

Figure 7.3: The quasi-steady model compared to experimental data.

omitted since it is identical to the C_L curve for a wing at 45°. In the wing reference frame, using the empirical data has given the correct result of zero plate tangential force.

As a rough cut, the predicted and measured values of C_N are not all that different. Both have an initial sharp rise in force from the non-circulatory component, and have a subsequent rise in forces during the acceleration. For the model this rise is a quadratic function, and the measured date has a similar shape. The models also predict peak force near the end of acceleration at $t^* = 4$. The empirical quasi-steady model misses the magnitude of the peak by a fair margin, however, and does not capture the subsequent relaxation to steady state. It does match the forces once they have settled to steady state, but this is no great feat considering the force coefficients used have been taken the measured steady state values.

The model's failing in capturing the magnitude of the peak forces and their subsequent relaxation is related directly to the model's complete disregard of the wake. As was shown in section 4.2, the actual flow contains significant wake vorticity dynamics, in particular the formation of a leading edge vortex above the suction side of the wing. The presence of this vortex close to the wing produces a low pressure region that augments the force and leads to the extra force and dynamics that the model

misses. A quasi-steady model has no hope of capturing this, because by definition all terms related to the wake and time history have been neglected. In spite of this, the model is not a complete failure. The non-circulatory force, which does not depend on the wake, captures the initial jump in force production as the wing begins to move quite well.

7.2 Wagner's Model

The traditional improvement to quasi-steady models to account for unsteady effects is to apply a fixed wake attached flow model, such as Wagner's model for step changes or Theodorsen's method for oscillatory motion. This method of modeling is discussed in detail in section 6.1.2. These models capture the way in which changes in bound circulation, either due to angle of attack change or a change in speed, must be balanced by opposite sign circulation shed from the trailing edge, but limit vorticity shedding to a flat wake from the trailing edge only. This shed circulation feeds back to change the amount of bound circulation needed, coupling the problem. These methods were investigated long before the advent of computers, and thus strove for analytical solution at the expense of physical accuracy. They were formulated for low angles of attack and disregard wake self convection. The net result of these assumptions is that they always predict a lower than steady state value of lift that gradually rises to the steady value. For the Wagner problem, this rise is captured in a lift deficiency function, an example of which is shown in figure 6.1. It shows the growth of the bound circulation, and hence lift force, from half its steady state value as the wing moves. A different function from Theodorsen describes the magnitude and phase change from an oscillatory motion. These models have been shown to work quite well when the assumptions of the theory (low angle of attack attached flow in a steady free stream) are met and they have enjoyed widespread popularity in the aircraft and helicopter community.

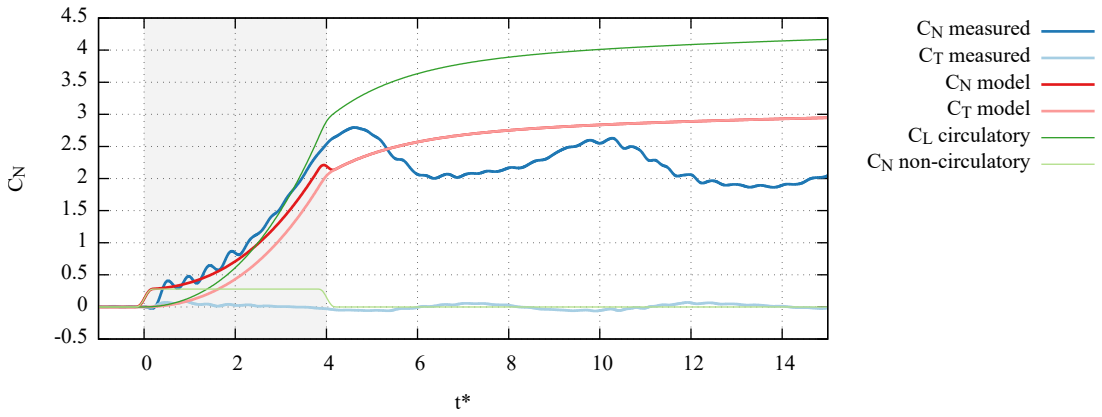

Figure 7.4: The Wagner model compared to experimental data.

These models are formulated on the same thin-airfoil attached flow theory underpinning as the quasi steady model of section 7.1. Thus they predict the same value of steady state $C_l = 2\pi \sin\alpha$ and $C_d = 0$, and are subject to the same shortcomings. With this caveat in mind, the results of applying Wagner's model figure 7.4. This figure has the same curves as the results of the quasi-steady model shown in figure 7.1: the measured C_N and C_T curves alongside their predicted counterparts, and the C_L circulatory and C_N non-circulatory model components.

As expected, Wagner's model shows many of the same features as the quasi-steady model of section 7.1. The obvious difference is the delay in the buildup of the circulatory force. Adding this delay causes the model to do a reasonable job of predicting the magnitude of the normal force during acceleration ($t^* < 4$), and instead of over-predicting the peak force just before $t^* = 5$, as in the quasi-steady case, it under-predicts it. The steady state values are, as before, vastly over predicted. The alignment of the normal forces is disingenuous however, as it neglects the plate tangent component of force. In keeping with the Kutta-Joukowski lift theorem, the model predicts the presence of lift with no drag. In the wing-normal and tangential axes, this corresponds to equal plate normal and tangential components at $\alpha = 45°$. It is only a twist of fate that the normal force has close to the correct magnitude.

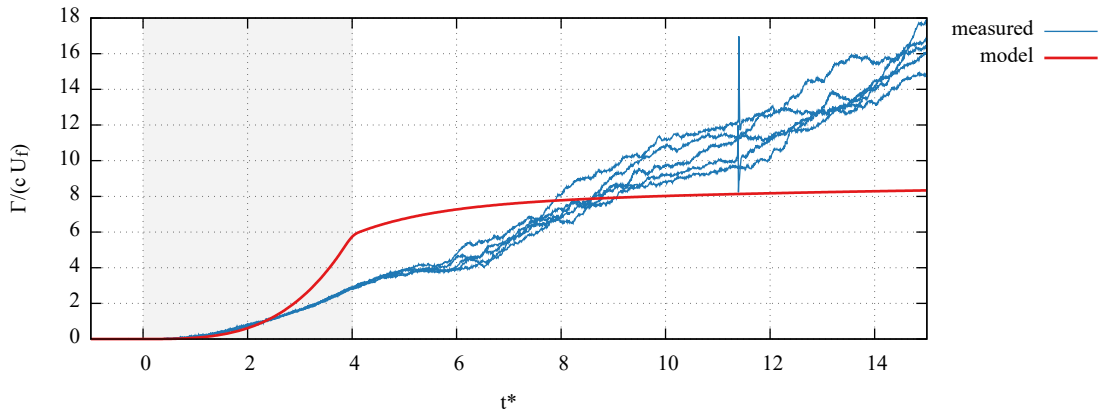

(a) Total Circulation

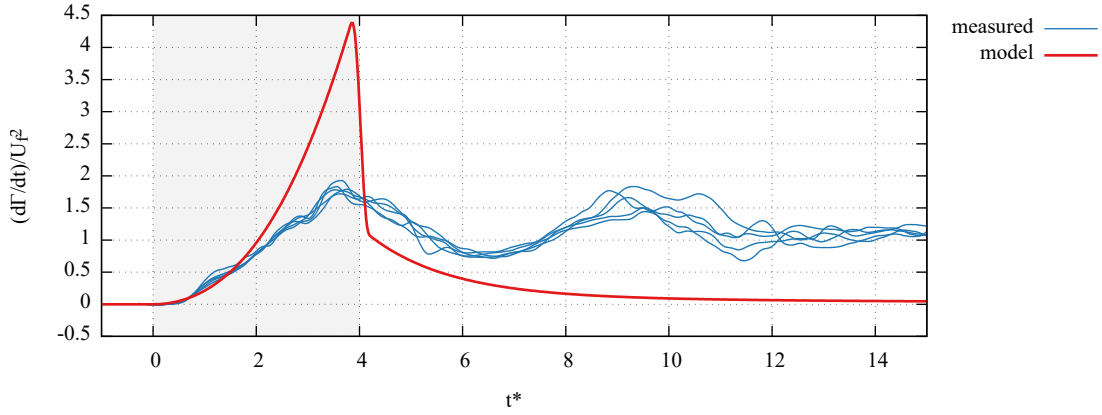

(b) Circulation Production

Figure 7.5: A comparison of the circulation predicted by Wagner's model and the measured values. Note that technically the measured data is that of the LEV in the wake, while the model curves show bound circulation.

The plate tangential force, which was measured at close to zero, is modeled to have the same magnitude as the normal force. The total force is thus predicted by the model to be much larger that in reality.

To see why the lift is overpredicted, the results of figure 7.5 show a comparison of the bound circulation in the model to the measured LEV circulation, as well as the predicted rate of change of circulation to the measured vorticity flux at the leading edge. This shows the same over-prediction of total circulation and circulation production that was seen in quasi-steady model during the acceleration portion ($t^* < 4$) followed by an under prediction at steady state. The Wagner model, being

an attached flow model, also shares the same deficiency in predicting the long term behavior that the quasi-steady model has. Attached flow models predict a fixed total amount of circulation, while the actual stalled case continues to create circulation ad-infinitum.

The early portion of the circulation production ($t^* < 6$) and total circulation ($t^* < 3$) has been significantly improved, however. The circulation production matches quite well until $t^* = 2$, and the decay after the end of acceleration ($t^* = 4$ to 6) at least has the correct shape. This is a good sign that the addition of a wake to the model has improved the overall quality of the prediction. The wake as modeled here is still a very poor reflection of the separation that occurs, but it is an improvement nonetheless.

7.3 Similarity Solution

The similarity solution from Pullin and Wang[103], discussed in section 6.1.3, produces a prediction for the force at short times experienced by the plate and includes shedding from both plate edges. As discussed previously, the model is built to work with simple polynomial velocity profiles, so here a constant acceleration profile is used. The experiments switch to a constant velocity at $t^* = 4$; the model cannot change velocity profile, limiting its predictions to the acceleration portion of the motion.

The force results of figure 7.6 show good agreement with the measured results through $t^* = 2$, after which time they predict a smaller normal force than was measured. This is the expected results based on conclusions in Pullin and Wang's paper [103]. A reason for the under-prediction of the forces can be found in the circulation prediction of figure 7.7. The total circulation is predicted reasonably well, until it is under-predicted after $t^* = 1.5$. The circulation production clearly does not scale properly with time, and does not display the linear growth of the experimental measurements, resulting in the low circulation and force values. At short times,

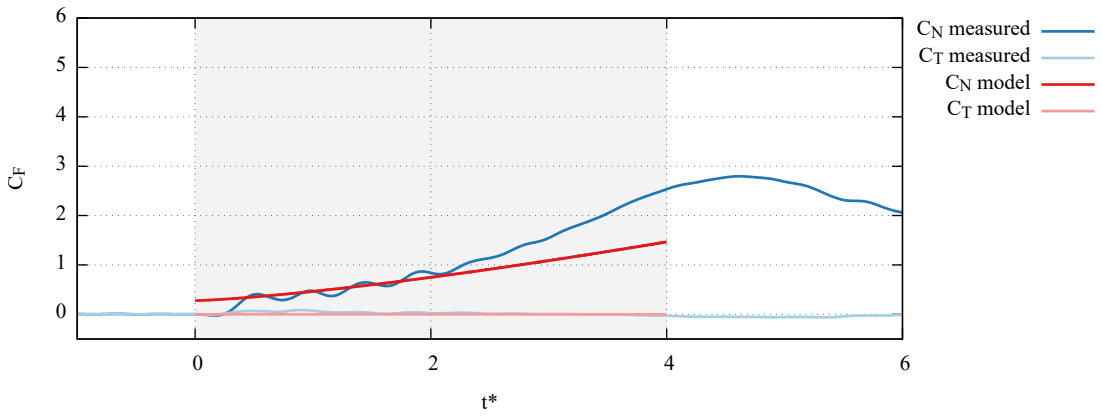

Figure 7.6: The similarity solution model compared to experimental data.

the difference in shape between the measured and predicted circulation productions are likely due to the model's ignorance of the smoothing used for the experimental velocity profile.

At longer times there must be high-order terms, particularly those that deal with the interaction between the LEV and TEV, that have been neglected, causing the error. The model assumes that the leading and trailing edge vortices have no first order effect on each other, though this is not actually the case. As time progresses, the vortices induce a velocity on each other, and the assumption of their independence becomes less valid. The induced velocity of the vortex pair would push them towards the plate, resulting in an increase in circulation production. The similarity solution ignores this interaction, leading to the low values of circulation and force predicted.

The similarity solution model does, however, present a closed form solution to the separated flow that correctly accounts for the lack of plate tangential force. This is a significant step forward from the previous models, which ignored separation from the leading edge. In doing this, the model provides valuable insight into how the flow behaves, at least for early times. The model also serves to illustrate the limits of what a purely analytical model is capable of capturing. While the assumption of no LEV-TEV interaction in the Pullin and Wang model produces viable results for short times,

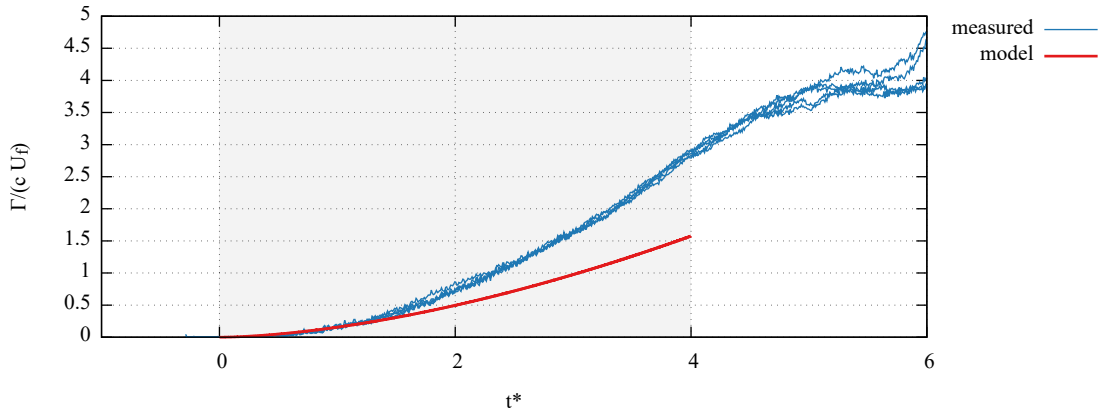

(a) Total Circulation

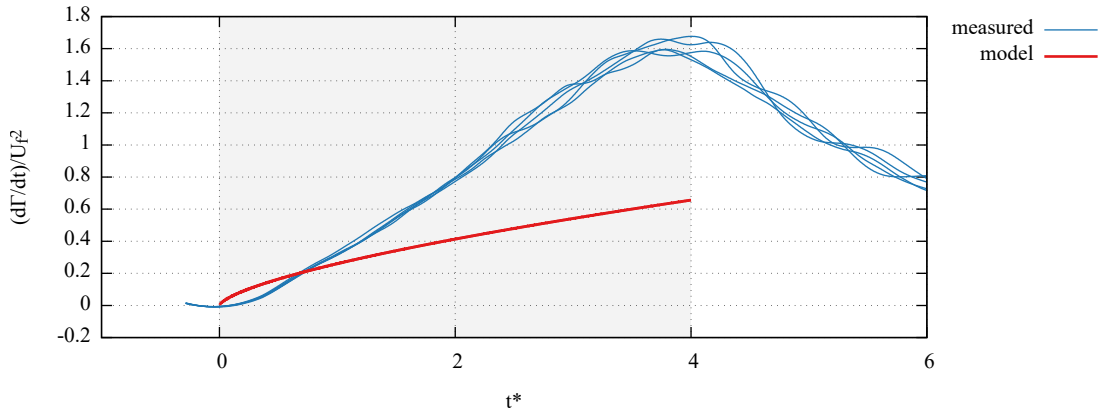

(b) Circulation Production

Figure 7.7: A comparison of the circulation predicted by similarity solution model and the measured values.

at longer times the interaction must be captured. Further, the similarity solution model is not capable of dealing with anything except single term polynomial velocity profiles. These deficiencies in the model exist because of the highly non-linear nature of the wake evolution brought about by the wake's self convection. Unfortunately, those non-linearities cannot be ignored in the present problem if one hopes to produce a reasonably general answer for force prediction. In order to implement a more general solution method, Pullin admits, and this author concurs, that a numerical procedure must be used. [183]

7.4 Multiple Vortex Wake Model

To allow for separation from both plate edges and unrestricted convection of the wake, a numerical model must be used. The problem is simply too varied and interconnected to have an analytical solution. This section presents the results from a discrete vortex model. The model uses a point vortex panel method to represent the wing, similar to that described in Katz and Plotkin [118]. The Kutta condition is enforced at both plate edges by shedding a new vortex into the wake at each time step. The wake vortices are subsequently convected according to the velocity induced by all other vortices in the flow. Further details of the model are discussed in section 6.1.4.

Adding point vortices each time step at both edges and convecting them individually directly addresses the problems with the wake representations in the previously discussed methods. By continuously shedding vorticity, the shear layer is properly captured. Allowing the vorticity to convect naturally results in the roll-up and shedding of the vortices. As seen in figure 7.8, the resultant model wake compares favorably with the experimental frozen wake result. Using a large ($\mathcal{O}(10^3)$) number of vortices also captures the effect of the spatial extent of shed vorticity, as opposed to concentrating the vorticity into a single point vortex or constraining it to lie on a single line. In sum, these make for a highly resolved wake, at the expense of mild

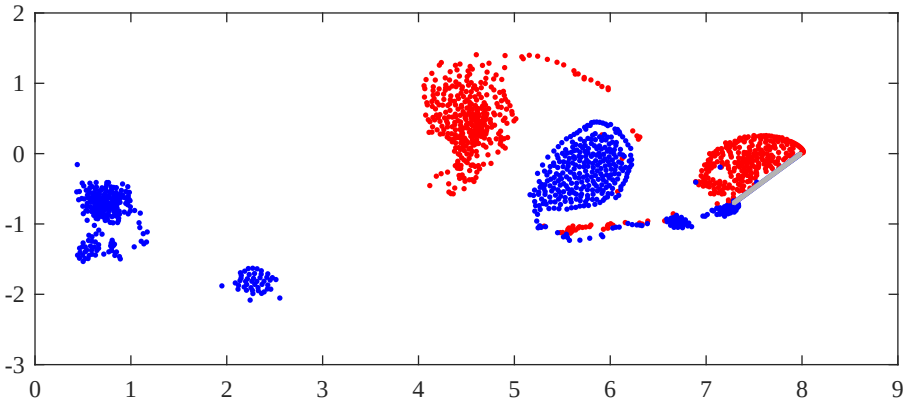

(a) Multiple vortex model

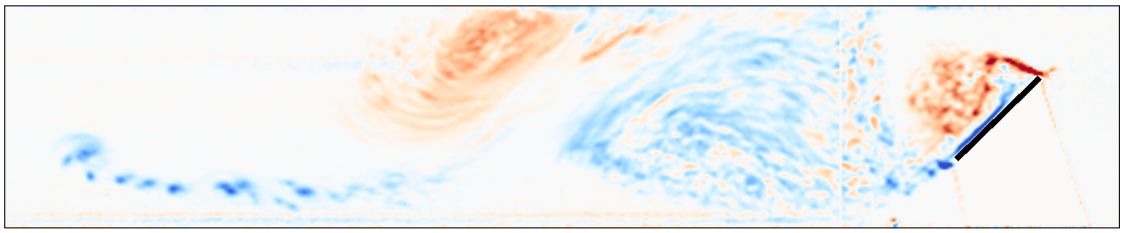

(b) Vorticity field from PIV with frozen wake hypothesis

Figure 7.8: Wake comparison at $t^* = 10.0$

additional computational cost.

The force results from the multiple vortex model are shown in figure 7.9. The first feature of note is that the model correctly predicts the lack of plate tangent force, making it a vast improvement on the quasi-steady and Wagner models. The second important feature is that the shapes of the measured forces are captured fairly well. The model correctly predicts the peak force connected with shedding of the first LEV around $t^* = 5$, as well as the second force peak due to the formation of a second LEV around and after $t^* = 8$. The magnitude of the force is not perfect. In particular, the minimum at $t^* = 7$ is under-predicted and the model over-predicts after $t^* = 8$. The results could likely be tuned with significant improvement as in Hammer *et al.* [184] or Ramesh *et al.* [110].

The total circulation and leading edge circulation production are shown in figure 7.10. The model does a remarkably good job of reproducing the leading edge

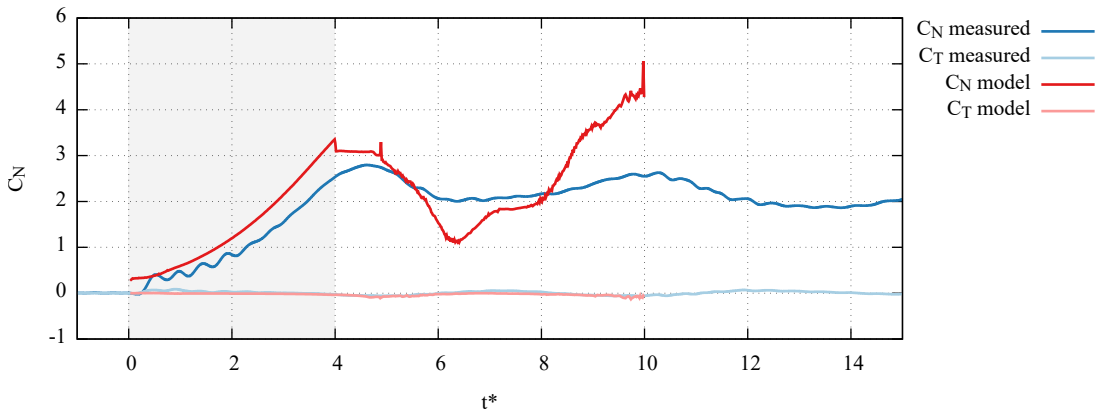

Figure 7.9: The point vortex model compared to experimental data.

circulation production, especially through $t^* = 6$. The minimum at $t^* = 6$ and second maximum at $t^* = 9$ are not quite as well resolved. The success in matching the circulation production carries over to the total circulation which falls well in line with the measured values, outside of a slight over-prediction between $t^* = 5$ and 6. A salient point to make here is that the Kutta condition performs quite well at the leading edge in spite of earlier misgivings. Based on this data, the conclusion is clearly that the Kutta condition is both valid and useful for determination of leading edge shedding. This statement is further supported by subjecting the model to the same parameter variations discussed in chapter 5. The model predictions of circulation production for each of the different kinematics are documented in appendix B. The model produces good predictions in all cases, but encounters numerical difficulties when simulating the $\alpha = 30°$ case.

The question that now arises is how the circulation production can be well predicted throughout the test, but the forces have a much higher percent error in the present test. It is not clear what causes the performance of the force prediction to decrease throughout the test. It could be the accumulation of integration error in the vortex locations. The time step used was largely selected to give reasonable results within a reasonable amount of time. Converting the code to a compiled

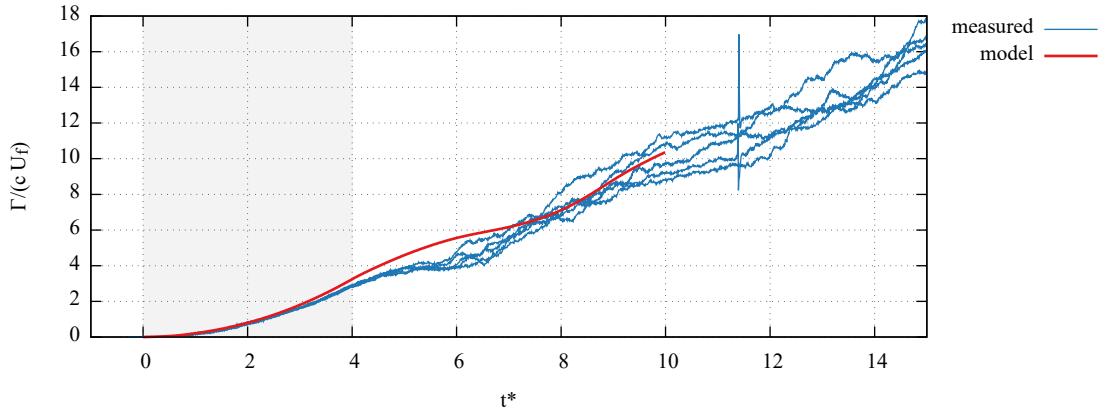

(a) Total Circulation

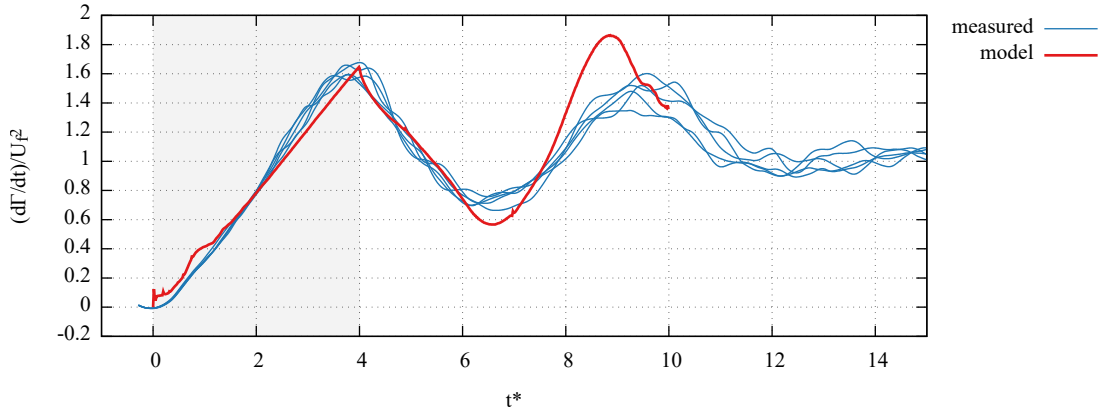

(b) Circulation Production

Figure 7.10: A comparison of the circulation predicted by point vortex model and the measured values.

language (e.g. C or Fortran) and using a Fast Multipole Method would allow for a much better resolved wake and more accurate vortex convection. These problems are related to the implementation, and not the underlying physics. A physical issue is perhaps the three-dimensional nature of the measured finite aspect ratio case as opposed to the two-dimensional model. When two-dimensional measured force data is available, two-dimensional models such as this have been shown to compare quite well [184, 110, 189].

These calculations could also be improved for more general kinematics, such as low angles of attack, pitching, and oscillation, with some method for determining

when shedding should or should not occur from the leading edge. In a low order model such as this, such a determination is generally left to ad-hoc methods such as the LESP [110], a flow angle limit [189], or a simple force limit [6].

These results, and others in the literature, show that computational methods like those considered in this section are excellent tools for determining the force on a two-dimensional profile under arbitrary motion. The necessary leap to make them a complete answer to the full flapping wing problem is to extend these methods into the third dimension, although this seems to exist only rarely in practice (e.g. Roccia *et al.* [142]). For dynamic stall problems, these types of models are unfortunately still too expensive for use in comprehensive rotorcraft codes. Similarly, fluids researchers who seek fundamental understanding tend to overlook them because they stray too far from pen and paper models into numerical methods.

7.5 Two Vortex Wake Model

Wang and Eldredge [3] proposed a conformal mapping based model which captured the wake in a very low order sense with just two vortices shed from the leading and trailing edges and convected with the flow. These vortices change strength in time so that the Kutta condition is met at both plate edges for each time step. This constitutes a wake model that still captures the separation from both edges while keeping the degrees of freedom to an absolute minimum, making it extremely computationally efficient.

The results of applying the model to the present case are shown in figure 7.11. The figure shows the measured forces in the wing-relative reference frame, C_N and C_T, compared with their model predictions. The figure also shows the model's circulatory and non-circulatory components. The model correctly captures the lack of plate-tangential force, but over-predicts the strength of the plate-normal force by almost a factor of two. The non-circulatory forces are captured in exactly the same manner

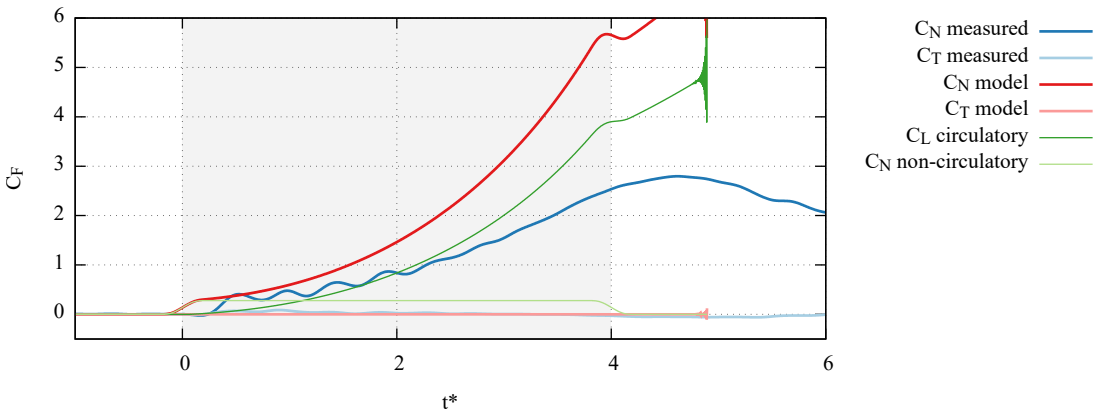

Figure 7.11: The Wang and Eldredge point vortex model.

as in the previous models, with similarly successful results. The discussion will once again focus on the all important circulatory force contribution from the wake.

The force history does not extend past $t^* = 5$ because the simulation becomes unstable and diverges. In certain configurations, it happens that the vortices have little impact on the enforcement of the Kutta condition at the edges. This leads to large changes in circulation for small changes in vortex location. When coupled with the Brown-Michael convection scheme, which alters the vortex velocity to account for circulation change, these two effects feed back into each other and cause the divergence of vortex strength and location. The initial stages of divergence can be seen in the squiggles of rapidly increasing magnitude at the end of force curves.

Another issue with the model is that it cannot, in its present form, predict the natural shedding of the LEV. In order to do that, the model must include a representation of the shear layer. That is where the roll up of new vortices occurs, and without capturing its dynamics either an additional ad-hoc shedding relationship must be added or shedding forgone altogether. These deficiencies would merely limit the model to short times if it were not for its gross overestimation of the forces.

It was initially assumed that the over-prediction of force stemmed from the enforcement of the Kutta condition at the leading edge. Either the Kutta condition

was an incorrect, overly aggressive, choice for the leading edge or that using a point vortex far from the shedding edge lead to overzealous addition of circulation. The effect of a point vortex falls off roughly with $1/r$, so the vortex strength must increase faster than it would if the shedding took place in a shear layer to maintain the same condition at the edge. However, looking the measured circulation data in figure 7.12 shows that the strength of the LEV is well captured by the model. The expected effect of the vortex receding from the plate is seen in increasing overshoot of the model circulation production after $t^* = 3$, but the overall circulation production matches quite well with the measured data. Better, in fact, than the force data, which rapidly diverges from the measurement. Based on the circulation prediction, one would expect reasonable force predictions through at least $t^* = 2$. Note there is some noise in the circulation flux just after the start of the motion. This is associated with the vortex not being placed in quite the correct location by the initial conditions, but the noise quickly settles out.

Since the circulation itself appears to be predicted reasonably well, the error in force prediction must come from elsewhere. The answer lies in the location of the vortex. The model predictions for LEV location are shown in figure 7.13. The two subfigures show the x/c and y/x values from the model, as well as the measurement with both the vorticity centroid and Γ_1 criteria. While the x/c location of the LEV is on the right track, the model predicts a lower value than the measurements, indicating an LEV in the model that is closer, in the horizontal direction, to the wing than in experiment. The trend in y/c in the model is backwards, predicting an LEV that rises above the leading edge, rather than sinks below it. Incorrectly predicting the location of the LEV has a direct impact on the force experienced by the wing, although a physical explanation for the present over-prediction of force is elusive.

The two vortex wake model is extremely attractive from a conceptual and computational cost standpoint, but is unfortunately hamstrung by its over-simplified wake

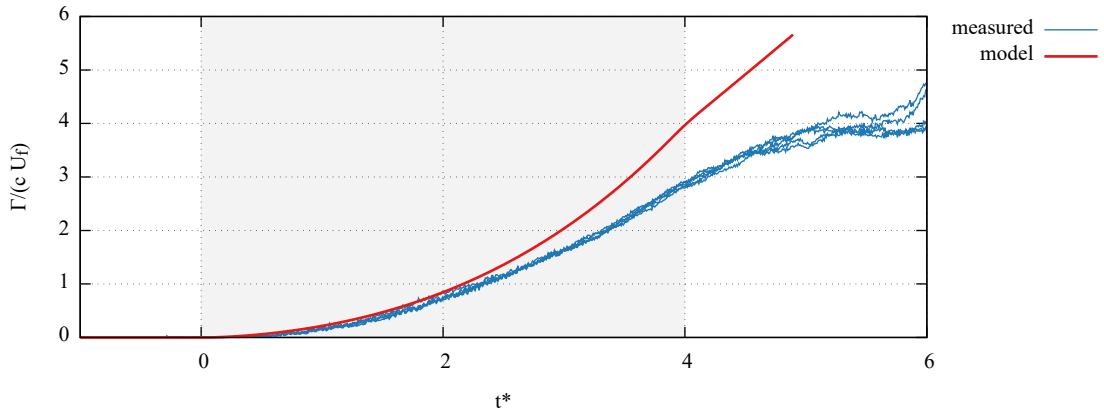

(a) Total Circulation

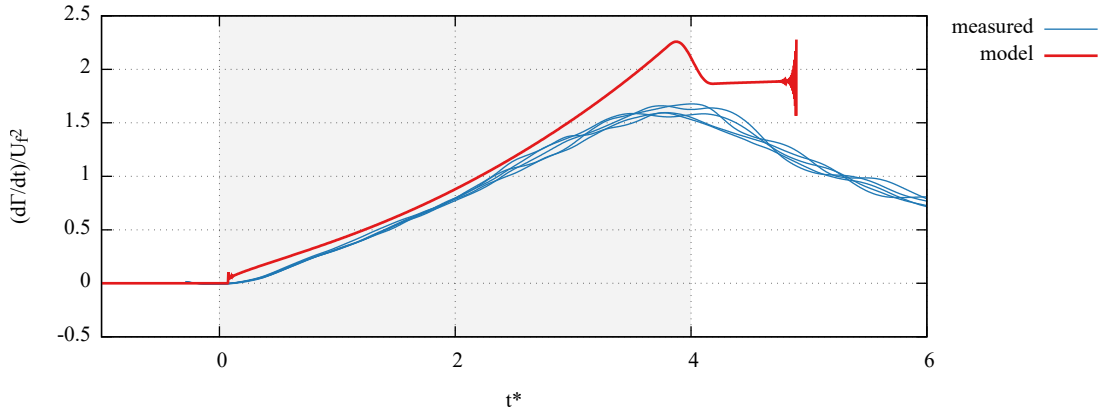

(b) Circulation Production

Figure 7.12: A comparison of the circulation predicted by Wang and Eldredge's model and the measured values.

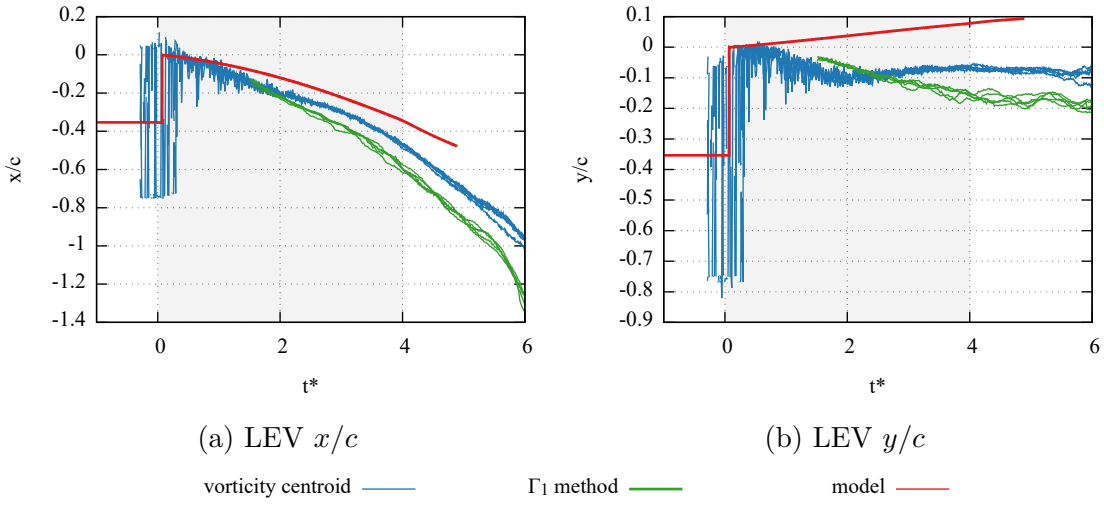

(a) LEV x/c (b) LEV y/c

Figure 7.13: A comparison of the location predicted by Wang and Eldredge's model [3] and the measured values.

representation. The key omission appears to be the effect of the shear layers. This has been recognized by the Eldredge group, and an extension of the present model has been proposed that includes the shear layer [190]. While promising, in this author's opinion the addition of the shear layer causes the model to lose its elegance, which is its main attraction when compared to the multiple vortex wake model.

7.6 Boundary Layer Analogy

The boundary layer analogy (BLA) presented in section 6.2 presents a different approach to predicting the generation of circulation at the leading edge. Instead of relying on the Kutta condition, the BLA seeks a relationship between the measured flow parameters and circulation production based on experimental observation and intuition. As such, it should be kept in mind that the BLA is not a rigorous mathematical analysis of the flow, but has been designed to mimic the observed large scale features. The predictions from the resulting relationship can be compared to the measured circulation flux without forming a complete potential model (i.e. a tied together body representation, wake model, and circulation condition).

The results of applying the BLA relationship to the baseline case are shown in figure 7.14. This figure shows the time history of the measured circulation flux, as well as the results of the BLA from knitting together the plate kinematics and measured wake location and strength. To aid in explaining the behavior of the BLA, the components of the model are shown in figure 7.14b.

The BLA captures the initial rise in circulation production (from $t^* = 0$ to 4) quite well, but with a slightly delayed timing. After the initial peak in production, the model predicts a tapering to steady state, without the subsequent maximum seen in the measured data. A comparison of the slip velocity components in figure 7.14b shows that the largest portion of slip is the kinematic portion. In fact, during the steady state portion, the kinematic portion accounts for essentially the entirety of

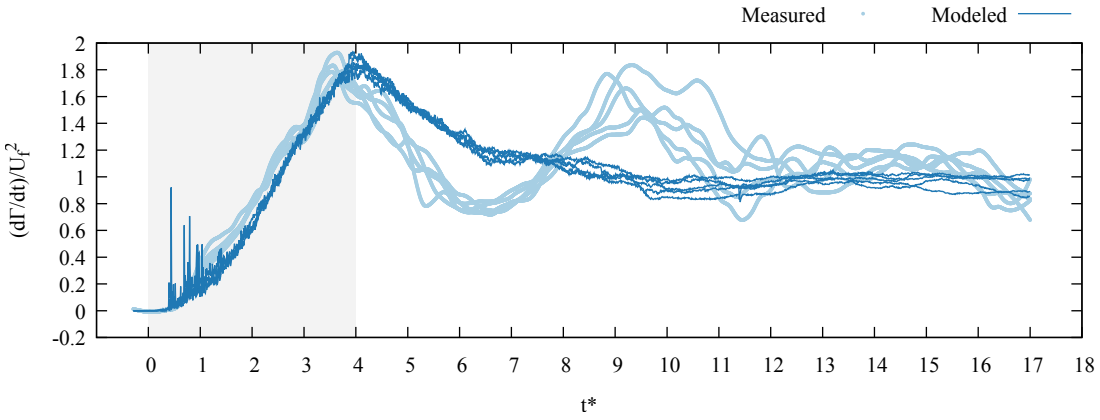

(a) The boundary layer analogy relation applied to the baseline case.

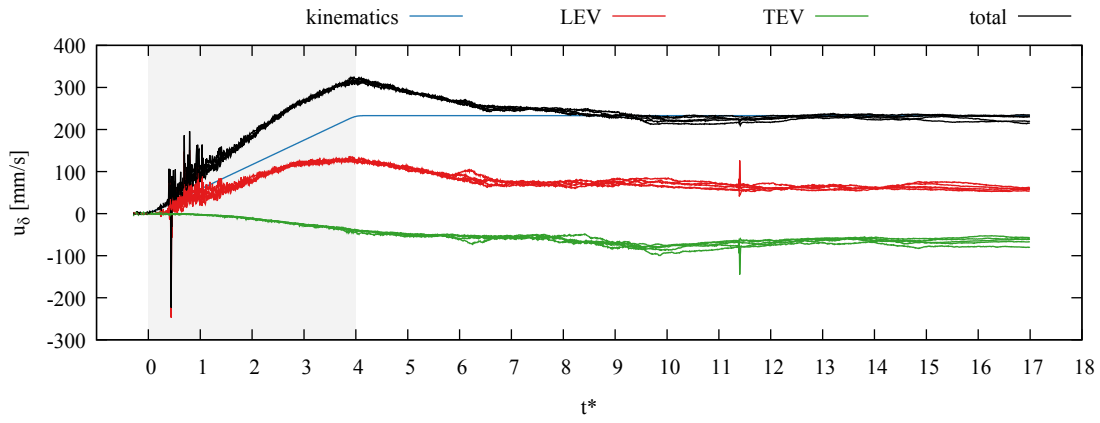

(b) The components of the slip velocity, u_δ, in the model.

Figure 7.14: The baseline case.

the circulation production. This helps to justify the assumptions used in deriving the kinematics portion (i.e. the cylinder model) of the BLA. The choice of using a cylinder to represent the bluff body flow gives a prediction that matches quite well. The initial hump at $t^* = 4$ is also seen to be due largely to the leading edge vortex term, though it is somewhat attenuated by the effect of the trailing edge vortex. A strong LEV producing a proportionally strong circulation production was a design consideration in the BLA, but the shape of the curve has arisen naturally. During the early part of the run the LEV remains close to the wing while quickly gaining circulation, resulting in an increase in circulation production at the leading edge due to the increased induced velocity there. At some point (around $t^* = 4$), the LEV begins to convect away faster than the increase in circulation, causing the induced velocity at the leading edge, and therefore the circulation production, to drop.

After the end of acceleration ($t^* = 4$), the model prediction of circulation production does not match with the measured trends. The blame for this lies on the shoulders of the wake representation. As the flow progresses, and particularly after the initial LEV sheds, a single point vortex at the centroid of vorticity does a poor job of accounting for the wake effect at the leading edge. A slightly better approach can be had by only using the vorticity in the PIV frame. This is something of an ad-hoc boundary, but it nevertheless serves to limit the included vorticity to that closest to the wing. Including only the near wake makes the point vortex representation better by ignoring the less important far wake. The results of this are seen in figure 7.15. This clearly does a better job of accounting for the dynamics of the wake, but results in an over-prediction. It is important to keep in mind that the BLA relationship is not capturing the driving physics of vortex shedding (i.e. the shear layer dynamics) or convection, only the results of the shedding process on the leading edge environment.

The BLA has also been compared to the results of parameter variation experiments, with complete results listed in appendix B. In summary, the BLA maintains

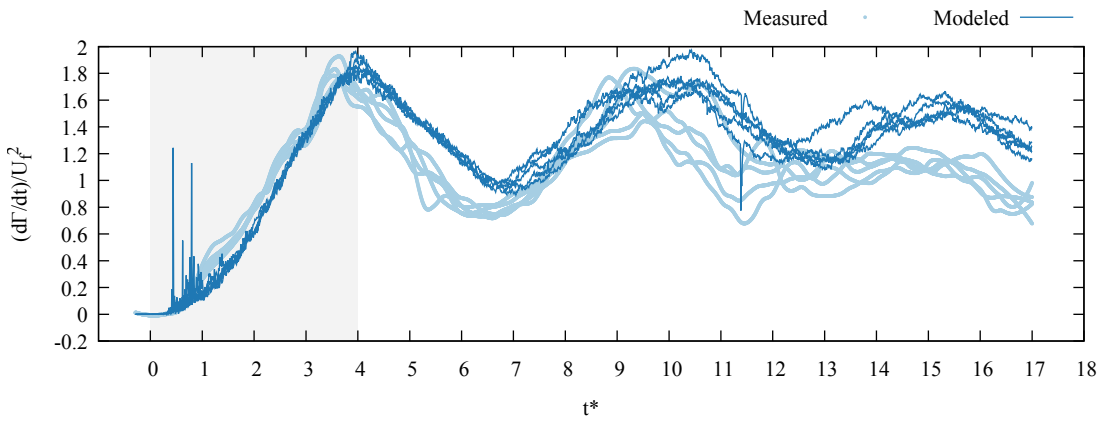

Figure 7.15: The boundary layer analogy using only the in-frame circulation and centroid.

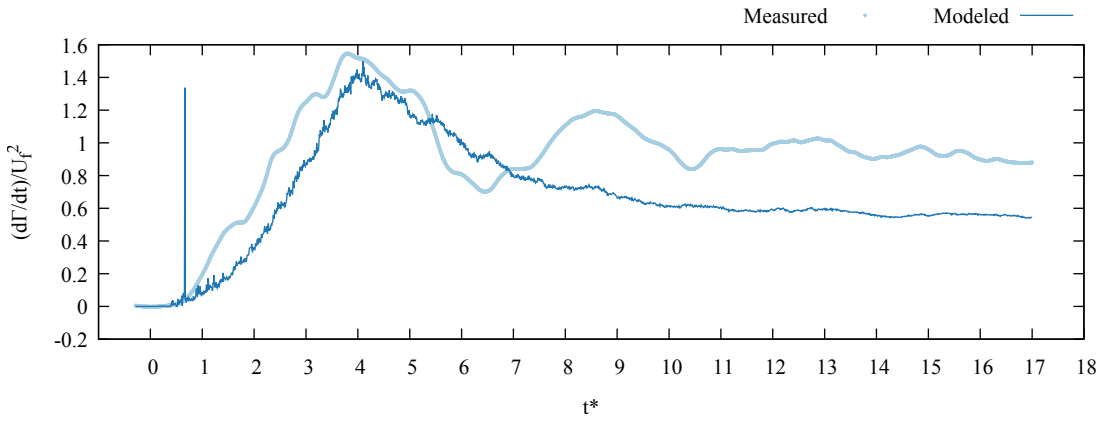

Figure 7.16: The BLA model applied an $\alpha = 30°$ case. (This is the same data shown in figure B.8)

similar performance as that seen for the baseline case when predicting the timing and magnitude of the initial peak as well as the steady state production. The most prominent result was that the model did not predict the steady state value well for the $\alpha = 30°$ case. The results of that case are shown in figure 7.16 and figure B.8. As shown by figure 7.14b, the steady state prediction relies entirely on the plate kinematics portion of the model, described in section 6.2. The plate kinematics component use a representative cylinder model for the bluff body flow, and at $\alpha = 30°$ that assumption appears to break down. One can observe from figure 5.12 that the angle between the leading edge shear layer and the wing is approximately 90° for both the

$\alpha = 45°$ and $\alpha = 60°$ case for which the BLA model predicts steady state production well. At $\alpha = 30°$, the angle appears closer to 60°, and the model under-predicts steady state production. This is likely evidence that the model will not work below $\alpha = 45°$ due to changing wake geometry, although the magnitude of the initial peak at $t^* = 4$ is still well captured.

While not the most physical of models, the success of the BLA in matching the circulation production at the leading edge gives credence to the hope that it captures the underlying relationship between the flow state and the rate of circulation production at the leading edge. Thus it can serve as an intuitive guide to understanding the flow. Perhaps it could also be added into the two vortex wake model to account for the lack of a shear layer.

7.7 Summary

This chapter presented a comparison of several models to measured force data, and used wake measurement results to help establish the root cause of model success and/or failure. All of the models considered were able to capture the non-circulatory forces on the wing, thus the evaluation of the different types of model focused almost entirely on the circulatory, or wake-induced, component of the forces.

The quasi-steady and Wagner models both gave reasonable predictions of the wing-normal force during the acceleration portion of the kinematics, but over-predicted the steady state values due to their attached flow assumption. The attached flow assumption also leads to a prediction of lift without drag. For the separated flow in the present case, the measured force values show a primarily wing-normal force, corresponding to equal lift and drag at $\alpha = 45°$. Thus while the normal force may be reasonably well predicted by the quasi-steady and Wagner models, the total force is not. Using empirical coefficients can fix this problem as well as reproduce the steady state results they are built on. However, even using empirical coefficients does not

capture the lift increment from the formation of the LEV because both the quasi-steady and Wagner models ignore leading edge shedding.

The multiple vortex wake model with Kutta condition and the two vortex wake model both did an excellent job of predicting the circulation production, but were less successful in predicting the overall forces. Given the success of their circulation predictions, their failures in predicting forces must be due to other factors such as vortex convection or wake distribution. Of the models considered, only the multiple vortex model was able to represent the shear layers, and thereby capture the dynamics needed to predict vortex shedding. The results from the complete models in this chapter strongly suggest that, contrary to the initial hypothesis, the Kutta condition is both valid and useful at the leading edge. The models that included shedding at the leading edge (the multiple vortex and two vortex models) both matched the circulation in the LEV better than they matched the forces.

On the other hand, the boundary layer analogy (BLA) did a reasonable job of capturing the relationship between the wake and the circulation production without a full potential flow model. The BLA presents an alternative to the Kutta condition for explaining the way in which the flow conditions at the leading edge relate to the circulation production. This could be parlayed into better intuitive understanding of the flow, and serve as an avenue for improvement of simple models such as the two vortex wake model.

The classic attached flow models, both quasi-steady and Wagner, are still best used in their traditional context. The massive leading edge separation in the present case makes them poor choices here. The two vortex wake model is attractively simple, but alterations must be made to improve its force predictions. Bringing the LEV convection more in line with the measured results may present a useful first step in this regard. If one wants to predict forces, the multiple vortex wake model will serve admirably. In its present panel method form, however, it is not able to provide the

same conceptual divide in the origin of the forces. Switching from a panel method to a conformal mapping body representation, as in Xia and Mohseni [122], would allow for this. Multiple vortex wake models may not, however, always be the best tool when looking for ways to control the shedding process, as the physics of the wake are captured numerically and are thus rather opaque. Yet at the same time, they are the only available model that captures the shedding process at all. It should also be noted that both the multiple vortex model and BLA shown signs of difficulty for the $\alpha = 30^\circ$ case. This indicates that these models, designed for high angle of attack, may struggle when confronted with low angles of attack.

Chapter 8: Conclusions

8.1 Summary and Conclusions

This first portion of the thesis represents the results of an extended experimental campaign to quantify the flow around a thin wing at large angle of attack starting from rest. These tests were almost entirely conducted in the water towing tank at the University of Maryland. The test article used was a thin flat plate with a rectangular planform. Chapter 4 examined a single case in which an aspect ratio eight wing was held at 45° angle of attack and accelerated from rest to a Reynolds number of 12,500 over a distance of two chords. This examination included two-dimensional flow visualization, time-resolved force measurement, vortex tracking and circulation measurement, and finally time-resolved leading edge circulation measurement. This analysis showed how even this simplified case exhibits complex and interconnected wake dynamics. It also highlighted leading edge circulation production as the critical element of the wake system, and the need to understand the wake dynamics in order to understand the forces on the wing.

The baseline case results prompted the parameter variations of chapter 5 to elucidate what kinematic factors the wake depends upon. Parameter variations were conducted to observe the effects of altering the Reynolds number, acceleration distance, angle of attack, and aspect ratio. These changes in kinematic and geometric parameters were used to evaluate the correct way to scale the total circulation and circulation production to collapse the measurements across the cases. It was found

that the leading edge circulation results for the Reynolds number and acceleration distance studies could be collapsed with a combination of the instantaneous velocity and distance traveled. This philosophy could not be extended to the angle of attack or aspect ratio variations. This lead to the conclusion that scaling laws, while successful for some rudimentary kinematic variations, can not handle the complex nature of separated flows. The wake's self convection creates non-linearities the cannot be captured considering only the plate kinematics. Thus, models of the system as a whole must be sought in order to make predictions that are robust to changes in kinematics. The aspect ratio variations also showed that the flow remains largely two-dimensional at early times.

The second portion of the thesis implements various physically based models to test their ability to predict the forces experienced by the wing. These models were described in chapter 6 and included an quasi-steady attached flow model, Wagner's fixed wake model, Pullin's similarity solution, a multiple vortex convected wake model, and a two-vortex convected wake model. Of these, only the last three consider shedding at both plate edges. Chapter 7 performs this comparison, and in particular uses the leading edge circulation production measurements to evaluate the use of the Kutta condition at the leading edge. These models, for the most part, split the force production into non-circulatory (sometimes called "added mass") and circulatory components. Splitting the forces in this way helped to provide insight into the underlying causes of the forces on the wing. The non-circulatory force component of all models was able to successfully predict the initial jump in forces at the start of the motion. This led to the conclusion that forces due to plate motion (neglecting the wake) are well captured in present models The circulatory components account for the action of the wake, and required a case-by-case analysis, as each model uses a different method of representing the wake.

The quasi-steady attached flow models, which ignore the wake entirely, were

examined in section 7.1. These models were unable to predict the forces on all but the most rudimentary level. Applying pure thin-airfoil theory resulted in an over-prediction of circulatory forces. The extra force was found to be due to the excess of circulation erroneously present from enforcing attached flow where none exists in experiment. The attached flow assumption also lead to an incorrectly predicted plate tangent force of magnitude equal to the normal force, while experiment and models that included leading separation show zero plate tangent force. These problems could be alleviated in the steady state prediction by using empirical value of the lift and drag coefficients, but this still neglects the extra forces produced by the formation and shedding of the initial LEV.

Wagner's model, examined in section 7.2, is the traditional go-to model for unsteady problems, as it considers the effect of the circulation shed from the trailing edge. Wagner's model is based on the small disturbance and planar wake assumptions. It was, however, shown to be of little help here because it still neglects leading edge separation. The effect of the trailing edge circulation is to delay the buildup in circulatory force production, and so the Wagner model gave a slightly better prediction than quasi-steady analysis for the plate-normal force during the transient. Like the quasi-steady model, however, Wagner's model is still predicated on attached flow, and so also predicted a large plate-tangent force where none should be (and also significantly over-predicts the steady force).

Pullin's similarity solution model, examined in section 7.3, presents an analytical method for obtaining the force on the plate, and was the first model considered to include leading edge separation. The addition of leading edge shedding brought the direction of the predicted force in line with the measurements, i.e. Pullin's model predicted only plate normal force. To form the analytical expression, Pullin was forced to ignore higher order terms, and this limits the applicability to a short time after the start of the motion. Limitations were also seen in the growth of the circulation.

The total circulation (i.e. the leading term) matched well with experiment only up to $t^* = 1$, as the circulation production (a higher order term) did not have the correct dependence on time. This was attributed to the model's neglect of the induced flow between leading and trailing edge wake sheets.

The next model, considered in section 7.4, was the multiple vortex model, which includes shedding from both plate edges and convects the wake numerically. Shedding was accomplished by adding a vortex to the wake at each time step. This model enforces the Kutta condition at both plate edges, and was found to give excellent agreement with the measured leading edge circulation production. Like the similarity solution model, the multiple force model correctly predicted the lack of plate tangential force. The magnitude of the normal force was slightly over-predicted. Allowing the wake fully convect allowed this model to accurately capture the shedding and reformation of the LEV, something that was not seen in any of the other models.

The final model considered was Wang and Eldredge's two-vortex wake model [3], examined in section 7.5. This model uses two point vortices of changing strength to enforce the Kutta condition at both plate edges. It was found to predict the production of circulation at the leading edge well up to the end of the acceleration period. The lack of a shear layer representation prevented the model from predicting the shedding of the leading edge vortex. The model also, curiously, vastly over-predicted the forces on the plate by a factor of two or more. This was traced to the model's incorrect convection of the LEV when compared to experiment.

Aside from complete models, this thesis also proposed the boundary layer analogy (BLA) relationship between wake characteristics, plate motion, and the leading edge circulation production. The BLA was formulated using the results of the leading edge circulation measurements as a guide, rather than from a rigorous first-principals approach. The comparison to experiment in section 7.6 showed an encouraging match between the BLA and measured circulation production. The BLA represents an al-

ternative to the Kutta condition for explaining the way in which the flow conditions at the leading edge relate to the circulation production. It should be noted that this model relied on experimental data for the wake state, and so cannot be said to be predictive in the full sense. However, the results indicate that it could be parlayed into a better intuitive understanding of the flow, and serve as a possible replacement of the Kutta condition in simple models such as the two-vortex wake model.

The models presented here account for the leading schools of thought in low cost force prediction methods. The classic attached flow models, both quasi-steady and Wagner, are hamstrung by their neglect of leading edge shedding, and still best applied only in their traditional attached flow context. The two vortex wake model is attractively simple, but alterations must be made to improve its force predictions for it to be useful in that regard. Bringing the LEV convection more in line with the measured results may present a useful first step. Its simplicity does make it an attractive option for those seeking a truly minimal wake representation, and it provides a conceptual divide between the force components that aids in intuitive understanding. If one wants to predict forces, the multiple vortex wake model will serve admirably. In its present panel method form, it is not able to provide the same conceptual divide in the origin of the forces. Switching from a panel method to a conformal mapping body representation, as in Xia and Mohseni [122], would allow for this. Multiple vortex wake models may not, however, always be the best tool when looking for ways to control the shedding process, as the physics of the wake are captured numerically and are thus rather opaque. Yet at the same time, they are the only available model that captures the shedding process at all.

In addition to evaluating the models as a whole, another purpose of this work was to assess the validity of applying the Kutta condition at the leading edge. Earlier work and intuition cast doubt on the validity of Kutta condition at the leading edge based the observed lack of flow leaving tangent to the plate. The models that included

leading edge separation all used the Kutta condition at the edge, and were all, within limits, successful at predicting the circulation in the LEV. The limitations that did appear were in the low angle of attack ($\alpha = 30°$) case for which both the multiple vortex model and the BLA were not as successful. However, the overall analysis still leads to the conclusion that the Kutta condition, despite earlier misgivings, is both valid and useful at the leading edge for high angle attack flows ($\alpha > 30°$). Errors in the model force predictions come from other sources, such as the plate discretization or the convection of the wake. This constitutes probably the most useful results of this thesis, and serves to validate the approach of evaluating the models on their wake characteristics rather than solely on the force prediction.

8.2 Original Contributions

The work presented here makes several important contributions that will inform future studies and provides invaluable analysis of the presently available modeling techniques.

1. The time-resolved separated wake of a thin wing at high angle of attack has been quantified with vortex tracking, circulation measurements, and leading edge circulation production measurements.

2. An original method for relating the wake state to the circulation production was proposed in the boundary layer analogy.

3. The state-of-the-art low order potential modeling techniques have been evaluated against experimental measurements. In additional to the traditional comparison of force results, the reasons for the models' successes and failures were ascertained from the wake measurements.

4. The circulation production of the models was compared to the measured circu-

lation production. This data was used to affirm that the Kutta condition is, in fact, appropriate for the treatment of the leading edge.

8.3 Future Work

This section offers suggestions for future avenues of experimental research and theoretical analysis.

1. The work here is limited to relatively large angles of attack. Further experiments should be directed at evaluating the Kutta condition and BLA at lower angles of attack. The results here at $\alpha = 30°$ indicate that lower angles of attack and the transition to attached flow likely represent more of a challenge than higher values of α. In addition, the various methods for modifying or terminating leading edge shedding at low angles of attack (e.g. Xia and Mohseni [122], Ramesh *et al.* [110], or Chabalko *et al.* [189]) are generally ad-hoc and evaluated based on overall model force prediction. Comparing their low angle of attack performance to the measured circulation production could help to reveal which models are the most successful in replicating the real physics.

2. The present work considers only constant angle of attack translation kinematics. Additional studies on pitch and plunge motions would help provide a more comprehensive understanding of circulation production under a broader range of kinematics.

3. Three-dimensional effects have been neglected almost entirely in the present work. The experimental results showed that at longer times (e.g. $t^* > 8$), the tip effects play a significant role in determining the development and shedding the LEV. Addressing these effects by make measurements of the tip vortex development would greatly aid in accounting for the three dimensional effect in low order models.

4. The thin flat plates studied here have the distinct advantage of forcing separation to occur at the leading edge, greatly easing analysis by providing an *a priori* known separation point. While this may be an appropriate model for insect wings, prediction of dynamic stall for helicopter or wind turbine design requires the analysis to be extended to thick airfoil profiles with rounded leading edges [108]. Recommended future work includes replicating the simplified kinematics used here with thicker airfoil sections, focusing on measuring and predicting the point of separation.

5. The model of Wang and Eldredge [3] remains attractive due to its extremely low order wake representation. Its very low computational cost makes it a possible candidate for implementation in control laws. However, bringing the model to a state where it could be used for such applications requires researchers to address its shortcomings, including the over-prediction of forces and the observed numerical instability.

6. Ramesh *et al.* 's [110] leading edge suction parameter (LESP) represents an intriguing alternative to the Kutta condition. The LESP allows for intermittent leading edge shedding, and may prove useful in dealing with low angles of attack. It remains to be seen, however, if the LESP is appropriate for general kinematics. The method used here (i.e. using the measured circulation production) could serve as an excellent tool for evaluating the LESP.

7. The theoretical prediction of the exterior vortex force and moment on a plate in appendix A could be improved by finding a way to place all the terms in the same mapping plane and reference frame. This could form the basis of an expression for the vortex force and moment in dynamic stall models.

8. As mentioned in section 2.6.3.1, the Kutta condition is implemented reactively by adding circulation to maintain a specified condition. A rigorous expression

for the Kutta condition that gives the rate of circulation production directly as a function of known finite values (e.g. the circle plane velocities) would be extremely useful from an understanding and modeling standpoint, but remains elusive due to the difficulties discussed in section 2.6.3.1.

Appendix A: Complex Potential Details

This appendix documents the complex potential formulation in excruciating detail.

A.1 Problem Statement

The problem in question is that of a flat plate in arbitrary motion relative to a stationary reference frame. The fluid far from the plate is always at rest with respect to the lab-fixed inertial reference frame. Complex numbers will be used throughout to represent locations, vectors, and velocities, with the usual representation of the complex plane. The variables associated with the plate are defined in figure A.1. The plate's length is defined by the half-chord, a. The plate's location is defined by the location of the pitch point, represented by $z_b = x_b + iy_b$. The pitch point is defined by the value of b, and is located a distance ab from the plate center. Positive values of b are closer to the leading edge, with $b = 1$ being the leading edge itself. The plate has an angle α relative to the horizontal (the real or x axis). Combining these, the center of the plate is then located at $z_c = z_b - abe^{i\alpha}$.

The motion of the plate is defined by its horizontal and vertical velocities, $\dot{z}_b = U + iV$, and the rate of rotation, $\dot{\alpha} = \Omega$. In classical aerodynamics, the motion is termed steady if U, V, and α are constant in time. This is not the case considered here, and all three are functions of time. Further, the angle of attack, α usually denotes the angle of the wing to the free stream, but here it is strictly relative to the horizontal.

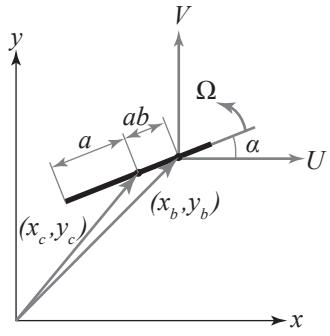

Figure A.1: The problem statement.

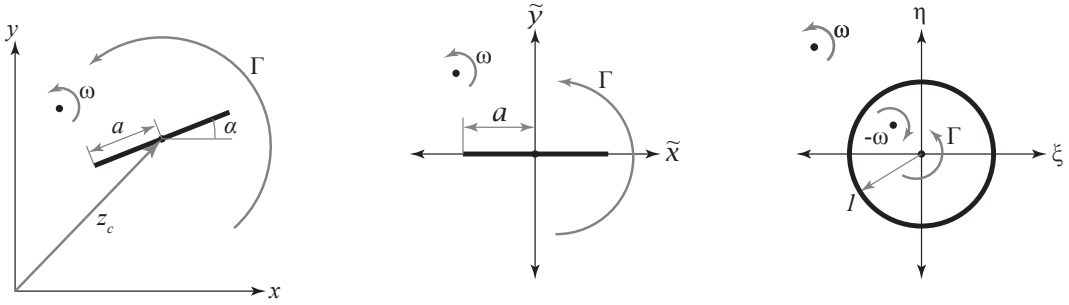

(a) The physical, z, plane. (b) The plate, $\tilde{z}$, plane. (c) The cylinder, ζ, plane.

Figure A.2: The 3 reference frames.

A.2 Joukowski Transform

In order to solve for the flow around a plate, the Joukowski transform is employed to map the flat plate into a circle. The Joukowski transform can actually create airfoil-like shapes with finite thickness as well,[1] but the present work is only concerned with flat plates. The mapping to a cylinder is done because the solution for a flow around a circle is known and easy to obtain. The mapping process occurs in two steps as shown in figure A.2. The physical plane, figure A.2a, with complex coordinate $z = x + iy$, is a lab fixed reference frame. As in section A.1, the wing center is denoted with z_c

[1]The mapping stays the same, but the cylinder is offset from the center of the ζ plane while still containing one of the singular points at $\zeta = \pm 1$. The Karman-Trefftz transform is similar in nature and produces an airfoil shape with finite trailing edge angle. See Milne-Thompson "Theoretical Aerodynamics" [120] for more information.

and angle of attack is α measured counter clockwise from the horizontal. The wing-relative reference frame, figure A.2b, is $\tilde{z} = \tilde{x} + i\tilde{y}$, in which the wing is on the real ($\tilde{x}$) axis between $-a$ and a. Note that this is not a wing-fixed reference frame and so motion of the wing does not correspond to a free stream in this plane. Instead, this reference frame is merely a wing-relative frame included so that velocities normal and tangential to the wing may be easily expressed. Finally, the Joukowksi transform is used to map the flat plate to a circle, giving the ζ plane in figure A.2c. The circle plane is denoted with the complex coordinate $\zeta = \xi + i\eta$ in which the flat plate corresponds to a circle centered at the origin with radius one. The transforms are defined by the functions $z = f(\tilde{z})$ and $\tilde{z} = g(\zeta)$:

$$z = f(\tilde{z}) = z_c + \tilde{z}e^{i\alpha} \tag{A.1a}$$

$$\tilde{z} = g(\zeta) = \frac{a}{2}\left(\zeta + \frac{1}{\zeta}\right) \tag{A.1b}$$

These function define a one-to-one mapping of locations across the three planes. Locations will be referred to interchangeably by z, $\tilde{z}$, and ζ depending on the context. Using equation (A.1), they can all be substituted for each other as required without ambiguity.

The main rule of complex potential states that the potential, G, at corresponding points in the three planes must be equal:

$$G(z) = G(\tilde{z}) = G(\zeta) \tag{A.2}$$

The complex velocity, W, is defined as the derivative of the potential (note that taking the derivative with respect to a complex variable is analogous to taking the gradient in the corresponding vector relation). The way in which space is stretched and rotated by the mapping therefore changes the resulting complex velocity between the planes. To explicitly identify the velocity in a given plane, a functional notation

is used where $W(z)$, $W(\tilde{z})$, and $W(\zeta)$ are the complex velocity in the z, $\tilde{z}$, and ζ planes, respectively.

In the cylinder plane the surface of the plate can be naturally parameterized with an angle θ as $\zeta = e^{i\theta}$, which gives $\tilde{x} = a\cos(\theta)$. The "leading edge" will be defined as the right edge of the plate, variously $\zeta = 1$, $\tilde{z} = a$, and $z = z_c + ae^{i\alpha}$. The trailing edge is then $\zeta = -1$, $\tilde{z} = -a$, and $z = z_c - ae^{i\alpha}$. a is half the chord length of the plate. The inverse transforms are:

$$\tilde{z} = (z - z_c)e^{-i\alpha} \tag{A.3a}$$

$$\zeta = \frac{1}{a}\left(\tilde{z} + \sqrt{\tilde{z} - a}\sqrt{\tilde{z} + a}\right) \tag{A.3b}$$

The square root term in equation (A.3b) is sometimes listed as $\pm\sqrt{\tilde{z}^2 - a^2}$, as this is what follows directly from applying the quadratic theorem to equation (A.1b). The form listed in equation (A.3b) moves the branch cuts from the two singularities so that there is only a discontinuity on the plate (assuming the branch cut for each square root is located on the negative real axis), and none in the flow field, making that formula much easier to use. If directly implemented in this form in Matlab, no checks are required to ensure that the mapped point lies outside the cylinder, as would be necessary if the $\pm\sqrt{\tilde{z}^2 - a^2}$ form is used.

Computing velocities in complex potential is done by taking the derivative of the potential with the spatial coordinate. Since the flow is solved in the ζ plane and then mapped back to the $\tilde{z}$ and z planes, the chain rule applies and will require the derivative of the mappings:

$$f'(\tilde{z}) = e^{i\alpha} \tag{A.4a}$$

$$g'(\zeta) = \frac{a}{2}\left(1 - \frac{1}{\zeta^2}\right) \tag{A.4b}$$

Finally, the motion of the plate can be describe relative to the plate itself with plate tangential velocity, $\tilde{U}$, and plate normal velocity, $\tilde{V}$. Velocities in the plate relative frame are simply rotations of those in the z plane, giving:

$$\tilde{U} + i\tilde{V} = \dot{z}_c e^{-i\alpha} \tag{A.5}$$

To hammer home the point about $\tilde{z}$ being a wing-relative, and not wing-fixed, reference frame, note that $\dot{\tilde{z}}_c = 0 \neq \tilde{U} + i\tilde{V}$. This is because the plate always remains centered on the origin in the $\tilde{z}$ plane. The relation of equation (A.5) can be written explicitly for each component:

$$\tilde{U} = U\cos(\alpha) + V\sin(\alpha) \tag{A.6a}$$

$$\tilde{V} = -U\sin(\alpha) + V\cos(\alpha) \tag{A.6b}$$

Now that the description of the mapping and kinematics of plate motion are taken care of, we can move on to solving the fluid motion.

A.3 Ambiguity of the Joukowski Mapping

The exact form of the Joukowski mapping can vary between sources, leading to some consternation about their equivalence. It is instructive to walk through some of the differences and their impact on the problem. The mapping used in this thesis is take from Wang and Eldredge [3]:

$$z = \frac{c}{4}\left(\zeta + \frac{1}{\zeta}\right)$$

which transforms the plate into a cylinder of radius one. Dr. Babinsky's Cambridge group tends to use a slightly different mapping (e.g. in Graham *et al.* [169]):

$$z = \zeta + \left(\frac{c}{4}e^{-i\alpha}\right)^2 \frac{1}{\zeta} \tag{A.7}$$

which transforms the plate into a cylinder of radius $c/4$ and performs some rotations. For lack of better names, I will call them the American and British transforms, respectively. At first glance these may appear to be incompatible, but in reality they both come from the same place. The most basic version looks like this:

$$z = \zeta + \frac{1}{\zeta} \tag{A.8}$$

This transforms a cylinder of radius one to a plate on the x-axis spanning from -2 to 2, giving a chord of 4. We want to control how long the chord is, so we scale the z coordinate and say $z_1 = zc/4$. This makes the plate span from $-c/2$ to $+c/2$ in the z_1 plane and gives us explicit control over the chord length. Then we happily forget the middle step and just call z_1 a new name, z. Here though I will keep it explicit a substitute the basic transform of equation (A.8) into our scaling, leaving us with the American transform:

$$z_1 = \frac{c}{4}z = \frac{c}{4}\left(\zeta + \frac{1}{\zeta}\right) \tag{A.9}$$

To get the scaling right in the cylinder plane and match the British transform, we apply the same philosophy to ζ. Here we want to set the radius of the cylinder to a desired value, r, so scale ζ and say $\zeta_1 = r\zeta$. Subbing $\zeta = \zeta_1/r$ into the above gives:

$$z_1 = \frac{c}{4}\left(\frac{\zeta_1}{r} + \frac{r}{\zeta_1}\right) \tag{A.10}$$

Note that the units actually make sense in this version[2]. At this point, you can

[2]Thanks to Dr. Gino Perrotta for showing me this version.

probably see where this is going. To match the British transform, we set $r = c/4$ and distribute the leading $c/4$:

$$z_1 = \zeta_1 + \left(\frac{c}{4}\right)^2 \frac{1}{\zeta_1} \tag{A.11}$$

Now for the $e^{-i\alpha}$: this follows the same argument as the scaling, except that we are instead rotating the reference frame. In the British transform, the plate is rotated off the x-axis, so we have another layer: $z_2 = z_1 e^{-i\alpha}$. Why is α negative? Because their implementation uses a free stream going left to right, so the plate rotates clockwise to achieve a positive angle of attack, rather than the tradition counterclockwise definition of positive rotation. For example, the plate is on the x-axis in the z_1 frame, so the point $z_1 = -c/2$ is the leading edge, giving $z_2 = -c/2e^{-i\alpha} = -c/2\cos\alpha + ic/2\sin\alpha$.

The same process happens in the cylinder plane, giving $\zeta_2 = \zeta_1 e^{i\alpha}$ Here, α is positive, to rotate the free-stream counterclockwise. Putting it all together and simplifying gives the British transform:

$$z_2 = e^{-i\alpha}\left(\zeta_2 e^{i\alpha} + \left(\frac{c}{4}\right)^2 \frac{e^{-i\alpha}}{\zeta_2}\right) = \zeta_2 + \left(\frac{c}{4}e^{-i\alpha}\right)^2 \frac{1}{\zeta_2} \tag{A.12}$$

The difference between the American and the British transforms are the scaling of the cylinder plane and the inclusion of two reference frame rotations. Both are perfectly valid, and various combinations of scaling and/or rotation are quite common alterations to the Joukowski transform.

A.4 Potential Flow

In order to solve for the flow around the cylinder we must find the complex potential such that the velocity at the surface of the plate meets the no-through flow boundary condition. In complex potential flow the flow is described by its potential $G = \phi + i\psi$, which is a function of the spacial coordinate. The value of ϕ at a given location is usually referred to as the velocity potential, and ψ as the stream function since

contours of constant ψ are the instantaneous streamlines of the flow. The complex velocity $W = u - iv$ is given by the derivative of the potential, so that in the ζ plane $W(\zeta) = \partial G/\partial\zeta$. In the z and $\tilde{z}$ planes, the chain rule must be applied, thus:

$$W(\zeta) = \frac{\partial G(\zeta)}{\partial \zeta} \tag{A.13a}$$

$$W(\tilde{z}) = \frac{\partial G(\zeta)}{\partial \zeta}\frac{\partial \zeta}{\partial \tilde{z}} = \frac{W(\zeta)}{g'(\zeta)} \tag{A.13b}$$

$$W(z) = \frac{\partial G(\zeta)}{\partial \zeta}\frac{\partial \zeta}{\partial \tilde{z}}\frac{\partial \tilde{z}}{\partial z} = \frac{W(\zeta)}{g'(\zeta)}e^{-i\alpha} \tag{A.13c}$$

Since potential flow is based on solutions to Laplace's equation, and that equation is linear, the flow can be broken down into various contributions. For most flows this results in flow due to an object's translation and rotation, any bound vortices, and vortices outside the body (e.g. the wake). Fortunately, the solutions to each of these flows already exists. These will be listed here and differentiated with subscripts: $\cdot_t$ for translation, $\cdot_r$ for rotation, $\cdot_b$ for bound vortex, and $\cdot_w$ for wake vortex.

The scaling of these formulae are set to work with the exact form of the Joukowski transform used here. If a different form of the Joukowski mapping is used, these functions will have the same dependence on ζ and the singularity strength ($\tilde{V}$, Ω, Γ) but will be scaled differently to account for the differences in the mapping.

A.4.1 Translation

For flow due to translation is:

$$G_t = -\frac{ia\tilde{V}}{\zeta} \tag{A.14a}$$

$$W_t = \frac{ia\tilde{V}}{\zeta^2} \tag{A.14b}$$

where $\tilde{V}$ is the plate normal component of the velocity at mid-chord, and is given by equation (A.6b). This function is does not depend on $\tilde{U}$, as the plate is infinitely thin

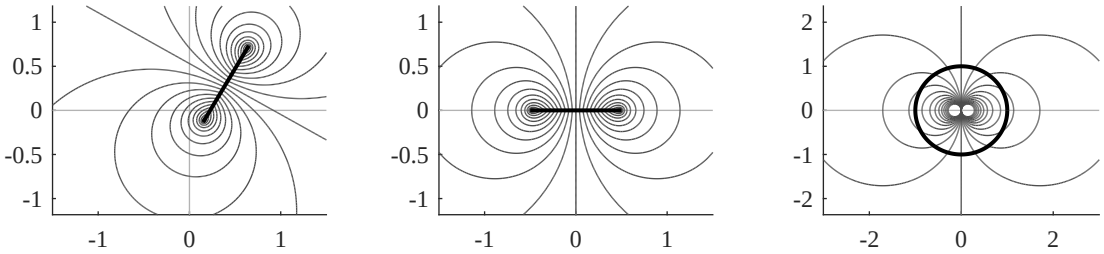

(a) The physical, z, plane. (b) The plate, $\tilde{z}$, plane. (c) The cylinder, ζ, plane.

Figure A.3: Streamlines for the flow induced by translation.

and plate tangential motion induces no flow. This produces the streamlines shown in figure A.3. The angle of attack has been arbitrarily chosen as $\alpha = \pi/3$, and the plate offset an arbitrary amount from the origin. The actual translation velocity does not matter, as the streamlines will always have the same shape. The flow in the ζ plane is recognizable as that due to a doublet.

The velocity on the surface of the plate can be found by specifying $\zeta = e^{i\theta}$ (recall that $\tilde{x} = a\cos(\theta)$), and using equation (A.13b). This gives:

$$\tilde{u}_t = \frac{\tilde{V}}{\tan(\theta)} \tag{A.15a}$$

$$\tilde{v}_t = \tilde{V} \tag{A.15b}$$

The introduction of the double singularity to the flow has therefore unforced no through-flow on the plate by making the fluid velocity, $\tilde{v}$, match the plate's kinematic velocity, also $\tilde{V}$. As a side effect there is now a slip velocity on the surface of the plate. This slip velocity can be thought of as an infinitely thin boundary layer. It can also be used to find the strength of the vortex sheet along the plate by using

$$\gamma(\theta) = -\tilde{u}(\theta) + \tilde{u}(-\theta) \tag{A.16}$$

where γ is the vortex sheet strength in circulation per distance. For translation, this

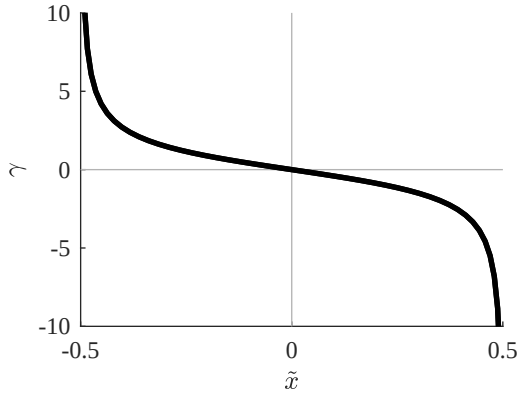

Figure A.4: The vorticity distribution on the plate induced by translation ($\tilde{V} = 1$)

results in:

$$\gamma_t(\theta) = -2\tilde{V}\frac{\cos(\theta)}{\sin(\theta)} = -\frac{2\tilde{V}x}{\sqrt{a^2 - x^2}} \tag{A.17}$$

Figure A.4 depicts the distribution. It is singular at the edges, as are all the distributions considered. This can be seen the other way around from the fluid velocity creating a vortex sheet: i.e. that this is the vorticity distribution that creates constant plate normal velocity.

Finally, we can integrate this vorticity distribution across the chord to check its net circulation. Lo and behold, this produces zero net circulation. Hence any force associated with translating the plate will described as a non-circulatory force.

A.4.2 Rotation

The same treatment will be given for flow due to plate rotation. The induced flow from plate rotation is given by:

$$G_r = -\frac{ia^2\Omega}{4\zeta^2} \tag{A.18a}$$

$$W_r = \frac{ia^2\Omega}{2\zeta^3} \tag{A.18b}$$

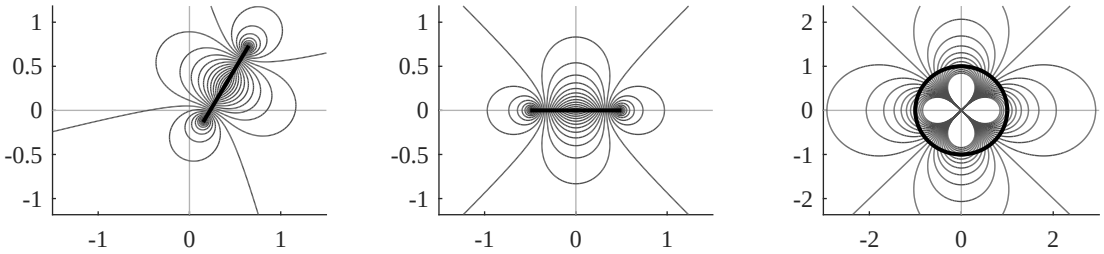

(a) The physical, z, plane. (b) The plate, $\tilde{z}$, plane. (c) The cylinder, ζ, plane.

Figure A.5: Streamlines for the flow induced by rotation.

This function depends only on the plate's angular velocity, Ω, which is independent of pitch axis location. The streamlines are depicted in figure A.5. Since the streamlines have a singularity that is one order higher than the doublet used for translation, the streamline pattern has four lobes instead of two, and could perhaps be called a "quadlet."

Applying the same process as above yields the surface velocities:

$$\tilde{u}_r = \frac{a\Omega}{2}\frac{\cos(2\theta)}{\sin(\theta)} \tag{A.19a}$$

$$\tilde{v}_r = a\Omega\cos(\theta) = \tilde{x}\Omega \tag{A.19b}$$

Once again, we have met the boundary condition of no-through flow on the wing. The surface vorticity distribution follows directly from equation (A.19a), and is shown in figure A.6.

$$\gamma_r(\theta) = a\Omega\frac{\cos(2\theta)}{\sin(\theta)} = \frac{\Omega\left(a^2 - 2x^2\right)}{\sqrt{a^2 - x^2}} \tag{A.20}$$

This distribution is symmetric about the mid chord of the plate.

Integrating this distribution across the plate reveals that it also has a net zero circulation. Thus both kinematic sources of slip velocity have no associated circulation, even though they both produce a bound vortex sheet. Hence, any forces that arise from these components of the induced flow are termed non-circulatory. Often they are given the added moniker of "added-mass" because, as will be shown later,

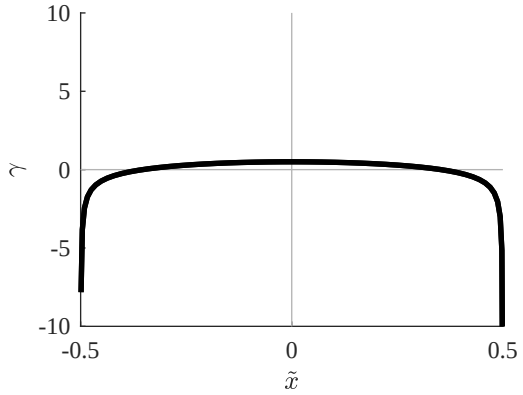

Figure A.6: The vorticity distribution on the plate induced by rotation ($\Omega = 1$)

they are dependent on the acceleration of the plate, and thus behave like a mass. As Bisplinghoff, Halfman and Ashley [4] point out, this is a tricky concept because the amount of "mass" associated with translation is different from that used for rotation. In addition, personal experience has shown that individuals in the community have widely varying definitions for added mass that do not always coincide with one another. Because of this, I will stick to the names "circulatory" and "non-circulatory" to break apart the flow and force components.

A.4.3 Bound Vortex

A vortex located at $\zeta = 0$ is considered a "bound" vortex that travels with the plate. It induces a potential:

$$G_b = \frac{\Gamma}{2\pi i} \ln(\zeta) \tag{A.21a}$$

$$W_b = \frac{\Gamma}{2\pi i} \frac{1}{\zeta} \tag{A.21b}$$

The streamlines in the ζ plane are concentric circles. As one might suspect, this

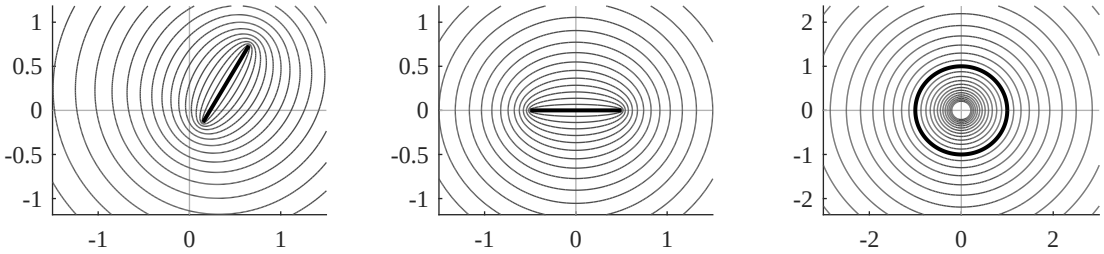

(a) The physical, z, plane. (b) The plate, $\tilde{z}$, plane. (c) The cylinder, ζ, plane.

Figure A.7: Streamlines for the flow induced by a bound vortex.

means that a bound vortex induces no plate normal velocity component:

$$\tilde{u}_b = -\frac{\Gamma}{2\pi a}\frac{1}{\sin(\theta)} \tag{A.22a}$$

$$\tilde{v}_b = 0 \tag{A.22b}$$

The upshot of this is that adding a bound vortex has no effect on the no-through flow boundary condition, and can thus be added at any time with any strength and the solution will still be "valid" from a mathematical standpoint. This is the crux of what is meant when people refer to the non-uniqueness of potential flow solutions. In order to choose a solution, we must resort to an addition physically based restriction on the flow because the boundary required by Laplace's equation alone are insufficient to uniquely define the solution. This usually comes in the form of a condition at the edge of the plate, discussed in section 2.6.3.

Applying the same process as before (equation (A.16)) yields the bound vorticity distribution on the plate, given in equation (A.23) and depicted in figure A.8.

$$\gamma_b(\theta) = \frac{\Gamma}{a\pi}\frac{1}{\sin(\theta)} = \frac{\Gamma}{\pi\sqrt{a^2 - x^2}} \tag{A.23}$$

When integrated, this gives a bound circulation of Γ. This is expected, as circulation is conserved in the conformal mapping. It also means that any forces that arise from vortices create a circulation on the plate and will be termed "circulatory" forces.

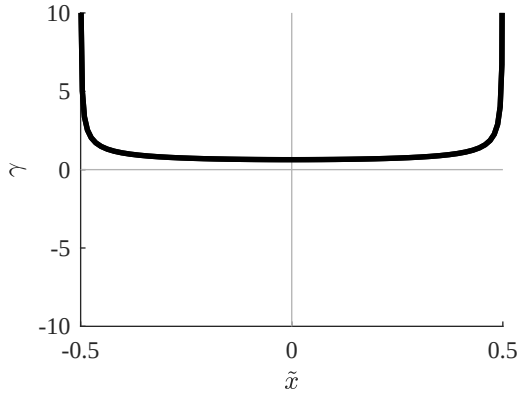

Figure A.8: The vorticity distribution on the plate induced by a bound vortex ($\Gamma = 1$)

A.4.4 Exterior Vortex

An extension of the bound vortex is to place the vortex off the plate at $\zeta = re^{i\beta}$ ($r \geq 1$). To keep the circle a streamline, an image vortex of opposite sign is added inside the cylinder at $\zeta = (1/r)e^{i\beta}$. With these two together, the potential is:

$$G_w = \frac{\Gamma}{2\pi i}\Big[\ln\left(\zeta - re^{i\beta}\right) - \ln\left(\zeta - (1/r)e^{i\beta}\right)\Big] \tag{A.24a}$$

$$W_w = \frac{\Gamma}{2\pi i}\Big[\frac{1}{\zeta - re^{i\beta}} - \frac{1}{\zeta - (1/r)e^{i\beta}}\Big] \tag{A.24b}$$

Note that if $r \to \infty$, then these equations simplify to those of a bound vortex. This is the usual justification for how a bound vortex comes about, i.e. that it is the image of a starting vortex that has been left far behind.

For the exterior vortex, the shape of the streamlines depends on the location of the vortex. This is the only singularity whose streamlines can change shape. An example of the the streamlines is shown in figure A.9.

As in the case of the bound vortex, the cylinder corresponds to one of the streamlines in the ζ plane, and thus this flow has no effect on the boundary condition:

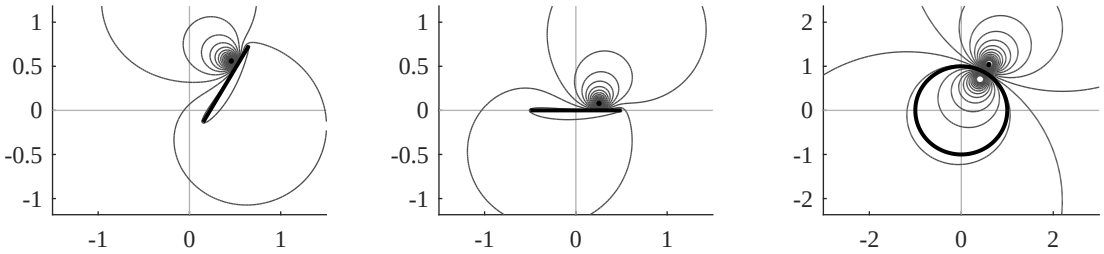

(a) The physical, z, plane. (b) The plate, $\tilde{z}$, plane. (c) The cylinder, ζ, plane.

Figure A.9: Streamlines for the flow induced by a vortex outside the plate.

$$\tilde{u}_w = \frac{\Gamma}{2\pi a}\frac{1}{\sin(\theta)}\frac{r^2-1}{1+r^2-2r\cos(\beta-\theta)} \tag{A.25a}$$

$$\tilde{v}_w = 0 \tag{A.25b}$$

Following the same procedure gives the bound vorticity distribution, whose shape is also dependent on the location of the vortex:

$$\begin{aligned}\gamma_v &= \frac{-\Gamma}{a\pi}\frac{1}{\sin(\theta)}\frac{(r^2-1)(1+r^2-r\cos(\beta-\theta)-r\cos(\beta+\theta))}{(1+r^2-2r\cos(\beta-\theta))(1+r^2-2r\cos(\beta+\theta))} \\ &= \frac{a\Gamma\,(r^2-1)\,(a(r^2+1)-2\xi x)}{\pi\sqrt{a^2-x^2}\left(2\eta\sqrt{a^2-x^2}+a(r^2+1)-2\xi x\right)\left(2\eta\sqrt{a^2-x^2}-a(r^2+1)+2\xi x\right)}\end{aligned} \tag{A.26}$$

Integrating these distributions always gives a total circulation on the plate of $-\Gamma$, or precisely that of the image vortex inside the plate.

A.5 Flow Evolution

The description of the flow in section A.4 is valid for any given instant in time, but here we are primarily concerned with unsteady flows. If the flow consists only of the motion of the plate and possibly a bound vortex, the flow changes only very simply in time as the only thing that changes are the strengths of the singularities and the

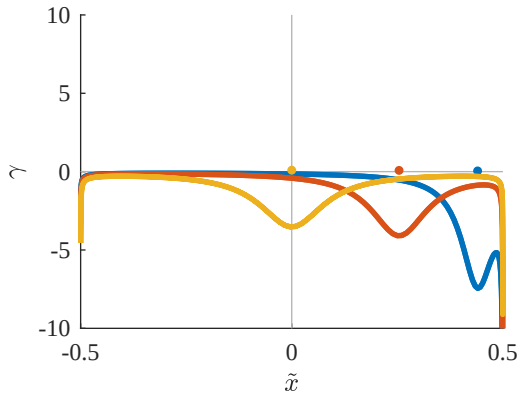

Figure A.10: The vorticity distribution on the plate induced by an exterior vortex. The vortex is located at $r = 1.2$, and $\beta = \{\pi/6, \pi/3, \pi/2\}$, with positions in the $\tilde{z}$ plane marked by the dots.

location of the plate. If there are external vortices in the flow, the situation is more complicated. According to the vorticity evolution equation, discussed in section 2.6.2, any vorticity in the fluid will convect with the local fluid velocity. Thus the point vortices should do the same. This means that a time integration is required to solve for the evolution of the vortex locations, and this is the focus of this section.

The situation is made slightly more complex because of the singular nature of a point vortex, and this is dealt with via "Kirchoff Convection". The use of conformal mapping also has an effect on the velocity, leading to the "Routh Correction." Finally, a vortex with changing strength will also have a "Brown-Michael Correction."

A.5.1 Kirchoff Convection

The most basic solution is to simply ignore the vortex for the purposes of computing the vortex velocity. To do this we split the velocity field into that due to a vortex and that due to everything else (including its image):

$$W = W_{-v} + \frac{\Gamma}{2\pi i}\frac{1}{\zeta - \zeta_v} \tag{A.27}$$

Then the vortex is said to move with W_{-v}:

$$\dot{z}_v = \left(\frac{W_{-v}}{f'(\tilde{z})g'(\zeta)} \right)^* \tag{A.28}$$

Where the $\cdot^*$ indicates complex conjugation (recall that $W = u - iv$). In this equation, the complex velocity in the ζ plane, W, is transformed to the z and $\tilde{z}$ planes with the chain rule used in equation (A.13b), and equation (A.13c). This is termed the *Kirchoff velocity*.

If there is no conformal mapping (e.g. the ζ plane is physical and one seeks the flow around a cylinder), this method will give the true vortex velocity. However, the presence of the conformal mapping requires a slightly more subtle approach.

A.5.2 Routh Correction

The Routh correction accounts for the curvature of the mapping and the vortex's self-contribution in the determination of the vortex convection velocity. The topic is discussed in Clements [191], Saffman sec. 7.2 [132], Milne-Thompson sec. 13.50 [120], and Lin [192][193]. Note that both Saffman and Milne-Thompson are attempting to find analytic functions for the vortex path as opposed to just the vortex velocity, and I found them only vaguely helpful. The derivation presented here is my own path to the same result as the cited works.

Our goal is to evaluate the velocity at the location of a vortex, $\tilde{z}_v$, to determine how that vortex will move. Vorticity convects with the flow, so the vortex motion should be the same as the flow velocity at the vortex location, denoted $W(\tilde{z}_v)$. We begin by splitting the potential into that due to the vortex and that due to everything else:

$$G(\tilde{z}) = G_{-v}(\tilde{z}) + \frac{\Gamma}{2\pi i} \ln(\tilde{z} - \tilde{z}_v)$$

where $G_{-v}(\tilde{z})$ the potential from everything else, including the current vortex' image

system, and the ln() term is the potential from the vortex in question. All we have to do to get the velocity is take the derivative and see what the value is at $\tilde{z}_v$. Easy right?

$$W(\tilde{z}) = \frac{dG(\tilde{z})}{d\tilde{z}} = G'_{-v}(\tilde{z}) + \frac{\Gamma}{2\pi i}\frac{1}{\tilde{z} - \tilde{z}_v}$$

Oh no! That can't be right, the second term becomes 1/0 and is indeterminate. If this was the whole story, we would be forced to simply drop the vortex term and say,

$$W(\tilde{z}_v) = G'_{-v}(\tilde{z}_v),$$

resulting in Kirchoff convection, discussed in the previous section. This is obviously not the whole story, or the section would be over. We must now include the mapping. Since we usually define the complex potential only in the ζ plane, the above equation should really have been:

$$W(\tilde{z}_v) = G'_{-v}(\zeta_v)\left.\frac{d\zeta}{d\tilde{z}}\right|_{\zeta_v}$$

But that doesn't really get us anywhere either. The crux of the Routh correction is that we must go all the way back to the start and single out the vortex in both the $\tilde{z}$ plane and the ζ plane:

$$G(\tilde{z}) = G_{-v}(\tilde{z}) + \frac{\Gamma}{2\pi i}\ln(\tilde{z} - \tilde{z}_v) = G_{-v}(\zeta) + \frac{\Gamma}{2\pi i}\ln(\zeta - \zeta_v) = G(\zeta)$$

This statement says that the potential has the same value at both $\tilde{z}$ and its mapped ζ location. The mapping between $\tilde{z}$ and ζ can be written by stating:

$$\tilde{z} = g(\zeta)$$

substituting this for $\tilde{z}$ gives:

$$G_{-v}(\tilde{z}) + \frac{\Gamma}{2\pi i}\ln(g(\zeta) - g(\zeta_v)) = G_{-v}(\zeta) + \frac{\Gamma}{2\pi i}\ln(\zeta - \zeta_v)$$

Instead of simply dropping the vortex terms, we can move the vortex term on the left over to the right:

$$G_{-v}(\tilde{z}) = G_{-v}(\zeta) + \frac{\Gamma}{2\pi i}\ln\left(\frac{\zeta - \zeta_v}{g(\zeta) - g(\zeta_v)}\right)$$

and apply our definition of the vortex velocity:

$$W(\tilde{z}) = \frac{dG_{-v}}{d\tilde{z}} = \left\{G'_{-v}(\zeta) + \frac{\Gamma}{2\pi i}\left(\frac{(g(\zeta) - g(\zeta_v)) - g'(\zeta)(\zeta - \zeta_v)}{(\zeta - \zeta_v)(g(\zeta) - g(\zeta_v)}\right)\right\}\frac{d\zeta}{d\tilde{z}}$$

That still looks pretty gnarly, and plugging in $\tilde{z} = \tilde{z}_v$ still does not produce an answer. But if we instead take the limit as $\tilde{z} \to \tilde{z}_v$, we get (focusing on only the big fraction):

$$\lim_{\tilde{z}\to\tilde{z}_v} \frac{(g(\zeta) - g(\zeta_v)) - g'(\zeta)(\zeta - \zeta_v)}{(\zeta - \zeta_v)(g(\zeta) - g(\zeta_v)} = \frac{0}{0}$$

It might not look like it, but this is much better because we can now apply L'Hôpital's rule and take the derivative of both numerator and denominator resulting in:

$$\lim_{\tilde{z}\to\tilde{z}_v} \frac{-g''(\zeta)(\zeta - \zeta_v)}{(\zeta - \zeta_v)g'(\zeta) + (g(\zeta) - g(\zeta_v))} = \frac{0}{0}$$

Apply L'Hôpital once more:

$$\lim_{\tilde{z}\to\tilde{z}_v} \frac{-g''(\zeta) - g'''(\zeta)(\zeta - \zeta_v)}{2g'(\zeta) + (\zeta - \zeta_v)g''(\zeta)} = -\frac{g''(\zeta_v)}{2g'(\zeta_v)}$$

At last we have produced the fabled Routh correction. This makes our expression for

the vortex velocity (or more precisely the limit of velocity as $\tilde{z} \to \tilde{z}_v$):

$$W(\tilde{z}_v) = \lim_{\tilde{z}\to\tilde{z}_v} G'_{-v}(\tilde{z}) = \left\{ G'_{-v}(\zeta_v) - \frac{\Gamma}{4\pi i}\frac{g''(\zeta_v)}{g'(\zeta_v)} \right\} \left.\frac{d\zeta}{d\tilde{z}}\right|_{\zeta_v}$$

Finally, note that:

$$\frac{d\zeta}{d\tilde{z}} = \left(\frac{d\tilde{z}}{d\zeta}\right)^{-1} = \frac{1}{g'(\zeta)}$$

Substituting this expression in gives the vortex velocity as it is implemented in the code:

$$W(\tilde{z}_v) = \lim_{\tilde{z}\to\tilde{z}_v} G'_{-v}(\tilde{z}) = \left\{ G'_{-v}(\zeta_v) - \frac{\Gamma}{4\pi i}\frac{g''(\zeta_v)}{g'(\zeta_v)} \right\} \frac{1}{g'(\zeta_v)}$$

This matches what is given in most texts. Clements [191] has a slightly different expression that results from choosing to set $\zeta = g(\tilde{z})$ instead of $\tilde{z} = g(\zeta)$. Also note that in some texts the i is on the other side of the fraction, and this will change the sign of the correction.

A.5.3 Brown-Michael Correction

The Brown-Michael correction comes into play when dealing with point vortices of changing strength. As per the inviscid vorticity evolution equation, discussed in section 2.6.2, point vortices usually have constant strength, as the vorticity equations state than in inviscid flow a fluid particle maintains its circulation for all time. This condition is relaxed in some models to allow for a more compact description of the flow field. In making that relaxation, Brown-Micheal [194] argued that the change in circulation strength resulted in unbalanced forces in the flow, and this concept was later formalized by Michelin and Llewellyn Smith [195]. In order to maintain a force-free branch cut joining the vortex and its associated edge, a new term is added

to the convection velocity:

$$\dot{z}_v + (z_v - z_e)\frac{\dot{\Gamma}}{\Gamma} = W(z_v)^* \tag{A.29}$$

where z_e is the z location of the edge "tied" to this vortex by the Kutta condition. $W(z_v)$ is the velocity given by Kirchoff plus the Routh Correction, and $\cdot^*$ indicates the complex conjugate.

A.5.4 Motion in the ζ plane

The equations so far have given the vortex motion in the z plane from its convection with the fluid. However, since equations for the flow are given in terms of ζ it is desirable to carry out the integration of the particle motion there as well. Using equation (A.1) for the mapping gives us the kinematics of how to transfer $\dot{z}_v$ to $\dot{\zeta}_v$. First, the time derivative of mapping from z to $\tilde{z}$ (equation (A.3a)) is taken:

$$\dot{\tilde{z}}_v = \left[\dot{z}_v - \dot{z}_c - i(z_v - z_c)\Omega\right] e^{i\alpha} \tag{A.30}$$

This gives the rate of change of vortex location in the $\tilde{z}$ plane due to both convection and the change in reference frame. This velocity is then transformed into the ζ plane by taking the time derivative of equation (A.1b):

$$\dot{\zeta}_v = \frac{\dot{\tilde{z}}_v}{g'(\zeta_v)} \tag{A.31}$$

This includes the derivative of the mapping, $g'(\zeta)$, and so vortex velocity tends to infinity near the edges of the plate, even in the ζ plane. The vortices are birthed at the edge of the plate however, so a small time similarity solution is used to jump-start their convection away from the singular point.

A.5.5 Small Time Solution

The mapping function causes the vortex velocity to be singular near the leading and trailing edges. This make integration difficult, so a similarity solution is employed to move the vortex away from the singular point before numerical integration begins. This also solves the critical issue of where the tangential velocity required to convect vorticity off the leading edge arises from.[3] These solution can employ either a vortex sheet formulation as in Pullin's work [183, 103], or a point vortex approximation of the vortex sheet, as developed by Jones [106, 128] and later used by Wang and Eldredge [3]. The point vortex solution is more tractable for numerical implementations, and is more common.

A.6 Force Computation

The three most popular methods for computing the force on an object in potential flow are via the unsteady Bernoulli equation, the Blasius integral, and the impulse method. For my work I have chosen to use the impulse method because it gives clean results (i.e. does not require the computation of edge suction). All the methods come from the Navier-Stokes equations in one fashion or another, and so they all give the same answer. The only difference is in ease of computation. This is the central idea behind the VonKarman and Sears [126] approach, and the reasoning behind it has been rigorously derived and extended more recently by Wu [186] and Saffman [132]. These papers served as the basis for Eldredge [196], which is the source of the present formulae.

The force exerted on a body by the fluid is written as the rate of change of linear impulse. The area A_f is the complete fluid domain, stretching to infinity, and

[3] Without an LEV to start with, the natural motion of the plate pushes flow particles at the leading edge back along the chord.

the surface S is the exterior boundary of the body.

$$\vec{F} = -\frac{d}{dt}(\vec{P}_\omega + \vec{P}_\gamma + \vec{P}_b) \tag{A.32a}$$

$$\vec{P}_\omega = \rho \int_{A_f} \vec{x} \times \vec{\omega} dA \tag{A.32b}$$

$$\vec{P}_\gamma = \rho \oint_S \vec{x} \times \vec{\gamma} ds \tag{A.32c}$$

$$\vec{P}_b = \rho_b \oint_S \vec{x} \times (\hat{n} \times \vec{u}_b) ds \tag{A.32d}$$

Equation (A.32b) is the impulse of the vorticity, ω, in the fluid (e.g. the wake and LEV). Equation (A.32c) is the impulse from the vorticity on the surface of the body (e.g. the boundary layer). For the present model one assumes that the potential flow represents the Euler limit of zero viscosity and hence the boundary layer is infinitely thin. This leads to the definition of $\vec{\gamma}$ as the slip velocity across the surface. Thus $\vec{\gamma} = \hat{n} \times (\vec{u}_f - \vec{u}_b)$ where $\vec{u}_f$ is the fluid velocity and $\vec{u}_b$ is the body velocity. Finally, equation (A.32d) represents the impulse of the body itself. This formulation treats the entire domain, both body and fluid, via the same kinematic laws, and hence makes no distinction between the body and fluid (save the change in density) since vorticity is defined the same way for both.

The torque on the body is defined in a similar fashion:

$$\vec{M}^0 = -\frac{d}{dt}(\vec{\Pi}_\omega + \vec{\Pi}_\gamma + \vec{\Pi}_b) \tag{A.33a}$$

$$\vec{\Pi}_\omega = \frac{\rho}{2} \int_{A_f} \vec{x} \times [\vec{x} \times \vec{\omega}] dA \tag{A.33b}$$

$$\vec{\Pi}_\gamma = \frac{\rho}{2} \oint_S \vec{x} \times [\vec{x} \times \vec{\gamma}] ds \tag{A.33c}$$

$$\vec{\Pi}_b = \frac{\rho_b}{2} \oint_S \vec{x} \times [\vec{x} \times (\hat{n} \times \vec{u}_b)] ds \tag{A.33d}$$

This formulation computes the force and moment about the origin given a vorticity distribution. We have already developed those from the various potential singularities,

so all the remains is to plug them in and evaluate the integrals.

We must first compute the linear and angular impulses, $\vec{P}$ and $\vec{\Pi}$. First, we note that $\vec{P}_b$ and $\vec{\Pi}_b$ are 0 because our plate is infinitely thin, and body velocities cancel around the plate surface. Thus the it only remains to compute $\vec{P}_\gamma$ and $\vec{\Pi}_\gamma$ for the various sources of slip velocity.

First, we shall conquer the linear impulse. Restating equation (A.32c):

$$\vec{P}_\gamma = \rho \oint_S \vec{x} \times \vec{\gamma} ds = \rho \int_{-a}^{a} (\vec{x} \times \vec{\gamma}) d\tilde{x} = a\rho \int_0^\pi (\vec{x} \times \vec{\gamma}) \sin(\theta) d\theta \qquad \text{(A.32c revisited)}$$

To keep things general, substitute $\vec{x} = x\hat{\imath} + y\hat{\jmath}$, $\vec{\gamma} = \gamma\hat{k}$, and carry out the cross product:

$$\vec{P}_\gamma = a\rho \int_0^\pi (y\gamma\hat{\imath} - x\gamma\hat{\jmath}) \sin(\theta) d\theta \tag{A.34}$$

Thus we have the two components of momentum:

$$\vec{P}_\gamma \cdot \hat{\imath} = a\rho \int_0^\pi y\gamma \sin(\theta) d\theta \tag{A.35a}$$

$$\vec{P}_\gamma \cdot \hat{\jmath} = -a\rho \int_0^\pi x\gamma \sin(\theta) d\theta \tag{A.35b}$$

Expanding x and y, we have the expressions for plate location from the definition of reference frames in section A.1:

$$x = x_c + \tilde{x}\cos(\alpha) = x_c + a\cos(\theta)\cos(\alpha) \tag{A.36a}$$

$$y = y_c + \tilde{x}\sin(\alpha) = y_c + a\cos(\theta)\sin(\alpha) \tag{A.36b}$$

Plugging these into equation (A.35) gives:

$$\vec{P}_\gamma \cdot \hat{\imath} = a\rho \left[y_c \int_0^\pi \gamma \sin(\theta) d\theta + a\sin(\alpha) \int_0^\pi \gamma \cos(\theta)\sin(\theta) d\theta \right] \tag{A.37a}$$

$$\vec{P}_\gamma \cdot \hat{\jmath} = -a\rho \left[x_c \int_0^\pi \gamma \sin(\theta) d\theta + a\cos(\alpha) \int_0^\pi \gamma \cos(\theta)\sin(\theta) d\theta \right] \tag{A.37b}$$

This gives a total of six distinct integrals to evaluate for the three vorticity distributions discussed. The first set of three integrals are the product of γ and x_c or y_c and have the same form as those used to determine total circulation. The second set of three integrals adds the $\cos(\theta)$ term to the integration (thanks WolframAlpha):

$$a\int_0^\pi \gamma_t \sin(\theta)d\theta = 0 \qquad a\int_0^\pi \gamma_t \cos(\theta)\sin(\theta)d\theta = -\pi a\tilde{V} \tag{A.38a}$$

$$a\int_0^\pi \gamma_r \sin(\theta)d\theta = 0 \qquad a\int_0^\pi \gamma_r \cos(\theta)\sin(\theta)d\theta = 0 \tag{A.38b}$$

$$a\int_0^\pi \gamma_v \sin(\theta)d\theta = \Gamma \qquad a\int_0^\pi \gamma_v \cos(\theta)\sin(\theta)d\theta = 0 \tag{A.38c}$$

$$a\int_0^\pi \gamma_\omega \sin(\theta)d\theta = -\omega \qquad a\int_0^\pi \gamma_\omega \cos(\theta)\sin(\theta)d\theta = -\frac{\omega\cos(\beta)}{r} = -\omega A \tag{A.38d}$$

These are then substituted back into equation (A.37) to yield final expressions for the momentum of the plate:

$$\vec{P}_{\gamma,t} = \rho\pi a^2\tilde{V}\Big[-\sin(\alpha)\hat{\imath} + \cos(\alpha)\hat{\jmath}\Big] \tag{A.39a}$$

$$\vec{P}_{\gamma,r} = 0\hat{\imath} + 0\hat{\jmath} \tag{A.39b}$$

$$\vec{P}_{\gamma,v} = \rho\Gamma\left[y_c\hat{\imath} - x_c\hat{\jmath}\right] \tag{A.39c}$$

$$\vec{P}_{\gamma,w} = -\rho\omega\Big[\left(y_c + aA\sin(\alpha)\right)\hat{\imath} - \left(x_c + aA\cos(\alpha)\right)\hat{\jmath}\Big] \tag{A.39d}$$

These expressions are easily (?) differentiable in time based on the desired kinematics to produce the forces via equation (A.32a).

Having dealt with the linear momentum, we now consider the angular momentum. A similar procedure is used to evaluate equation (A.33a), based on equation (A.33c):

$$\vec{\Pi}_\gamma = \frac{\rho}{2}\oint_S \vec{x}\times[\vec{x}\times\vec{\gamma}]ds \tag{A.33c revisited}$$

making the same substitutions as equation (A.34) results in the single $\hat{k}$ component

of angular momentum:

$$\vec{\Pi}_\gamma \cdot \hat{k} = -\frac{a\rho}{2}\int_o^\pi \gamma(x^2+y^2)\sin(\theta)d\theta \tag{A.40}$$

Squaring the location results in a new set of integrals containing $\cos^2(\theta)$:

$$a\int_0^\pi \gamma_t \cos^2(\theta)\sin(\theta)d\theta = 0 \tag{A.41a}$$
$$a\int_0^\pi \gamma_r \cos^2(\theta)\sin(\theta)d\theta = -\frac{\pi a^2\Omega}{4} \tag{A.41b}$$
$$a\int_0^\pi \gamma_v \cos^2(\theta)\sin(\theta)d\theta = \frac{\Gamma}{2} \tag{A.41c}$$
$$a\int_0^\pi \gamma_\omega \cos^2(\theta)\sin(\theta)d\theta = -\frac{\omega}{2}\frac{r^2+\cos(2\beta)}{r^2} = -\frac{\omega}{2}(1+A^2-B^2) \tag{A.41d}$$

In the last equation, the substitutions $A = \cos(\beta)/r$ and $B = \sin(\beta)/r$ have been used to result in a simpler expression. Plugging the values into equation (A.40) and using the results of the integrations one arrives at:

$$\vec{\Pi}_{\gamma,t} = \rho\pi a^2\tilde{V}[x_c\cos(\alpha)+y_c\sin(\alpha)]\hat{k} \tag{A.42a}$$
$$\vec{\Pi}_{\gamma,r} = \frac{\rho\pi a^4\Omega}{8}\hat{k} \tag{A.42b}$$
$$\vec{\Pi}_{\gamma,v} = -\frac{\rho\Gamma}{2}\left[x_c^2+y_c^2+\frac{a^2}{2}\right]\hat{k} \tag{A.42c}$$
$$\vec{\Pi}_{\gamma,w} = \frac{\rho\omega}{2}\left[x_c^2+y_c^2+2a\Big(x_c\cos(\alpha)+y_c\sin(\alpha)\Big)A+\frac{a^2}{2}\Big(1+A^2-B^2\Big)\right] \tag{A.42d}$$

Notice that in the limit $r \to \infty$ the equations for the external vortex reduce to those of a bound vortex with opposite circulation. Now that we have expressions for the impulse from the bound vortex sheet we can proceed to evaluating the forces and moments on the plate.

A.7 Forces and Moments About an Arbitrary Pitch Axis

To be as explicit as possible, the time derivatives in equations A.32a and A.33a will be carried out to present the final expressions for the force and moment on a plate. The kinematics are with reference to a pitch point located at a distance ab from the plate center, the moments are shown with reference to that location as well.

Note that simply computing the time derivative in equation (A.33a) produces the moment about the origin of the coordinate system. In order to get the moment about the pitch axis, the moment about the origin is modified by

$$\vec{M}^b = \vec{M}^0 - \vec{r}_b \times \vec{F} \tag{A.43}$$

These equations are left in their fixed frame components: the x force component $\vec{F} \cdot \hat{\imath}$, the y force component $\vec{F} \cdot \hat{\jmath}$, and the out-of-plane moment $\vec{M} \cdot \hat{k}$. This is done because lift, L, and drag, D, are defined relative the free stream (or wing) velocity, further complicating the formulas. For the simple case of a horizontally translating wing with positive U velocity the conversion is simple: $L = \vec{F} \cdot \hat{\jmath}$ and $D = -\vec{F} \cdot \hat{\imath}$.

A.7.1 Translation (Non-Circulatory)

These equations give the force and moment that a plate experiences from the flow it induces by its motion. As discussed in section A.4.1, this produces no net circulation and is thus a non-circulatory force.

$$\vec{F}_t \cdot \hat{\imath} = \frac{1}{2}\pi a^2 \rho \Bigg(-2ab\Omega^2 \cos(\alpha) - 2ab\dot{\Omega} \sin(\alpha) + 2\dot{U} \sin^2(\alpha) + \sin(2\alpha)\left(\dot{V} - 2U\Omega\right) + 2V\Omega \cos(2\alpha) \Bigg) \tag{A.44a}$$

$$\vec{F}_t \cdot \hat{\jmath} = \frac{1}{2}\pi a^2 \rho \Bigg(2ab\dot{\Omega}\cos(\alpha) - 2ab\Omega^2 \sin(\alpha) \\ - 2\dot{V}\cos^2(\alpha) + \sin(2\alpha)\left(\dot{U} + 2V\Omega\right) + 2\Omega U \cos(2\alpha)\Bigg) \quad \text{(A.44b)}$$

$$\vec{M}_t^b \cdot \hat{k} = -\frac{1}{2}\pi a^2 \rho \Bigg(2ab\left(ab\dot{\Omega} + \dot{U}\sin(\alpha) - \dot{V}\cos(\alpha)\right) \\ + \sin(2\alpha)\left(V^2 - U^2\right) + 2UV\cos(2\alpha)\Bigg) \quad \text{(A.44c)}$$

Note also that the divide between rotation and translation forces has been rather muddied, as these equations include Ω terms. They are also quite long an unwieldy. The situation is assuaged when considering everything referenced to the plate center and setting $b = 0$. The kinematic definitions in section A.1 gives an expression for $\tilde{V}$, restated here along with its time derivative:

$$\tilde{V} = -U\sin(\alpha) + V\cos(\alpha)$$
$$\dot{\tilde{V}} = -\dot{U}\sin(\alpha) + \dot{V}\cos(\alpha) - \Big(U\cos(\alpha) + V\sin(\alpha)\Big)\Omega$$

Substituting $b = 0$ and finding places to apply $\tilde{V}$ in equation (A.44) results in:

$$\vec{F}_t \cdot \hat{\imath} = \rho\pi a^2 \left(\tilde{V}\Omega\cos(\alpha) + \dot{\tilde{V}}\sin(\alpha)\right) \quad \text{(A.45a)}$$
$$\vec{F}_t \cdot \hat{\jmath} = \rho\pi a^2 \left(\tilde{V}\Omega\sin(\alpha) - \dot{\tilde{V}}\cos(\alpha)\right) \quad \text{(A.45b)}$$
$$\vec{M}_t^c \cdot \hat{k} = -\frac{1}{2}\pi a^2 \rho \Big(\left(V^2 - U^2\right)\sin(2\alpha) + 2UV\cos(2\alpha)\Big) \quad \text{(A.45c)}$$

These equations show the origin of the term added mass. The leading factors have the units of mass, and are equal to the mass of fluid in a cylinder with diameter equal to the chord. The terms in parentheses are the components of the plate-normal

acceleration at mid-chord. Further, in the wing relative frame, the force is entirely plate-normal. This leads to a simple definition of the non-circulatory force in words: it is a plate normal force that corresponds to the plate-normal acceleration of a mass equal to a cylinder with diameter equal to the chord. This word definition is often confused as defining, rather that describing, the non-circulatory force. The moment does not lend itself to an easy metaphor, and is often not discussed. Note that the moment, unlike the force, is entirely a steady phenomenon (i.e. it does not depend on time derivatives of velocity).

A.7.2 Rotation (Non-Circulatory)

Just as translation of the plate creates a resultant force and moment, so does rotation. The form of these forces is much simpler than translation, however:

$$\vec{F}_r \cdot \hat{\imath} = 0 \tag{A.46a}$$

$$\vec{F}_r \cdot \hat{\jmath} = 0 \tag{A.46b}$$

$$\vec{M}_r^b \cdot \hat{k} = -\frac{1}{8}\pi a^4 \rho \dot{\Omega} \tag{A.46c}$$

Obviously, rotation produces no force, only a moment. The "added mass" analogy still holds, as the moment has the form of a moment of inertia multiplied by a angular acceleration. As Bisplinghoff *et al.* [4] point out, this is not the moment of intertia of the cylinder used for the translation added mass analogy. Interestingly, b does not enter these equations and thus the pitch point has no effect on the non-circulatory rotation moment.

A.7.3 Bound Vortex (Circulatory)

The force on a plate due to a bound vortex mimics the results of the Kutta-Joukowski lift formula:

$$\vec{F}_b \cdot \hat{\imath} = \rho\Gamma\big(ab\Omega\cos(\alpha) - V\big) \tag{A.47a}$$

$$\vec{F}_b \cdot \hat{\jmath} = \rho\Gamma\big(ab\Omega\sin(\alpha) + U\big) \tag{A.47b}$$

$$\vec{M}_b^b \cdot \hat{k} = -\rho ab\Gamma\big(U\cos(\alpha) + V\sin(\alpha)\big) \tag{A.47c}$$

The Kutta-Joukowksi formula is encapsulated in the $\vec{F}_b \cdot \hat{\jmath}$ term, which reduces to $\vec{F}_b \cdot \hat{\jmath} = L = \rho U\Gamma$ when there is no rotation. Moving the bound vortex always produces a force normal to the direction of travel, leading to the thin-airfoil prediction of lift with no drag.

The eagle-eyed reader will note that the time derivative of Γ has been neglected. Including it would cause both the forces and the moments to become non-physically dependent on the plate location. This is a hint that the bound circulation should not change without shedding equal circulation into the wake, as per Kelvin's circulation theorem. If this process does occur, then it will be represented in the current model by wake vorticity, and not a bound vortex. Thus the strength of a bound vortex should not change in time, and in general $\dot{\Gamma} = 0$.

A.7.4 Wake Vorticity (Circulatory)

A vortex in the wake also produces a force on the plate. Note that the vortex location is described by its ζ plane location, $\zeta = re^{i\beta}$. This complex variable is represented by $A = \cos(\beta)/r$, $B = \sin(\beta)/r$. Doing so makes the following expressions significantly

shorter:

$$\vec{F}_w \cdot \hat{\imath} = \rho\omega \left(a\dot{A}\sin(\alpha) + a\Omega\cos(\alpha)(A-b) + V - \dot{y}_v \right) \tag{A.48a}$$

$$\vec{F}_w \cdot \hat{\jmath} = -\rho\omega \left(a\dot{A}\cos(\alpha) + a\Omega\sin(\alpha)(b-A) + U - \dot{x}_v \right) \tag{A.48b}$$

$$\vec{M}_w^b \cdot \hat{k} = -\frac{1}{2} a\rho\omega \left(a\dot{A}(A-2b) - aB\dot{B} + 2(A-b)(U\cos(\alpha) + V\sin(\alpha)) \right) \tag{A.48c}$$

Note that if the vortex is stationary relative to the plate ($\dot{A} = \dot{B} = \Omega = 0$, and $U = \dot{x}_v$ and $V = \dot{y}_v$) then the vortex induces no force on the plate. This stems directly from the VonKarman and Sears vortex pair impulse derivation [126], which relates the force due to a vortex pair, in this case the wake vortex and its image, to the rate of change of the circulation times the distance between them. If the vortex is of constant strength and stationary relative to the plate, then neither the circulation nor the distance between the vortex and its image is changing, and hence there is no change in flow momentum with time and no resulting force on the plate. This has implications for modeling the rotating case. It must be the continuous creation of circulation and its motion in the shear layer and out of plane that creates the augmented force, at least from an impulse perspective.

Appendix B: Surge Parameter Variation Model Results

This appendix documents the circulation production predictions of the multiple vortex wake model and boundary layer analogy (BLA) for the surge parameter variations. For reference, the baseline case is an $\mathcal{AR} = 8$ wing undergoing pure surge from rest at $\alpha = 45°$. The final velocity was set to achieve $Re = 12,500$ with acceleration occurring over two chords of travel. The variations altered the Reynolds number to $Re = 5,000$ and $Re = 20,000$, the acceleration distance to one and three chords, and the angle of attack to 30° and 60°.

The experimental results of the parameter variation were discussed in chapter 5. The nultiple vortex model was described in section 6.1.4 and evaluated against the baseline case data in section 7.4. Similarly, the BLA was described in section 6.2 and evaluated in section 7.6.

B.1 Multiple Vortex Model

This section contains the circulation production results from the multiple vortex model. The baseline case results are reproduced in figure B.1. The variation in Reynolds number produces essentially identical model results between the cases, shown in figure B.2. Altering the acceleration distance, shown in figure B.3, resulted in changes to the magnitude and timing of the initial peak circulation production that the model captured well. The change in angle of attack, shown in figure B.4, had mixed results. The model responded well to $\alpha = 60°$, resulting in a prediction that matched well with measurement throughout the entire run. At $\alpha = 30°$, how-

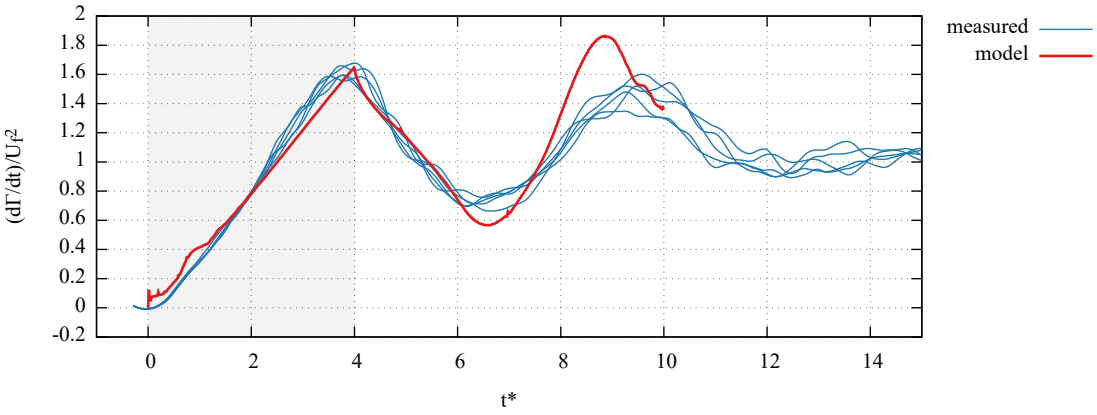

Figure B.1: The baseline case.

ever, the model experienced difficulty. The low angle of attack caused the vortices produced at the leading edge to convect back close to the edge. As they passed, they induce a velocity on the edge causing the rippling changes in production seen in the results. This is a common difficulty seen when attempting to shed vortices from the leading edge at low angles of attack [106]. Outside of the oscillations, the circulation production is a reasonable match to the measured value.

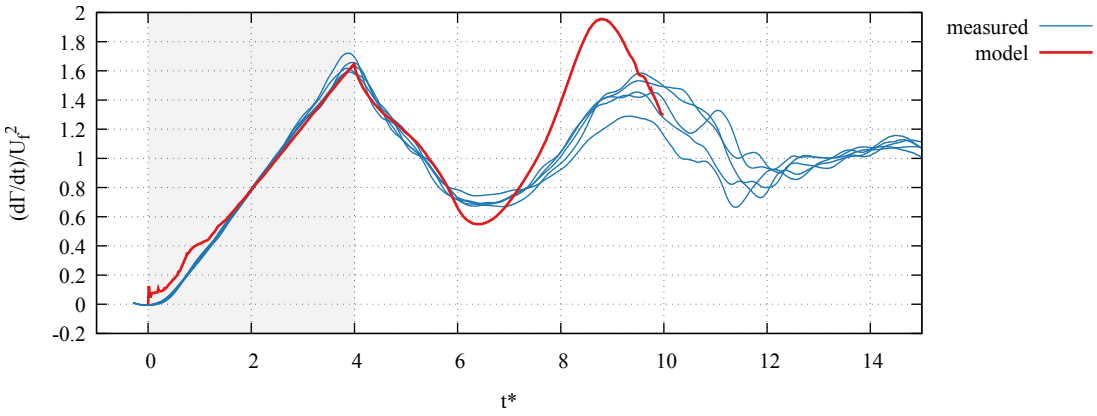

(a) $Re = 5,000$

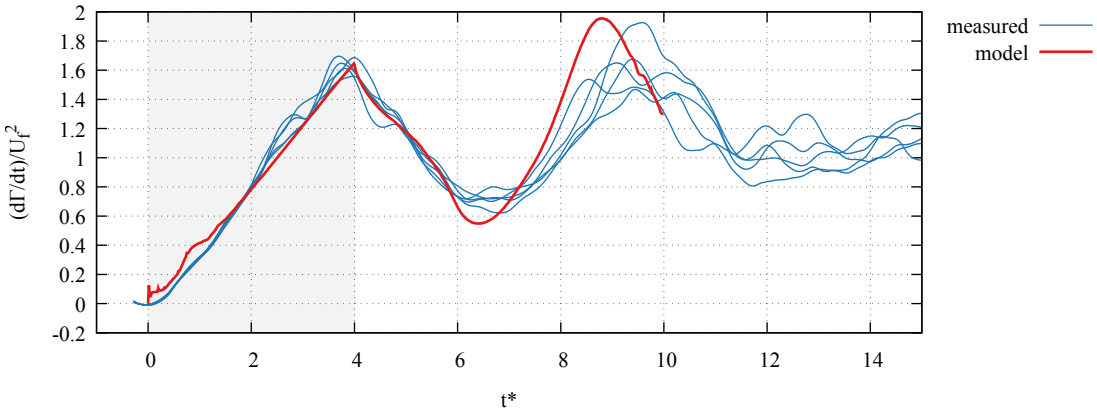

(b) $Re = 20,000$

Figure B.2: Variation of the Reynolds number.

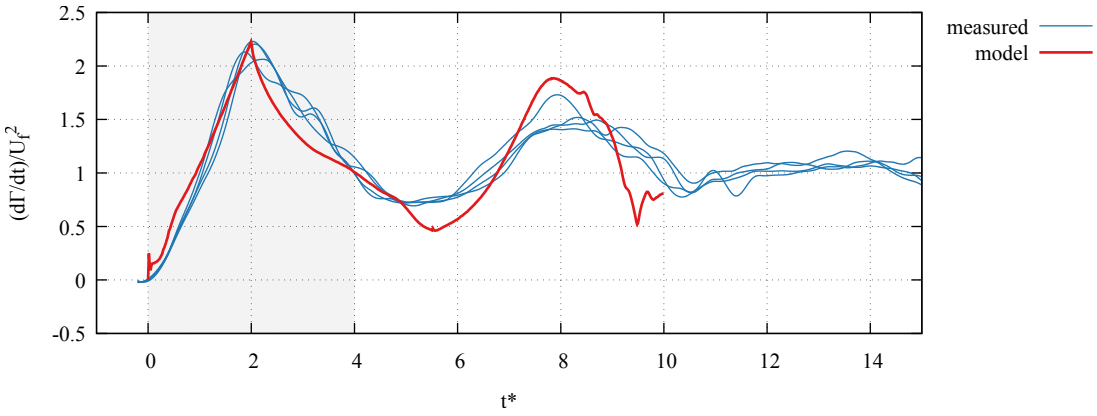

(a) $s_a/c = 1$

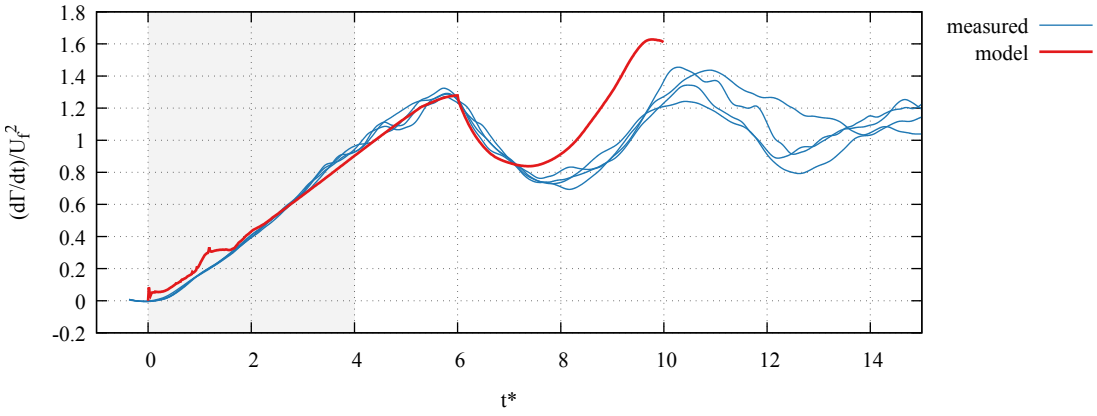

(b) $s_a/c = 3$

Figure B.3: Variation of the acceleration.

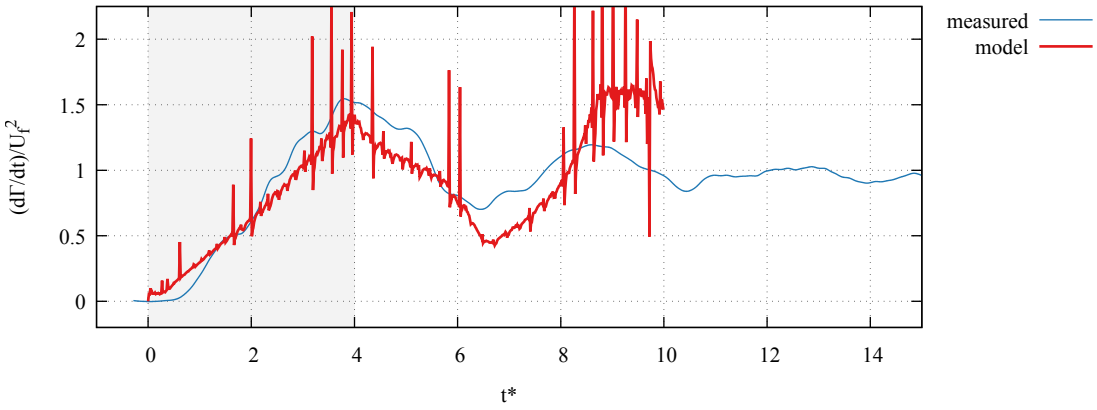

(a) $\alpha = 30°$

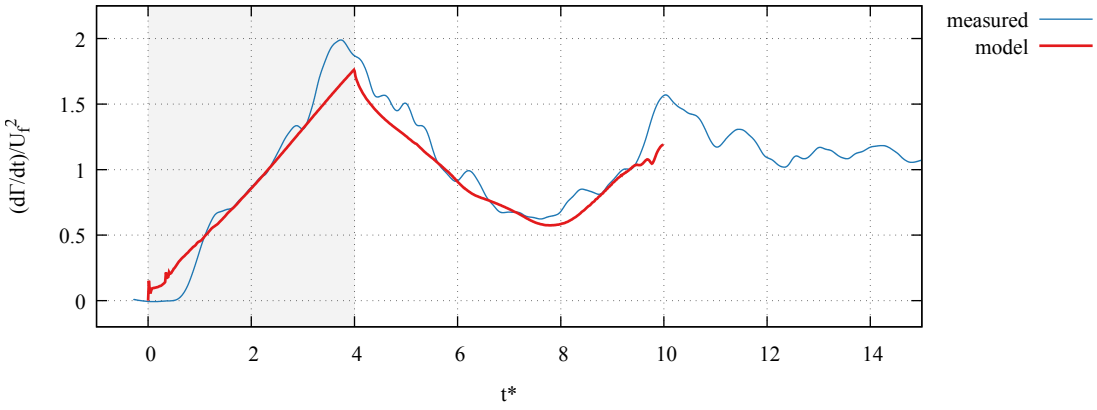

(b) $\alpha = 60°$

Figure B.4: Variation of the angle of attack.

B.2 Boundary Layer Analogy

The section contains the circulation production results from the BLA. The results use the frozen wake hypothesis for the wake centroid and circulation strength, as opposed to the in-frame only measurements. The baseline case results are reproduced in figure B.1. Note the focus is on matching the magnitude and timing of the first peak (near $t^* = 4$). The results of figure B.6 show a good agreement across the Reynolds numbers considered. This is largely due to the change in the plate motion term in the model, which captures the bulk effect of increasing the wing velocity. The amplitude of oscillation in circulation production also scale well, thanks to the increase in circulation of the LEV. Results from changing acceleration are shown in figure B.7. Results from changing angle of attack are shown in figure B.8. Fnally, results from changing aspect ratio are shown in figure B.9. The most notable result from the variations is that the steady state circulation production for the $\alpha = 30°$ case is not matched well as in the other cases. This could possible be due to the cylinder model for the body breaking down at lower angles of attack, though the initial peak production at $t^* = 4$ is still well captured. Outside of that caveat, all of the variations considered here are captured reasonably well by the BLA, owing largely to its reliance on the experimental measurement to account for the changed wake state. This speaks well to BLA as a correct relationship between the wake and the circulation production.

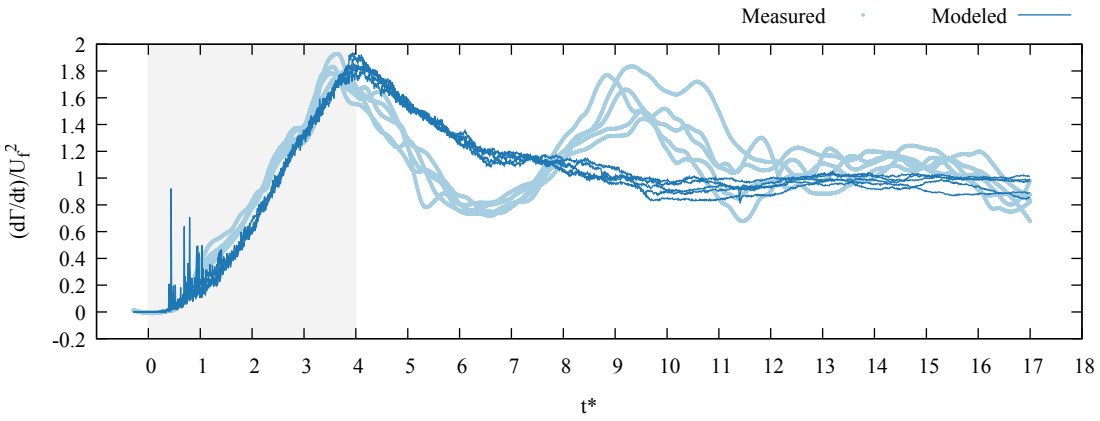

Figure B.5: The baseline case.

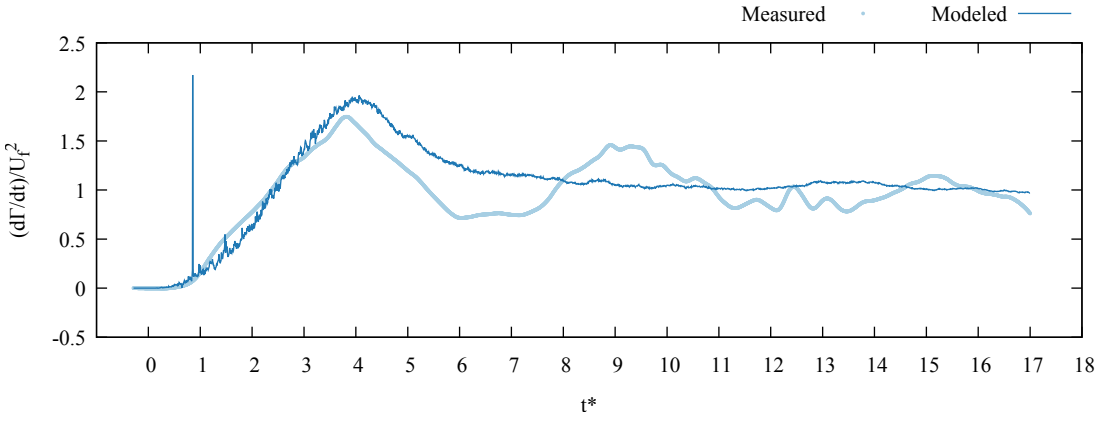

(a) $Re = 5,000$

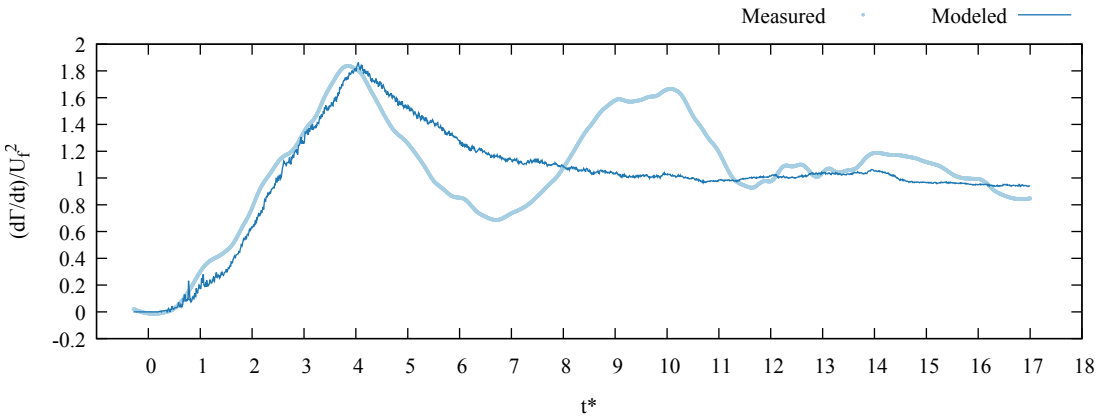

(b) $Re = 20,000$

Figure B.6: Variation of the Reynolds number.

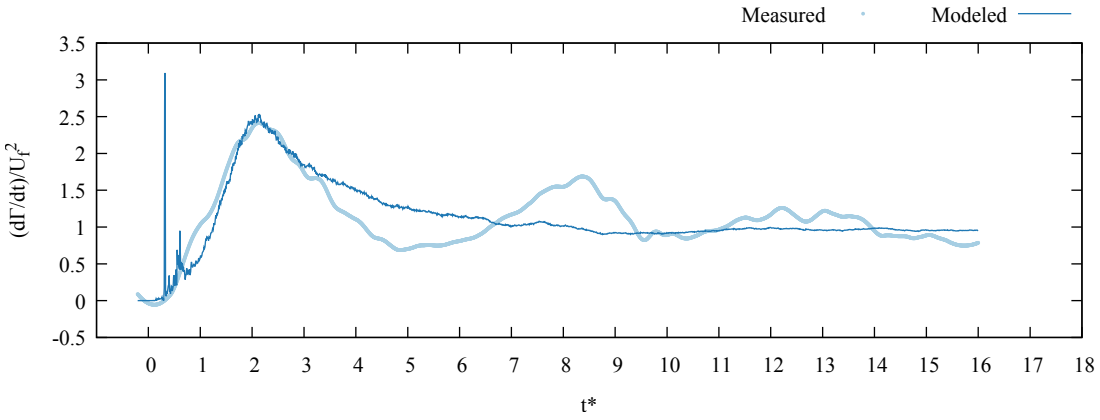

(a) $s_a/c = 1$

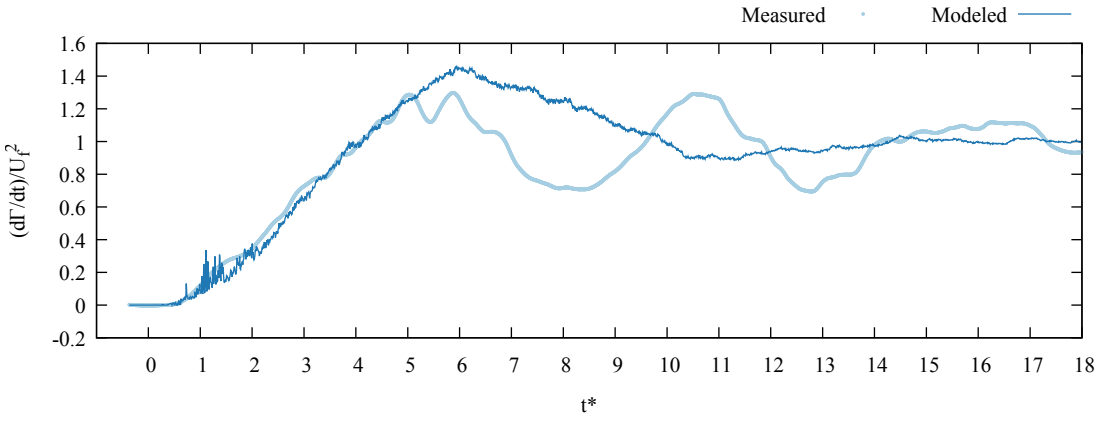

(b) $s_a/c = 3$

Figure B.7: Variation of the acceleration.

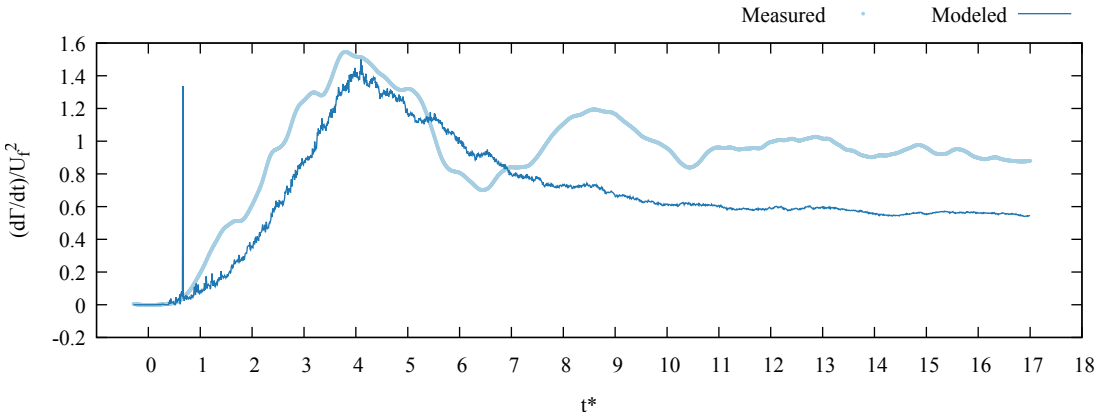

(a) $\alpha = 30°$

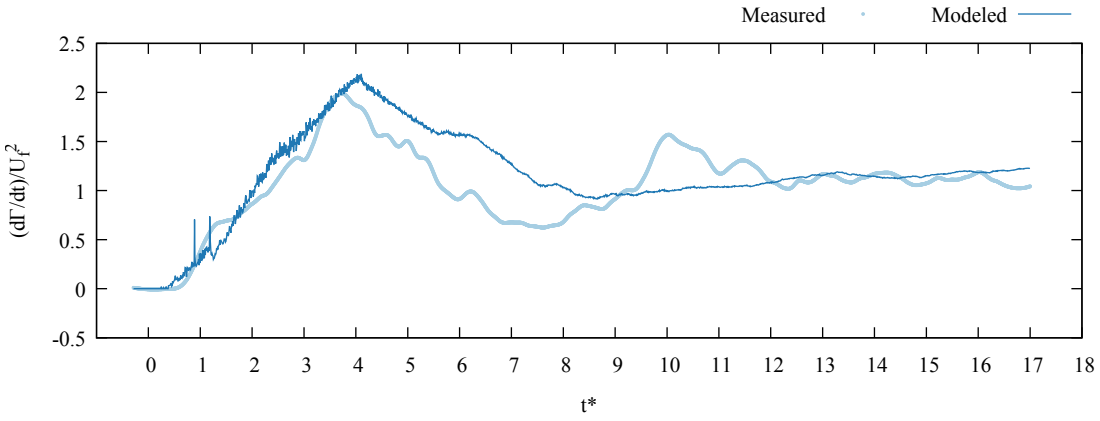

(b) $\alpha = 60°$

Figure B.8: Variation of the angle of attack.

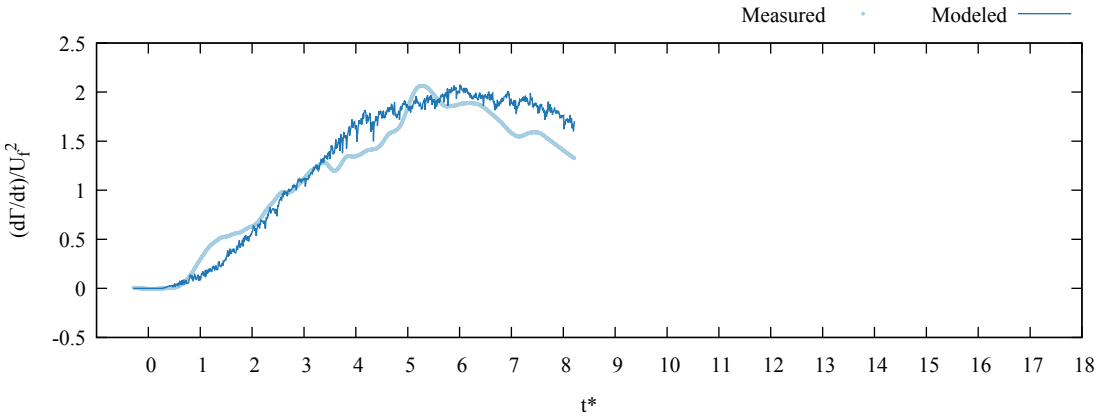

(a) $\mathcal{AR} = 4$

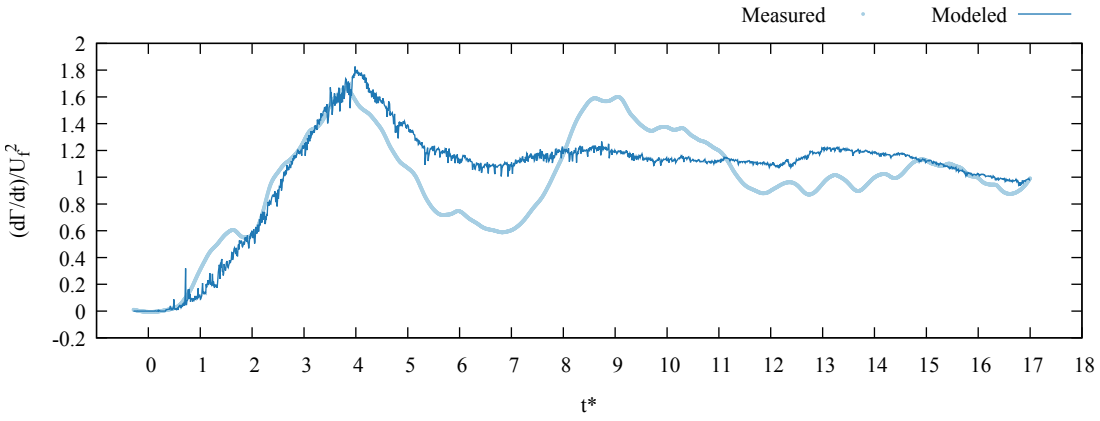

(b) $\mathcal{AR} = 6$

Figure B.9: Variation of the aspect ratio.

Bibliography

[1] Thomas J Mueller. *Fixed and flapping wing aerodynamics for micro air vehicle applications*, volume 195. AIAA, 2001.

[2] Azar Eslam Panah, James M Akkala, and James HJ Buchholz. Vorticity transport and the leading-edge vortex of a plunging airfoil. *Experiments in Fluids*, 56(8):1–15, 2015.

[3] Chengjie Wang and Jeff D Eldredge. Low-order phenomenological modeling of leading-edge vortex formation. *Theoretical and Computational Fluid Dynamics*, 27(5):577–598, 2013.

[4] Raymond L Bisplinghoff, Holt Ashley, and Robert L Halfman. *Aeroelasticity*. Dover Corporation, 1996.

[5] Michael H Dickinson and Karl G Gotz. Unsteady aerodynamic performance of model wings at low Reynolds numbers. *Journal of Experimental Biology*, 174(1):45–64, 1993.

[6] J Gordon Leishman and TS Beddoes. A semi-empirical model for dynamic stall. *Journal of the American Helicopter society*, 34(3):3–17, 1989.

[7] Wei Shyy, Y Lian, J Tang, H Liu, P Trizila, B Stanford, L Bernal, C Cesnik, P Friedmann, and P Ifju. Computational aerodynamics of low Reynolds number plunging, pitching and flexible wings for MAV applications. *Acta Mechanica Sinica*, 24(4):351–373, 2008.

[8] Craig J Wojcik and James HJ Buchholz. Vorticity transport in the leading-edge vortex on a rotating blade. *Journal of Fluid Mechanics*, 743:249–261, 2014.

[9] Herbert Wagner. Über die entstehung des dynamischen auftriebes von tragflügeln. *ZAMM-Journal of Applied Mathematics and Mechanics/Zeitschrift für Angewandte Mathematik und Mechanik*, 5(1):17–35, 1925.

[10] James M McMichael and Michael S Francis. Micro air vehicles- toward a new dimension in flight. *DARPA document*, 1997.

[11] Matthew T Keennon and Joel M Grasmeyer. Development of the black widow and microbat MAVs and a vision of the future of MAV design. In *AIAA/ICAS International Air and Space Symposium and Exposition*, volume 100, pages 14–17, 2003.

[12] Joel M Grasmeyer and Matthew T Keennon. Development of the black widow micro air vehicle. *Progress in Astronautics and Aeronautics*, 195:519–535, 2001.

[13] Matthew Keennon, Karl Klingebiel, Henry Won, and Alexander Andriukov. Development of the nano hummingbird: A tailless flapping wing micro air vehicle. In *AIAA Aerospace Sciences Meeting*, pages 1–24. AIAA Reston, VA, 2012.

[14] Gordon J Leishman. *Principles of Helicopter Aerodynamics*. Cambridge university press, 2006.

[15] Alex Kushleyev, Daniel Mellinger, Caitlin Powers, and Vijay Kumar. Towards a swarm of agile micro quadrotors. *Autonomous Robots*, 35(4):287–300, 2013.

[16] Justin Michael Winslow. *Understanding of Low Reynolds Number Aerodynamics and Design of Micro Rotary-Wing Air Vehicles*. PhD thesis, University of Maryland at College Park, 2016.

[17] Felipe Bohorquez. *Rotor hover performance and system design of an efficient coaxial rotary wing micro air vehicle*. PhD thesis, University of Maryland, College Park, 2007.

[18] James Paulos and Mark Yim. Cyclic blade pitch control for small uav without a swashplate. In *AIAA Atmospheric Flight Mechanics Conference*, page 1186, 2017.

[19] Inderjit Chopra. Hovering micro air vehicles: challenges and opportunities. In *Proceedings of American Helicopter Society Specialists Conference, International Forum on Rotorcraft Multidisciplinary Technology*, pages 15–17, 2007.

[20] Manikandan Ramasamy, J Gordon Leishman, and Timothy E Lee. Flowfield of a rotating-wing micro air vehicle. *Journal of aircraft*, 44(4):1236–1244, 2007.

[21] Moble Benedict, Justin Winslow, Zohaib Hasnain, and Inderjit Chopra. Experimental investigation of micro air vehicle scale helicopter rotor in hover. *International Journal of Micro Air Vehicles*, 7(3):231–255, 2015.

[22] David Coleman, Moble Benedict, and I Chopra. Design, development and flight-testing of a robotic hummingbird. In *71st Annual Forum of the American Heli. Society, Virginia Beach, VA*, 2015.

[23] PS Sreetharan and Robert J Wood. Passive torque regulation in an underactuated flapping wing robotic insect. *Autonomous robots*, 31(2-3):225–234, 2011.

[24] Nahid Phillips. *Experimental unsteady aerodynamics relevant to insect-inspired flapping-wing micro air vehicles*. PhD thesis, Cranfield University, 2011.

[25] Ryan B George, Mark B Colton, Christopher A Mattson, and Scott L Thomson. A differentially driven flapping wing mechanism for force analysis and trajectory optimization. *International journal of micro air vehicles*, 4(1):31–49, 2012.

[26] Ahmed M Hassan and Haithem E Taha. A combined averaging-shooting approach for the trim analysis of hovering insects/flapping-wing micro-air-vehicles. In *AIAA Guidance, Navigation, and Control Conference*, page 1734, 2017.

[27] Wei Shyy, Hikaru Aono, Satish Kumar Chimakurthi, P Trizila, C-K Kang, Carlos ES Cesnik, and Hao Liu. Recent progress in flapping wing aerodynamics and aeroelasticity. *Progress in Aerospace Sciences*, 46(7):284–327, 2010.

[28] Darryll J Pines and Felipe Bohorquez. Challenges facing future micro-air-vehicle development. *Journal of aircraft*, 43(2):290–305, 2006.

[29] John McMasters and M Henderson. Low-speed single-element airfoil synthesis. *Technical Soaring*, 6(2):1–21, 1980.

[30] PBS Lissaman. Low-Reynolds-number airfoils. *Annual Review of Fluid Mechanics*, 15(1):223–239, 1983.

[31] Frank M White. *Viscous fluid flow*. McGraw-Hill Higher Education Boston, 3rd edition, 2006.

[32] Eastman N Jacobs and Albert Sherman. Airfoil section characteristics as affected by variations of the Reynolds number. *NACA TR 586*, 1937.

[33] CP Ellington. The aerodynamics of hovering insect flight. i. the quasi-steady analysis. *Philosophical Transactions of the Royal Society of London. B, Biological Sciences*, 305(1122):1–15, 1984.

[34] David J Willis, Jaime Peraire, and Jacob K White. A combined pfft-multipole tree code, unsteady panel method with vortex particle wakes. *International Journal for numerical methods in fluids*, 53(8):1399–1422, 2007.

[35] CP Ellington. The aerodynamics of hovering insect flight. ii. morphological parameters. *Philosophical Transactions of the Royal Society B: Biological Sciences*, 305:17–40, 1984.

[36] A Roland Ennos. The kinematics and aerodynamics of the free flight of some diptera. *Journal of Experimental Biology*, 142(1):49–85, 1989.

[37] SA Combes and TL Daniel. Flexural stiffness in insect wings ii. spatial distribution and dynamic wing bending. *Journal of Experimental Biology*, 206(17):2989–2997, 2003.

[38] Steven N Fry, Rosalyn Sayaman, and Michael H Dickinson. The aerodynamics of free-flight maneuvers in drosophila. *Science*, 300(5618):495–498, 2003.

[39] JT Vance, I Faruque, and JS Humbert. Kinematic strategies for mitigating gust perturbations in insects. *Bioinspiration & biomimetics*, 8(1):016004, 2013.

[40] David Lentink and Michael H Dickinson. Rotational accelerations stabilize leading edge vortices on revolving fly wings. *Journal of Experimental Biology*, 212(16):2705–2719, 2009.

[41] Philip C Withers. An aerodynamic analysis of bird wings as fixed aerofoils. *Journal of Experimental Biology*, 90(1):143–162, 1981.

[42] Wei Shyy, Yongsheng Lian, Jian Tang, Dragos Viieru, and Hao Liu. *Aerodynamics of low Reynolds number flyers*, volume 22. Cambridge University Press, 2007.

[43] Gordon J Berman and Z Jane Wang. Energy-minimizing kinematics in hovering insect flight. *Journal of Fluid Mechanics*, 582:153–168, 2007.

[44] Torkel Weis-Fogh. Quick estimates of flight fitness in hovering animals, including novel mechanisms for lift production. *Journal of experimental Biology*, 59(1):169–230, 1973.

[45] Michael H Dickinson, Fritz-Olaf Lehmann, and Sanjay P Sane. Wing rotation and the aerodynamic basis of insect flight. *Science*, 284(5422):1954–1960, 1999.

[46] CP Ellington. The aerodynamics of hovering insect flight. v. a vortex theory. *Philosophical Transactions of the Royal Society B: Biological Sciences*, 305(1122):115–144, 1984.

[47] Tony Maxworthy. Experiments on the weis-fogh mechanism of lift generation by insects in hovering flight. part 1. dynamics of the fling. *Journal of Fluid Mechanics*, 93(1):47–63, 1979.

[48] David Rival and Cam Tropea. Characteristics of pitching and plunging airfoils under dynamic-stall conditions. *Journal of Aircraft*, 47(1):80–86, 2010.

[49] T Yilmaz, M Ol, and D Rockwell. Scaling of flow separation on a pitching low aspect ratio plate. *Journal of Fluids and Structures*, 26(6):1034–1041, 2010.

[50] Kenneth O Granlund, Michael V Ol, and Luis P Bernal. Unsteady pitching flat plates. *Journal of Fluid Mechanics*, 733:R5, 2013.

[51] Jeff D Eldredge. Numerical simulation of the fluid dynamics of 2d rigid body motion with the vortex particle method. *Journal of Computational Physics*, 221(2):626–648, 2007.

[52] Michael Ol, Jeff Eldredge, and Chengjie Wang. High-amplitude pitch of a flat plate: an abstraction of perching and flapping. *International Journal of Micro Air Vehicles*, 1(3), September 2009.

[53] Miguel R Visbal, Raymond E Gordnier, and Marshall C Galbraith. High-fidelity simulations of moving and flexible airfoils at low Reynolds numbers. *Experiments in Fluids*, 46(5):903–922, 2009.

[54] Daniel J Garmann and Miguel R Visbal. Numerical investigation of transitional flow over a rapidly pitching plate. *Physics of Fluids (1994-present)*, 23(9), 2011.

[55] AR Jones, CW Pitt Ford, and H Babinsky. Three-dimensional effects on sliding and waving wings. *Journal of Aircraft*, 48(2):633–644, 2011.

[56] Siddarth Kolluru Venkata and Anya R Jones. Leading-edge vortex structure over multiple revolutions of a rotating wing. *Journal of Aircraft*, 50(4):1312–1316, 2013.

[57] Field Manar, Albert Medina, and Anya R Jones. Tip vortex structure and aerodynamic loading on rotating wings in confined spaces. *Experiments in Fluids*, 55(9):1–18, 2014.

[58] M Bross and D Rockwell. Flow structure on a simultaneously pitching and rotating wing. *Journal of Fluid Mechanics*, 756:354–383, 2014.

[59] Zakery R Carr, Adam C DeVoria, and Matthew J Ringuette. Aspect-ratio effects on rotating wings: circulation and forces. *Journal of Fluid Mechanics*, 767:497–525, 2015.

[60] Daniel J Garmann, Miguel R Visbal, and Paul D Orkwis. Three-dimensional flow structure and aerodynamic loading on a revolving wing. *Physics of Fluids (1994-present)*, 25(3):034101, 2013.

[61] P. R. R. J. Stevens. *Unsteady Low Reynolds Number Aerodynamic Forces*. PhD thesis, University of Cambridge, 2015.

[62] CW Pitt Ford and Holger Babinsky. Lift and the leading-edge vortex. *Journal of Fluid Mechanics*, 720:280–313, 2013.

[63] Anya R Jones, Albert Medina, Hannah Spooner, and Karen Mulleners. Characterizing a burst leading-edge vortex on a rotating flat plate wing. *Experiments in Fluids*, 57(4):52, 2016.

[64] James HJ Buchholz, Melissa A Green, and Alexander J Smits. Scaling the circulation shed by a pitching panel. *Journal of Fluid Mechanics*, 688:591–601, 2011.

[65] Pooria Sattari, David E Rival, Robert J Martinuzzi, and Cameron Tropea. Growth and separation of a start-up vortex from a two-dimensional shear layer. *Physics of Fluids (1994-present)*, 24(10):107102, 2012.

[66] Jochen Kriegseis, Matthias Kinzel, and David E Rival. On the persistence of memory: do initial conditions impact vortex formation? *Journal of Fluid Mechanics*, 736:91–106, 2013.

[67] Jaime G Wong, Jochen Kriegseis, and David E Rival. An investigation into vortex growth and stabilization for two-dimensional plunging and flapping plates with varying sweep. *Journal of Fluids and Structures*, 43:231–243, 2013.

[68] A Widmann and C Tropea. Parameters influencing vortex growth and detachment on unsteady aerodynamic profiles. *Journal of Fluid Mechanics*, 773:432–459, 2015.

[69] M Lighthill. *Laminar Boundary Layers*. Oxford University Press, 1963.

[70] M Wolfinger and D Rockwell. Flow structure on a rotating wing: effect of radius of gyration. *Journal of Fluid Mechanics*, 755:83–110, 2014.

[71] Kristy L Schlueter, Anya R Jones, Kenneth Granlund, and Michael Ol. Effect of root cutout on force coefficients of rotating wings. *AIAA journal*, 52(6):1322–1325, 2014.

[72] Jan W Kruyt, GertJan F van Heijst, Douglas L Altshuler, and David Lentink. Power reduction and the radial limit of stall delay in revolving wings of different aspect ratio. *Journal of The Royal Society Interface*, 12(105):20150051, 2015.

[73] CA Ozen and Donald Rockwell. Flow structure on a rotating plate. *Experiments in fluids*, 52(1):207–223, 2012.

[74] D Kim and M Gharib. Experimental study of three-dimensional vortex structures in translating and rotating plates. *Experiments in Fluids*, 49(1):329–339, 2010.

[75] Zakery R Carr and Matthew J Ringuette. Flow structure of low-aspect-ratio-rotating wing from dye visualization. *AIAA Journal*, 52(5):1081–1086, May 2014.

[76] Charles P Ellington, Coen Van Den Berg, Alexander P Willmott, and Adrian LR Thomas. Leading-edge vortices in insect flight. *Nature*, 384(6610):626–630, 1996.

[77] James M Birch and Michael H Dickinson. Spanwise flow and the attachment of the leading-edge vortex on insect wings. *Nature*, 412(6848):729–733, 2001.

[78] Wei Shyy, Patrick Trizila, Chang-kwon Kang, and Hikaru Aono. Can tip vortices enhance lift of a flapping wing? *AIAA journal*, 47(2):289–293, 2009.

[79] TT Lim, CJ Teo, KB Lua, and KS Yeo. On the prolong attachment of leading edge vortex on a flapping wing. *Modern Physics Letters B*, 23(03):357–360, 2009.

[80] Craig J Wojcik and James HJ Buchholz. Parameter variation and the leading-edge vortex of a rotating flat plate. *AIAA journal*, 2014.

[81] Simon M Walker, Adrian LR Thomas, and Graham K Taylor. Deformable wing kinematics in free-flying hoverflies. *Journal of the Royal Society Interface*, page rsif20090120, 2009.

[82] A Roland Ennos. The inertial cause of wing rotation in diptera. *Journal of experimental biology*, 140(1):161–169, 1988.

[83] Stacey A Combes and Thomas L Daniel. Into thin air: contributions of aerodynamic and inertial-elastic forces to wing bending in the hawkmoth manduca sexta. *Journal of Experimental Biology*, 206(17):2999–3006, 2003.

[84] Hiroto Tanaka, John P Whitney, and Robert J Wood. Effect of flexural and torsional wing flexibility on lift generation in hoverfly flight. *Integrative and comparative biology*, 2011.

[85] Pinunta Rojratsirikul, Zhijin Wang, and Ismet Gursul. Unsteady aerodynamics of membrane airfoils. In *46th AIAA Aerospace Sciences Meeting and Exhibit, Reno, NV, Jan*, pages 7–10, 2008.

[86] Arnold Song, Xiaodong Tian, Emily Israeli, Ricardo Galvao, Kristin Bishop, Sharon Swartz, and Kenneth Breuer. Aeromechanics of membrane wings with implications for animal flight. *AIAA journal*, 46(8):2096–2106, 2008.

[87] Raymond E Gordnier. High fidelity computational simulation of a membrane wing airfoil. *Journal of Fluids and Structures*, 25(5):897–917, 2009.

[88] James M Akkala, Azar Eslam Panah, and James HJ Buchholz. Vortex dynamics and performance of flexible and rigid plunging airfoils. *Journal of Fluids and Structures*, 54:103–121, 2015.

[89] Hu Dai, Haoxiang Luo, and James F Doyle. Dynamic pitching of an elastic rectangular wing in hovering motion. *Journal of Fluid Mechanics*, 693:473–499, 2012.

[90] M Nicholas J Moore. Torsional spring is the optimal flexibility arrangement for thrust production of a flapping wing. *Physics of Fluids (1994-present)*, 27(9), 2015.

[91] C-K Kang, Hikaru Aono, Carlos ES Cesnik, and Wei Shyy. Effects of flexibility on the aerodynamic performance of flapping wings. *Journal of fluid mechanics*, 689:32–74, 2011.

[92] Peter M Mancini, Anya R Jones, Kenneth O Granlund, and Michael V Ol. Unsteady aerodynamic response of a rapidly started flexible wing. *International Journal of Micro Air Vehicles*, 7(2):147–157, 2015.

[93] AVT-202. Extensions of fundamental flow physics to practical MAV aerodynamics. Technical Report TR-AVT-202, NATO RTO, September 2014.

[94] K Granlund, M Ol, and L Bernal. Quasi-steady response of free-to-pivot flat plates in hover. *Journal of Fluids and Structures*, 40:337–355, 2013.

[95] Hui Wan, Haibo Dong, and George P Huang. Hovering hinge-connected flapping plate with passive deflection. *AIAA journal*, 50(9):2020–2027, 2012.

[96] Nathan Beals and Anya R Jones. Lift production by a passively flexible rotating wing. *AIAA Journal*, 2015.

[97] Chengyu Li, Haibo Dong, and Geng Liu. Effects of a dynamic trailing-edge flap on the aerodynamic performance and flow structures in hovering flight. *Journal of Fluids and Structures*, 58:49–65, 2015.

[98] Jeff D Eldredge, Jonathan Toomey, and Albert Medina. On the roles of chordwise flexibility in a flapping wing with hovering kinematics. *Journal of Fluid Mechanics*, 659:94–115, 2010.

[99] Jonathan Toomey and Jeff D Eldredge. Numerical and experimental study of the fluid dynamics of a flapping wing with low order flexibility. *Physics of Fluids (1994-present)*, 20(7), 2008.

[100] Marcos Vanella, Timothy Fitzgerald, Sergio Preidikman, Elias Balaras, and Balakumar Balachandran. Influence of flexibility on the aerodynamic performance of a hovering wing. *Journal of Experimental Biology*, 212(1):95–105, 2009.

[101] Hermann Glauert. *The force and moment on an oscillating aerofoil*. HM Stationery Office, 1929.

[102] Theodore Theodorsen. General theory of aerodynamic instability and the mechanism of flutter. *NACA Report*, (496), 1935.

[103] DI Pullin and Z Jane Wang. Unsteady forces on an accelerating plate and application to hovering insect flight. *Journal of Fluid Mechanics*, 509:1–21, 2004.

[104] Edward C Polhamus. Predictions of vortex-lift characteristics by a leading-edge suctionanalogy. *Journal of aircraft*, 8(4):193–199, 1971.

[105] Yeon Sik Baik, Luis P Bernal, Kenneth Granlund, and Michael V Ol. Unsteady force generation and vortex dynamics of pitching and plunging aerofoils. *Journal of Fluid Mechanics*, 709:37–68, 2012.

[106] Marvin A Jones. The separated flow of an inviscid fluid around a moving flat plate. *Journal of Fluid Mechanics*, 496:405–441, 2003.

[107] SA Ansari, R Żbikowski, and K Knowles. Non-linear unsteady aerodynamic model for insect-like flapping wings in the hover. part 1: methodology and analysis. *Proceedings of the Institution of Mechanical Engineers, Part G: Journal of Aerospace Engineering*, 220(2):61–83, 2006.

[108] J Katz. A discrete vortex method for the non-steady separated flow over an airfoil. *Journal of Fluid Mechanics*, 102:315–328, 1981.

[109] Ratnesh K Shukla and Jeff D Eldredge. An inviscid model for vortex shedding from a deforming body. *Theoretical and Computational Fluid Dynamics*, 21(5):343–368, 2007.

[110] Kiran Ramesh, Ashok Gopalarathnam, Jack R Edwards, Michael V Ol, and Kenneth Granlund. An unsteady airfoil theory applied to pitching motions validated against experiment and computation. *Theoretical and Computational Fluid Dynamics*, 27(6):843–864, 2013.

[111] Sanjay P Sane and Michael H Dickinson. The aerodynamic effects of wing rotation and a revised quasi-steady model of flapping flight. *Journal of experimental biology*, 205(8):1087–1096, 2002.

[112] Haithem E Taha, Muhammad R Hajj, and Philip S Beran. State-space representation of the unsteady aerodynamics of flapping flight. *Aerospace Science and Technology*, 34:1–11, 2014.

[113] Holger Babinsky, PRRJ Stevens, Anya R Jones, Luis P Bernal, and Michael V Ol. Low order modeling of lift forces for unsteady pitching and surging wings. In *54th AIAA Aerospace Sciences Meeting*, page 0290, 2016.

[114] Frank M Bos, David Lentink, BW Van Oudheusden, and Hester Bijl. Influence of wing kinematics on aerodynamic performance in hovering insect flight. *Journal of fluid mechanics*, 594:341–368, 2008.

[115] Pat Trizila, Chang-Kwon Kang, Hikaru Aono, Wei Shyy, and Miguel Visbal. Low-Reynolds-number aerodynamics of a flapping rigid flat plate. *AIAA journal*, 49(4):806–823, 2011.

[116] James Lankford, David Mayo, and Inderjit Chopra. Computational investigation of insect-based flapping wings for micro air vehicle applications. *International Journal of Micro Air Vehicles*, page 1756829316646640, 2016.

[117] John David Anderson Jr. *Fundamentals of aerodynamics*. McGraw-Hill Education, 2010.

[118] Joseph Katz and Allen Plotkin. *Low-speed aerodynamics*. Cambridge University Press, 2nd edition, 2001.

[119] Ronald L Panton. *Incompressible Flow*. John Wiley & Sons, 3rd edition, 2006.

[120] Louis M Milne-Thomson. *Theoretical Hydrodynamics*. Dover Publications, fifth edition, 1968.

[121] George Keith Batchelor. *An Itroduction to Fluid Dynamics*. Cambridge university press, 1967.

[122] X Xia and K Mohseni. Lift evaluation of a two-dimensional pitching flat plate. *Physics of Fluids*, 25(9):091901, 2013.

[123] SA Ansari, R Żbikowski, and K Knowles. Non-linear unsteady aerodynamic model for insect-like flapping wings in the hover. part 2: implementation and validation. *Proceedings of the Institution of Mechanical Engineers, Part G: Journal of Aerospace Engineering*, 220(3):169–186, 2006.

[124] FO Minotti. Unsteady two-dimensional theory of a flapping wing. *Physical Review E*, 66(5):051907, 2002.

[125] Jeff D. Eldredge. *Mathematical Modeling of Unsteady Inviscid Flow (in preparation)*. Personal Communication, 2017.

[126] TH VonKarman and WR Sears. Airfoil theory for non-uniform motion. *Journal of the Aeronautical Sciences*, 5(10):379–390, 1938.

[127] Hermann Glauert. *The elements of aerofoil and airscrew theory*. Cambridge University Press, 2nd edition, 1947.

[128] Marvin A Jones and Michael J Shelley. Falling cards. *Journal of Fluid Mechanics*, 540:393–425, 2005.

[129] John L Hess and AM Smith. Calculation of non-lifting potential flow about arbitrary three-dimensional bodies. Technical report, Douglas Aircraft Co Long Beach CA, 1962.

[130] JL Hess. Panel methods in computational fluid dynamics. *Annual Review of Fluid Mechanics*, 22(1):255–274, 1990.

[131] Georges-Henri Cottet and Petros D Koumoutsakos. *Vortex methods: theory and practice*. Cambridge university press, 2000.

[132] Philip G Saffman. *Vortex dynamics*. Cambridge university press, 1992.

[133] GS Winckelmans and Anthony Leonard. Contributions to vortex particle methods for the computation of three-dimensional incompressible unsteady flows. *Journal of Computational Physics*, 109(2):247–273, 1993.

[134] S Shankar and L Van Dommelen. A new diffusion procedure for vortex methods. *Journal of Computational Physics*, 127(1):88–109, 1996.

[135] Matthias Kirchhart and Shinnosuke Obi. A splitting-free vorticity redistribution method. *Journal of Computational Physics*, 330:282–295, 2017.

[136] Alexandre Joel Chorin. Numerical study of slightly viscous flow. *Journal of Fluid Mechanics*, 57(4):785–796, 1973.

[137] Alexandre Joel Chorin and Peter S Bernard. Discretization of a vortex sheet, with an example of roll-up. *Journal of Computational Physics*, 13(3):423–429, 1973.

[138] Robert Krasny. Desingularization of periodic vortex sheet roll-up. *Journal of Computational Physics*, 65(2):292–313, 1986.

[139] Georgios H Vatistas, V Kozel, and WC Mih. A simpler model for concentrated vortices. *Experiments in Fluids*, 11(1):73–76, 1991.

[140] Norman J Zabusky, MH Hughes, and KV Roberts. Contour dynamics for the euler equations in two dimensions. *Journal of computational physics*, 30(1):96–106, 1979.

[141] Mark J Stock, Werner JA Dahm, and Grétar Tryggvason. Impact of a vortex ring on a density interface using a regularized inviscid vortex sheet method. *Journal of Computational Physics*, 227(21):9021–9043, 2008.

[142] Bruno A Roccia, Sergio Preidikman, Julio C Massa, and Dean T Mook. Modified unsteady vortex-lattice method to study flapping wings in hover flight. *AIAA journal*, 51(11):2628–2642, 2013.

[143] MJ Stock. Summary of vortex method literature. via http://markjstock.org/research/, downloaded 12/24/2017, 2006.

[144] L Cortelezzi and A Leonard. Point vortex model of the unsteady separated flow past a semi-infinite plate with transverse motion. *Fluid dynamics research*, 11(6):263, 1993.

[145] L Cortelezzi. On the unsteady separated flow past a semi-infinite plate: Exact solution of the brown and michael model, scaling, and universality. *Physics of Fluids (1994-present)*, 7(3):526–529, 1995.

[146] Mark Drela. Xfoil: An analysis and design system for low Reynolds number airfoils. In *Low Reynolds number aerodynamics*, pages 1–12. Springer, 1989.

[147] Turgut Sarpkaya. Computational methods with vortices- the 1988 freeman scholar lecture. *ASME, Transactions, Journal of Fluids Engineering*, 111:5–52, 1989.

[148] Robert Krasny. Vortex sheet computations: roll-up, wakes, separation. *Lectures in Applied Mathematics*, 28(1):385–401, 1991.

[149] Robert Krasny and Monika Nitsche. The onset of chaos in vortex sheet flow. *Journal of Fluid Mechanics*, 454:47–69, 2002.

[150] Xi Xia and Kamran Mohseni. Unsteady aerodynamics and vortex-sheet formation of a two-dimensional airfoil. *Journal of Fluid Mechanics*, 830:439–478, 2017.

[151] IE Garrick. Propulsion of a flapping and oscillating airfoil. *NACA*, (567), 1937.

[152] Field Manar, Peter Mancini, David Mayo, and Anya R Jones. Comparison of rotating and translating wings: force production and vortex characteristics. *AIAA Journal*, 2016.

[153] Field Manar and Anya R Jones. Transient response of a single degree-of-freedom wing at high angle-of-attack. *AIAA Journal*, pages 1–12, 2017.

[154] Jeff D Eldredge, Chengjie Wang, and MV Ol. A computational study of a canonical pitch-up, pitch-down wing maneuver. In *39th AIAA Fluid Dynamics Conference*, San Antonio, TX, 22-25 June 2009 2009. AIAA 2009-3687.

[155] Min S Chong, Anthony E Perry, and Brian J Cantwell. A general classification of three-dimensional flow fields. *Physics of Fluids A: Fluid Dynamics*, 2(5):765–777, 1990.

[156] Julian CR Hunt, Alan A Wray, and Parviz Moin. Eddies, streams, and convergence zones in turbulent flows. In *Studying Turbulence Using Numerical Simulation Databases, 2. Proceedings of the 1988 Summer Program*, pages p 193–208, 1988.

[157] Jinhee Jeong and Fazle Hussain. On the identification of a vortex. *Journal of fluid mechanics*, 285:69–94, 1995.

[158] Jigen Zhou, Ronald J Adrian, S Balachandar, and TM Kendall. Mechanisms for generating coherent packets of hairpin vortices in channel flow. *Journal of fluid mechanics*, 387:353–396, 1999.

[159] Pinaki Chakraborty, S Balachandar, and Ronald J Adrian. On the relationships between local vortex identification schemes. *Journal of fluid mechanics*, 535:189–214, 2005.

[160] Václav Kolář, Pavel Moses, and Jakub Šístek. Triple decomposition method for vortex identification in two-dimensional and three-dimensional flows. In *Computational Fluid Dynamics 2010*, pages 225–231. Springer, 2011.

[161] R Cucitore, M Quadrio, and A Baron. On the effectiveness and limitations of local criteria for the identification of a vortex. *European Journal of Mechanics-B/Fluids*, 18(2):261–282, 1999.

[162] Matthew P Rockwood, Kunihiko Taira, and Melissa A Green. Detecting vortex formation and shedding in cylinder wakes using lagrangian coherent structures. *AIAA Journal*, 2016.

[163] Yangzi Huang and Melissa A Green. Detection and tracking of vortex phenomena using lagrangian coherent structures. *Experiments in Fluids*, 56(7):147, 2015.

[164] Melissa A Green, Clarence W Rowley, and Alexander J Smits. Using hyperbolic lagrangian coherent structures to investigate vortices in bioinspired fluid flows. *Chaos: An Interdisciplinary Journal of Nonlinear Science*, 20(1):017510, 2010.

[165] Melissa A Green, Clarence W Rowley, and George Haller. Detection of lagrangian coherent structures in three-dimensional turbulence. *Journal of Fluid Mechanics*, 572:111–120, 2007.

[166] Laurent Graftieaux, Marc Michard, and Nathalie Grosjean. Combining piv, pod and vortex identification algorithms for the study of unsteady turbulent swirling flows. *Measurement Science and Technology*, 12(9):1422, 2001.

[167] Horace Lamb. *Hydrodynamics*. Cambridge university press, 1932.

[168] Pijush Kundu, Ira Cohen, and David Dowling. *Fluid Mechanics*. Academic Press, 5th edition, 2012.

[169] William Richard Graham, CW Pitt Ford, and Holger Babinsky. An impulse-based approach to estimating forces in unsteady flow. *Journal of Fluid Mechanics*, 815:60–76, 2017.

[170] Simon J Corkery, PRRJ Stevens, and Holger Babinsky. Low Reynolds number surge response of a flat plate wing at 90 degrees incidence. In *AIAA SciTech Forum-55th AIAA Aerospace Sciences Meeting*, 2017.

[171] Osborne Reynolds. Xxix. an experimental investigation of the circumstances which determine whether the motion of water shall be direct or sinuous, and of the law of resistance in parallel channels. *Philosophical Transactions of the Royal Society of London*, 174:935–982, 1884.

[172] Brian Cabral and Leith Casey Leedom. Imaging vector fields using line integral convolution. In *Proceedings of the 20th annual conference on Computer graphics and interactive techniques*, pages 263–270. ACM, 1993.

[173] Detlev Stalling and Hans-Christian Hege. Fast and resolution independent line integral convolution. In *Proceedings of the 22nd annual conference on Computer graphics and interactive techniques*, pages 249–256. ACM, 1995.

[174] Leslie Greengard and Vladimir Rokhlin. A fast algorithm for particle simulations. *Journal of computational physics*, 73(2):325–348, 1987.

[175] Leon Van Dommelen and Elke A Rundensteiner. Fast, adaptive summation of point forces in the two-dimensional poisson equation. *Journal of Computational Physics*, 83(1):126–147, 1989.

[176] PRRJ Stevens, Holger Babinsky, F Manar, P Mancini, AR Jones, T Nakata, N Phillips, RJ Bomphrey, AC Gozukara, KO Granlund, et al. Experiments and computations on the lift of accelerating flat plates at incidence. *AIAA Journal*, pages 1–11, 2017.

[177] J Mayo Greenberg. Airfoil in sinusoidal motion in a pulsating stream. 1947.

[178] JG Leishman and KQ Nguyen. State-space representation of unsteady airfoil behavior. *AIAA journal*, 28(5):836–844, 1990.

[179] Hans Georg Kussner. Stresses produced in airplane wings by gusts. *NACA-TM-654*, 1932.

[180] William R Sears. Some aspects of non-stationary airfoil theory and its practical application. *Journal of the Aeronautical Sciences*, 8(3), 1941.

[181] JG Leishman. Validation of approximate indicial aerodynamic functions for two- dimensional subsonic flow. *Journal of Aircraft*, 25(10):914–922, 1988.

[182] Anatol Roshko. A new hodograph for free-streamline theory. *NACA-TR-3168*, 1954.

[183] DI Pullin. The large-scale structure of unsteady self-similar rolled-up vortex sheets. *Journal of Fluid Mechanics*, 88(3):401–430, 1978.

[184] Patrick Hammer, Aaron Altman, and Frank Eastep. Validation of a discrete vortex method for low Reynolds number unsteady flows. *AIAA journal*, 2014.

[185] L. Greengard. The fmmlib2d suite. https://cims.nyu.edu/cmcl/fmm2dlib/fmm2dlib.html.

[186] JC Wu. Theory for aerodynamic force and moment in viscous flows. *AIAA Journal*, 19(4):432–441, 1981.

[187] Ira Herbert Abbott and Albert Edward Von Doenhoff. *Theory of wing sections, including a summary of airfoil data*. Courier Corporation, 1959.

[188] CE Brennen. A review of added mass and fluid inertial forces. Technical report, Naval Civil Engineering Laboratory, 1982.

[189] Chris Chabalko, Richard D Snyder, Philip S Beran, and Gregory Parker. The physics of an optimized flapping wing micro air vehicle. In *47th AIAA Aerospace Sciences Meeting Including The New Horizons Forum and Aerospace Exposition*, pages 2009–801, 2009.

[190] Darwin Darakananda, Jeff Eldredge, Tim Colonius, and David R Williams. A vortex sheet/point vortex dynamical model for unsteady separated flows. In *54th AIAA Aerospace Sciences Meeting (AIAA SciTech)*, pages 4–8, 2016.

[191] RR Clements. An inviscid model of two-dimensional vortex shedding. *Journal of Fluid Mechanics*, 57(02):321–336, 1973.

[192] CC Lin. On the motion of vortices in two dimensions: I. existence of the kirchhoff-routh function. *Proceedings of the National Academy of Sciences of the United States of America*, 27(12):570–575, 1941.

[193] CC Lin. On the motion of vortices in two dimensions: Ii. some further investigations on the kirchhoff-routh function. *Proceedings of the National Academy of Sciences of the United States of America*, 27(12):575–577, 1941.

[194] CE Brown and WH Michael. Effect of leading-edge separation on the lift of a delta wing. *Journal of the Aeronautical Sciences (Institute of the Aeronautical Sciences)*, 21(10), 1954.

[195] Sébastien Michelin and Stefan G Llewellyn Smith. An unsteady point vortex method for coupled fluid–solid problems. *Theoretical and Computational Fluid Dynamics*, 23(2):127–153, 2009.

[196] Jeff D Eldredge. A reconciliation of viscous and inviscid approaches to computing locomotion of deforming bodies. *Experimental Mechanics*, 50(9):1349–1353, 2010.